

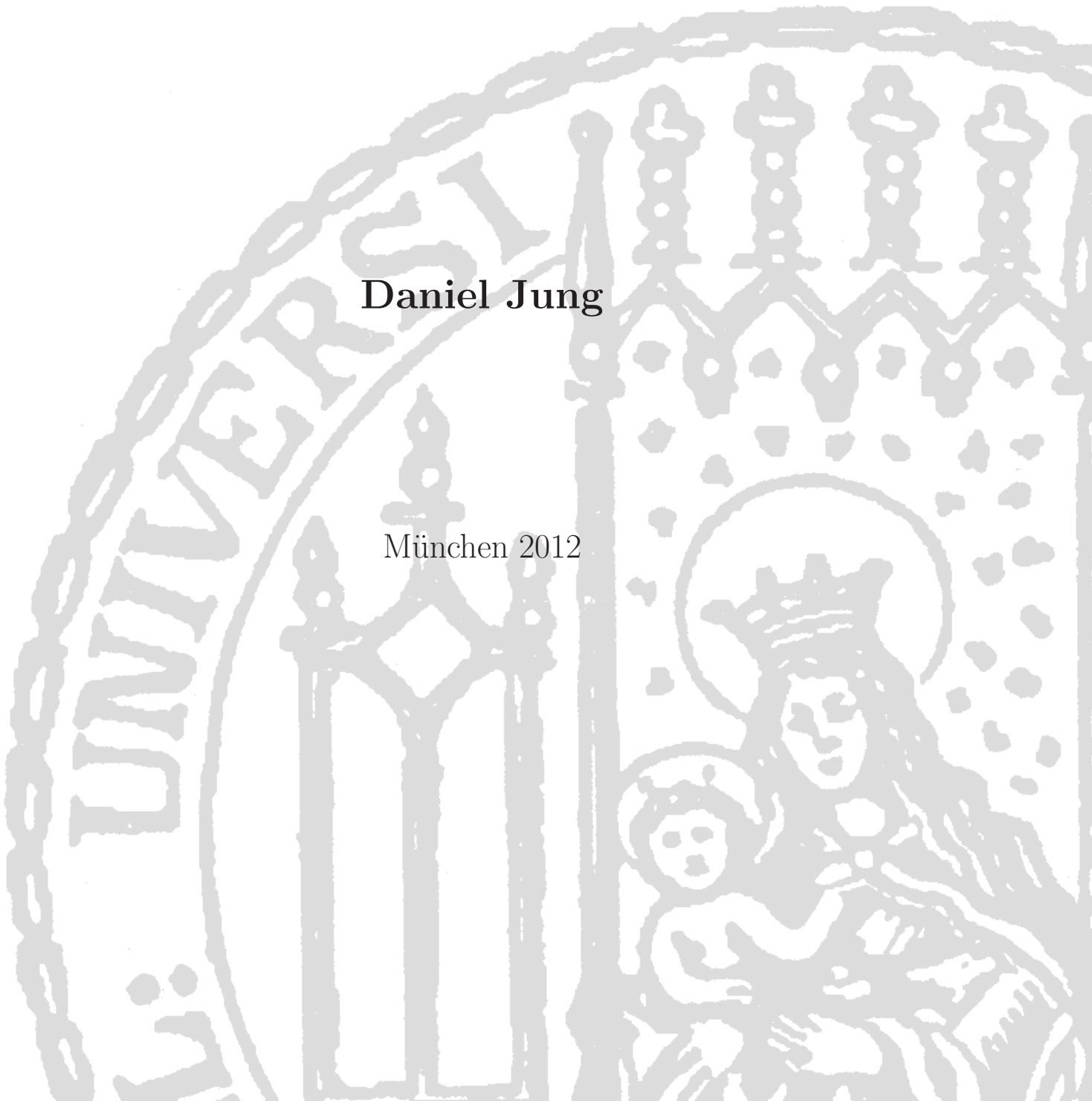
---

**Ion acceleration  
from relativistic  
laser nano-target interaction**

---

**Daniel Jung**

München 2012





---

**Ion acceleration  
from relativistic  
laser nano-target interaction**

---

**Dissertation**

an der Fakultät für Physik

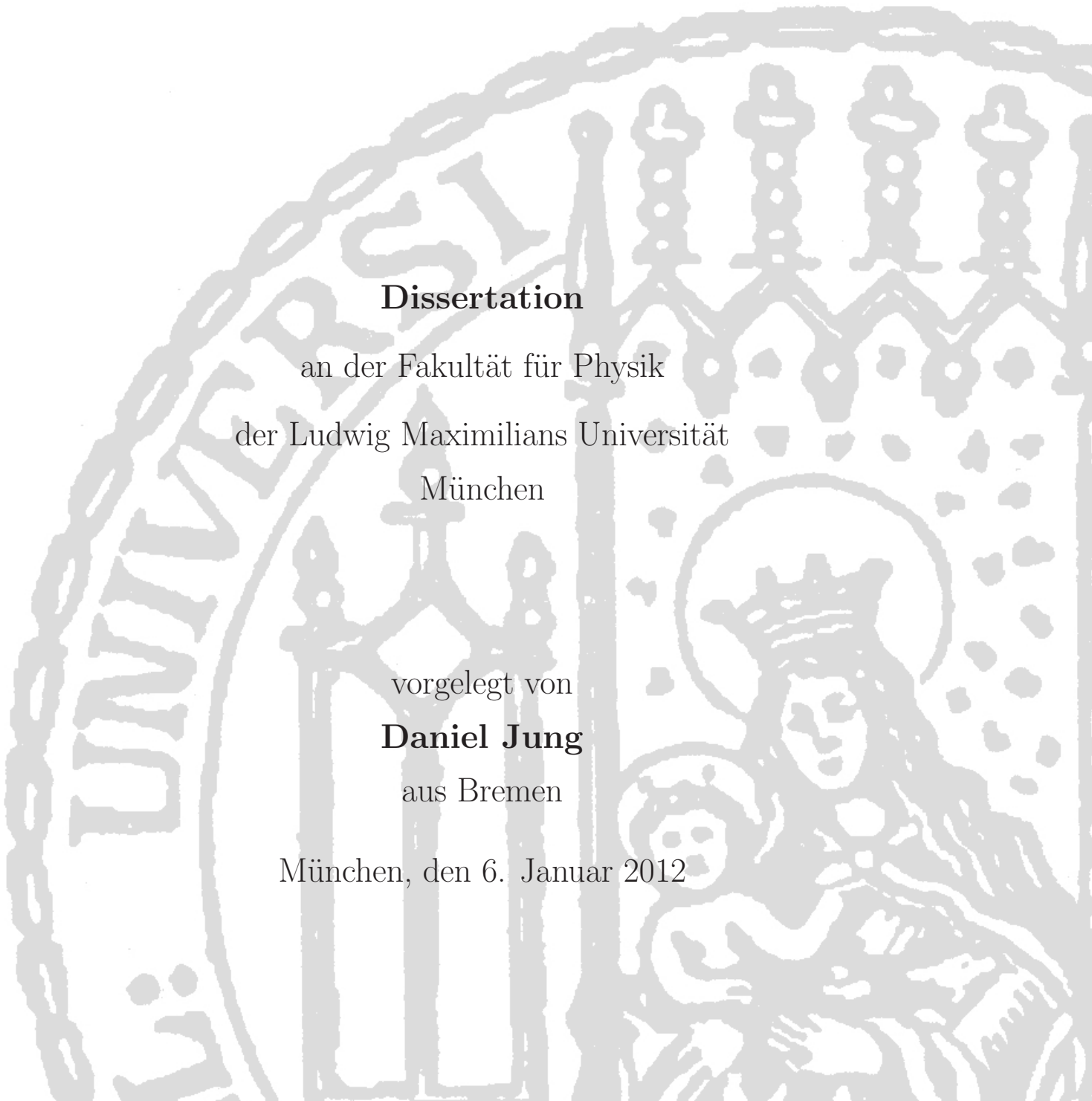
der Ludwig Maximilians Universität  
München

vorgelegt von

**Daniel Jung**

aus Bremen

München, den 6. Januar 2012



Erstgutachter: Prof. Dr. Dietrich Habs

Zweitgutachter: Prof. Dr. Jörg Schreiber

Tag der mündlichen Prüfung: 9. Februar 2012

Unclassified - LA-UR 12-00308

*In theory, there is no difference between theory and practice. But, in practice,  
there is.*

[J. L. A. van de Snepscheut]



# Abstract

Laser-ion acceleration has been of particular interest over the last decade for fundamental as well as applied sciences. Remarkable progress has been made in realizing laser-driven accelerators that are cheap and very compact compared with conventional rf-accelerators. Proton and ion beams have been produced with particle energies of up to 50 MeV and several MeV/u, respectively, with outstanding properties in terms of transverse emittance and current. These beams typically exhibit an exponentially decaying energy distribution, but almost all advanced applications, such as oncology, proton imaging or fast ignition, require quasi-monoenergetic beams with a low energy spread. The majority of the experiments investigated ion acceleration in the target normal sheath acceleration (TNSA) regime with comparably thick targets in the  $\mu\text{m}$  range.

In this thesis ion acceleration is investigated from nm-scaled targets, which are partially produced at the University of Munich with thickness as low as 3 nm. Experiments have been carried out at LANL's Trident high-power and high-contrast laser (80 J, 500 fs,  $\lambda=1054$  nm), where ion acceleration with these nano-targets occurs during the relativistic transparency of the target, in the so-called Break-out afterburner (BOA) regime. With a novel high resolution and high dispersion Thomson parabola and ion wide angle spectrometer, thickness dependencies of the ions angular distribution, particle number, average and maximum energy have been measured. Carbon  $\text{C}^{6+}$  energies reached 650 MeV and 1 GeV for unheated and heated targets, respectively, and proton energies peaked at 75 MeV and 120 MeV for diamond and  $\text{CH}_2$  targets. Experimental data is presented, where the conversion efficiency into carbon  $\text{C}^{6+}$  (protons) is investigated and found to have an up to 10fold (5fold) increase over the TNSA regime.

With circularly polarized laser light, quasi-monoenergetic carbon ions have been generated from the same nm-scaled foil targets at Trident with an energy spread of as low as  $\pm 15\%$  at a central energy of 35 MeV. High resolution kinetic simulations show that the acceleration is based on the generation of ion solitons due to the circularly polarized laser. The conversion efficiency into monoenergetic ions is increased by an order of magnitude compared with previous results in the TNSA regime. The advances in ion energies and the control over the spectra mark an important basis for future research of laser-driven ion acceleration and might enable laser-based implementation of these applications in the future.



## Zusammenfassung

Seit nunmehr über 10 Jahren wird intensive Grundlagenforschung im Bereich der Laserionenbeschleunigung betrieben. Im Vordergrund steht dabei die Realisierung laserbasierter Beschleuniger als kostengünstige und kompakte Alternative zu konventionellen Beschleunigeranlagen. Die meisten Experimente wurden mit Folien im  $\mu\text{m}$ -Bereich durchgeführt und dementsprechend im Bereich der *Target Normal Sheath Acceleration* (TNSA). Dabei wurden Protonen (Ionen) mit bis zu 50 MeV (einigen MeV/u) erzeugt mit sehr guter Emittance und sehr hohen Strömen. Die vergleichsweise niedrigen Energien und das in der Regel exponentiell abfallende Spektrum machen die Teilchenstrahlen für die meisten Anwendungen, wie z. B. der Onkologie oder der Fusion, die ein monoenergetisches Spektrum benötigen, unbrauchbar.

In dieser Arbeit werden nun Ergebnisse zur Ionenbeschleunigung vorgestellt, welche zur Lösung dieses Problems beitragen könnten. Dazu wurden an der LMU München Diamantfolien mit Dicken von nur 3 nm hergestellt und an LANL's Hochenergie und Hochkontrast Laser (80 J, 500 fs,  $\lambda=1054$  nm) zur Ionenbeschleunigung verwendet, welche während der relativistischen Transparenz des Targets stattfindet, dem sogenannten *Break-Out Afterburner* (BOA) Mechanismus. Mit einer hochauflösenden Thomson Parabel und einem eigens entwickelten Ionenweitwinkelspektrometer wurden die Winkelverteilung, Teilchenzahl und die mittlere und maximale Energie in Abhängigkeit der Targetdicke gemessen. Für  $\text{C}^{6+}$  wurden Energien von 650 MeV (1 GeV) mit ungeheizten (geheizten) Targets gemessen und für Protonen 75 MeV (120 MeV mit  $\text{CH}_2$  Folien). Des Weiteren zeigen die experimentellen Daten Anstieg in der Konversionseffizienz für  $\text{C}^{6+}$  (Protonen) um einen Faktor 10 (5) gegenüber dem TNSA Mechanismus. Mit zirkularpolarisiertem Licht konnten außerdem monoenergetische  $\text{C}^{6+}$  Strahlen erzeugt werden, wobei die Energiebandbreite  $\pm 15\%$  beträgt bei einer mittleren Energie von 35 MeV. Hochauflösende Simulationen haben gezeigt, dass diese monoenergetischen Spektren durch Ionensolitonen, welche durch das zirkulare Laserlicht ermöglicht werden, entstehen. Die Konversionseffizienz ist dabei über eine Größenordnung höher als bei bisherigen Ergebnissen zu TNSA. Die Verbesserung der Ionenenergien und der Energiespektren stellt eine wichtige Basis für zukünftige Forschung im Bereich der Ionenbeschleunigung dar und könnte bald Anwendungen mit kompakten, laserbasierten Ionenquellen ermöglichen.



# Contents

<b>Abstract</b>	<b>7</b>
<b>Zusammenfassung</b>	<b>9</b>
<b>Contents</b>	<b>i</b>
<b>List of Figures</b>	<b>iii</b>
<b>1 Introduction</b>	<b>1</b>
1.1 A decade of laser-driven ion acceleration . . . . .	1
1.1.1 Ion beam therapy of cancer . . . . .	3
1.1.2 Ion fast ignition . . . . .	5
1.1.3 Active interrogation . . . . .	6
1.2 Thesis overview . . . . .	7
<b>2 Relativistic laser-matter interaction</b>	<b>9</b>
2.1 Relativistic laser intensities . . . . .	9
2.1.1 Motion of a single electron in the laser field . . . . .	10
2.2 Laser-induced relativistic plasmas . . . . .	14
2.2.1 Laser-induced ionization . . . . .	14
2.2.2 Laser transport in plasmas . . . . .	17
2.2.3 Relativistic transparency . . . . .	19
2.2.4 Self focusing . . . . .	20
2.2.5 Laser absorption and energy transfer in plasmas . . . . .	21
2.2.6 Plasma instabilities . . . . .	24
2.3 Laser-driven ion acceleration . . . . .	26
2.3.1 Target normal sheath acceleration . . . . .	27
2.3.2 Radiation pressure acceleration (RPA) . . . . .	30

2.3.3	Break-out afterburner (BOA) . . . . .	34
<b>3</b>	<b>Methods: Laser, targets and diagnostics</b>	<b>43</b>
3.1	A short introduction into Lasers and laser beams . . . . .	43
3.1.1	Chirped pulse amplification (CPA) . . . . .	44
3.1.2	Time-bandwidth product . . . . .	44
3.1.3	The Trident laser facility . . . . .	45
3.1.4	Trident laser focus . . . . .	47
3.1.5	Trident laser contrast . . . . .	49
3.2	Targets and target fabrication . . . . .	53
3.3	Target alignment . . . . .	58
3.4	Particle detectors . . . . .	60
3.4.1	Detector materials . . . . .	61
3.4.2	The Thomson parabola . . . . .	64
3.4.3	The high resolution ion wide angle spectrometer . . . . .	71
<b>4</b>	<b>Ion acceleration during relativistic transparency</b>	<b>79</b>
4.1	Experimental Setup . . . . .	82
4.2	Proton and carbon ion acceleration . . . . .	83
4.2.1	Thickness scaling . . . . .	86
4.2.2	The problem with the protons . . . . .	92
4.2.3	Efficient acceleration of ions with $Z > 1$ . . . . .	95
4.2.4	Angular energy dependency . . . . .	97
4.2.5	Conversion efficiency . . . . .	103
4.2.6	Energy scaling . . . . .	112
4.3	Optimizing BOA for maximum carbon and proton energies . . . . .	115
4.4	Mono-energetic ion beams from BOA . . . . .	118
4.4.1	BOA soliton acceleration . . . . .	122
<b>5</b>	<b>Summary and perspectives</b>	<b>131</b>
5.1	Summary and conclusions . . . . .	132
5.2	Outlook and perspectives . . . . .	137
	<b>References</b>	<b>141</b>
	<b>Peer reviewed publications</b>	<b>163</b>

# List of Figures

1.1	Linear accelerator and table-top laser . . . . .	2
1.2	Hadron cancer therapy . . . . .	4
1.3	Active interrogation . . . . .	7
2.1	$e^-$ motion in relativistic laser field . . . . .	13
2.2	$e^-$ motion in relativistic laser focus . . . . .	14
2.3	Self-focusing in relativistic plasma . . . . .	22
2.4	Target Normal Sheath Acceleration . . . . .	28
2.5	Radiation Pressure Acceleration . . . . .	32
2.6	BOA VPIC simulation . . . . .	35
2.7	Sketch of the Break-out Afterburner . . . . .	37
2.8	Break-out Afterburner prediction for Trident . . . . .	40
3.1	Chirped pulse amplification . . . . .	44
3.2	Trident laser schematics . . . . .	46
3.3	Raw focus image . . . . .	47
3.4	Focus analysis . . . . .	48
3.5	OPAPE cleaning . . . . .	50
3.6	Trident laser contrast . . . . .	51
3.7	“Good” and “bad” laser contrast . . . . .	52
3.8	Cathodic arc deposition . . . . .	54
3.9	DLC targets . . . . .	56
3.10	DLC characterization I . . . . .	57
3.11	DLC characterization II . . . . .	58
3.12	Target and focus alignment . . . . .	59
3.13	CR39 analysis . . . . .	62
3.14	Sketch of a Thomson parabola . . . . .	65

## LIST OF FIGURES

---

3.15 Thomson parabola at different energy resolutions . . . . .	67
3.16 Mother of all Thomson parabolas . . . . .	69
3.17 Corruption of Thomson parabola traces I . . . . .	71
3.18 Corruption of Thomson parabola traces II . . . . .	72
3.19 Sketch of iWASP setup . . . . .	73
3.20 Raw iWASP data . . . . .	74
3.21 iWASP calibration . . . . .	76
3.22 Angularly resolved proton spectrum . . . . .	77
4.1 Experimental setup . . . . .	83
4.2 Carbon $C^{6+}$ and $H^+$ spectra . . . . .	84
4.3 Data of the 6 experimental campaigns at a glance . . . . .	85
4.4 Thickness scaling for $C^{6+}$ . . . . .	87
4.5 a) Laser on-target contrast in comparison with a $\sin^2$ laser envelope	88
4.6 Optimum target thickness and initial target density . . . . .	90
4.7 Optimum target thickness in the analytical model . . . . .	91
4.8 Thickness scaling for $H^+$ . . . . .	93
4.9 Proton self-cleaning . . . . .	94
4.10 $C^{6+}$ and $H^+$ velocity ratios . . . . .	96
4.11 Snapshot of BOA acceleration in a 3D VPIC simulation . . . . .	97
4.12 Maximum ion energies on- and off-axis . . . . .	99
4.13 Integrated particle numbers vs. angle . . . . .	100
4.14 Ion lobes in the BOA acceleration . . . . .	101
4.15 Estimating the conversion efficiency from the measurements . . .	104
4.16 Carbon $C^{6+}$ and proton conversion efficiency . . . . .	105
4.17 Thickness scaling for the average particle energy . . . . .	106
4.18 Thickness scaling for particle numbers . . . . .	107
4.19 Energy gain during BOA . . . . .	110
4.20 Conversion efficiency in comparison with the model and VPIC sim- ulations . . . . .	111
4.21 Pulse duration dependency of the BOA mechanism . . . . .	113
4.22 Energy scaling of the BOA mechanism . . . . .	114
4.23 1 GeV carbon ions from a heated diamond target . . . . .	116
4.24 120 MeV protons from a $CH^2$ foil target . . . . .	117
4.25 From exponentially decaying to mono-energetic spectra . . . . .	118

## LIST OF FIGURES

---

4.26	Mono-energetic $H^+$ spectra with CP laser light (I) . . . . .	120
4.27	Mono-energetic $H^+$ spectra with CP laser light (II) . . . . .	121
4.28	Mono-energetic $C^{6+}$ spectra with CP laser light . . . . .	123
4.29	Simulation of the BOA-soliton acceleration . . . . .	125
4.30	BOA-soliton acceleration at higher laser intensities . . . . .	128
5.1	Backscatter with OPAPE cleaned frontend . . . . .	133

## LIST OF FIGURES

---

# Chapter 1

## Introduction

### 1.1 A decade of laser-driven ion acceleration

The history of the laser started in 1917 with Albert Einstein setting the basic theory for stimulated emission [1]. The first realization of an optical laser took place more than 40 years later by Theodore Maiman [2] in 1960. With the implementation of Q-switching [3], mode-locking [4, 5] and finally the chirped pulse amplification by D. Strickland and G. Mourou in 1985, it was possible to build a “table-top” laser system. These systems are capable of generating laser pulses exceeding 10th of TW up to several PW and focused laser intensities exceeding the relativistic limit of  $10^{18}\text{W}/\text{cm}^2$  by orders of magnitude. In the last 10 to 15 years experimental ion acceleration with high-intensity lasers has been an active research topic [6–14] driven by the goal to develop a compact and cheap alternative to conventional radio-frequency accelerators. In the linear accelerator (Linac), patented by R. Widerøe in 1928, electrons, protons and ions are accelerated by a series of oscillating electric potentials over a acceleration length of several meters to hundreds of meters; the accelerating fields of the Linac are limited by the breakdown voltage to about 100 MV/m. At LANL’s Linac, the Los Alamos Neutron Science Center (LANSCE, see Fig 1.1), protons are accelerated over a distance of 1 km to energies of up to 800 MeV with a very narrow energy spread. In the laser-driven ion acceleration, the accelerating fields present in the plasma are not limited by the breakdown voltage and have already exceeded several TV/m [15] allowing acceleration of particles to MeV energies within a few

## LANSCE



## Trident Laser facility



Figure 1.1: Left frame: Los Alamos Neutron Science Center (LANSCE) with its 1 km long linear accelerator to generate protons of up to 800 MeV. Middle and right frame: LANL's Trident Laser facility building and table-top front-end, where protons with 120 MeV and carbon  $C^{6+}$  ions with 1 GeV can be generated.

micrometers. In the past the target normal sheath acceleration (TNSA) [6, 7, 15–17] has been investigated intensively. In these TNSA experiments, hot thermal electrons are generated at the critical density in the preplasma at the front of the target. They propagate through the target and set up a sheath field at the rear surface, where protons and ions are accelerated normal to the target surface over a very short distance to energies of up to 67 MeV [6, 18] with conversion efficiencies on the order of 1-2% (e.g. Ref. [16, 17]). These beams have been produced with outstanding properties in terms of transverse/longitudinal emittance ( $< 0.004$  mm mrad /  $< 10^{-4}$  eVs), outperforming conventional accelerators by two orders of magnitude [19]. Acceleration of heavier ions ( $Z > 1$ ) in the TNSA regime has been less efficient with energies of  $\sim 5$  MeV/u [7, 20, 21] and typically requires removal of the hydro-carbon contamination surface of the targets, which strongly limits the usability for advanced applications. However, the accelerated ions usually exhibit broad exponential energy spectra. Almost all prospective applications for these ion beams, including oncology [22], proton imaging [23] or ion fast ignition [24, 25] require quasi-monoenergetic beams with a low energy spread as provided by a rf-accelerator. By using in-situ engineered targets, quasi-monoenergetic spectra have been generated in the TNSA regime, but with a very low ion flux [26, 27] not competitive with conventional Linacs.

To improve the maximum particle energies, the energy spectrum and the con-

## 1. INTRODUCTION

---

version efficiency, other laser-ion acceleration mechanisms have been studied in numerical experiments using PIC-codes on massively parallel supercomputers. The most studied ones are the radiation pressure acceleration (RPA) [10–14] and the Break-Out Afterburner (BOA) [28–31]. Typically, these mechanisms efficiently transfer the laser’s energy to all target ions in contrast to the TNSA. In the RPA regime, the light pressure of a linearly polarized fs-laser pulse exceeding  $10^{23}$  W/cm<sup>2</sup> drives an overcritical nm-scaled target in the laser piston regime [14]; at lower intensities RPA is predicted to occur with circularly polarized laser light. Simulations have shown that for a single species target, the laser can drive the plasma as a single block to a monoenergetic ion spectrum with ultra-high energies. In the BOA regime, the laser penetrates a classically overdense, yet relativistically underdense target. Strong volumetric heating [30] of virtually all plasma electrons enables acceleration of protons and ions to energies in the 100 MeV and 1 GeV range (see Chap. 4) with the Trident laser. These new mechanisms however, have much more demanding requirements for the laser parameters, such as an ultrahigh laser contrast (RPA, BOA), flat top focusing (RPA) and ultra-high laser intensities ( $> 5 \times 10^{19}$  for BOA,  $> 1 \times 10^{22}$  for light sail RPA). Those stringent requirements have only allowed first tentative steps towards RPA [32, 33], so far not realizing its full potential. For acceleration of particles in the BOA regime, LANL’s Trident laser facility is one of the very few systems currently available, that meets these requirements. In the framework of this thesis, substantial increase in maximum carbon C<sup>6+</sup> energies has been demonstrated and progress has been made in manipulating the energy spectra [31, 34, 35] marking an important step towards a competitive alternative to conventional rf-accelerators. The low costs (compared with rf-accelerators) and compact size of the lasers could lead to a widespread implementation of laser-ion acceleration based applications, such as the ion beam therapy of cancer, which today is only available to very few people at only a handful places around the globe.

### 1.1.1 Ion beam therapy of cancer

The ion beam therapy (IBT) of cancer offers optimum dose deposition in the tumor tissue superior to conventional treatment with X-rays. Protons and heavier ions ( $Z > 1$ ) that penetrate a material (other than vacuum) deposit most of their kinetic energy right before they are stopped at the so-called Bragg peak. Fig. 1.2

## 1.1. A DECADE OF LASER-DRIVEN ION ACCELERATION

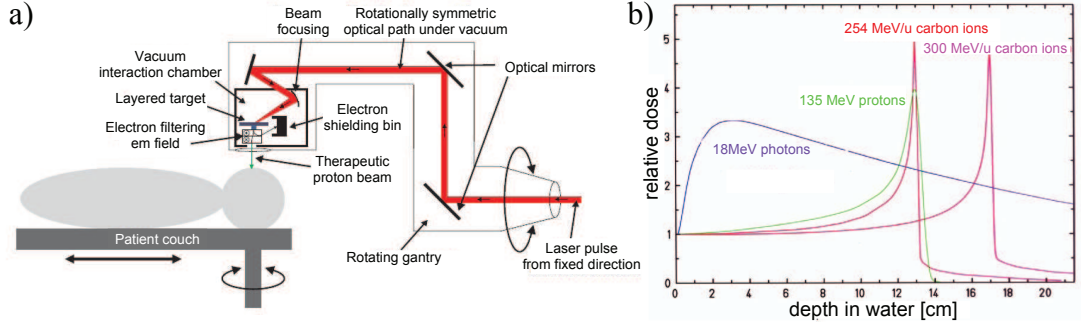


Figure 1.2: a) Schematic depiction of a laser-driven hadron cancer therapy. Comparison of photon and ion energy deposition in water b), where the ions deposit most of their energy end the end of their path around the Bragg peak.

b) shows the energy deposition of protons and carbon ions in comparison with photons in water (which makes most of the human body), where the photons lose most of their energy at the beginning. The depth of the Bragg peak on the other hand, can easily be controlled by changing the initial kinetic energy of the particles, so that healthy tissue in the path of the particle beam receives a much lower dose than the tumor itself. To treat a tumor at virtually any position in a human body, mono-energetic protons of up to  $\sim 250$  MeV or mono-energetic carbon  $C^{6+}$  ions of up to  $\sim 300$  MeV/u are necessary. The recently completed Heidelberg Ion-Beam Therapy Center (HIT) [36, 37] offers protons and a variety of heavier ions of up to 221 MeV and 430 MeV/u, respectively. HIT has a gantry system that weighs 660 metric tons of which 600 are movable to rotate the ion beam by  $360^\circ$ . The gantry alone is three stories high and 25 m long. The particles are accelerated in a synchrotron that is seeded by a 5 m long Linac. The costs for the facility are about 119 Million Euro. A laser-driven solution of the IBT could not only significantly reduce the costs but also the size of the facility. Fig. 1.2 a) depicts such a solution, where the gantry only guides the laser beam and the ions are generated as close as possible to their destination.

For a successful treatment of a tumor, a dose between 2 Gy and 10 Gy ( $1 \text{ Gy} = 1 \text{ J/Kg}$ ) is necessary depending on its type (where particles typically deposit  $1/3$  to  $2/3$  of their energy on the way to the tumor). This correlates to  $2 \times 10^{10}$  protons at 250 MeV stopped in 1 Kg. Depending on the number of particles that are available per pulse and the volume of the tumor, a full treatment can require several 10.000 pulses.

## 1. INTRODUCTION

---

Right now, laser-driven implementation of an IBT is still at a level of basic research, where major problems are that

- proton and especially carbon ion energies from laser-ion acceleration are up to an order of magnitude too low.
- the energy spectra are exponentially decaying and usually far from being monoenergetic ( $\Delta E/E \gg 10\%$ ).
- high power lasers have repetition rates of typically 1 shot per hour.

A path to solve some of these problems will be discussed in Chap. 4 of this thesis.

### 1.1.2 Ion fast ignition

Fusion is another potential application for laser-driven ion sources and aims for producing energy in a much cleaner way than coal or nuclear/fission power plants do. Today there are two major schemes that are being researched in order to achieve fusion, which are the magnetic confinement fusion (MCF) and the inertial confinement fusion (ICF). In both schemes the fuel has to be heated to  $\sim 10$  keV (deuterium and tritium fuel) for a certain time so that fusion occurs at a feasible high rate.

In the MCF, a low density plasma ( $10^{15} \text{ cm}^{-3}$ ) is confined for a few seconds and heated in a large toroidal magnetic field, a so-called tokamak. The international thermonuclear experimental reactor (ITER) [38], currently being build in France, will have the largest and most advanced tokamak [39, 40]. Its completion is scheduled for 2019, where the costs for this facility range between 5 and 16 billion Euro.

In ICF [41, 42] a fuel pellet is compressed to ultra-high densities ( $10^{26} \text{ cm}^{-3}$ ) and heated within nanoseconds. In the direct ICF approach [43] the pellet is compressed by multiple laser beams focused onto the surface of the spherical pellet, which requires precise temporal tailoring of the beams and a nearly perfect spherical symmetric irradiation geometry. In indirect ICF [44] the pellet is positioned within a hohlraum. The interior walls of this radiation confinement cavity are heated by these lasers instead, which convert the laser light into soft x-ray radiation, that evenly compresses and heats the pellet. The National Ignition Facility

## 1.1. A DECADE OF LASER-DRIVEN ION ACCELERATION

---

(NIF) [45] at the Lawrence Livermore National Laboratory (LLNL) works on the indirect ICF scheme and irradiates hohlraum targets with 192 laser with a total of 1.8 MJ in laser energy.

In a modified scheme of the ICF the pellet is pre-compressed by direct/indirect laser irradiation and ignited with a beam of electrons or protons/ions, mainly in order to relax the symmetry requirements, but also to increase the gain and to reduce the energy requirements for the driver, which here only has to compress and not to heat the pellet. [46]. This method is called fast ignition (FI), where the use of protons or ions brings the advantage that energy deposition is much more localized at the Bragg peak compared to electron fast ignition. In the scheme of ion fast ignition a monoenergetic beam of protons or carbon ions is needed with an energy spread  $\Delta E/E$  of less than 10% (for  $C^{6+}$ ) at an central energy of 7 – 20 MeV [47] and  $\sim 450$  MeV [24] (for typical pellet dimensions), respectively. The use of a laser-driven ion accelerator would again significantly reduce the size of the setup and remove the requirement for a complex beam guiding system. In such a scenario, the conversion efficiency from laser energy into ions dictates the necessary laser energy. In the case of the carbon FI, where an ion beam power density of  $\sim 10$  kJ/10 ps is suggested, a conversion efficiency of 10% relates to a 1 kJ drive laser for the ion acceleration. The previously mentioned TNSA mechanism is unlikely to be able to deliver these parameters. While the energies might be reached, a high conversion efficiency into these energies seems to be impossible at the moment. However, the BOA regime that is investigated in great detail in Chap. 4 seems to be a promising mechanism for a carbon driven fast ignition concept in the future.

### 1.1.3 Active interrogation

Next to medicine and energy production, laser-driven acceleration has also been envisioned for applications in the threat reduction for national/homeland security. Here, the objective is to determine the presence or absence of fissile materials such as weapons-grade Pu or highly enriched uranium (HEU) in an object of unknown content, such as a truck or a container ship (see Fig. 1.3). The passive detection of fissile materials suffers from the fact that  $\gamma$ -ray and neutron emission from spontaneous fission can easily be shielded with layers of lead and (borated) polyethylene. In the active interrogation the radiation signatures of the fissile

## 1. INTRODUCTION

---

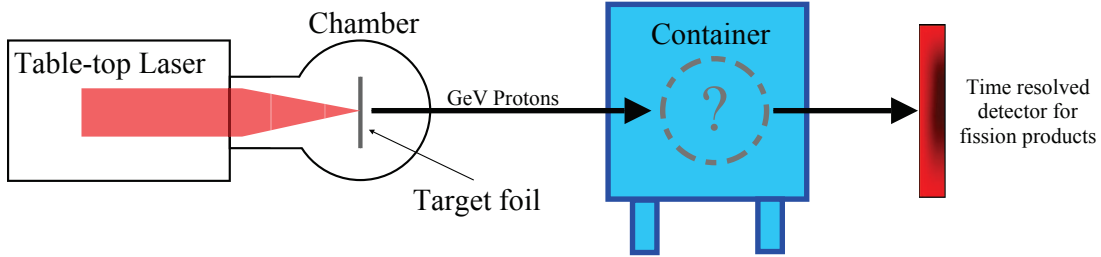


Figure 1.3: Schematic depiction of a laser-driven active interrogation, where the high energy proton beam is used to probe an container for fissile material.

material can be increased enormously provided the probe beam can penetrate the shielding. The increased signal of the delayed neutron and  $\gamma$ -signatures offers improved detection of fissile and fissionable material. Probe beams consisting of neutrons ( $\sim 14$  MeV) or  $\gamma$ -rays ( $\sim 15$  MeV) are currently being explored [48, 49], but can also be blocked by the same shielding. The use of protons as a probe beam offers [50] a much better attenuation length at a similar fission cross-section of about 1 barn, where a 1 GeV proton can penetrate 0.5 m of lead shielding. It is also possible to guide the proton probe beam with magnetic optics, to achieve a higher flexibility of such a setup. At the moment, proton beams of these energies can only be generated at conventional rf-accelerators, such as LANSCE. With a laser-driven source, the proton active interrogation could not only be made much cheaper, but also highly mobile when installed on a ship or large truck. Proton maximum energies have stagnated at about 50 MeV for the past 10 years in the TNSA regime. In the framework of this these, proton energies exceeding 100 MeV have been generated in the BOA regime with a comparably low laser power of only 100 TW. With a favorable energy scaling, proton energies could reach the necessary energies for active interrogation in the near future and allow a compact and very effective tool for detecting fissile materials.

## 1.2 Thesis overview

The main topic of the thesis is carbon  $C^{6+}$  ion and proton acceleration from nm-scaled foil targets in the relativistic transparent regime, the Break-Out afterburner (BOA). For the research 6 experimental campaigns have been fielded at LANL's Trident laser facility investigating the physics of the BOA regime. The

thesis is divided into 5 chapters, where the first one is this introduction followed by

- the second chapter, which gives an introduction into relevant plasma physics and laser-plasma interactions followed by an overview of the most important ion acceleration mechanisms that are currently being researched.
- the third chapter that gives an overview of LANL's Trident laser with an in-detail description of the laser contrast and its importance to the experiments. It follows a description of the targets and the target production and the alignment procedures. The chapter ends with an overview of the used particle spectrometers and detectors.
- the fourth chapter that presents and explains the results of the 6 experimental campaigns fielded at Trident. It covers the principal acceleration of protons and carbon  $C^{6+}$  ions in the BOA regime and investigates the energy, conversion efficiency and divergence scaling with thickness and the laser polarization impact on the accelerated particle beams, especially in terms of their spectral shape.
- the fifth and last chapter, where the results are summarized and future perspectives and plans concluding this research are presented.

# Chapter 2

## Relativistic laser-matter interaction

This chapter is intended to give a brief introduction into relativistic laser-matter interactions, i.e., physical phenomena that arise when a laser pulse with relativistic laser intensities interacts with a (solid) target. In such an interaction the target is rapidly ionized under the laser light and turns into a highly transient plasma of particular interest to this thesis. With relativistic laser intensities the plasma electrons are accelerated to relativistic quiver energies, opening a field of plasma physics which has only recently started to be investigated experimentally in greater detail. Relativistic laser-plasma interactions are the source of not only laser-driven ion acceleration, but also many other interesting research fields covering for example the high order harmonic generation [51] (HHG) and the electron wake field acceleration [52]. These interactions exhibit a huge number of different physics, as the laser intensities steadily increase and enable hotter and denser plasmas and higher fields. This introductory chapter will only highlight the most important aspects - which are of particular interest to laser-driven ion acceleration - starting with the laser field itself.

### 2.1 Relativistic laser intensities

The laser field, or in more general, the field of a plane wave propagating along  $\hat{e}_x$  can be described by the vector potential  $\vec{A}$  which is given (in Gaussian units)

## 2.1. RELATIVISTIC LASER INTENSITIES

---

as [53]

$$\vec{A}(\vec{r}, t) = \text{Re} \left\{ \vec{A}_{\text{pol}} e^{i\psi} \right\}, \quad (2.1)$$

where  $\psi = \vec{k} \cdot \vec{r} - \omega t$  is the phase of the light wave with  $\omega$  and  $\lambda$  the frequency and wavelength of the laser,  $\vec{k} = 2\pi/\lambda$  the wavenumber and  $\vec{r}$  and  $t$  the common variables for space and time;  $\vec{A}_{\text{pol}}$  can for instance be  $A_0 \hat{e}_y$  for a linearly polarized (LP) wave or  $A_0 (\hat{e}_y \pm \hat{e}_z)$  for a circularly polarized (CP) wave. According to Maxwell's equation it follows that

$$\vec{E} = -\frac{1}{c} \frac{\partial \vec{A}}{\partial t} = \text{Re} \left\{ \frac{i\omega}{c} \vec{A}_{\text{pol}} e^{i\psi} \right\} \quad (2.2)$$

and

$$\vec{B} = \nabla \times \vec{A} = \text{Re} \left\{ i\vec{k} \times \vec{A}_{\text{pol}} e^{i\psi} \right\}, \quad (2.3)$$

where  $\vec{E}$  and  $\vec{B}$  are the electric and magnetic field of the laser/light wave.

### 2.1.1 Motion of a single electron in the laser field

In order to quantify the regime of relativistic laser-matter interactions, it is useful to analyze the motion of a single electron in such a field. The equation of motion can be derived from the Lorentz force, which in mks units is

$$\frac{d\vec{p}}{dt} = q \left( \vec{E} + \frac{\vec{p}}{m_e \gamma} \times \vec{B} \right), \quad (2.4)$$

where  $p = \gamma m_e \vec{v}_e$  and  $\gamma = 1/\sqrt{1 - v_e^2/c^2}$  are the relativistic momentum and the Lorentz factor of the electron;  $\vec{v}_e$ ,  $m_e$  and  $q = -e$  are the velocity, mass and charge of the electron. The time  $t$  is measured in the laboratory frame. Neglecting the magnetic field of the light wave with  $m d\vec{v}/dt \approx qE$ , the maximum velocity  $v_{\text{max}}$  of the electron (initially at rest, after a quarter wave cycle in the LP case) in the non-relativistic limit is

$$|v_{\text{max}}| \approx \frac{eA_0}{m_e c}. \quad (2.5)$$

This relation can be used to introduce the normalized vector amplitude  $a_0 = v_{\text{max}}/c = eA_0/m_e c^2$ . The maximum kinetic energy of the electron can then be written as

$$\hat{E}_{\text{kin}} = \frac{a_0^2}{2} m_e c^2, \quad (2.6)$$

## 2. RELATIVISTIC LASER-MATTER INTERACTION

---

so that the electron approaches the speed of light  $c$  for  $a_0 \geq 1$ , where its kinetic energy exceeds its rest mass of 511 keV for  $a_0 = \sqrt{2}$ . Accordingly a focused laser with a normalized amplitude of  $a_0 > 1$  is commonly referred to as *relativistic*. In order to express that in a more useful quantity, the intensity of the light wave needs to be derived. The averaged (and normalized) intensity is given by the absolute value of the pointing vector  $\vec{S}$  of the wave

$$I_0 \lambda^2 = |\vec{S}| \lambda^2 = \left| \frac{c}{4\pi} (\vec{E} \times \vec{B}) \right| \lambda^2 = \xi_{\text{pol}} \frac{\pi}{2} c A_0^2 \quad (2.7)$$

where  $\xi_{\text{pol}}$  accounts for the polarization dependency of  $I_0$  with  $\xi_{\text{pol}} = 1$  for LP and  $\xi_{\text{pol}} = 2$  for CP. In units of the normalized field amplitude, this relates to an average laser intensity of

$$I_0 \lambda^2 = \xi_{\text{pol}} \left[ 1.37 \times 10^{18} \frac{\text{W}}{\text{cm}^2 \mu\text{m}^2} \right] a_0^2. \quad (2.8)$$

In a real laser-plasma interaction the laser interacts with many electrons, which in general cannot be solved analytically. The motion of a single electron without a plasma background in vacuum, however, can still be analyzed in order to get a better insight into these complex interactions. For the case of a single electron and a plane wave (with arbitrary envelope), Lorentz equation can be solved analytically; a more detailed derivation can be found in Ref [53]. Introducing the normalized vector potential

$$\vec{a} = \frac{e\vec{A}_\perp}{m_e c^2}, \quad (2.9)$$

where  $\vec{A}_\perp = \vec{A}_0$  for a plane wave propagating along  $\hat{e}_x$ . The equations of motion result in the simple form of [53]

$$\frac{dx}{d\tau} = c \frac{a^2}{2} \quad (2.10a)$$

$$\frac{dy}{d\tau} = c a_y \quad (2.10b)$$

$$\frac{dz}{d\tau} = c a_z \quad (2.10c)$$

for  $\vec{a}(t - x/c)$  and  $\tau = t - x(t)/c$  and  $\vec{a} = (a_x, a_y, a_z)$  with  $|\vec{a}| = a(t) = a$ . In the simple scenario of an infinite LP plane wave with  $\vec{a} = a_0 \cos(\omega\tau) \hat{e}_z$  the electron

## 2.1. RELATIVISTIC LASER INTENSITIES

---

motion in  $x$  and  $z$  yields [53]

$$x(\tau) = \frac{ca_0^2}{4} \left( \tau + \frac{1}{2\omega} \sin(2\omega\tau) \right) \quad (2.11a)$$

$$z(\tau) = \frac{ca_0}{\omega} \sin(\omega\tau) \quad (2.11b)$$

with the boundary condition, that the electron is initially at rest with  $\vec{r}(\tau = 0) = 0$ . From these equations two important effects of relativistic laser electron interactions can be derived immediately:

1. The transverse motion in  $z$ , caused by the electric field of the laser, is solely oscillatory with its amplitude depending linearly on  $a_0$ .
2. The longitudinal motion in  $x$  (the laser propagation direction), caused by the  $v \times B$  term of the Lorentz equation, has a linear term in  $\tau$  in addition to the oscillatory term, which also depends quadratically on  $a_0$ .

In other words, for large laser amplitudes ( $a_0 \gg 1$ ), the electron motion is dominated by the magnetic field of the laser and the linear term in  $\tau$  results in a net displacement of the electron in the laser propagation direction with a drift velocity of  $v_d = ca_0^2/(a_0^2 + 4)$ . In Fig. 2.1 a) the motion of a single electron in an infinite plane wave (with LP) is depicted for  $a_0 = 15$  (red) and  $a_0 = 1$  (blue) with  $\vec{a} = a_0 \cos(\omega\tau)\hat{e}_x$  and  $\omega = 2\pi c/1.054 \mu\text{m}$ ; comparing both, one can see that the electron motion is significantly bent towards the x-direction for the larger laser amplitude in the relativistic regime. Fig. 2.1 b) shows the motion of a more realistic case with a finite plane wave with Gaussian envelope, where  $\vec{a} = a_0 \exp[-((\tau - 15\pi/\omega)/(30/\omega))^2] \cos(\omega\tau)$  with  $a_0 = 15$ . Both plots show a net displacement of several tens of micrometers, where the latter immediately shows, that there is also no net energy transfer from the laser to the electron, once the laser has passed the electron.

In a real laser matter interaction, the electron is subject to

- a finite laser pulse in space and time
- a plasma background consisting of electrons and atoms/ions.

This will eventually result in the ejection of the electron from the laser field by collisional or collisionless absorption/scattering or by the tight laser focus itself,

## 2. RELATIVISTIC LASER-MATTER INTERACTION

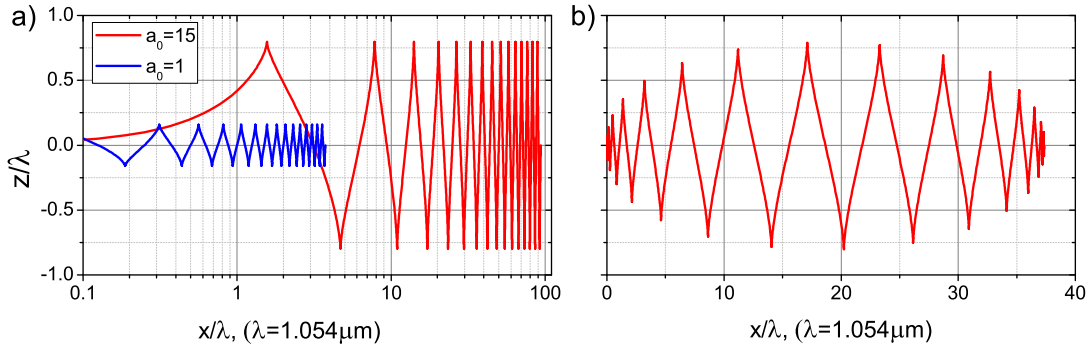


Figure 2.1: a) Electron motion in an infinite plane wave with LP and an  $a_0 = 1$  (blue) and  $a_0 = 15$  (red), where the highly relativistic laser amplitude of 15 strongly bents the electron motion into the laser propagation direction; b) Electron motion in a finite plane wave with a Gaussian envelope and an  $a_0 = 15$ , showing that there is no net energy transfer to the electron (in the case of a single electron in vacuum).

resulting in a net energy transfer (heating) of the electron. For the latter process, one can calculate the scattering angle  $\theta$  of the electron within the framework of the previous derivations. A real laser pulse, that is finite in space and time, has a fast varying intensity envelope and hence a strong radial intensity gradient; for this case it is useful to introduce the so-called *ponderomotive force* of the laser. The ponderomotive force is defined as the gradient of the time-averaged vector potential [54], where the final kinetic energy  $E_{\text{pond}}$  of an electron due to the ponderomotive force is

$$E_{\text{pond}} = (\gamma_s - 1)m_e c^2 \quad (2.12)$$

where  $\gamma_s = 1 + a^2/2$  is the Lorentz factor for a single electron in units of the normalized laser light amplitude. The angle between the transverse momentum  $\vec{p}_\perp = E_{\text{pond}}/c$  and the longitudinal momentum  $\vec{p}_x = \vec{p}_\perp/(2m_e c)$  gives [53]

$$\tan^2(\theta) = \left( \frac{\vec{p}_\perp}{\vec{p}_x} \right) = \frac{2}{\gamma_s - 1}, \quad (2.13)$$

correlating the ejection angle with the final energy of the electron (see Fig.2.2). In Sect. 2.2.3, a selection of electron heating mechanisms based on the plasma background will be discussed in more detail.

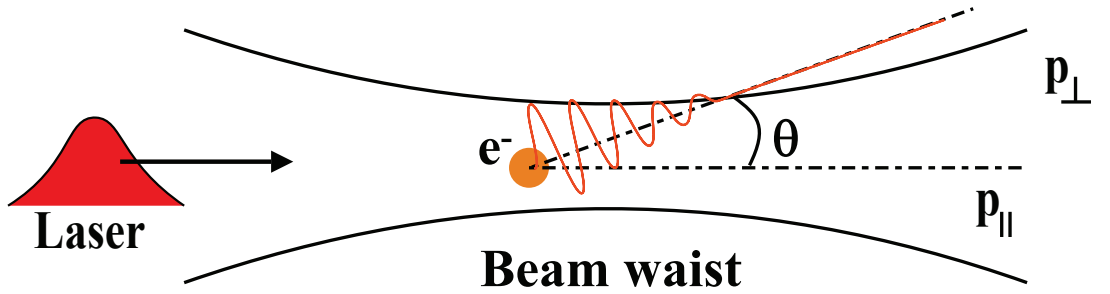


Figure 2.2: Electron ejection from a tightly focused LP laser due the relativistic intensities (adaption of Ref. [54]).

## 2.2 Laser-induced relativistic plasmas

Now, that the basic motion of a single electron in a laser field has been described, it is time to analyze the laser interaction with matter and the thus created plasma. The analysis starts with the various ionization processes, that will turn the target into a plasma and continue with the description of laser transport and absorption in the plasma. The last part of the section is devoted to plasma effects, that are important in the framework of this thesis, such as laser-induced relativistic transparency.

### 2.2.1 Laser-induced ionization

At the beginning of each high power laser-matter interaction with solid/gas/liquid targets stands the ionization process, that turns the target into a plasma. The dominant mechanism responsible for the ionization strongly depends on the actual laser intensity and hence the electric field that acts on the target electrons. Typically, the ionization process itself is of minor interest in laser-ion acceleration experiments; however, it is still important to know, at which laser intensities a target will start to ionize, especially with respect to the contrast of a real laser pulse, that can have a significant impact on the ion acceleration, as will be explained in more detail in Chap. 3.1.5.

In order to obtain a rough estimate of the necessary laser intensities, it is useful to calculate the electric field strength that binds an electron to its atom. For the

## 2. RELATIVISTIC LASER-MATTER INTERACTION

---

hydrogen atom, the binding electric field is given (in SI units) by [54]

$$E_b = \frac{e}{4\pi\epsilon_0 a_B^2} \approx 5.1 \times 10^9 \frac{V}{cm} \quad (2.14)$$

with  $a_B = 5.3 \times 10^{-9}$  cm the Bohr radius,  $e$  the electron charge and  $\epsilon_0$  the dielectric constant. Equating the binding field  $E_b$  with the laser intensity yields

$$I_i = \frac{\epsilon_0 c E_b^2}{2} \approx 3.51 \times 10^{16} \frac{W}{cm^2}, \quad (2.15)$$

which is the intensity at which any target material will be ionized solely by the laser electric field.

### Multi-photon ionization

However, laser-induced ionization typically occurs at intensities orders of magnitude below this value ( $\sim 10^{10}$  W/cm<sup>2</sup>), which is caused by multi-photon ionization. Here, the bound electron absorbs  $m$  photons, so that it is ejected from the potential of the atom its bound to. Its final energy is given by

$$E_{e^-} = (n + s)\hbar\omega - E_{\text{bound}} \quad (2.16)$$

where  $n + s = m$  is the sum of the photons  $n$  - necessary for the ejection of the electron - and the number  $s$  of additionally absorbed photons;  $E_{\text{bound}}$  denotes the binding energy of that specific electron. For example,  $E_{\text{bound}} = 13.6$  eV for the hydrogen atom and a photon of a laser with  $\lambda = 1$   $\mu\text{m}$  has an energy of 1.24 eV, which gives  $n \approx 11$ . For  $s = 0$  the process can be described by a perturbation theory of the atomic potential, which gives the ionization rate  $\Gamma_n$  of the  $n$ -th multi-photon ionization process as [54]

$$\Gamma_n = \sigma_n I_L^n, \quad (2.17)$$

where  $\sigma_n$  is the cross-section of this process that decreases with increasing  $n$ . With laser intensities exceeding  $\sim 10^{10}$  W/cm<sup>2</sup>, the photon density is high enough so that the  $I_L^n$  term enables the multi-photon ionization process.

### Tunneling & barrier suppression ionization

When the laser intensity approaches  $I_i$  (see Eq. 2.15), the atomic binding po-

## 2.2. LASER-INDUCED RELATIVISTIC PLASMAS

---

tential itself starts to deform under the influence of the laser electric field. For cases where the potential barrier of the thus deformed atomic potential is still above the binding energy of the electron of interest, ionization can occur quantum mechanically by tunneling. Whether the ionization of a material is dominated by tunneling or multi-photon ionization can be approximated with the Keldysh parameter [55]

$$\gamma_K \propto \sqrt{\frac{E_{\text{bound}}}{\Phi_{\text{pond}}}} \quad (2.18)$$

where  $\Phi_{\text{pond}}$  describes the *ponderomotive potential* of the laser. The ponderomotive potential describes, in close relation to the ponderomotive force in Sect 2.1.1, the *quiver energy* or the cycle-averaged energy an oscillating electron acquires in the laser field and can be estimated by

$$\Phi_{\text{pond}} = m_e c^2 (\gamma - 1) = m_e c^2 \left( \sqrt{1 + \frac{a_0^2}{2}} - 1 \right). \quad (2.19)$$

where  $\gamma = \sqrt{1 + \frac{a_0^2}{2}}$  is the cycle-averaged relativistic Lorentz factor in units of the normalized laser amplitude. For  $\gamma_K < 1$ , where the binding energy  $E_{\text{bound}}$  is larger than  $\Phi_{\text{pond}}$  multi-photon ionization dominates, while for  $\gamma_K > 1$  tunneling is the dominant ionization process.

For cases where the potential barrier of the deformed atomic potential is lower than the electron binding energy, the electron will eventually escape spontaneously. This ionization process is called the barrier-suppression (BS) ionization. The threshold intensity  $I_{\text{BS}}$  for this process can be estimated by assuming a stationary homogeneous electric field that is deforming the atomic potential as [54]

$$I_{\text{BS}} = 4 \times 10^9 \left( \frac{E_{\text{bound}}}{\text{eV}} \right)^4 q_i^2 \frac{\text{W}}{\text{cm}^2}, \quad (2.20)$$

where  $q_i$  is the final charge of the ion. For the single ionization of carbon to  $\text{C}^+$  - the targets used in the experiments are diamond or diamond like carbon (see Chap. 3.2 and Chap. 4) - the threshold intensity is  $\sim 6.4 \times 10^{13} \text{ W/cm}^2$ .

In a real laser-matter experiment, where the laser not only interacts with a single bound electron, *collisional ionization* also plays an important role. Once, enough electrons are set free through field ionization by any of the above processes, these electron will subsequently ionize other atoms by collisional ionization.

## 2. RELATIVISTIC LASER-MATTER INTERACTION

---

### Average plasma ionization

In many cases, including the laser-driven acceleration of these ions or the theoretical treatment of plasmas, it is important to know the average ionization state of the laser-induced plasma; see for example Chap. 3.4.3, where the development of an ion detector is based on the assumption that the plasma is fully ionized. For a plasma that is in the state of local thermal equilibrium (LTE), the ionization rate can be calculated with the Saha-equation, also known as *Saha-Boltzmann equation* [56] (which is based on the assumption that the atoms follow a Boltzmann distribution).

However, in the experiments conducted in the framework of this thesis, the ultra-intense laser leads to a highly transient plasma, so that it is in a state of strong non-LTE. Here, time-dependent rate equations need to be considered, also including recombination (the inverse of the ionization) and recombination radiation, which is eventually escaping the plasma. More details regarding the rate equations and the ionization of matter under these conditions can be found for example in Ref. [54, 57]

### 2.2.2 Laser transport in plasmas

Now, that the target ionization and the single electron motion have been described, the laser propagation in the plasma - or the interaction with the plasma electrons - should be introduced. The description will be restricted to the fundamental aspects, that are necessary in the framework of this thesis; detailed information can be found in many textbooks, such as [54, 58, 59].

In a “cold” plasma, where the ions are at rest (immobile) and the **electron temperature**  $T_e = 0$ , the **plasma frequency**  $\omega_p$  is given (in Gaussian units) as

$$\omega_p(n_e) = \sqrt{\frac{4\pi e^2 n_e}{m_e}} \approx 5.95 \times 10^4 \sqrt{\frac{n_e}{[cm^{-3}]}} \quad (2.21)$$

where  $n_e$  is the **electron density** of the plasma. Note, that for relativistic laser intensities  $\omega_p'^2 = \omega_p^2/\gamma$ . The plasma frequency can be understood as the reaction of the plasma to a perturbation, for instance by the laser electric field [58].

The collisionless **dispersion relation** for a transverse plane wave in the (cold)

## 2.2. LASER-INDUCED RELATIVISTIC PLASMAS

---

plasma is

$$k \approx \pm \frac{\omega_L^2}{c} \sqrt{1 - \frac{\omega_p^2}{\omega_L^2}} \quad (2.22)$$

which immediately shows, that a laser cannot propagate through a plasma with  $\omega_p > \omega_L$ ; in other words, the plasma is *opaque* to the laser light. The density, where  $\omega_p = \omega_L$ , is called the **critical density**  $n_c$  and follows from  $\omega_p(n_c)$  as

$$n_c(\lambda) = \frac{m_e \gamma \omega_L^2}{4\pi e^2} \approx 1.1 \times 10^{21} \left( \frac{\lambda_L}{[\mu\text{m}]} \right)^{-2} \text{ cm}^{-3}. \quad (2.23)$$

The plasma is consequently called underdense for  $n_e < n_c$  and overdense (opaque) for  $n_e > n_c$ . At the critical surface ( $n_e = n_c$ ) a part of the laser light is reflected (or absorbed, see Sect. 2.2.3); an evanescent component of the wave, however, penetrates the plasma beyond the critical surface into the overdense region of the plasma. The distance  $l_s$  from the critical surface to where the evanescence wave has dropped to  $1/e$  is called the *skin depths* which follows

$$l_s \propto \frac{c}{\omega_p}. \quad (2.24)$$

When a plasma is heated (by a laser), it will start to expand. While the ablation pressure of the plasma will launch a shock wave into the overdense target, the plasma will also expand into the vacuum. The expansion velocity, the **ion sound speed**  $c_s$ , is

$$c_s = \sqrt{\left( \frac{Z k_B T_e}{m_i} \right)} \approx 3.1 \times 10^7 \sqrt{\left( \frac{T_e}{[\text{keV}]} \right) \left( \frac{Z}{A} \right)} \frac{\text{cm}}{\text{s}}. \quad (2.25)$$

where  $k_B$  is the Boltzman constant and  $Z$  and  $A$  are the charge and the mass number of the (dominant) plasma ions.

The ion sound speed of the plasma plays an important role in the laser-plasma interaction, as it is a dominant effect for the decrease of the plasma density. Moreover, a real laser pulse is usually preceded by a pedestal, much longer than the main pulse, with intensities rapidly exceeding the ionization threshold ( $\sim 10^{10} \text{ W/cm}^2$ , see Sect. 2.2.1). This premature expansion might alter the laser interaction or even destroy the target prior to the arrival of the peak (see Chap. 3.1.5 for more details).

## 2. RELATIVISTIC LASER-MATTER INTERACTION

---

It is furthermore useful to introduce the plasma *scale length*  $L$  as

$$L = c_s \tau_L \approx 3 \sqrt{\frac{T_e}{[\text{keV}]}} \sqrt{\frac{Z}{A}} \left( \frac{\tau_L}{[\text{fs}]} \right) \text{ \AA} \quad (2.26)$$

where  $\tau_\lambda$  is the laser pulse duration. The scale length is commonly used as a measure of the plasma steepness and is often used as a boundary condition for effects such as the high harmonic generation. The steepness and the electron density of the plasma define the dominant process of laser absorption, as will be described in the next section.

Especially for relativistic intensities ( $a_0 > 1$  or  $I_L > 10^{18} \text{ W/cm}^2$ ), the electron temperature of the plasma has at least one “cold” ( $T_e$ ) and one “hot” Boltzmann component ( $T_h$ ), where obviously  $T_e \ll T_h$ . The hot electron temperature mainly depends on which absorption process (see Sect. 2.2.5) is dominant during the interaction. Assuming that the hot electron production is dominated by  $\vec{j} \times \vec{B}$  heating, one gets as an approximation [60]

$$k_B T_h \approx m_e c^2 (\gamma - 1) \approx 0.511 \left( \sqrt{1 + 0.73 I_L \left[ 10^{18} \frac{\text{W}}{\text{cm}^2} \right] \lambda^2 [\mu\text{m}] - 1} \right) \text{ MeV} \quad (2.27)$$

in close relation to the single electron motion in the laser field, described in Sect. 2.1.1.

### 2.2.3 Relativistic transparency

As has been derived in the previous section, a plasma is opaque to the laser light, when  $\omega_p > \omega_L$ . With relativistic laser intensities, however, electron energies exceed their rest mass, resulting in an effective electron mass increase by  $\gamma$  (due to the Minkovsky metric of space time [61]). As already pointed out, Eq. 2.21 needs to be corrected for relativistic intensities, so that  $\omega_p^2 = \omega_p'^2 / \gamma$  with the cycle-averaged Lorentz factor  $\gamma = \sqrt{1 + a_0^2 / 2}$ . Using the normalized electron density  $n' = n_e / n_c$  one obtains in the non-relativistic case that the plasma is opaque when  $n' > 1$  and transparent to the laser light when  $n' < 1$ .

In the relativistic case this translates to an opaque plasma when  $n' / \gamma > 1$  and a *relativistically transparent* plasma when  $n' / \gamma < 1 < n'$ . The relativistic transparency of the plasma is of great importance in the framework of this thesis. With

## 2.2. LASER-INDUCED RELATIVISTIC PLASMAS

---

intensities on the order of  $10^{20}$  W/cm<sup>2</sup> targets of the right thickness and initial electron density can turn relativistically transparent during the laser-plasma interaction. This can be beneficial for certain laser-plasma interactions - here the laser ion acceleration - as will be shown in the last section and in Chap. 4.

A caveat is, that the direct measurement of the relativistic transparency is rather difficult. While a PIC simulation (see Sect. 2.3.3) can supply all the necessary information (instantaneous Lorentz factor  $\gamma(t, \vec{r})$  and electron density  $n_e(t, \vec{r})$ ) to identify the state of transparency, this information is not accessible in the experiment. The required time resolved measurements of these plasma parameters in short-pulse laser ( $\tau_L \ll 1ps$ ) experiments with a good resolution in time and space are very challenging. For example, in the experiments conducted here, the target thicknesses are on the order of 100 nm and the pulse duration is 0.5 ps, which would require a UV or XUV probe for the direct measurement of the electron density. In addition, the probe would measure the density as  $n_e/\gamma$  and not separately as it would be necessary.

A solution to this could be indirect measurements or the measurement of signatures of the relativistic transparency. One can for instance measure the reflected and transmitted light during the interaction and compare the data with PIC simulation results in order to identify whether the target has been relativistically transparent during the laser-plasma interaction or not. These measurements have already been done at Trident [62, 63]. Trident has a normalized laser intensity  $a_0$  of  $\sim 16$  which gives a maximum  $\gamma = \sqrt{1 + a_0^2/2} = 11.4$ . The measurements have shown that the target turns transparent at the peak of the laser pulse for thicknesses of 100 to 200 nm. Hence, one can conclude that the target is indeed relativistically transparent with  $n'/\gamma < 1 < n'$  as  $\gamma$  is larger one and steadily increasing towards the peak pulse up to  $\gamma = 11.4$ , while  $n_e$  is steadily decreasing.

### 2.2.4 Self focusing

Another important plasma effect that sets in at relativistic laser intensities is the *self-focusing* of the laser in the plasma. Two mechanisms can turn the plasma into a “positive” lens, causing further focusing of the laser beyond the geometrical limits of the actual experimental setup

- the  $\vec{v} \times \vec{B}$  term of the Lorentz force expels electrons from the focus (see

## 2. RELATIVISTIC LASER-MATTER INTERACTION

---

Sect. 2.1.1 and Eq. 2.13) leading to an electron depletion in the focus center (ponderomotive self-focusing)

- the strong transverse gradient of the laser amplitude in the focus causes in the same way a transversely varying relativistic mass increase of the electrons (relativistic self-focusing)

Both mechanism cause self-focusing by generating a transverse gradient in the refractive index. In particular, the relativistic refractive index for the laser in the plasma is [54]

$$N(r) = \frac{ck_L}{\omega_L} = \sqrt{\left(1 - \frac{\omega_p^2}{\omega_L^2 \gamma(r)}\right)} \quad (2.28)$$

with  $\gamma(r) = \sqrt{1 + a^2(r)/2}$  for a laser with beam profile  $a(r)$  peaking on the laser axis for  $r = 0$  (which is typically a Gaussian or super-Gaussian beam profile). In both cases a local decrease of the plasma frequency (see Eq. 2.21) at  $r = 0$  results in an increased refractive index; while the  $\vec{v} \times \vec{B}$  term causes the electron density to locally decrease, the transverse beam profile causes  $\gamma$  to locally increase. The phase velocity  $v_p(r) = c/N(r)$  is hence larger off-axis than on-axis, resulting in the self-focusing (see Fig. 2.3). For the relativistic self-focusing, the threshold value is  $a_0^2(\omega_p w_0)/c \geq 8$  [54], where the self-focusing overcomes the laser divergence (with  $w_0$  the beam waist, see Chap.3.1.4).

Self-focusing can have a significant and also unpredictable effect on the overall laser-matter interaction due to the fact that it results in higher intensities in the axis of the laser-propagation direction. In addition, relativistic channels might form in the (relativistic) transparent plasma [64] that can guide the laser pulse tightly focused over many times the Rayleigh length  $z_r$  (see Chap.3.1.4) along the plasma.

### 2.2.5 Laser absorption and energy transfer in plasmas

The laser absorption is probably the most important process during the laser-plasma interaction, as it transfers energy from the laser to the plasma. With the laser intensities available today, the laser electric fields are still too low to directly act on the plasma ions; hence, laser energy transfer is mediated by the plasma electrons, i.e, electrons gain energy ( $T_h$ ) in the laser field, which is “distributed”

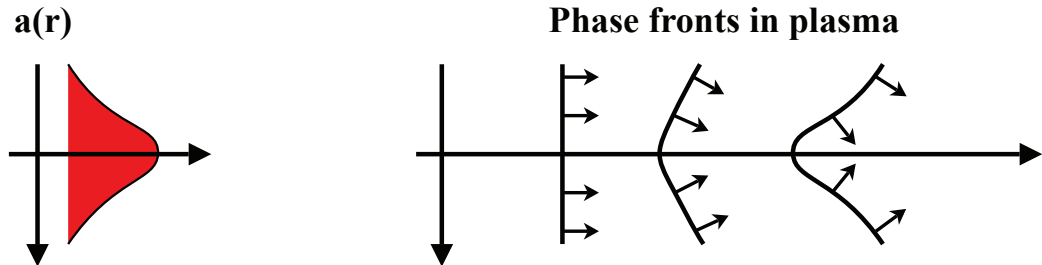


Figure 2.3: Self-focusing in a relativistic plasma due to a transverse gradient in the refractive index causing slower group velocity  $v_p$  on-axis than off-axis (Adaption of Ref. [65])

to the plasma ions and atoms through subsequent thermalization (collisions) of the electrons ( $T_e$ ) or other processes like instabilities. The laser absorption by electrons in a plasma can be separated into collisional and collisionless processes. In order to identify the dominant process it is useful to introduce the ion-electron collision frequency  $\nu_{ei}$ , which is given by [59, 66]

$$\nu_{ei} \propto \frac{n_e Z}{T_e^{3/2}}. \quad (2.29)$$

For high density plasmas (and high  $Z$ ) at low electron temperatures collisional absorption is the dominant mechanism. The collisional absorption, which is also called “inverse Bremsstrahlung”, is the collision of an electron with an ion under the presence of an electric field, i.e., the electron absorbs a photon during the collision process. Moreover, as shown in the last section, the highest densities accessible by the laser are found at the critical surface of the plasma, so that the collisional absorption is most effective here.

With increasing laser intensities the electron temperature rises and collisional absorption becomes more and more ineffective. Typically, in interactions where the laser intensity exceeds  $\gg 10^{15}$  W/cm<sup>2</sup>, collisionless absorption is the dominant process once the electron temperature is  $\approx 10^3 Z^2$  eV[61]. The collisionless absorption cannot be treated analytically in general, but has been studied with computer simulations for many years now. As a result, a large number of mechanisms has been identified in this regime, where the most prominent are the **resonance absorption** [67], the  $\vec{j} \times \vec{B}$  heating [68] and the **vacuum/Brunel heating** [69], which will be explained in the following; examples of other mech-

## 2. RELATIVISTIC LASER-MATTER INTERACTION

---

anism are stochastic heating [70], Landau damping [71] and the anomalous skin layer absorption [72]. These mechanisms typically result in the generation of very “hot” electrons in contrast to the collisional absorption.

### Resonance absorption

The resonance absorption is a process that in general requires oblique laser incidence of a p-polarized light wave and a long density scale length. The laser, that is incident on the plasma at an angle  $\theta$  is reflected near the critical surface of the plasma (where  $n_e = n_c \cos^2(\theta)$ ). Due to the p-polarization of the light wave, the (tangential) electric field of the laser can reach/tunnel into the plasma and excite electron oscillations at the critical surface. These oscillations can grow resonantly over several laser oscillations and drive an electron plasma wave into the plasma. Energy can be transferred to the plasma through dampening of this wave by wave breaking or collisions [59].

### Vacuum/Brunel heating

For steep or step-like plasmas, where the amplitude of the electron oscillations exceed the plasma scale length [54], resonantly driven plasma waves are no longer supported. Here, the vacuum heating plays an important role in the laser absorption, which has been introduced by Brunel in 1987 [69] as the “not-so-resonant, resonant absorption”. In particular, an electron at this sharp plasma-vacuum interface is first accelerated by the laser electric field into the vacuum. When the field of the laser reverses, the electron is pushed back into the plasma. However, the laser electric field can only penetrate the steep and highly overdense plasma to its skin depth  $l_s$  (see Sect. 2.2.2 and Eq. 2.24). Now that the electric field is screened by the plasma, the electron can penetrate deeper into the plasma without being dragged out by the laser again and eventually thermalize by subsequent collisions.

### Relativistic $\vec{j} \times \vec{B}$ heating

In the  $\vec{j} \times \vec{B}$  heating the electron is directly accelerated in the laser field, where for relativistic intensities, i.e., for  $a_0 > 1$ , the electron motion is dominated by the  $\vec{v} \times \vec{B}$  term of the Lorentz force (see Sect.2.1). For a LP light wave propagating

## 2.2. LASER-INDUCED RELATIVISTIC PLASMAS

---

along  $x$ , the (ponderomotive) force is given as [54]

$$f_x = -\frac{m_e}{4} \frac{\partial v^2(x)}{\partial x} (1 - \cos(2\omega t)) . \quad (2.30)$$

Here, the first term describes the motion of the electron in the laser propagation direction and the second one the motion under the fast oscillating vector potential of the LP wave. For an electron in a plasma, the latter term is responsible for the heating of the plasma similar to the vacuum heating. However, the  $j \times B$  heating works best with normal incidence and is mostly independent of the laser polarization; only for CP, where the vector potential has no oscillating component,  $\vec{j} \times \vec{B}$  heating ceases to work. This is an important effect, that is sometimes used to reduce plasma heating due the laser light and alter the overall laser-plasma interaction; an example is given in Sect. 2.3.2 and in Chap. 4.4, where the reduced plasma heating results in a strongly modified energy spectrum of the laser-accelerated ions.

### 2.2.6 Plasma instabilities

The plasma generated from high intensity laser pulses is in general subject to a variety of instabilities, that can be beneficial or disadvantageous depending on the desired outcome of the laser-plasma interaction. Some of them are the **Rayleigh-Taylor** (RT), the Richtmyer-Meshkov (RM), the Kelvin-Helmholtz (KH) and in more general the Raman, Brillouin, **streaming**, two-plasmon, ion-acoustic and parametric instabilities. A full theoretical description of these plasma instabilities is far beyond the scope of this work, but can be found in many textbooks [54, 59, 65]. In general an instability is a wave mode that grows exponentially driven by the free energy of a system not in perfect thermodynamic equilibrium. The instability reduces the free energy of the system growing at an rate of  $\gamma_i$  (provided it exceeds a certain threshold value to compensate for damping, e.g. collisional or Landau damping). It is useful to classify the instability by the type of the driving free energy.

#### Rayleigh-Taylor instability

The RT instability is probably the most prominent one, where a low density material (fluid, gas or plasma) pushes or accelerates a high density material or vice

## 2. RELATIVISTIC LASER-MATTER INTERACTION

---

versa. The free energy comes from an external, non-electromagnetic force [73], such as the gravitational field. The interface between both materials is subject to the RT instability, where perturbations can start to grow; the low density material eventually penetrates into the high density material through bubbles and the high density material through spikes vice versa [58]. The mushroom cloud, typically seen from above-ground nuclear explosions, is the result of a RT instability; during the explosion massive amounts of low density gas are accelerated and pushed against higher density gas regions above the explosion center.

In the laser-plasma interaction, this can, for example, be related to the plasma created on the target surface (which is of lower density than the target itself) that is pushed and accelerated into the still overdense target. This will result in a strongly perturbed plasma, which might result in a non-uniform beam pattern of accelerated particles from this plasma [74] or even destroy an ultra-thin nm to  $\mu\text{m}$  scale target provided that the growth rate of the instability is fast enough. The RT instability is of great interest for the inertial confinement fusion, where the instability can result in heavy perturbation or destruction of the capsule and capsule shell [65].

### **Streaming instabilities and the Buneman instability**

In the case of a streaming instability a beam of particles or a current drives through the plasma in a way that different species experience different drifts relative to one another [75]. The drift energy enables the streaming instability, such as the Buneman instability, by exciting wave modes and transferring energy into oscillations. The (Farley-)Buneman instability [76] is a two stream fluid instability, that can also be observed in the lower E and upper D layers of earth ionosphere (heights of 80 km to 120 km) or in klystrons used in microwaves. This instability has been identified as a possible energy transfer mechanisms (electrons to ions) in the Break-Out Afterburner ion-acceleration mechanism [29] (see next section). Here, a stream of (magnetized) electrons driven by the laser through the relativistically transparent target has a significantly larger (relativistic) velocity relative to the (unmagnetized) plasma ions [77]. Such a system is susceptible to the Buneman instability. In the non-relativistic case (see Ref. [29] for the relativistic case) the dispersion relation can be derived from the linearized motions

## 2.3. LASER-DRIVEN ION ACCELERATION

---

of equation and Poisson's equation as [73]

$$1 = \omega_{\text{pe}}^2 \left( \frac{m_e}{M_i} + \frac{1}{(\omega - kv_e)^2} \right), \quad (2.31)$$

where  $\omega_{\text{pe}}$  is the plasma frequency,  $v_e$  the electron drift and  $m_e$  and  $M_i$  the electron and ion mass. For complex wave modes  $\omega$  with a positive imaginary part  $\text{Im}(\omega)$  the instability grows exponentially. The growth rate follows as  $\gamma_i \approx (m_e/M_i)^{1/3}$ . In this case, the drift energy of the electrons can be transferred to the plasma ions by exciting wave modes with a phase velocity comparable to the velocity of the bulk ions, hence resonantly accelerating them (which can in a way be understood as “inverse” Landau damping).

### 2.3 Laser-driven ion acceleration

This section of the introductory chapter is intended to give a more detailed insight into laser driven ion-acceleration, which is in general based on the basic laser plasma physics described in the previous sections. Over the past ten to twenty years a large number of different mechanisms has been introduced theoretically; some of them have been demonstrated experimentally. Recalling the ponderomotive potential accelerating an electron (see Eq.2.6) and considering the mass of a proton as the lightest of all ions, one can derive an approximate threshold intensity for direct laser ion acceleration to relativistic energies. In Eq. 2.8 the threshold for electrons is  $\sim 10^{18} \text{ W/cm}^2$  ( $a_0 = 1$ ), which turns into  $6 \times 10^{24} \text{ W/cm}^2$  ( $a_0 = 2000$ ) with the proton mass  $m_p \approx 2000m_e$ . Maximum laser intensities nowadays are on the order of  $10^{21} \text{ W/cm}^2$  (Trident delivers  $5 \times 10^{20} \text{ W/cm}^2$ ), i.e., direct acceleration of ions in the laser field can be neglected. In fact, most acceleration mechanisms proposed so far are based on charge separation; electrons are exerted from the ions by the laser ponderomotive force, which results in strong electric fields accelerating the plasma ions to MeV energies [6–14, 28–31].

In other words, electrons mediate the laser energy by the various laser absorption mechanisms (see Sect. 2.2.5) to the ions; the overall effectiveness of the acceleration is hence coupled to the laser absorption efficiency into electrons and the subsequent energy transfer to the ions. The accelerating fields can reach several tens of TV/m, which is six orders of magnitude above conventional rf-accelerators.

## 2. RELATIVISTIC LASER-MATTER INTERACTION

---

Beam currents of kA and more have been measured in these laser-driven ion beams with transverse emittance below  $10^{-3} \pi \text{mm mrad}$  [78].

An exemption to the acceleration by charge separation is the acceleration by Coulomb explosion [22, 79, 80], where all electrons are “removed” from the ions by the laser light, so that the ions explode under the resulting Coulomb force.

In most laser-ion acceleration experiments one can usually expect to find a mixture of different acceleration types. Which one is dominant, depends not only on the basic laser and plasma parameters, that have been defined earlier in this chapter, but also on dynamic parameters that are much more complicated to determine. Some of these are described in the next chapter, such as the laser contrast (see 3.1.5) that can alter the overall interaction significantly. Moreover, even the alignment and quality of the laser focus (see 3.1.4) and the target (see 3.3) can ultimately change or even stop the ion-acceleration.

In order to identify the dominant acceleration mechanism, it is useful to measure the properties of the ion beam, such as the maximum ion energy, the energy spectrum, the conversion efficiency and the beam shape, i.e., its angular dependency (see Chap. 3.4 and Chap. 4). This data can then be compared with theoretical predictions - which are usually based on PIC simulations - to draw conclusions about the acceleration.

However, one should note the caveat, that these measurements are typically time integrated, spatially limited and that information about the plasma itself are usually not accessible experimentally with the necessary time and spatial resolution, especially in experiments involving ultra-thin nm-scale targets. Such measurements ideally require probe pulses much shorter than the drive pulse, a capability none of the current ultra-high intensity laser facilities can provide.

### 2.3.1 Target normal sheath acceleration

More than 10 years ago the Target normal sheath acceleration (TNSA) has first been observed by Hatchett, *et al.* [15] and Snavely, *et al.* [6] and later been described by Wilks, *et al.* [81]. In the TNSA mechanism, a laser with  $a_0 \geq 1$  is incident on a several micron thick solid target, which will stay opaque to the laser during the whole interaction time. The irradiated front side of this target is rapidly ionized (see Sect.2.2.1) in the laser pulse pedestal, forming an plasma expanding into the vacuum (see Sect.2.2.2). The main pulse will be partially absorbed in

### 2.3. LASER-DRIVEN ION ACCELERATION

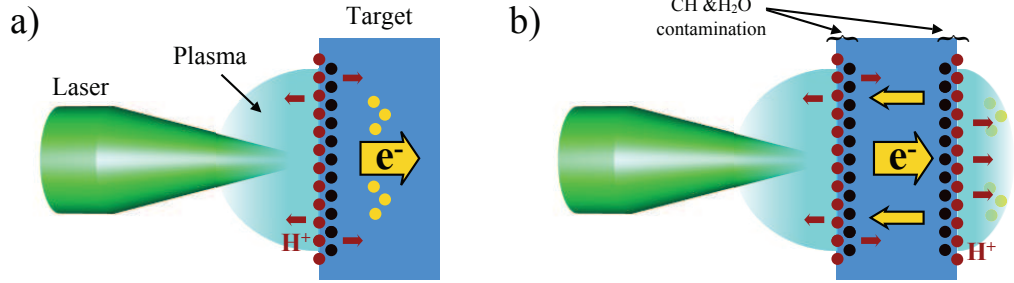


Figure 2.4: Schematic depiction of the Target Normal Sheath Acceleration (TNSA). The obliquely incident laser heats electrons on the front side of the target. The electrons penetrate the target, that is several micron thick and opaque to the laser light. A charge separation field is created by these hot electrons on the back side of the target due to subsequent field ionization of the target surface. Protons (and ions) are accelerated in this virtual cathode target normal to the back surface (see text for details).

this plasma (at the critical surface) and create “hot” electrons (with temperature  $k_B T_h$  and density  $n_{e(h)}$ ) via for instance  $\vec{j} \times \vec{B}$  heating and resonance absorption in the case of obliquely incident p-polarized laser light. From the  $\vec{j} \times \vec{B}$  heating, hot electrons gain a temperature on the order of  $k_B T_h = m_e c^2 (\sqrt{1 + a_0^2/2} - 1)$ . These electrons penetrate the target and form a hot electron cloud at its back side (see Fig. 2.4 a). Subsequent field ionization of the backside surface by the hot electron cloud leads to a strong charge separation field  $E_s$ . The extent of this field is given by the Debye length  $\lambda_{Deh}$  of the hot electrons (in SI units)

$$\lambda_{Deh} = \sqrt{\frac{\epsilon_0 k_B T_h}{e^2 n_{e(h)}}} \quad (2.32)$$

which describes the reduction in the Coulomb interaction range due to cancellation of the fields by the surrounding plasma. The charge separation field hence scales as  $E_s \approx k_B T_h / e \lambda_{Deh}$  [7] and has typically a length of a few microns, giving rise to a strong ambipolar field on the order of several TV/m [82–86]. The field can be considered quasi-static, as electrons are continuously pulled back into the target by the fields and replaced by recirculating hot electrons from the front (see Fig. 2.4 b).

Ions are accelerated normal to the back surface in this quasi-static charge separation field, which is also called a *virtual cathode*, with  $dp/dt \approx q_i E_s$ , where  $q_i$

## 2. RELATIVISTIC LASER-MATTER INTERACTION

---

is the charge of the ion. The acceleration time is on the order of the pulse duration, i.e., as long as the hot electrons can sustain the virtual cathode. Several attempts have been made, to estimate the final ion energy [81, 82, 85], which typically scales as  $E_{\max} \propto T_h \propto a_0 \propto \sqrt{I_L}$ . However, these scalings are rather doubtful; measurements from Ti:Sapphire lasers [87, 88] (with lower laser energy, but shorter pulse duration) can have intensities comparable to Nd:Glass laser systems, and do typically not follow these scalings. In Ref. [16, 17, 89] additional conditions for the scalings are suggested, such as that the areal density  $n_e d = \sigma$  has to be  $\sigma/n_{cr}\lambda_L \approx 3 + 0.4a_0$ .

Acceleration of ions also occurs on the front side counter-propagating the laser, but the strongly expanded plasma, i.e., the larger scale length, results in significantly lower charge separation fields. This *front side acceleration* (FSA) [90] typically results in lower ion energies due to the lower field in combination with a limited acceleration time. As the plasma on the front side is more likely to be bent (due to the ponderomotive force and the longer expansion), these ions typically exhibit a larger angular spread. A part of the ions is also subject to the *shock acceleration* [91] that drives the ions into and through the bulk of the target.

In a real experiment, targets typically have a  $\sim$ nm thick water vapor (from imperfect vacuum) and hydro carbon surface contamination layer (from vacuum pump oil). Protons (ionized hydrogen) have the lowest inertia due to their low mass and the highest charge to mass ratio among the ions and are hence accelerated first in the charge separation fields. As they are accelerated, they electro-statically shield the sheath field to heavier ions, preventing further ionization of substrate ions and their subsequent acceleration to higher energies. As a result, the dominant ion species accelerated in TNSA is protons; in other words, most of the laser energy transferred to the ions ends up with the protons from the target surface. The energy spectra are in general exponentially decaying with a sharp high energy cutoff; maximum proton energies experimentally observed range between 58 MeV measured in 2000 [15] and 67 MeV [18] measured in 2010. The exponentially decaying spectrum is a result of the transversely inhomogeneous charge separation field, that extends over several times the laser focus on the back side. The most energetic electrons are located closer to the laser axis and lower energetic electrons from scattering or recirculation result in a radially decaying field in the transverse direction.

## 2.3. LASER-DRIVEN ION ACCELERATION

---

Two proof-of-principle experiments have been published, that resulted in quasi-monoenergetic ion spectra, instead of the typically exponentially decaying spectra. By using in-situ engineered targets, i.e., by artificially restricting the source of ions to a smaller volume, the effective accelerating field is more homogeneous. Quasi-monoenergetic protons with 1 MeV [27] and carbon  $C^{5+}$  with 2.5 MeV/u to 3.5 MeV/u [26] have been observed. However, the conversion efficiency turned out to be very low due to the small source volume. In order to accelerate heavier ions more effectively in the TNSA regime, the hydro and hydro carbon contamination layer has to be removed.

This has been done experimentally with cw-laser heating, resistive heating and ion gun etching. Ion energies of up to  $\sim 7$  MeV/u for carbon, fluorine, aluminum and lead [7, 20, 21] and  $\sim 10$  MeV/u iron  $F^+$  [92] have been generated this way. In summary, the TNSA mechanism has the following distinct signatures

- the acceleration dominantly happens in a virtual cathode at the back side of the target with reported energies of up to 67 MeV (protons)
- the dominant species is protons due to their high charge to mass ratio
- protons originate from nm-thin surface contamination layer
- the energy spectrum is typically exponentially decaying with a sharp high energy cutoff (at up to 67 MeV for protons)
- acceleration of heavier ions requires removal of the contamination layer with target heating
- the target is opaque to the laser during the whole laser interaction

### 2.3.2 Radiation pressure acceleration (RPA)

The ion acceleration by the laser light pressure has drawn a lot of attention recently and resulted in many theory publications [10, 13, 14, 93, 94] due to its inherent ability of accelerating all plasma ions with a mono-energetic spectrum. This is in general done by accelerating the whole target as a single block of plasma by the laser light pressure ( $I_L/c$ ), i.e., the laser transfers momentum to the target while it is reflected at its critical surface. For laser intensities on the order of

## 2. RELATIVISTIC LASER-MATTER INTERACTION

---

$10^{23}$  W/cm<sup>2</sup> Esirkepov *et al.* [14] has published simulations showing that protons gain relativistic energies within the first half cycle of the laser irradiating the target. In this *Laser piston* regime, the ponderomotive force of the LP laser pushes and compresses the electrons into the target, which set up an ultra-high charge separation field accelerating the ions rapidly. The accelerated plasma slab can be considered a relativistically moving mirror co-propagating with the laser pulse; energy is transferred to the electrons by momentum transfer of the reflected and down-shifted laser. As a result, the ion beam will be very mono-energetic.

A caveat is the condition of a “quasi-one-dimensional geometry” [14]. This requires even more laser energy to reach these intensities, as the laser focus needs to be considerably larger than the target thickness. In addition, radiation back reactions [95–98] are not considered in this study, which might significantly alter the laser-matter interaction and probably render this mechanism less efficient at these intensities.

For lower intensities of  $> 10^{20}$  W/cm<sup>2</sup>, simulations suggest that the use of a CP laser enables a similar regime of ion acceleration. A model for this *radiation pressure acceleration* (RPA) with CP laser light has first been proposed by Macchi *et al.* [93] and extended with a ballistic evolution of the ion beam by Klimo *et al.* [10]. Due to the CP laser light, the ponderomotive force has no fast oscillating component that would lead to electrons being strongly heated and leaving the interaction area after a few laser cycles as in the TNSA. Instead, the ponderomotive force is slowly varying and electrons are adiabatically compressed.

The following analytical description of the RPA mechanism is, for the sake of simplicity, based on these non-relativistic studies; an analytical theory with relativistic corrections can be found in [13, 94]. At first, the laser rapidly ionizes the front surface of the target and compresses and pushes electrons deeper into the overdense target until the radiation pressure is balanced by the increasing charge separation field. This results in an electron depletion area of length  $l_d$  at the plasma surface, which is followed by the electron compression area (see Fig. 2.5). The electrostatic charge separation field  $E_s$  peaks at the interface of both areas and can be described (in S.I. units) by [10]

$$E_s^2 = \frac{2(1+R)}{\epsilon_0 c} I_L, \quad (2.33)$$

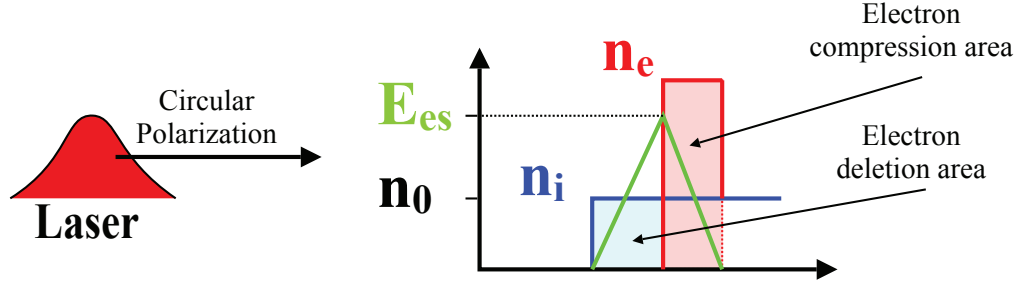


Figure 2.5: Schematic picture of the RPA. Due to the CP laser light, electron heating mechanisms are suppressed and electrons are pushed into the target until the charge separation field balances the radiation pressure. This forms an electron depletion area and an electron compression area. Ions from the latter are accelerated into a mono-energetic spectrum by successive propagation through the target and cycling in the charge separation field  $E_s$ . (Adaption of [14])

where  $R$  denotes the reflectivity of the target. The length  $l_d$  of the depletion area sets the lower limit for the target thickness  $d$  and can be derived by calculating  $E_s$  with the Poisson equation as  $E_s = en_0 l_d / \epsilon_0$  and combining it with the above equation to

$$l_d = \sqrt{\frac{2(1+R)I_L \epsilon_0}{cn_0^2 e^2}} \quad (2.34)$$

with  $n_0 = n_e(t=0)$  the initial electron density of the target. Using Eq. 2.8 and Eq. (2.23) this can be related to the normalized laser amplitude  $a_0$

$$\frac{n_0}{n_c} \frac{l_d}{\lambda_L} = \sqrt{\frac{(1+R)\xi_{\text{pol}}}{4\pi^2}} a_0 \approx a_0 \quad (2.35)$$

and

$$d \geq l_d = \frac{\lambda_L}{n'_0} a_0, \quad (2.36)$$

where  $\xi_{\text{pol}} = 2$  for the CP laser light and  $n'_0 = n_0/n_c$ . In cases when  $d < l_d$ , the radiation pressure cannot be canceled by the electrostatic pressure and the electrons are permanently expelled from the target. This will cease the RPA mechanism, but the expelled electrons might be used as a relativistically “flying” mirror for massively up- or down-shifting of a second laser via Thomson backscattering [99–101]. For the Trident parameters, where  $\lambda_L = 1 \mu\text{m}$ ,  $a_0 \approx 15$

## 2. RELATIVISTIC LASER-MATTER INTERACTION

---

and  $n'_0 \approx 800$  (see Chap. 3.1.3), this would relate to a threshold target thickness of  $d \approx 18.7$  nm.

In the next step, ions are accelerated in the charge separation field. In this simple model, all ions that “start” in the compression area will reach the end of the compression layer at the same time due to the linearly decreasing charge separation field (see Fig. 2.5). The maximum velocity  $v_i$  these ions can reach is [10]

$$v_i = \sqrt{\frac{\epsilon_0 E_s^2}{m_i n_i}}, \quad (2.37)$$

where  $m_i$  and  $n_i$  are the ion mass and initial ion density, respectively. Ions that “start” in the depletion area will not catch up with those ions, since the charge separation field is increasing towards the boundary of the depletion and compression area.

In the final step, this boundary will propagate through the target, as the ions from the compression area exit into the unperturbed plasma behind it. Electrons quickly follow to restore the balance between the laser pressure and charge separation field; this step will repeat until the compression layer reaches the end of the target (or the laser pulse is turned off, i.e., the radiation pressure ceases). In this repeating process, the *hole boring* phase, all ions are subsequently accelerated by the radiation pressure to approximately the same final velocity; slower ions will fall back and experience a higher charge separation field than the faster ions that run ahead of the field. This has also been described as *phase stable acceleration* (PSA) in Ref. [12]. When the compression layer reaches the end of the target, the whole focal volume is accelerated as single slab of plasma by the radiation pressure provided the electron distribution stays sufficiently cold preventing the plasma from expansion. This *light sail* phase is the last stage of the RPA acceleration. The final velocity can be estimated according to [10] by equating the radiation pressure during the whole laser pulse duration  $\tau_L$  with the the momentum of the whole target

$$v_f = \frac{(1 + R)\xi\tau_L I_L}{cdn_i m_i}, \quad (2.38)$$

## 2.3. LASER-DRIVEN ION ACCELERATION

---

which gives a final kinetic energy of

$$E_{\text{kin}} = \frac{1}{2}n_i m_i d v_f^2. \quad (2.39)$$

The final ion energies scale here to zeroth order as  $E_{\text{max}} \propto (\tau_L I_L)^2$  in stark contrast to the TNSA mechanism.

According to this model, all plasma ion species should gain the same final velocity; however, recent follow-up studies have shown indications that different inertia of different species will effect the RPA mechanism. In particular, in Ref. [102] protons with the highest charge to mass ratio run ahead of the other species, gaining higher velocities.

Another regime of RPA has been described for targets of sub-skin-depth thickness ( $d \leq l_s$ ), where the laser light leaks through the target and accelerates electrons on the back side of the target into the vacuum. The afore mentioned basic equilibrium conditions do not apply anymore in this *leaky light sail* regime of RPA, resulting in a less efficient acceleration of ions and a broad energy spectrum [103]. Realizing RPA experimentally is difficult; a one-dimensional interaction geometry is necessary in order to suppress heating due to target denting under the laser pressure. A curved target will “see” the CP laser light partially as LP giving rise to electron heating, eventually destroying the RPA mechanism. So far, only one experimental publication [32] claims observation of RPA signatures; the observed spectra were not mono-energetic, but strongly modulated with a feature at the high energy tale.

### 2.3.3 Break-out afterburner (BOA)

All laser-driven ion acceleration described so far, namely the TNSA and RPA mechanism, is the result of a laser interacting with a opaque/overdense target during the complete interaction time, i.e.,  $n'/\gamma$  is is always larger than unity. In that matter, the Break-out afterburner (BOA) is fundamentally different: the dominant part of the acceleration takes place when  $n' > 1 > n'/\gamma$ , i.e., during the time the target is classically overdense, yet relativistically transparent to the laser light (see Sect. 2.2.3). The BOA has been identified as a novel mechanism by Yin *et al* [28, 104] and Albright *et al.*[29, 86] in high resolution PIC simulations. The used code is VPIC [105], which is a “fully explicit, massively parallel,

## 2. RELATIVISTIC LASER-MATTER INTERACTION

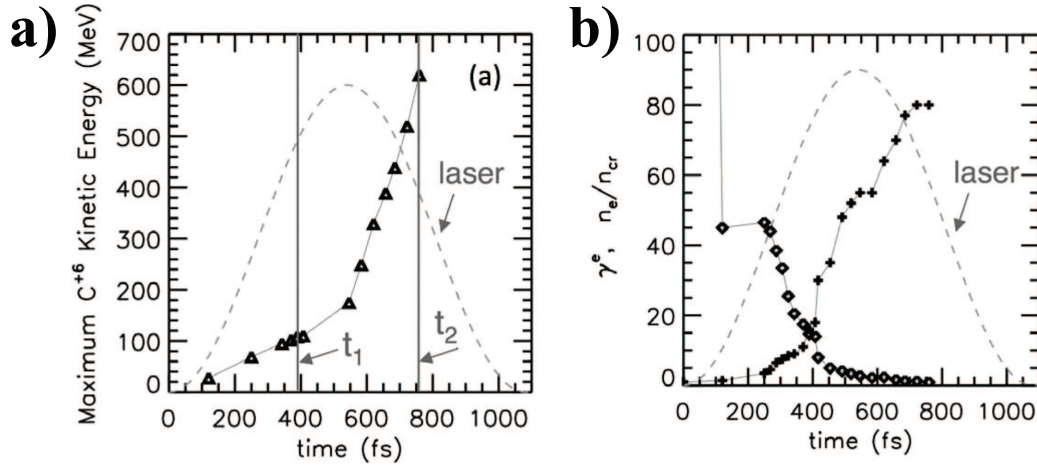


Figure 2.6: VPIC simulation results for Trident laser parameters and a 58 nm diamond like carbon target. In a) the maximum carbon C<sup>6+</sup> vs time (solid line with triangles) and the laser intensity envelope in arbitrary units (dashed line); between the times  $t_1$  and  $t_2$  90% of the energy gains occurs. In b) the related normalized electron densities (diamonds) and the electron Lorentz factor (pluses) are plotted and show that the target is relativistically transparent between the times  $t_1$  and  $t_2$ . (Figure adapted from Ref. [106])

relativistic, electromagnetic particle-in-cell (PIC) code that employs exact charge and magnetic field divergence-conserving algorithms, energy-conserving field interpolations ( $\vec{E}$  and  $\vec{B}$  solve), a sixth order magnetic field advance, and an exponentially differenced explicit field solver on a Cartesian Yee-mesh” [106].

### The physical picture of BOA

The BOA mechanism can be divided into 2 distinct phases, a phase of volumetric heating and an acceleration phase. The first phase starts as usual with the rapid ionization of the target with LP laser light normally incident on the highly overdense target (oblique incidence is also possible). At this point the interaction is not that different from TNSA; copious hot electrons are generated by the ponderomotive force of the laser light, i.e., through  $\vec{j} \times \vec{B}$  heating. These hot electrons travel through the target and eventually set up a sheath field on the rear side of the target. The opaque bulk of the target provides cold electrons for the return current into the laser conversion region, where they are subsequently converted to hot electrons.

### 2.3. LASER-DRIVEN ION ACCELERATION

---

At this stage the skin depth  $l_s$  is increasing as the the electron density starts to decrease, since  $l_s \propto c/\omega_p \propto c/\sqrt{n_e}$ , so that the laser evanescent field reaches further into the still opaque target, further enhancing hot electron generation. For a sufficiently thin target, the laser eventually converts all electrons into hot electrons with highly relativistic energies through this process of volumetric heating. As a result, the classically overdense target turns relativistically underdense with  $n' > 1 > n'/\gamma$ , introducing a strong longitudinal electric field in the target by means of plasma wave. In particular, the highly relativistic beam of electrons in the target and the comparatively slow (non-relativistic) plasma ions support a rapid growth of the two-stream Buneman instability (see Sect. 2.2.6). The phase velocity of the instability is resonant with the ions, so that it efficiently mediates the electron energy to the ions. [104]. This point in time will later on be referred to as  $t_1$  (see Fig. 2.6 and Fig. 2.7).

A 1D analysis of the relativistic kinetic Buneman instability with respect to the BOA mechanism is presented in Ref. [29] and closely matches the VPIC results. However, the experimental evidence for the instability as the dominant factor in the acceleration process is still open, as a clear signature of the stability is not obvious and direct time and spatially resolved measurements of the electron densities are quite challenging.

It should be noted here, that the VPIC simulations also show *self-cleaning* of the target. This means, that in the case of a multi species target the protons (from the contamination layer and bulk) are rapidly evacuated (*self-cleaned*) from the volumetrically heated target due to their low inertia and high charge to mass ratio; as a result, the following phase of extreme acceleration mainly effects the remaining heavier plasma ions. For CP laser light, the initial conditions are closer to RPA and the electrons are rather compressed and pushed into the target; this scenario will be discussed in greater detail in Chap. 4.4.1.

The second phase starts with  $t = t_1$ . The longitudinal field, that has been set up in the first phase, co-moves with the plasma ions accelerating them into a high energetic and initially mono-energetic beam; acceleration before  $t_1$  is only moderate and accounts for less than 10% of the final ion energies [106] (see Fig. 2.6). This is a fundamental difference to the RPA regime, where efficient acceleration occurs only for an opaque plasma (allowing momentum transfer by laser light reflection). Since the target is transparent to the laser light, the electrons constantly regain their lost energy sustaining the instability and hence the ion acceleration.

## 2. RELATIVISTIC LASER-MATTER INTERACTION

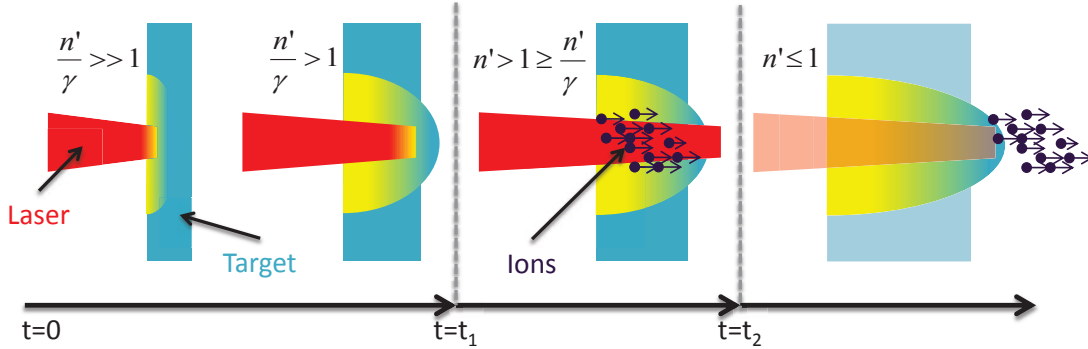


Figure 2.7: Sketch of the Break-out Afterburner: In the time between  $t = 0$  and  $t = t_1$  the target is volumetrically heated and all electrons are subsequently promoted to hot electrons. At  $t = t_1$  the plasma density has dropped to  $n' > 1 > n'/\gamma$  and the target turns relativistically transparent to the laser light. It follows a period of rapid and extreme ion acceleration, where the electrons energy is continuously replenished by the laser light. The acceleration ceases when the target turns classically underdense at  $t = t_2$  due to the strong expansion of the plasma with  $N < 1$ .

During this main acceleration phase, the initially mono-energetic beam gradually turns into an exponentially decaying energy spectrum. The acceleration continues until the plasma has expanded so far, that it has turned classically underdense with  $n'/\gamma \ll n' \leq 1$  (see Fig. 2.6 and Fig. 2.7). This point in time is referred to as  $t = t_2$ .

The ion acceleration quickly stops after the time  $t_2$ , as can be seen in the simulation results shown in Fig. 2.6 and Fig. 2.7; this is most likely a result of the significantly reduced electron density in the now strongly expanded plasma. The acceleration in the BOA regime is most effective when the time of relativistic transparency of the target overlaps with a large fraction of the laser pulse peak. While a too thin target will turn classically underdense prior to the peak of the pulse, a too thick target will turn relativistically transparent after the peak of the pulse or not at all, not even starting the BOA mechanism. The latter case can be seen as a gradual transition into the TNSA regime, where acceleration is purely done by the sheath field on the back side of the target.

### Analytical model

In Ref. [107] a simple model for the target expansion dynamics has been presented. A more complete self-similar analytical model that calculates the maximum ion

### 2.3. LASER-DRIVEN ION ACCELERATION

---

energies based on the times  $t_1$  and  $t_2$  has been derived by Yan *et al.* [108] and is summarized in the following. Based on the assumption that the target expands only 1D along the laser axis during the initial first phase, one can derive the time  $t_1$  as follows: in the beginning the ponderomotive force of the laser light is balanced by the charge separation force so that

$$\frac{dp}{dt} = q_i e E_s = -q_i e \nabla \Phi. \quad (2.40)$$

For a  $\sin^2$ -pulse, the ponderomotive potential  $\nabla \Phi$  can be approximated as

$$\nabla \Phi = m_e c^2 \left( \sqrt{1 + \frac{a_0^2 \sin^4 \left( \frac{\pi t}{2\tau_\lambda} \right)}{2}} - 1 \right) \approx m_e c^2 a_0 \sin^2 \left( \frac{\pi t}{2\tau_\lambda} \right), \quad (2.41)$$

where  $\tau_\lambda$  is the FWHM of the laser pulse and  $x$  the target front and assuming  $a_0 \gg 1$ . With  $dp_x = m_i dx$ , integrating twice over  $dt$  gives

$$x^2 - d^2 \approx \frac{m_e q_i c^2 a_0}{m_i 3} \left( \frac{\pi}{2\tau_\lambda} \right)^2 t^4, \quad (2.42)$$

with the boundary condition that the foil is initially at rest with a target thickness of  $x(t=0) = d$ . Relativistic transparency is reached, when  $n'/\gamma = 1$ ; with the target only expanding 1D in  $x$ , this relates to a length  $x(t=t_1) = x_1 = n_0 d / n_c \gamma = n'_0 d / \gamma$  and gives for  $t_1$

$$t_1 = \left( \frac{12 m_i}{\pi^2 c^2 m_e} \frac{N_0^2 d^2 \tau_\lambda^2}{q_i a_0^3} \right)^{\frac{1}{4}} \approx \left( \frac{12}{\pi^2} \right)^{\frac{1}{4}} \left( \frac{N_0 \tau_\lambda d}{a_0 \tilde{c}_s} \right)^{\frac{1}{2}} \quad (2.43)$$

with  $\gamma \approx \sqrt{a_0^2 + 1}$  and the maximum ion sound speed  $\tilde{c}_s \approx \sqrt{q_i m_e c^2 a_0 / m_i}$  (see Eq. 2.25).

For calculation of the time  $t_2$  a 3D isospheric expansion of the target is assumed. This approach is justified by the relativistic transparency of the target between  $t_1$  and  $t_2$ , where all electrons have been promoted to hot electrons by the laser light causing strong 3D expansion of the plasma.  $t_2$  is reached, when the target turns classically underdense with  $n' \leq 1$ . This relates to a volume change of  $\gamma$  and a length expansion by a factor of  $\gamma^{1/3}$  in each direction. Here, one can make the ansatz that the expansion in each direction is only due to the ion sound speed

## 2. RELATIVISTIC LASER-MATTER INTERACTION

---

$\tilde{c}_s(t = t_1)$  by

$$dx = \tilde{c}_s(t)dt = \sqrt{\frac{q_i e m_e c^2}{m_i} a_0 \sin^2\left(\frac{\pi t_1}{2\tau_\lambda}\right)} dt = \tilde{c}_s \sin\left(\frac{\pi t_1}{2\tau_\lambda}\right) dt, \quad (2.44)$$

with a  $\sin^2$  temporal envelope. This gives after integration over  $dt$

$$dx = x_1 \gamma^{\frac{1}{3}} - x_1 = \frac{N_0 d}{\gamma} \left(\gamma^{\frac{1}{3}} - 1\right) = \tilde{c}_s \sin\left(\frac{\pi t_1}{2\tau_\lambda}\right) (t_2 - t_1) \quad (2.45)$$

and can finally be rearranged for  $t_2$  so that

$$t_2 = \frac{N_0 d \left(\gamma^{\frac{1}{3}} - 1\right)}{\gamma \tilde{c}_s} \frac{1}{\sin\left(\frac{\pi t_1}{2\tau_\lambda}\right)} + t_1 = \Delta t + t_1. \quad (2.46)$$

The times  $t_1$  and  $t_2$  can now be used to estimate the maximum energy ions may gain in the BOA phase. The calculation follows the ansatz that the final ion energy only depends on the characteristic electron energy  $\bar{E}_0$ , which is given as the time averaged electron energy due to the ponderomotive force of the laser

$$\bar{E}_0 \approx \frac{m_e c^2}{t_1 - t_2} \int_{t_1}^{t_2} \left(\sqrt{a^2(t) + 1} - 1\right) dt, \quad (2.47)$$

where typically  $a(t) = a_0 \sin^2(\pi t/2\tau_\lambda)$ . Based on the *electron reflexing model* by Mako and Tajma [109], the response of the (non-relativistic) ions to the electrostatic field, i.e., to the characteristic electron energy  $\bar{E}_0$ , can be derived from the non-relativistic fluid equations (see Ref. [108] for a full derivation). This gives the following expression for the maximum energy ions may gain during the relativistic transparent laser interaction as

$$E_{\max} = (2\alpha + 1) q_i \bar{E}_0 \left( (1 + \omega_p(t_2 - t_1))^{\frac{1}{2\alpha+1}} - 1 \right), \quad (2.48)$$

where  $\alpha$  is the so-called *coherence parameter* in the reflexing model, that describes how efficiently the ions couple the electrons. The parameter has been extrapolated from PIC simulations in Ref. [108] and is  $\sim 3$  for a large parameter range where  $0.1 \leq n'_0 d/a_0 \lambda \leq 10$ . In Fig 2.8 the maximum carbon  $C^{6+}$  ion energy and the times  $t_1$  and  $t_2$  are plotted vs. the target thickness using the analytical model; Eq 2.47 is solved numerically for typical Trident parameters ( $\tau_\lambda = 600$  fs,

### 2.3. LASER-DRIVEN ION ACCELERATION

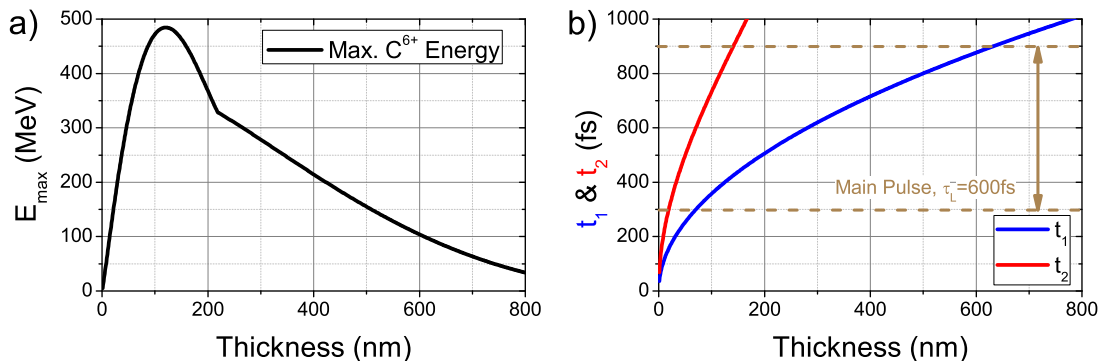


Figure 2.8: Model prediction a) of the maximum carbon  $C^{6+}$  energy vs. Thickness for Trident parameters with  $\tau_\lambda = 600$  fs,  $E_L = 80$  J,  $n'_0 = 660$ ,  $q_i = 6$  for carbon  $C^{6+}$  and  $a(t) = a_0 \sin^2(\pi t/2\tau_\lambda)$ , with  $a_0 = 16.8$ ; b) BOA acceleration times  $t_1$  and  $t_2$  for the same parameters

$E_L = 80$  J,  $n'_0 = 660$ ,  $q_i = 6$  for carbon  $C^{6+}$  and  $a(t) = a_0 \sin^2(\pi t/2\tau_\lambda)$ , with  $a_0 = 16.8$ ). The model shows, that for the Trident parameters targets on the order of 100 nm are needed. It further predicts peak carbon  $C^{6+}$  ion energy of  $\sim 500$  MeV (42 MeV/amu) at an optimum target thickness around 150 nm. As will be shown later in Chap. 4, the analytical model agrees remarkably well with actual experimental results obtained from several campaigns at Trident. Moreover, the model is also in good agreement with PIC simulations [106] as well as other experimental results, where the target turned relativistically transparent using a different laser system (Ti:Sapphire) [88] (with less energy ( $E_L = 0.7$  J) and much shorter pulse duration ( $\tau_\lambda = 45$  fs) operating at a very different point parameter space.

In summary the BOA mechanism has the following distinct signatures

- the acceleration happens during the time the target is relativistic transparent where  $n' > 1 > n'/\gamma$
- the acceleration promises to be more efficient than TNSA (with higher conversion efficiency and higher maximum energies), since the electron energies are continuously replenished by the laser as a result of the relativistic transparency and plasma ions along the whole focal volume can be accelerated
- self-cleaning of the volumetrically heated target, i.e., removal of protons from the main interaction volume, enables efficient acceleration of heavier ions

## 2. RELATIVISTIC LASER-MATTER INTERACTION

---

It should be noted here, that the BOA mechanism has specific pre-conditions in order to work. As shown above, for Trident laser parameters ultra-thin targets on the order of  $\sim 100$  nm are necessary to enter the relativistic transparency of the target and to enable the BOA acceleration. Keeping these targets overdense within the peak of the laser pulse demands ultra-high contrast at these relativistic laser intensities. A low contrast eventually results in premature ionization and target expansion up to the destruction of the nm-thin target prior to the arrival of the main pulse (see Chap. 3.1.5 for details). The Trident laser offers an exceptionally high laser contrast at relativistic laser intensities (see Chap. 3.1.5), which enabled in-detail study of the BOA mechanism in the framework of this thesis. A comprehensive experimental study of the BOA mechanism is presented in Chap. 4, that investigates thickness and laser intensity scalings, angular beam dependency, conversion efficiency and the control of the energy spectra for both proton and carbon C6+ ions using diamond and diamond like carbon (see Chap. 3.2) targets.

## 2.3. LASER-DRIVEN ION ACCELERATION

---

# Chapter 3

## Methods: Laser, targets and diagnostics

### 3.1 A short introduction into Lasers and laser beams

In this section a short introduction into lasers and laser beams, i.e., laser focusing and laser contrast will be given. Some important parameters will be defined that are necessary in order to qualify the Trident laser and to set a basis for the laser-plasma interactions that will be discussed in Chapt. 4.

The history of the laser (light amplification by stimulated emission of radiation) started in 1917 with Albert Einstein setting the basic theory for stimulated emission [1]. The first optical laser, based on a ruby crystal, was built more than 40 years later by Theodore Maiman [2] in 1960. It is interesting to note that within less than 1 year the first scheme for laser-driven ICF was proposed by John Nuckolls in an internal report at LANL, which was published later in Nature [110]. In the following 20 years laser intensities reached a level of  $10^{15}\text{W}/\text{cm}^2$  [111, 112]. In order to further increase laser intensities, it was necessary to further increase the beam diameter. While this kept the fluence on the laser optics (such as the amplifier rods/discs and mirrors) below their damage threshold, it also made intensities above  $10^{15}\text{W}/\text{cm}^2$  unfeasible by requiring huge and hence expensive optics. A solution to this problem was not found until D. Strickland and G. Mourou invented the chirped pulse amplification (CPA) in 1985. The invention

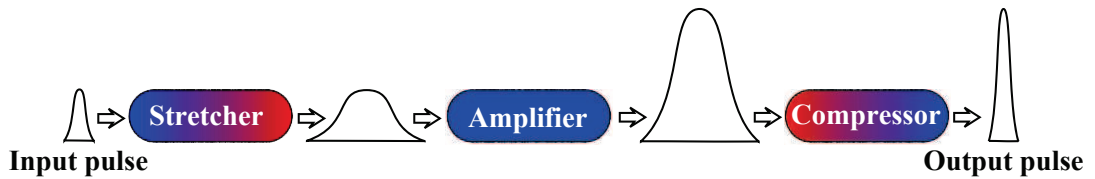


Figure 3.1: Schematic depiction of a CPA stage, where the pulse is first stretched in time, then amplified and finally recompressed.

of CPA finally lead to the possibility of building “table-top” laser systems capable of generating beams exceeding 10th of TW and focused laser intensities exceeding  $10^{20}\text{W}/\text{cm}^2$ .

### 3.1.1 Chirped pulse amplification (CPA)

Instead of further increasing the beam diameter in order to reduce the fluence on the optics, the pulse is stretched in time, then amplified and finally recompressed. In a typical CPA system, first a positive group-velocity dispersion is introduced into the laser path by a grating or prism, spatially and temporally separating different wavelengths of the laser pulse. The stretching in time is on the order of  $10^3$ , typically generating a pulse duration of  $\sim 100$  ps out of a fs seed pulse. In the next step, the pulse can now be amplified conventionally, as the fluence on the optics is below their damage threshold. In the last step, the pulse is recompressed by another grating or prism set up to introduce a negative group-velocity dispersion. The final pulse duration is slightly above the original one, as the pulse is usually affected by nonlinear dispersion effects and gain-narrowing in the amplifiers [54, 113] (gain-narrowing refers to the effect that the laser is preferentially amplified around the central wavelength, resulting in reduction of the bandwidth).

### 3.1.2 Time-bandwidth product

At this point it is useful to introduce the time-bandwidth product  $\Delta\nu\tau$  as a measure of the pulse compression [113]. Here,  $\Delta\nu$  and  $\Delta\tau$  correspond to the FWHM of the laser pulse in the frequency and time domain, respectively. Considering a typical laser pulse with a Gaussian shaped envelope, the corresponding electric

### 3. METHODS: LASER, TARGETS AND DIAGNOSTICS

---

field is given by [114]

$$E(t) = E_0 \exp\left(-2 \ln(2) \frac{t}{\tau}\right) \quad (3.1)$$

and hence the instantaneous intensity by

$$I(t) = E(t)^2 = E_0^2 \exp\left(-4 \ln(2) \frac{t}{\tau}\right) \quad (3.2)$$

resulting in  $\Delta\tau = \tau$ . The power spectrum  $I(\nu)$  of the Gaussian laser pulse can be derived by the Fourier transformation of  $E(t)$

$$E(\nu) = E_{\nu 0} \exp\left(\frac{(\pi\tau\nu)^2}{2 \ln(2)}\right) \quad (3.3)$$

and calculating

$$I(\nu) = E(\nu)^2 = E_{\nu 0}^2 \exp\left(\frac{(\pi\tau\nu)^2}{\ln(2)}\right) \quad (3.4)$$

The frequency FWHM  $\Delta\nu$  is thus  $2 \ln 2 / \pi \tau$  and the time bandwidth product consequently gives

$$\Delta\nu\tau = 2 \ln(2) / \pi \approx 0.4413. \quad (3.5)$$

Defining  $\Delta\nu$  and  $\Delta\tau$  as the rms (root mean square) of the laser pulse yields  $\Delta\nu\tau = 0.5$  in close relation to the well known uncertainty principle, where  $\sigma_x/\sigma_p \geq \hbar/2$ . A laser pulse with a time-bandwidth product close to this limit is usually referred to as *transform-limited*. Adding a phase to the laser pulse, such as a chirp due to imperfect compression in the CPA, will consequently result in larger FWHM values and a larger time-bandwidth product.

#### 3.1.3 The Trident laser facility

The Trident laser facility at the Los Alamos National Laboratory is a Nd:glass system with 150TW maximum power. It should be noted that Trident does not have highest laser intensities available today, several facilities already offer systems exceeding 1PW. However, it offers the best combination of ultra-high contrast and ultra-high on-target intensity and consequently still holds the world records for maximum energies of laser accelerated proton and carbon  $C^{6+}$  ions with  $\sim 120$  MeV and  $\sim 1$  GeV (see Chapt. 4), respectively, which have both been

### 3.1. A SHORT INTRODUCTION INTO LASERS AND LASER BEAMS

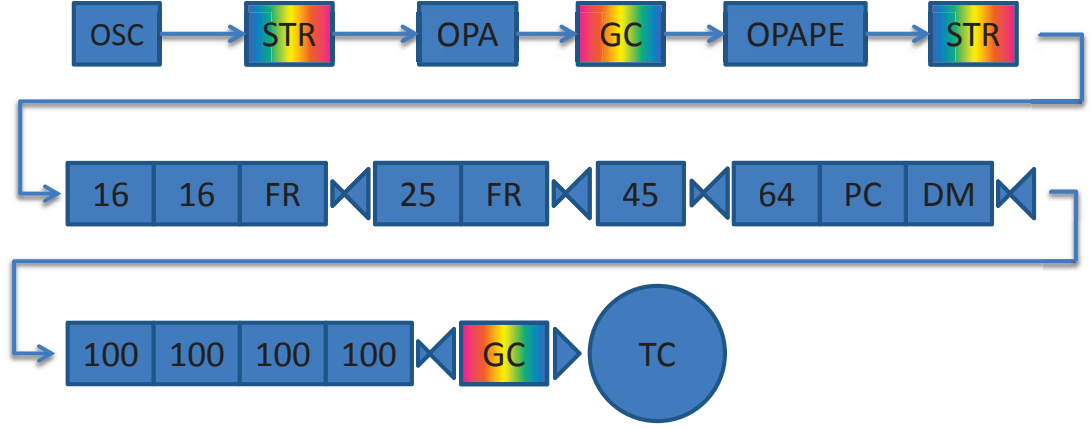


Figure 3.2: Trident laser schematics with “OSC” the seed oscillator, “STR” and “GC” the stretcher and compressor, respectively; with “OPA” and “OPAPE” the optical parametric amplifier and cleaner stage, “DM” the deformable mirror, “FR” a Faraday rotator and “TC” the target chamber. The numbered boxes are amplifier rods/discs of the same size.

produced in the framework of this thesis. Experiments can be fielded in two target chambers with a huge list of available diagnostics for focusing, reflected and transmitted beam analysis, target positioning, particle detection, X-ray generation etc. Trident offers 3 different beams, one short pulse and two long pulse beams, which can be used at the same time. The long pulse beams operate at 527 nm (frequency doubled) with 250J and duration of 5 ns down to 100 ps and at 1053 nm with 1kJ in 100 ps to 10  $\mu$ s. The short pulse beam, which has been used for all experiments described in Chapt. 4, generates pulses with typically 80 J on-target (100 J after last amplifier) in  $\sim$ 550 fs (FWHM) at its fundamental wavelength of  $\lambda=1053$  nm. Fig. 3.2 shows a schematic depiction of the Trident short pulse beam. Here, the laser is seeded by a GLX-200 diode pumped glass oscillator which produces 250 fs pulses with 2 nJ energy. The oscillator output is first stretched and then amplified by 3 OPA (optical parametric amplification in a non-linear optical medium) stages which are pumped by a frequency doubled Nd:YAG laser. The pulse is then recompressed by a grating compressor and cleaned by an OPAPE [115] stage (see Sect. 3.1.5 for details). After the OPAPE stage the now 4-5 mJ cleaned pulse is again stretched and then injected into the amplifier chain for further amplification with a series of 16 mm, 25 mm, 45 mm and 64 mm glass rod amplifiers. A deformable mirror reduces distortions induced by thermal heating/lensing of the amplifiers before the pulse is finally

### 3. METHODS: LASER, TARGETS AND DIAGNOSTICS

---

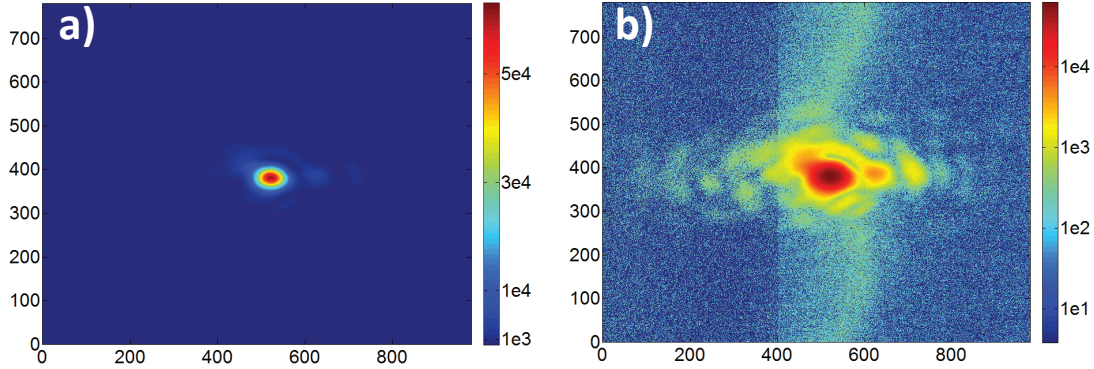


Figure 3.3: Raw image taken with the focus diagnostic camera a) with linear  $z$ -scale and b) with log  $z$ -scale. Axes are in original pixel values, where one pixel is  $\sim 0.086\mu\text{m}$ . Note, that the wavy haze above and under the focus visible in image b) is an artifact, most likely resulting from working near saturation of the camera.

amplified to the 100 J level by a series of 100 mm disc amplifiers [116, 117]. An overall shot cycle of 45 min to 60 min is necessary to suppress subsequent heating of the amplifiers over the course of a single day, limiting the number of shots to  $\sim 7$  a day. The output pulse has a typical FWHM duration of 550 fs and  $\sim 80\text{J}$  (minimum measured on-shot was 460 fs with 111 J giving a power of 241 TW); its envelope spans 157 laser cycles of each  $\sim 3.51$  fs. The wavelength bandwidth is typically  $\sim 3$  nm, where with  $d\nu d\tau = 0.4456$  (with  $\nu = c/\lambda$ ) the pulse is nearly transform-limited. It should be noted that a modern Ti:Sapphire laser system, such as the ATLAS Ti:Sa-system at the MPQ, generates laser pulses with  $<10$  J on the order of 30 fs with only a few laser cycles. Compared to these, the Trident short pulse beam is still quite long and while the maximum output powers and average intensities for both systems are of the same order, the physics of the laser-plasma interaction can be considerably different.

#### 3.1.4 Trident laser focus

In most of the experiments a F/3.375 off-axis parabolic (OAP) mirror ( $f=27$  inch, 68.58 cm) is used to focus the typically linearly polarized beam (diameter  $D=8$  inch, 20.32cm) after the final turning mirror onto the target, with  $F=f/D$  the  $f$ -number or relative aperture of the OAP. A typical focus image is shown in Fig 3.4 with a linear (left frame) and a logarithmic intensity scale (right frame). The image was

### 3.1. A SHORT INTRODUCTION INTO LASERS AND LASER BEAMS

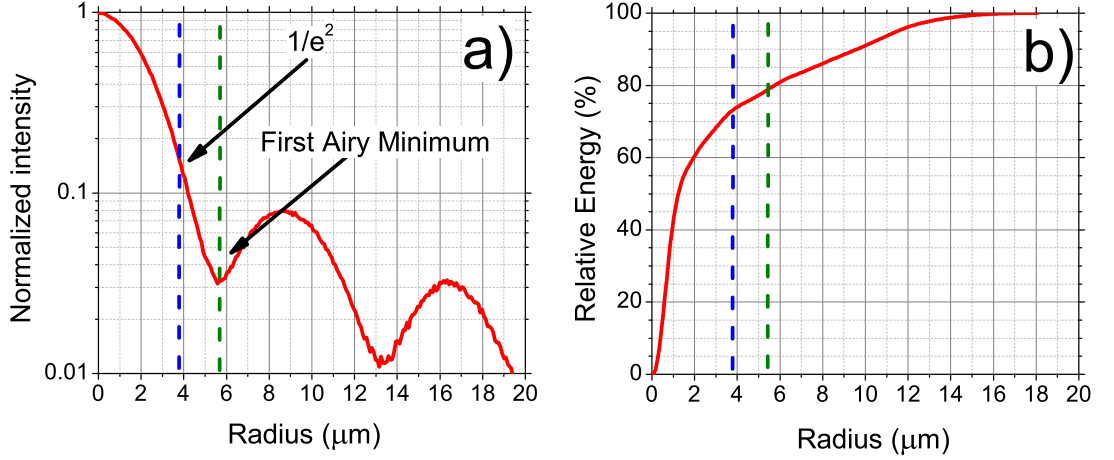


Figure 3.4: Analysis of the focus image shown in Fig.3.3. Frame a) shows a lineout normalized to the peak pixel intensity. The radius is  $\sim 3.9\mu\text{m}$  with respect to a  $1/e^2$  criterion, with an corresponding encircled energy for this radius of  $\sim 73\%$ , as shown in frame b). Values for the first Airy minimum are  $\sim 5.6\mu\text{m}$  with an encircled energy of  $\sim 76\%$

taken with a newly developed focusing diagnostic (see Chapter 3.3 for details), where the focus is magnified by an 20x plan-apochromatic microscope objective and subsequently imaged onto the camera’s 12bit sensor. The wavy haze visible above and under the focus in the right frame is an artifact most likely resulting from the camera’s sensor not being cooled and operated near saturation. X- and Y-axis of the images are in original pixels, where one pixel has been measured to correspond to  $0.086\mu\text{m}$ . From this image, the peak intensity has been estimated to  $\sim 4.5 \times 10^{20}\text{ W/cm}^2$  assuming 80 J and 550 fs in the fully amplified pulse.

In order to further quantify the focus of Trident’s short pulse beam, it is useful to give the radius of the focus and its encircled energy. Any real laser system usually contains circular apertures that cause Fraunhofer diffraction (in the farfield), and will give the well-known “Airy pattern” in the focus. For the following analysis, a laser pulse that is spatially Gaussian shaped will be considered, where the beam waist  $w_0$  is defined as the radius of the focal spot at which the intensity  $I(w_0)$  has decreased to 14% ( $1/e^2$ ) of its peak value. The beam is called *diffraction-limited*, if the focal spot has an encircled energy of 86% within  $w_0$  [118]. The waist is furthermore connected to the f-number by  $w_0 = F\lambda$ , which gives a  $w_0 = 3.375 \times 1.054 \approx 3.56\mu\text{m}$  (in the diffraction limit). Note, that for a planar wave, incident on the same circular aperture, the waist is usually given as the

### 3. METHODS: LASER, TARGETS AND DIAGNOSTICS

---

first Airy minimum of the diffraction pattern with  $w_0 = 1.22F\lambda$  (where the focal spot has an encircled energy of 84%) [114]. A more complete derivation can be found in many textbooks such as [114, 118–120].

In Fig. 3.4a) a lineout of the focus shown in Fig. 3.3 is shown. The beam waist of Tridents short pulse beam measures  $\sim 3.9\mu\text{m}$  (and  $5.6\mu\text{m}$  for the first Airy minimum). The encircled energy is depicted in Fig. 3.4a) and is measured to be  $\sim 73\%$ ; that gives a Strehl-ratio of  $73\%/86\%=0.85$ .

Another important parameter in terms of laser focusing is the Rayleigh length  $z_r$  of the focus, with  $z_r = \pi w_0^2/\lambda$ . The Rayleigh length gives the length along the propagation direction of the beam after which the area of focal spot has doubled (or the waist  $w_0$  has increased by a factor of  $\sqrt{2}$ ). Amongst other things, this parameter gives an upper limit of the accuracy needed for focus and target alignment. If the alignment of the target is off by more than the Rayleigh length, the resulting intensity on target is consequently reduced by a factor of 2; for Tridents focal spot  $z_r \approx 50\mu\text{m}$ .

#### 3.1.5 Trident laser contrast

In order to get a more complete picture of the possible laser-plasma interactions with Tridents short pulse beam, it is also necessary to identify its contrast. A typical laser pulse is usually preceded by a pedestal that is often caused by amplified spontaneous emission (ASE) in the amplifiers [118]. In addition it might also contain one or more pre- and post-pulses originating from unwanted double reflections somewhere in the laser chain. The laser pedestal and pre-pulses can change the initial properties of the target (such as the electron density and the electron temperature) prior to the main pulse arriving the target and hence dramatically change the main laser-plasma interaction. In the experiments explained in Chap. 4, an ultra-high contrast was necessary; here, the laser was incident on targets as thin as 3 nm and an insufficient low contrast would have destroyed the target before the arrival of the main pulse (see also Fig 3.7). Typically, intensities on the order of  $10^8$  to  $10^{12}\text{W}/\text{cm}^2$  will ionize the target surface and create a pre-plasma. Considering a maximum ion sound speed  $c_s$  of this pre-plasma on the order of  $10^6\text{m}/\text{s}$  (shortly before the main interaction), the plasma will expand at a rate of  $1\mu\text{m}$  per ps (1D expansion) and accordingly reduce the initial electron density the main pulse will interact with or even destroy the target. It

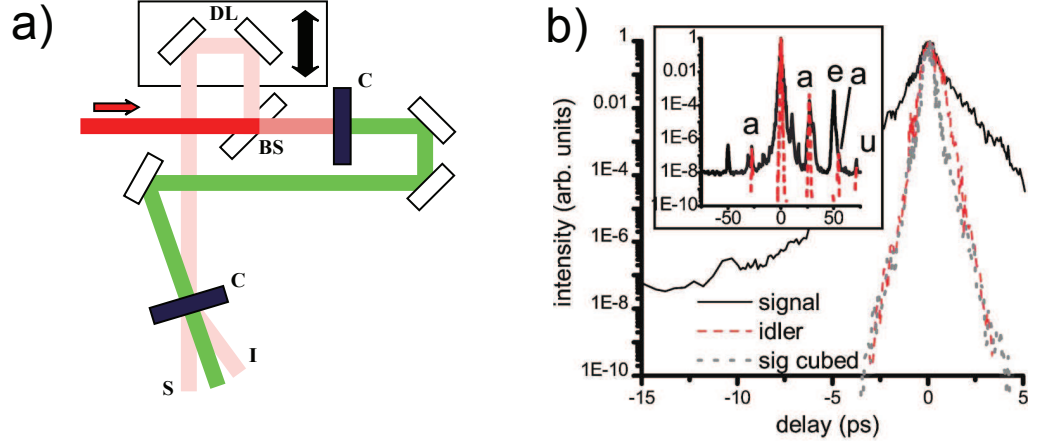


Figure 3.5: Sketch of the OPAPE cleaning technique used at Trident to improve the contrast; b) temporal contrast measurement of the signal (black solid line), the cubed signal (gray dashed line) and the idler (red dashed line). The inset shows a larger time window with some artifacts “a”, a reference pulse “e” and an unknown peak “u” (see text for details, adaption of Ref. [115]).

would thus make sense, to define the contrast of a laser pulse as the time  $t_c$  at which its intensity crosses  $\approx 10^{10} \text{W/cm}^2$ . However, the peak intensity of the Trident short pulse beam is  $4.5 \times 10^{20} \text{W/cm}^2$ , which is about 10 orders of magnitude above the ionization threshold; i.e, in order to measure  $t_c$  a dynamic range of at least 10 orders is necessary. The contrast of Tridents short pulse beam has been improved recently by an optical parametric amplifier based pre-pulse eliminator (OPAPE [115]). This technique is based on second order non-linear polarization. The polarization density of a transparent dielectric medium (such as a crystal) as the result of an applied electric field  $E$  can be written as [118]

$$p = \chi_{(1)}\epsilon_0 E + \chi_{(2)}\epsilon_0 E^2 + \chi_{(3)}\epsilon_0 E^3 + \dots, \quad (3.6)$$

where  $\chi_i$  is i-th order component of the electric susceptibility. In particular, the  $\chi_{(2)}$  term is responsible for second order non-linear processes such as the second harmonic generation or the optical parametric amplification (OPA). The latter is the dominant effect of the OPAPE cleaning technique.

Fig 3.5 a) shows a schematic depiction of the OPAPE stage in the Trident laser chain. Here, the incoming fundamental is first split by a 90/10 beam splitter (BS). The smaller fraction of the beam is later used as the signal wave (s); the larger fraction of the beam is frequency doubled in a beta-barium-borate (BBO)

### 3. METHODS: LASER, TARGETS AND DIAGNOSTICS

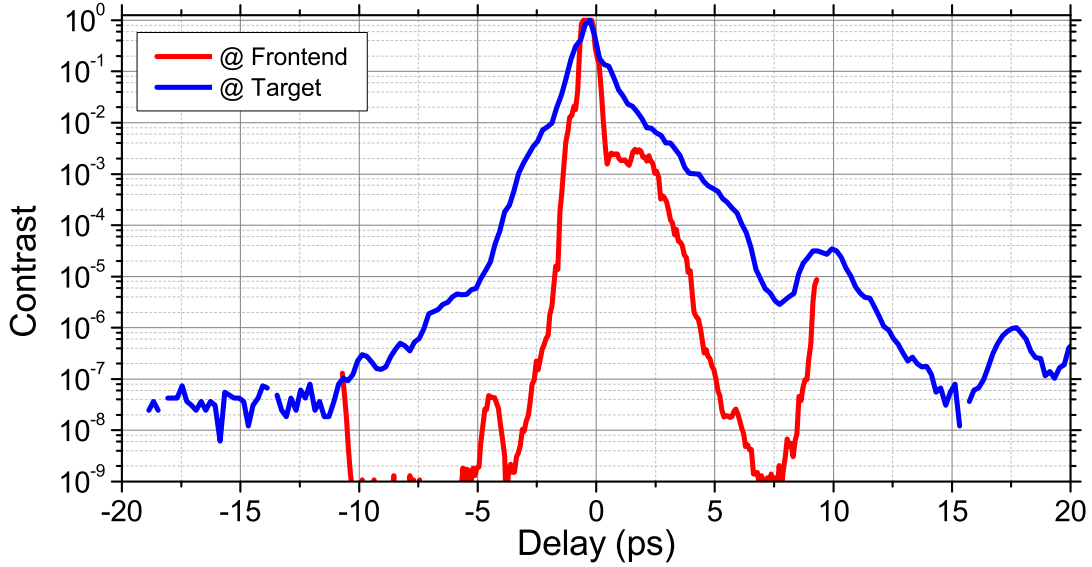


Figure 3.6: Typical contrast of the Trident laser as measured by a scanning-autocorrelator at the front-end (red solid line) and at the target chamber without charging the amplifiers (blue solid line). The decreased contrast at the target side results most likely from imperfect recompression in the final grating compressor.

crystal and serves as the pump wave ( $p$ ). The pump and signal wave are temporally overlapped in a second BBO crystal, which will generate a third beam, the idler wave ( $i$ ) in this second order non-linear process. With a linearized gain, the intensity of the idler wave follows  $I_i \propto I_p I_s$ . Since the pump wave is the frequency doubled signal wave, it follows that  $I_p \propto I_s$  (see Eq. 3.6). The temporal intensity of the idler wave consequently has a cubic dependency on the signal wave resulting in a significantly improved contrast over the original signal wave. The idler wave is then injected back into the laser chain for further amplification.

Fig 3.5 b) shows the temporal intensity profile of the signal (black solid line) and the idler (red dashed line) measured with a commercial third order autocorrelator (Del Mar Photonics). The gray dashed line shows the cube of the signal wave and closely resembles the idler wave, which should follow  $I_i \propto I_s^3$  as explained above. The contrast has here improved by orders of magnitude from  $10^{-4}$  to better than  $10^{-10}$  at -5 ps. The inset of Fig 3.5 b) shows the temporal contrast measurement over the whole time window, where  $a$  marks artifacts,  $e$  a second pulse generated with an etalon as reference and  $u$  an unknown peak (see Ref. [115] for more details). In summary, the OPAPE stage enhances the contrast of the laser pulse by temporally “cubing” its intensity profile in a second order non-linear process.

### 3.1. A SHORT INTRODUCTION INTO LASERS AND LASER BEAMS

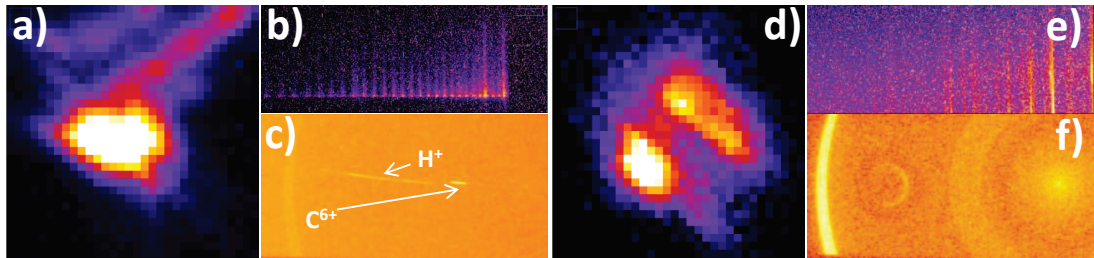


Figure 3.7: Effect of laser contrast on laser-plasma interaction; for a shot with “good” contrast the  $3\omega$  backscatter shows a) a full reflection of the laser focus, strong harmonic generation measured in transmission b) and high carbon  $C^{6+}$  and  $H^+$  energies c). In a “bad” contrast shot, premature target expansion lead to a hole in the backscatter d), intense line radiation without harmonic generation e) and no particles above the detector threshold (11 MeV for  $H^+$  and 220 MeV for  $C^{6+}$ ) f).

The contrast, as measured in Fig. 3.5 b), will, however, deteriorate during its propagation and subsequent amplification in the remaining laser chain. Most of the contrast degradation is expected to come from ASE in the rod and disc amplifiers and imperfect recompression in the final grating compressor (see Fig 3.2). The contrast of a typical Trident laser pulse, as measured with a 3rd order scanning-autocorrelator, is shown in Fig. 3.6 for the front-end (red solid line) and after passing the full amplifier chain (blue solid line) without actually charging the amplifiers (the dynamic range of this measurement is  $\sim 8$  orders of magnitude). The contrast degrades by several orders of magnitude from better than  $10^{-10}$  to  $\sim 10^{-6}$  at -5 ps; the best contrast has been measured to be  $10^{-7}$  at -4 ps (data not shown). This is the contrast as it will be seen by the target. Single-shot contrast measurements of the fully amplified beam ( $\sim 80$  J) have not shown a dramatic change in the contrast (data not shown). However, due to the nature of the single-shot measurement, the dynamic range was only about 4 orders of magnitude; concluding measurements with an advanced setup and improved dynamic range are planned.

The effects of the laser contrast are immediately visible when ultra-thin nm-scaled targets are used, as in most of the experiments described later in Chap. 4. A low contrast laser pulse will prematurely ionize the target, cause significant expansion and possibly destroy it before the peak of the pulse can interact with it. As a result, ion acceleration and other processes that require a small scale-length plasma with high density, such as high order harmonic generation, will work very

### 3. METHODS: LASER, TARGETS AND DIAGNOSTICS

---

inefficient or not at all. In Fig 3.7 results from a shots on targets with “good” (a through c) and “bad” contrast (d through f) are shown. The frames a) and d) show the  $3\omega$  backscatter measurement of the target; harmonics are generated by either the formation of a relativistically oscillating mirror (ROM [51, 121]) or coherent wake emission (CWE [122, 123]) at the critical density surface of the plasma. While frame a) shows a complete spot, i.e.,  $3\omega$  generation and reflection over the whole laser focal spot, frame d) show an incomplete reflection, where the target was most likely underdense to the peak of the laser pulse in the dark areas of the image. Consequently frame b), which shows XUV measurements in transmission, has harmonics exceeding the 20th order and frame e) shows only line radiation originating from different recombination processes in the underdense plasma. Frames c) and f) show the raw data from a Thomson parabola (see Sect. 3.4.2) that was set up to measure proton and carbon ions. For the “good” contrast shot, high energy protons and carbon  $C^{6+}$  ions were measured, while the “bad” contrast shot does not show any particles at all. With the up to date unprecedented high contrast for Nd:Glass laser systems, Trident holds the world records for ion acceleration of protons (120 MeV) and carbon  $C^{6+}$  ions (1 GeV) as shown in Chap. 4, illustrating the importance of contrast in relativistic laser matter interactions.

## 3.2 Targets and target fabrication

In this section a short overview of the targets used for the experiments conducted at the Trident laser will be given. The requirements for these targets are very stringent:

- they have to be ultra-thin, down to only a few nanometers; the optimal thickness for the BOA regime has been predicted to be about 100 nm for the Trident laser.
- they have to be free-standing over a hole with radius of at least a 0.5 mm; with smaller radii, ionization of the target holder could influence the laser-plasma interaction or even damage/destroy surrounding optics by debris or reflected laser light.

### 3.2. TARGETS AND TARGET FABRICATION

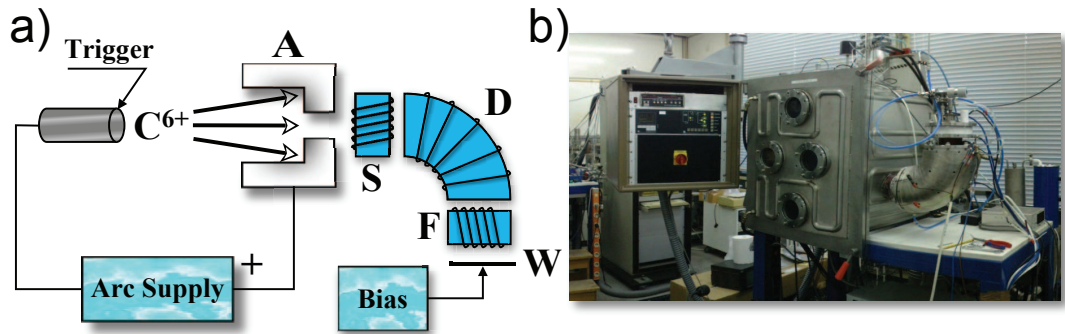


Figure 3.8: a) Sketch of the cathodic arc deposition process and b) picture of the actual setup used to fabricate diamond like carbon targets at the University of Munich.

- they have to have a good surface quality (less than 10% thickness variation over the focal diameter).

Diamond-like carbon (DLC) has most favorable characteristics; it can be manufactured with thicknesses of only a few atomic layers, where its tensile strength enables free-standing assembly (see Fig. 3.9) at affordable costs. DLC is an amorphous mixture of sp<sup>2</sup> and sp<sup>3</sup> hybridized carbon atoms, where the sp<sup>3</sup> bondings give the DLC its diamond like properties such as high tensile strength, hardness, optical transparency, chemical inertness, thermal conductivity and high resistance to radiation damage, as well as extreme heat resistance (sublimation temperature 3653 C°). Many commercial applications are using DLC coatings nowadays, mostly to improve wear resistance of materials, such as hard disk drives used in computers. There are many different ways of fabricating DLC, such as cathodic arc deposition (CAD [124]), pulsed laser deposition (PDL [125–127]) or chemical vapor deposition (CVD [128–130]). The CAD method has the advantage of being a relatively inexpensive and well understood method of producing DLC; it also enables growth of DLC films with very low hydrogen content, as its source - a graphite rod - is essentially pure carbon.

In the framework of this thesis, a laboratory for CAD has been set up at the Ludwig-Maximilians-University Munich with the support of V. Lichtenstein (from the russian Kurchatov institute), where now free-standing DLC films with thicknesses from 3 nm to 60 nm can be made [131]. In Fig. 3.8 a) a sketch of the basic CAD procedure is given, while b) shows a photograph of the actual laboratory. In particular, CAD is a low-voltage, high current plasma discharge and as the

### 3. METHODS: LASER, TARGETS AND DIAGNOSTICS

---

name implies, the ion source is a cathode. In order to coat DLC films a graphite rod is used as cathode material, which is commercially available from “POCO Graphite SARL”. The arc itself is triggered electronically with 25 kV potential at a rate of 5 to 10 Hz and supported by a nitrogen background gas at a pressure of  $10^{-4}$  mbar. The thus generated plasma on the cathode surface plumes off normal to the surface towards the anode; blow-off velocities of 1-3 cm/ $\mu$ s or 10-200 eV of ion drift energy have been reported [132]. The measured current of the arc is usually kept between 2 and 5 A at 30 to 50 V for best results of the DLC coating. A part of this ion beam passes through the cylindrical anode (marked as *A* in Fig. 3.8 a)) and is guided through a cleaning stage consisting of a focusing (*F*) and stabilizing element (*S*) and a 90° duct. In this stage, molten particles (typically on the order of 0.1 to 10  $\mu$ m [124]) from the cathode are removed from the beam. These molten macro particles are generated when the plasma is triggered at the cathode and will, if not removed, significantly deteriorate the quality of the DLC film. The main element of this cleaning stage is the 90° duct that guides the ionized beam through a bent solenoidal magnetic field and filters out the macro particles [133]. In front and behind the duct are a focusing and stabilizing (collimating) magnetic field, respectively. The magnetic fields are generated by coils wrapped around all three of these elements. The throughput of the cleaning stage has not been measured, but has been reported to be approximately 25% [124]. The beam is finally incident on the substrate (marked as *W* for wafer), where it finally forms an amorphous carbon film. The substrate is typically biased with -10 V [134]. The deposition rate achieved with this setup is approximately 0.3-0.5 nm/min, depending on the average arc current and voltage. Depending on the final ion drift energy, the film will have a certain sp<sup>2</sup> to sp<sup>3</sup> ratio; in Ref. [124] the optimal ion drift energy for DLC coating is recommended as  $\sim$ 100 eV, which gives a sp<sup>3</sup> content of up to 85%.

For the fabrication of free-standing DLC targets, a silicon substrate is used with a thin layer of NaCl. This dissolvent is necessary in order to remove the coated DLC film from the substrate after its deposition and to mount or float it onto the desired target holder. Note, that while silicon has a smooth surface on the nm-scale, NaCl is less flat and will eventually influence the macroscopic surface structure of the foils. Fig 3.9 a) shows such a silicon-NaCl substrate with a DLC coating and b) a typical target holder as used for many of the experiments conducted at the Trident laser, the ATLAS laser or the laser system of the Max-Born

### 3.2. TARGETS AND TARGET FABRICATION



Figure 3.9: a) Picture of a silicon strip with deposited DLC; b) Typical target holder with DLC targets used in many experiments and c) 20 nm thin DLC foil free standing over a diameter of 10 mm

institute in Berlin. In Fig 3.9 c) a 20 nm thin DLC foil has been floated onto a holder with a hole of 10 mm diameter, demonstrating the extreme tensile strength of these foils.

The characterization of these foils is probably even more challenging than their production itself and only a short summary of the results will be given here. A lot of effort has been put into measuring the main properties of these foils, which are the thickness, the density and the  $sp^3$  content. Measuring the thickness of a free-standing foil is difficult, due to its nm-thickness and high transparency; instead reference substrates - small stripes of silicon - are used to measure the thickness of the coated film with a high resolution atomic force microscope that has been purchased solely for this task (see Fig 3.10 c). The reference stripes are put on top of the silicon substrates and form a coarse meshed grid; this allows to not only measure the thickness, but also to measure the thickness inhomogeneities that are typical for CAD. In particular, an ordinary text marker is used to draw a line on these stripes before the deposition, which is afterwards removed; this creates a sharp edge in the coating, necessary in order to get accurate thickness measurements. The “shadow” of the reference grid can also be seen in Fig 3.9 a); a typical topographic measurement of a DLC coating on one of these reference stripes is shown in Fig 3.10 a) and a lineout through this map in b). Thicknesses for these coatings have been measured to range from 3 nm up to 60 nm, depending on the duration of the CAD. While the AFM can have sub-nm accuracy, the error of these measurements is most likely higher - approximately 1-3 nm - mainly coming from the hygroscopic nature of the films, which results in accumulation of water on the surface.

Knowing the thickness and the area of the coating, the density of the films has

### 3. METHODS: LASER, TARGETS AND DIAGNOSTICS

---

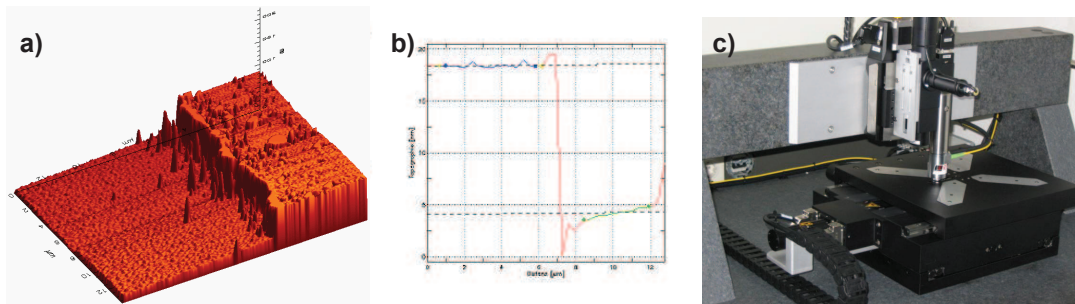


Figure 3.10: a) Topographic scan of a DLC foil at the edge of the coating and b) a lineout showing the thickness of the foil measured with c) an commercial atomic force microscope (AFM)

been measured to  $(2.7 \pm 0.3) \text{ g/cm}^3$ ; graphite has a density of  $\sim 2.15 \text{ gcm}^{-3}$  and diamond  $3.5 \text{ gcm}^{-3}$ . ERDA-measurements (**E**lastic **R**ecoil **D**etection **A**lysis [135, 136]) that have been done by A. Bergmaier and W. Assmann at the Tandem linear accelerator Meier-Leibnitz Laboratory, a LMU and TUM institute, show indications of this hygroscopic effect. These (preliminary) measurements of a DLC film on a silicon substrate revealed a huge proton contamination on the front surface, as shown in Fig. 3.11; with a free-standing foil, this contamination can be expected to appear on both sides of the target. The measurements also revealed a  $\sim 5\%$  bulk proton contamination of target; the origin of this contamination has not been identified yet.

This information is important, when the  $\text{sp}^3$  content of the foils is approximated; direct measurements of the  $\text{sp}^3$  content with for instance auger electron spectroscopy [137, 138], where the binding energy of the carbon  $s_1$  electron is measured, are time consuming and the resources have not been available. In Ref. [139] the  $\text{sp}^3$  content has been measured dependent on the density of the DLC material (see Fig. 3.11 a); here, it has to be distinguished between hydrogenated DLC (also ta-C:H, tetrahedral amorphous carbon) and hydrogen-free DLC (ta-C). The ERDA measurements have shown that the DLC is to some degree hydrogenated (in the bulk) and according to the scaling, the foils have an  $\text{sp}^3$  content of approximately 75%. Direct measurements of the  $\text{sp}^3$  content have to be done in the future, to verify this estimate.

Typically, targets up to a thickness of 30 nm can be floated onto target holders; with increasing thickness, internal stress starts to build up in the foil [140] that prevents floating and subsequent mounting on target holders. Targets with

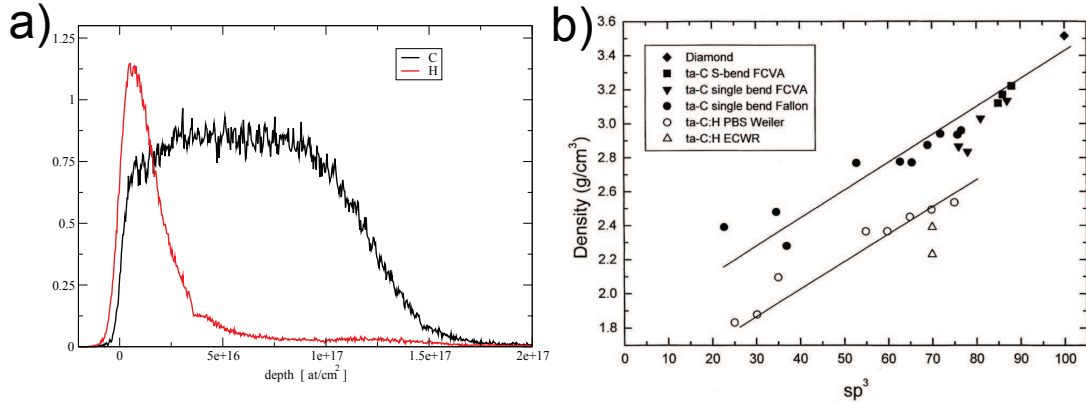


Figure 3.11: a) Preliminary ERDA measurement done at the Tandem accelerator of the Technical University of Munich (TUM) by A. Bergmaier and W. Assmann; b) graph taken from Ref. [139] showing density dependency of the  $sp^3$  content for various DLC foils, where ta-C is hydrogen free and ta-C:H is hydrogen contaminated DLC.

thickness from 30 nm up to several microns are bought from “Applied Diamond, Inc.” [141]. This supplier produces synthetic diamond by chemical vapor deposition. The foils are grown on a silicon substrate and later on down-etched to thicknesses of as low as 30 nm. In order to make the foils free-standing, a whole is etched into the backside of the silicon with a conventional lithographic technique.

### 3.3 Target alignment

As outlined in Sect. 3.1.4 accuracy of the target alignment needs to be significantly better ( $1/2 z_r$ ) than the Rayleigh length of the focus which is for the F/3 setup  $\sim 50 \mu\text{m}$ . Also, the better the alignment accuracy, the less the intensity variations during each target shot. In the framework of this thesis, the alignment procedure has been iteratively improved over the course of the different campaigns from an initial accuracy of  $\pm 20 \mu\text{m}$  to  $\pm 1 \mu\text{m}$ . This means, the front or back surface the target can now be positioned at the focal plane of the laser with an error of  $\pm 1 \mu\text{m}$ . This is especially important, when the OAP is changed to an  $F/\approx 1$  optic and the Rayleigh length reduces to much less than  $10 \mu\text{m}$ .

Fig. 3.12 a) shows a sketch of the setup, which is used for both, defining the focal plane of the laser and positioning the target into that plane. In particular, a 20x plan-apochromatic objective, corrected for infinity, is placed behind the focal

### 3. METHODS: LASER, TARGETS AND DIAGNOSTICS

---

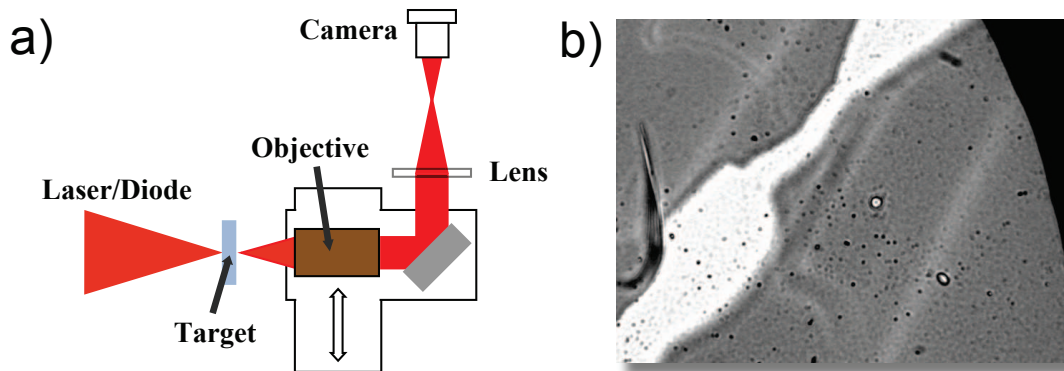


Figure 3.12: a) Schematic depiction of the target and focus alignment setup. The focus of the laser or the target are imaged through an 20x objective relayed out of the chamber with an 2f setup. b) Image of an double target seen through this setup (see text for details).

spot. A second lens and the camera sensor are placed behind the objective in a 2f configuration; i.e., the lens is positioned at a distance of 2f to the image plane of the objective and the camera at a distance of 2f to the image plane of the lens. This gives a 1:1 relay of the objectives image plane.

In this setup the objective is put on a linear stage that allows to move the objective in and out of the laser/particle beam, while the lens and the camera stay fixed, with the camera being outside the target chamber. Both, the linear stage and the camera are controlled by a software that has been written in MatLab specifically for this purpose. The linear stage runs in a closed-loop with a LVDT (linear variable differential transformer); the LVDT is very EMP resistant and supports  $> 1 \mu\text{m}$  accuracy feedback of the stage position. The camera software gives a real-time readout of the focal spot radius, peak intensity, ellipticity and encircled energy. Once the focal plane of the laser has been found by optimizing the above mentioned values, an IR-diode (central wavelength 1054 nm, bandwidth  $\pm 50$  nm) is placed in front of the objective. The diode illuminates the target that can now be positioned at the focal plane of the objective and thus the laser.

Fig. 3.12 b) shows an image of a double target (2 DLC foils separated by  $\sim 10 \mu\text{m}$ ) aligned this way; the light gray area is the target in the focal plane that is visible through a broken second target (dark gray). The improved focusing and target alignment procedure has greatly improved the reproducibility of the experimental results. With the old setup and the accuracy of  $\pm 20 \mu\text{m}$ , 2 out of 10 shots on the optimum target thickness resulted in carbon  $\text{C}^{6+}$  cut-off energies of  $> 500$  MeV;

with the procedure presented here 8 out of 10 shots gave these energies.

### 3.4 Particle detectors

In this section a short introduction into the detection of protons, higher Z ions and electrons will be given. Here, the “detection” of particles means, identifying the particle species, its charge and kinetic energy. There are two different approaches mostly used to do this, which are often mixed together in detector systems:

1. by using the stopping range of the particles, which depends on the particle mass and energy and the detector material
2. by using a combination of (usually parallel) magnetic and electric fields, i.e., reconstruct the particle species, charge and energy via Lorentz equation (see Eq. 3.8)

The energy loss  $S(E)$  per unit path length of an particle can be approximated via

$$S(E) = -\frac{\partial E}{\partial x} \approx S_n(E) + S_e(E) \quad (3.7)$$

where the term  $S_e(E)$  stands for electronic scattering, i.e., inelastic collision with bound electrons and  $S_n(E)$  for nuclear scattering, i.e., elastic collisions with the target material atoms. The calculation of the stopping range is typically done with SRIM (**S**topping and **R**ange of **I**ons in **M**atter). SRIM uses a Monte Carlo simulation method, based on the binary collision approximation [142] to calculate the stopping range of any ion in many materials. The energy loss peaks at the end of the particles path, the so called Bragg peak [143]; this property is very advantageous, when measuring the energy of particles via their stopping range and is also utilized in many other applications, such as the hadron cancer therapy (see Chap. 2.1).

The reconstruction of the particle properties via the Lorentz force takes a quite different approach. Here, a set of magnetic and electric fields is used to change the ion flight path. The deflection of the particle can be used to calculate the particles charge to mass ratio and its energy via the well-known Lorentz equation (see also Chap. 2.1.1)

$$\frac{d\vec{p}}{dt} = q \left( \vec{E} + \frac{\vec{p}}{m\gamma} \times \vec{B} \right), \quad (3.8)$$

### 3. METHODS: LASER, TARGETS AND DIAGNOSTICS

---

where  $p$  and  $\gamma$  are the relativistic momentum and the Lorentz factor of the particle;  $m$  and  $q$  the mass and charge of the particle and  $E$  and  $B$  the electric and magnetic fields. The time is measured in the laboratory frame. When constant parallel magnetic and electric fields are used (or approximated), the equation can be solved analytically in the non-relativistic case.

#### 3.4.1 Detector materials

For both of these techniques, a detector material is needed that measures the deflection of the particle and/or its stopping range. Three detector materials - commonly used in laser-ion acceleration - are introduced here, the radiochromic film, the nuclear track detector CR39 and the image plate (where only the latter two have been used in the experiments described in this thesis).

##### **Radiochromic film**

Radiochromic film (RCF) is a film widely used in medicine for dosimetry, commercially available from GafChromic. It is mainly sensitive to ionizing radiation, such as electrons, protons and other ions. On impact, it instantly turns blue due to a chemical process, where the color density depends on the absorbed dose. Stacks of RCF layers can be used to measure the energy distribution of laser-accelerated proton beams. Each proton deposits most of its energy - according to its stopping range/Bragg peak - in the corresponding layer of the RCF-stack. From the color density in each layer, an energy spectrum of the proton beam can be reconstructed. The full proton beam can be analyzed at once, but with poor energy resolution (depending on the numbers of layers in the stack). Other species, such as carbon, have a very short stopping range compared to the protons and are, if present, usually stopped within the first few layers of such a stack. Hence, in experiments, where other species are of interest, additional detectors or a completely different detection system is necessary, such as for this thesis.

##### **Nuclear track detector, CR39**

The nuclear track detector CR39 [144] (Columbia Resin #39) is widely used for eyeglass lenses and in astrophysics for detection of high energy particles in space [145]. CR39, a allyl diglycol carbonate polymer, is commercially available, for instance from TasTrack that supplies plates of CR39 with a density of

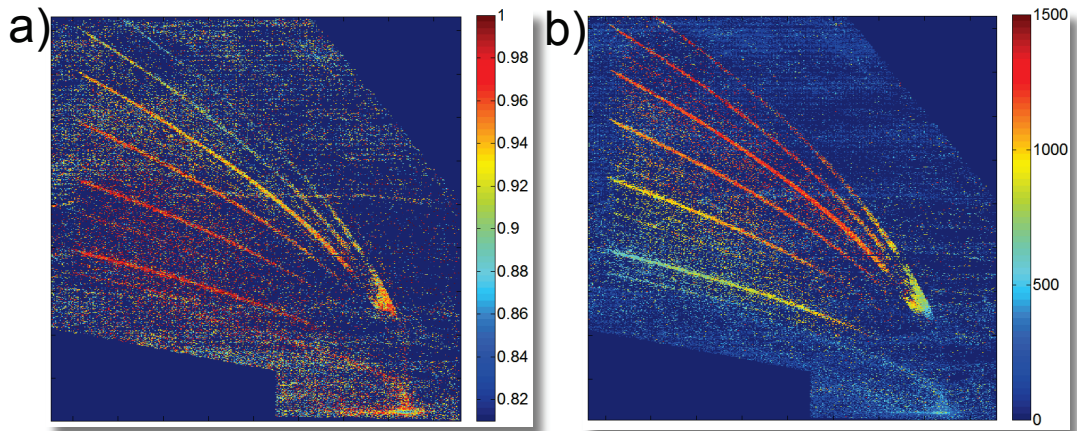


Figure 3.13: Image of an scanned CR39, showing parabolic particle tracks obtained from a Thomson parabola (see Sect. 3.4.2 for details), where in a) eccentricity is color coded in the z-axis and in b) the enclosed area of the pits (in arbitrary units).

$1.3 \text{ g/cm}^3$ . The plate dimensions used in the experiments are 100 mm by 50 mm by 1 mm. CR39 is not sensitive to electrons and photons, it is however an excellent detector material for protons and higher Z ions. On impact, the particle creates damage tracks in the polymer structure along its flight path; the track diameter directly depends on the energy loss of the particle and hence grows larger towards the Bragg peak and vanishes afterwards. In order to make these tracks visible the CR39 is etched in a solution of sodium hydroxide at  $80 \text{ C}^\circ$ ; the track diameter grows linearly with the etching time. Once the track diameter has passed the threshold for “visible” detection, a microscope can be used to count the particle tracks.

The scanning microscope is controlled by the pattern recognition software *SAMAICA*; this software recognizes the track entrances, the so-called pits, on the CR39 surface, by identifying a number of different parameters, such as the pit diameter, its eccentricity, its enclosed area and its relative position on the CR39 with respect to the scanning area. These parameters strongly depend on the deposited energy per unit length and thus the particle species and can later be used to distinguish pits of different species and for background elimination. For example, the eccentricity of pits created by “real” particles is typically close to 1 for normal incidence, while pits of other origin have a much lower ellipticity value.

In the framework of this thesis, a graphical user interface (GUI) has been written

### 3. METHODS: LASER, TARGETS AND DIAGNOSTICS

---

in MatLab that allows to clean the scanned images from background and also to isolate single particle species for accurate analysis. Fig 3.13 shows the image of an scanned CR39, with parabolic particle tracks obtained from a common Thomson parabola (see Sect. 3.4.2 for details). In frame a) the eccentricity is color coded in the z-axis and in frame b) the enclosed area ( $x$  and  $y$  are spatial dimensions of the scan area); both parameters change for the different parabola traces, which correspond to different charge to mass ratios of the particles and are clearly distinguishable from the background. The parameters change also along the single parabolic traces, which corresponds to a change in incident particle energy. The CR39 nuclear track detector has been used in most of the experiments described in this thesis.

#### Image plate

Image plates (IP) are commonly used in medicine (dental X-rays), material research and in biology and have almost completely replaced photographic X-ray films. The active layer of an typical IP consists of crystals of barium fluorohalide phosphor ( $\text{BaFBr:Eu}^{2+}$ ) and is supported by a magnetic support layer. This active layer has a linear response to X-rays over a large wavelength range starting at a few nm [146], but is also sensitive to electrons and ions. When such a particle or photon hits the active layer of the IP, electron hole pairs are created and trapped in lattice defects. In order to retrieve the data from the IP, it is processed by a special IP scanner (a FLA-7000 has been used in the framework of this thesis). The scanner illuminates the IP with laser light of wavelength  $\lambda = 632.8$  nm, which causes recombination of the trapped electron hole pairs under emission of a photon. This process is called photo stimulated luminescence (PSL) and is detected by the scanner to generate an the digital image of the irradiated IP within only a few minutes. The IP can also be erased with bright white light and be reused many times.

The data is stored in a logarithmic gray scale, usually at a spatial resolution of  $25 \mu\text{m}$ . The data can be transformed into the linear PSL scale via

$$PSL = \left( \frac{\text{psize}}{100} \right)^2 \frac{4000}{S} 10^{L(x/G-0.5)} \quad (3.9)$$

with  $\text{psize}$  the pixel size, i.e., the resolution of the scanner,  $L$  the latitude (typically 5),  $S$  the sensitivity of the scanner (with values from  $10^3$  to  $10^4$ ),  $x$  the

logarithmic gray scale value of the scanned pixel and  $G$  the gradation or the dynamic range of  $2^{16}$ . It should be noted here that the trapped electrons decay naturally[147], for which it is necessary to scan the IP at a fixed time after their exposure to obtain meaningful and comparable data.

A general problem of IP is to obtain an absolute calibration of PSL to particle or photon number, which is in addition complicated by the huge number of different IP and IP scanners. In Ref. [148] and Ref. [149] calibrations for IP and protons are published each for a specific type of IP and scanner (both different from the ones used for this thesis). The calibrations differ by about one order of magnitude with 0.01 and 0.08 PSL/proton in the more or less constant tail of the calibrations far behind the Bragg-peak.

One can speculate that the calibrations for other IP and scanner combinations should be somewhere in this region (they are after all a standard tool for many physicians). They should, however, only be used (if at all) as a rough guide for the data shown here, especially since the IP used in the framework of this thesis are BAS-TR2020, which have no protective layer on top of the active layer (of  $\sim 50 \mu\text{m}$  thickness, making them much more sensitive) as compared to the calibrations presented in the afore mentioned references.

#### 3.4.2 The Thomson parabola<sup>1</sup>

One of the two particle spectrometer types used for the experiments at the Trident laser is the Thomson parabola (TP). The first appearance of the TP dates back to 1911[151]. Today, it is probably the most commonly used diagnostic for detection of laser-accelerated ions. Its advantage is its inherent simplicity in both engineering and physics. However, designing a TP with sufficient energy resolution and charge separation at extreme ion energies requires considerable effort. In a small scale TP, premature merging of different ion species will occur at very low energies and eventually render the diagnostic and the acquired data useless. In the framework of this thesis, a TP has been designed and build that has superior energy resolution and charge separation at ion energies exceeding 100 MeV/amu (see Fig. 3.15 and Tab. 3.1 for details).

A TP spectrometer is based on an parallel electric and magnetic field; both

---

<sup>1</sup>This section is in part a summary of Jung, *et al.* [150], which has been written by the author of this thesis.

### 3. METHODS: LASER, TARGETS AND DIAGNOSTICS

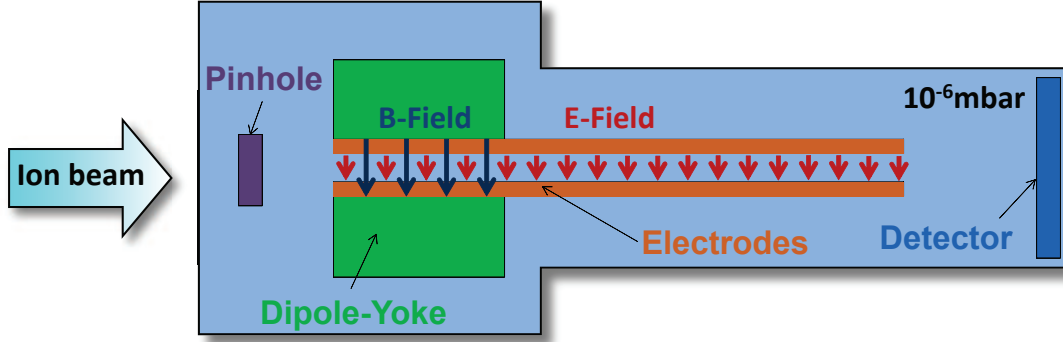


Figure 3.14: Sketch of a standard Thomson parabola, where the parallel magnetic and electric fields are perpendicular to the ion propagation direction. Ions are detected at the detector plane on parabolically shaped lines. (Figure and caption adapted from Jung, *et al.* [150])

fields are orientated parallel to each other and perpendicular to the ion flight path (see Fig. 3.14). The magnetic field is generated by a yoked pair of permanent magnets on the order of a few hundred mT (a setup with electro magnets is also possible [152]); the electric field is generated by two opposing electrodes - in this case two plane copper plates - with a potential of a few ten kV. In between the plates/magnets the fields are nearly parallel; at the edges, the fields are inhomogeneous. However, the fields decrease rapidly outside the yoke/electrodes and one can usually neglect the influence of these fringe fields.

The equations of motion for a charged particle passing the spectrometer, i.e. the electric and magnetic fields, can be calculated through Lorentz equation (see Eq. 3.8), which allows reconstruction of the particle charge, species and kinetic energy. *Taking into account the ion's flight (drift) after exiting the fields one can calculate the ion traces on the detector plane perpendicular to the ion's propagation direction as a function of their initial kinetic energy and their charge to mass ratio [150].* In the non-relativistic case one obtains for the x- and y-deflection of the particle after a first order Taylor expansion

$$x(E_k) = \frac{qEl_E(D_E + 0.5l_E)}{2E_k} \quad (3.10)$$

and

$$y(E_k) = \frac{qBl_B(D_B + 0.5l_B)}{\sqrt{2mE_k}}, \quad (3.11)$$

which yield the well-known parabola equation

$$y^2 = \frac{qB^2l_B^2 (D_B + 0.5l_B)^2}{mEl_E (D_E + 0.5l_E)} x, \quad (3.12)$$

where  $x$  and  $y$  describe the ion deflection in the plane perpendicular to the ion propagation direction resulting from an  $E$ - and  $B$ -field of length  $l_E$  and  $l_B$  and after a drift length  $D_B$  and  $D_E$  measured from the end of the magnetic and electric field, respectively [150]. See Fig 3.13 and Fig. 3.20 for examples of the parabolic traces that are measured on the detector.

This equation can in general be used for ions with a kinetic energy of less than 10% of their rest mass, before relativistic effects exceed the resolution of the spectrometer. It is worth noting that the maximum proton energies of 120 MeV measured here are approximately 13% of its rest mass in kinetic energy. For the analysis done in the framework of this thesis a comprehensive GUI has been written in MatLab, where tracing calculations can be done with either the relativistic Lorentz equation solved by a standard 4th order Runge-Kutta algorithm [153] or the analytical solution in Eq. 3.12 for non-relativistic particles; all calculations assume constant  $E$  and  $B$  fields with no fringe fields.

### TP energy resolution

*The main factors contributing to the intrinsic resolution of a TP for a specific charge to mass ratio are the drift length and the pinhole size used to limit and collimate the incoming ion beam and the properties of the magnetic field, i. e., its strength and length along the ion propagation direction. While a longer and stronger magnetic field increases energy resolution by higher dispersion, a larger pinhole decreases resolution due to an increased ion beam spot size on the detector. Although decreasing the pinhole diameter and increasing the drift will improve contrast of a TP, both methods will decrease the ion flux on the detector. Hence, an increase in magnetic field parameters is favorable. The intrinsic instrument resolution  $\Delta E_{kin}/E_{kin}$  can be approximated in the non-relativistic case via the parabola equation (Eq. 3.12) by calculating the energy range covered by the beam spot on the detector divided by its center energy*

### 3. METHODS: LASER, TARGETS AND DIAGNOSTICS

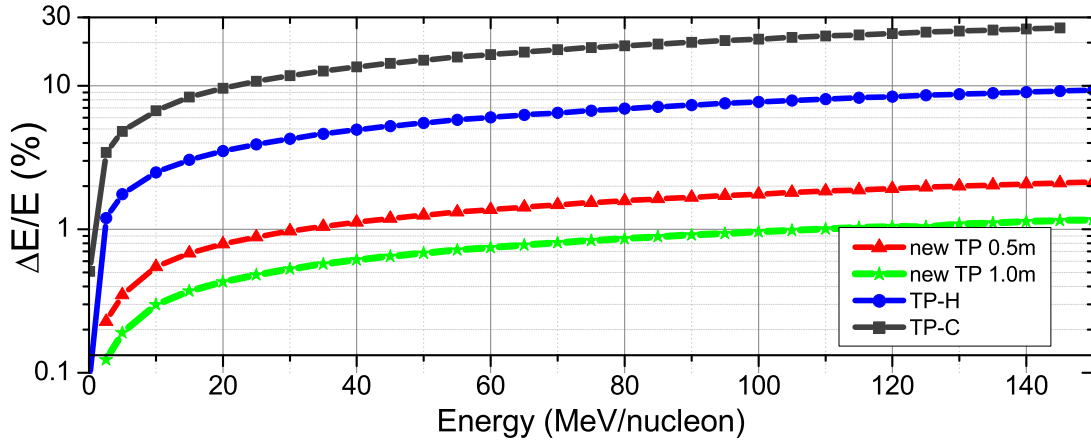


Figure 3.15: Comparison of Thomson parabola resolution for carbon  $C^{6+}$  ions: new high resolution TP (red diamonds, [green squares]) with 0.91 T over 20 cm and 50 cm [100 cm] drift, TP-H used in Ref.[31] (blue circles) with 0.57 T over 10 cm and 47.8 cm drift, TP-C described in Ref.[154] (orange triangles) with 0.6 T over 5 cm and 19.5 cm drift. All calculations are done with a  $200 \mu\text{m}$  pinhole 1 m behind the ion source. (Figure and caption adapted from Jung, *et al.* [150])

$$\frac{\Delta E_{\text{kin}}}{E_{\text{kin}}} = \frac{2s}{y \left( 1 - \left( \frac{s}{2y} \right)^2 \right)^2} \approx \frac{2s}{y}, \quad (3.13)$$

where  $y$  is  $(qBl_B(D_B + 0.5l_B))/(2mE_{\text{kin}})^{0.5}$  and  $s$  the ion beam spot size on the detector given by the pinhole size and the distances between the ion source, the pinhole and the detector plane [150].

In particular, the pinhole of the spectrometer introduces a pinhole-camera-like magnification of the particle source on the detector. The magnification and the resulting spot size  $s$  are given by the ratio of  $a$  to  $b$ , which are the distance pinhole-to-detector ( $a$ ) and pinhole-to-source ( $b$ ) and the pinhole diameter  $d$  and the source size  $x$  by

$$s = d + b/a(d + x). \quad (3.14)$$

In most TP, where  $d \gg x$ , the equation reduces to  $s \approx d(1 + b/a)$ , with  $b/a$  the magnification.

#### TP charge to mass separation

On the other side, separation of different charge to mass ratios depends on the electric field parameters and the drift together with the beam spot size on the

### 3.4. PARTICLE DETECTORS

	TP-C	TP-H	new TP-0.5	new TP-1
C <sup>5+</sup> into C <sup>6+</sup>	~3.3	13	25	59
C <sup>6+</sup> into C <sup>5+</sup>	~4.8	19	36	84
C <sup>6+</sup> into H <sup>+</sup>	~11.6	44	78	165
H <sup>+</sup> into C <sup>6+</sup>	~46	164	282	553

Table 3.1: Comparison of calculated merging energies of C<sup>6+</sup> into C<sup>5+</sup> and C<sup>6+</sup> into H<sup>+</sup> and vice versa in MeV/nucleon using a 200  $\mu\text{m}$  pinhole placed 1 m behind the ion source; values are shown for the new TP (TP-0.5 with 0.5 m and TP-1 with 1 m drift, two pairs of electrodes (40kV/2cm) and TP-H[31] and TP-C[154] (see text for details). (Table and caption adapted from Jung, *et al.* [150])

detector. The “merging” energy of two neighboring traces is calculated by the intersection point of the upper and lower boundary of the respective parabola traces, where the boundaries are given by the beam spot size on the detector. From the classic parabola equation (Eq. 3.12), i.e. in the non-relativistic limit, one can approximate the merging energy  $E_m$  for a pair of two different ion species as

$$E_m = \frac{q_i E l_E (D_E + 0.5l_E)}{sR_Q}, \quad (3.15)$$

where  $R_Q = (Q_1 + Q_2)/(Q_1 - Q_2)$  with  $Q_1 = q_1/m_1 > Q_2$  and  $E_m$  denotes the merging energy of the ion species having the charge  $q_i$  [150].

#### The new high resolution and charge separation TP

The new TP with exceptional high energy resolution and charge to mass separation that has been designed and build in the framework of this thesis, uses optimized electric and magnetic fields and offers a long drift area, as derived in Eq. 3.13 and Eq. 3.15. The body of the TP consists of two high vacuum areas, which are separated by a vacuum valve (see Fig. 3.16); a pressure of  $\sim 10^{-7}$  mbar can be set up within less than 5 minutes of pumping by the cryo pumps attached to each of the two spectrometer vacuum parts. The first vacuum part of the spectrometer is the core of the TP with two 20 cm long yoked NdFeB permanent magnets separated by 4 cm. The magnetic field between the magnets reaches 0.91 T, expanding very uniformly over the whole length. A pair of copper electrodes, separated by 2 cm (parallel), placed within the yoke can generate extremely high potentials of up 40 kV ( $\pm 20$  kV each side). The high vacuum reduces the possi-

### 3. METHODS: LASER, TARGETS AND DIAGNOSTICS

---

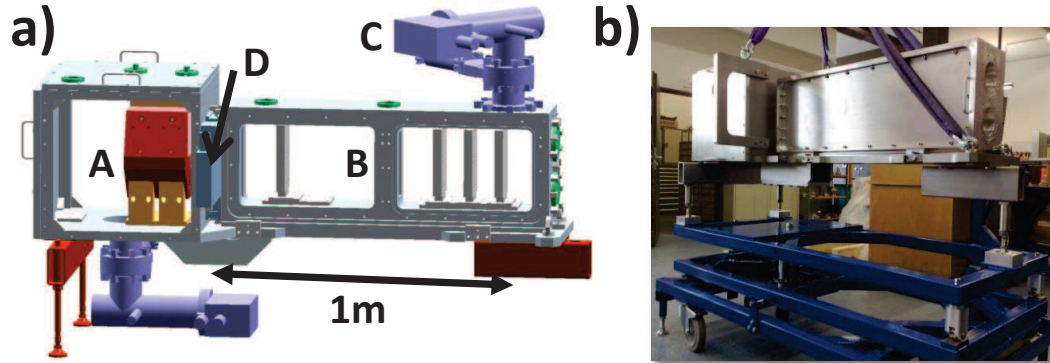


Figure 3.16: a) Schematics of the new Thomson parabola with *A* the core part containing the magnets and electrodes and *B* the drift and detector part and space for an additional pair of electrodes. Both parts are separated by a vacuum valve *D* and pumped by their own cryo pump *C*; b) photograph of the new TP, including its 6axis support. (Figure and caption adapted from Jung, *et al.* [150])

bility of vacuum breakdown (sparking) between the electrodes [155]. The second part of the TP serves as drift region and detector area and can host a second pair of electrodes of 30 cm length to further increase charge to mass separation of the the spectrometer.

A detector (for instance IP or CR39) can be placed at different positions, resulting in an effective drift length of 0.3 m up to 1 m. The spectrometer design allows use of a wide range of detectors; fused silica windows enable online readout with a scintillator [156] or a MCP as reported in Ref. [152]. In the experiments described in the next chapter, a stacked detector consisting of CR39 and IP has been used mainly. With the 6-axis micro scale support carrying the entire spectrometer (see Fig 3.16 b)) alignment of this 750 kg heavy diagnostic can be done easily.

#### Data analysis

In order to retrieve the energy spectra of the particles, the parabolic traces measured on the CR39 and IP are read in with a constant spatial binning. The center of each bin gives the energy and the number of particles within this bin gives the flux; the energy and charge to mass ratio is reconstructed by the bins distance to the zeroth order on the detector. The zeroth order is a spot on the detector that is generated by uncharged particles (recombined laser-accelerated ions) or X-rays.

The acceptance angle or solid angle of the spectrometer can be calculated from the pinhole diameter  $d$  and the distances  $a$  and  $b$  and is used to normalize the final energy spectra. The acceptance angle for most of the TP is on the order of  $10^{-4}$  to  $10^{-5}$  msr, i.e., the TP records only a small fraction of the laser-accelerated particle beam, but with high energy resolution and charge separation.

In Fig. 3.15 the energy resolution for carbon  $C^{6+}$  is plotted for this TP using a drift length of 0.5 and 1 m and a pinhole of  $200\mu\text{m}$  diameter. The resolution is furthermore compared to its predecessor, which has also been used in many of the experiments conducted at Trident. The old TP (hereafter referenced as "TP-H") is equipped with an magnetic field of 0.57 T over a length of 100 mm and a drift of 478 mm. In order to emphasize the unprecedented properties of the new TP, both TP are also compared to a TP described in Ref.[154] (hereafter referenced as "TP-C") that works with a magnetic field of 0.6 T over 50 mm and a drift of 195 mm. *Aiming for an energy resolution of better than 10% the TP-C only gives a feasible resolution at very low energies below 10 MeV/nucleon and the TP-H has reached its useability at 100 MeV/nucleon, while the new TP still gives a superior resolution below 5% at these energies [150].*

In Table 3.1 the merging energies of all three TP are compared. Values are given for the new TP using a drift of 0.5 and 1 m, a  $200\mu\text{m}$  pinhole and both pairs of electrodes at 40 kV each. The TP-C has a 6 kV potential along the 20 cm long electrodes in a wedged configuration; TP-H has one pair of parallel electrodes with 15 kV/2cm over 40 cm. Here, the newly developed TP is the only one, where the merging energies are far above 50 MeV/nucleon. For the other two, the too low dispersion of the different species could result un-evaluable data, meaning that the distinction of different ion species and hence determination of their high energy cut-off is rendered impossible.

An example of this problem is shown in Fig. 3.17, where two ion spectra are shown that have been measured with the new TP; one using too low and one using sufficient charge separation by changing drift length and the potential between the electrodes. Both spectra have the same high energy cut-off for  $C^{5+}$  and  $C^{6+}$ , which are 80 MeV and 280 MeV, respectively. The spectrum in Fig. 3.17 a) was measured with a potential of 25 kV/2cm over 20 cm and a drift 0.5 m drift and shows excellent charge to mass separation (see Fig. 3.17c)). The spectrum in Fig. 3.17 b) was measured with only 15 kV/2cm and a drift of 30 cm and shows severe merging of different particle traces (see Fig. 3.17d)). Following the latter

### 3. METHODS: LASER, TARGETS AND DIAGNOSTICS

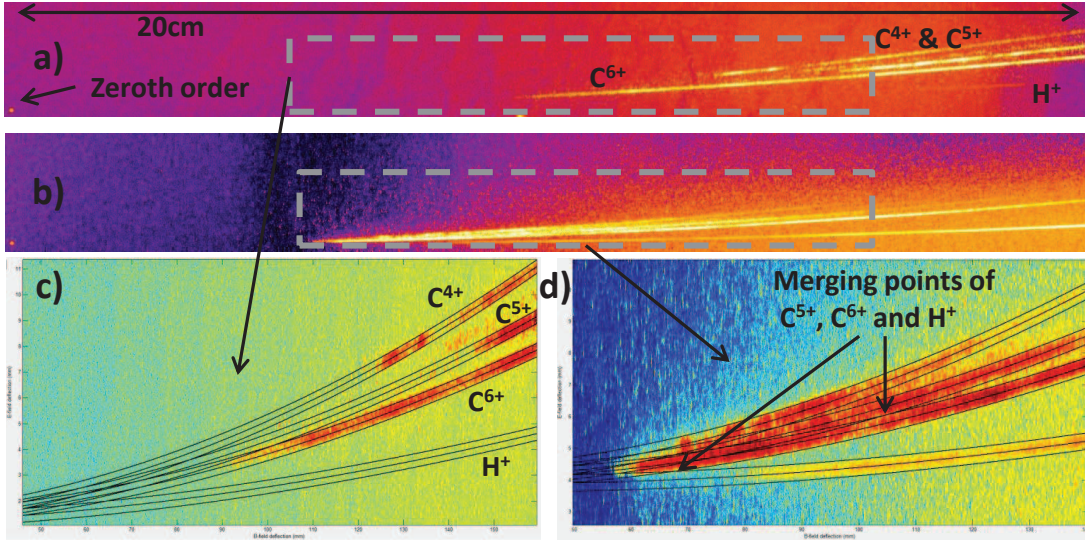


Figure 3.17: Comparison of ion spectra with identical high energy cut-off for  $C^{6+}$  (280MeV) and  $C^{5+}$  (120MeV) obtained using the novel high resolution and high separation TP with different drift and electric field to demonstrate influence on merging of traces: a) spectrum obtained using appropriate parameters (25 kV/2cm over 20 cm and 50 cm drift) to resolve different traces as shown in c); b) spectrum obtained with too low dispersion (15 kV/2 cm over 20 cm and 30 cm drift) resulting in premature merging of traces as shown in d); low to high energy from right to left side of each image, black lines in c) and d) are predicted traces with upper and lower boundaries. (Figure and caption adapted from Jung, *et al.* [150])

spectrum, Fig. 3.18 shows the analyzed carbon  $C^{6+}$  spectrum, where severe corruption of the energy spectrum is visible due to the merging of  $C^{5+}$  into  $C^{6+}$  at an energy  $E_{C^{5+}} \approx 50$  MeV and  $E_{C^{6+}} \approx 80$  MeV.

#### 3.4.3 The high resolution ion wide angle spectrometer<sup>2</sup>

The TP, as described in the previous section, has excellent energy resolution and charge to mass separation, but lacks acceptance angle. The analyzed fraction of the whole particle beam is too small to estimate for instance the conversion efficiency of laser light into particles. The ion beams accelerated at Trident typically cover a solid angle of  $> 500$  msr, while the TP “sees” only  $10^{-4}$  to  $10^{-5}$  msr. Other methods, such as stacks of RCF that are frequently used to measure angularly

<sup>2</sup>This section is in part a summary of Jung, *et al.* [157], which has been written by the author of this thesis.

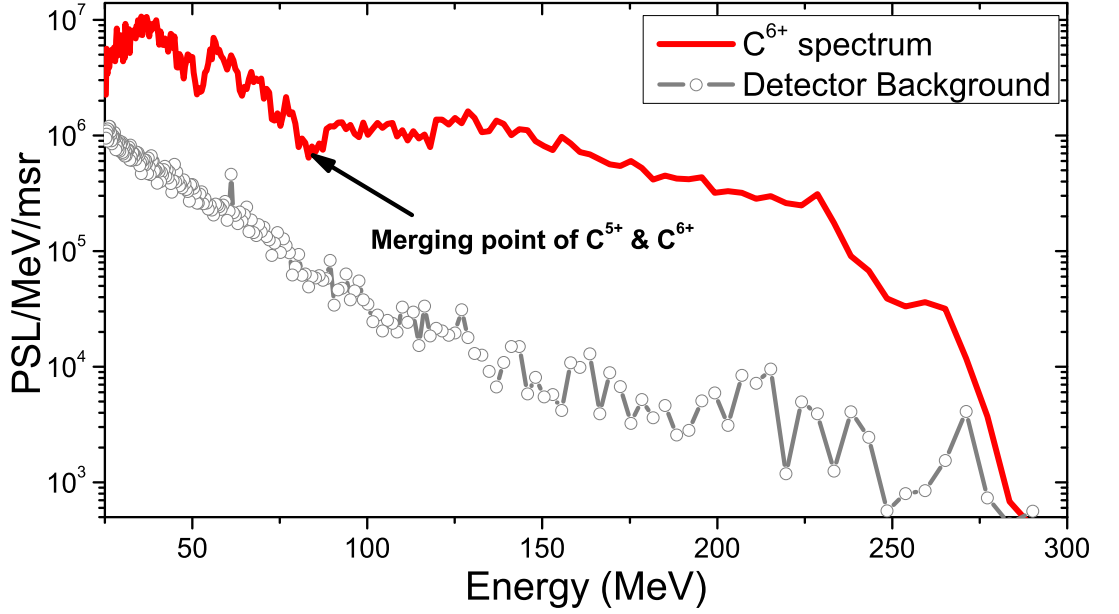


Figure 3.18: Carbon  $C^{6+}$  spectrum (red solid line) extracted from Fig. 3.17b including detector background (gray with circles) showing corruption of the spectrum after the merging of  $C^{5+}$  into  $C^{6+}$  at 80 MeV. (Figure and caption adapted from Jung, *et al.* [150])

resolved energy spectra of laser-accelerated protons cannot be applied here as the ion beam consists of different species. Heavier ions, such as  $C^{6+}$  ions, are stopped within the first few layers of the stack by virtue of their larger cross section; they will not only be indistinguishable from the protons in any of the layers, but also suffer from extremely poor energy resolution.

In the framework of this thesis a novel ion **Wide Angle Spectrometer**, the iWASP, has been designed and build that enables simultaneous measurements of angularly resolved proton and carbon  $C^{6+}$  energy spectra (under certain conditions). This spectrometer covers a solid angle of  $\sim 10^{-1}$  msr, which is 4 to 5 orders of magnitude higher than the acceptance angle of the TP described earlier. With the iWASP, a rectangular section covering up to  $30^\circ$  of the particle beam can be measured with high angular and energy resolution ( $\Delta E/E \leq 10\%$  at 50 MeV/nucleon carbon  $C^{6+}$ ).

The concept of the iWASP is quite similar to the TP setup. A schematic depiction of the iWASP is shown in Fig. 3.19. Here, a magnetic field that is orientated perpendicular to the ion propagation direction, introduces an energy (and  $q/m$ ) dependent dispersion. Instead of a pinhole, the iWASP consists of a long slit that

### 3. METHODS: LASER, TARGETS AND DIAGNOSTICS

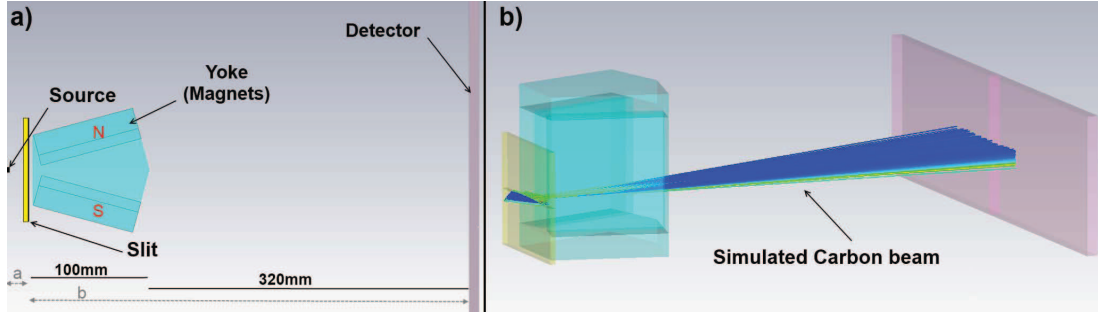


Figure 3.19: a) Top view of the ion wide angle spectrometer (iWASP), with from left to right, the source, the slit, the yoke and the detector. b) Side view showing a simulated trace of carbon  $C^{6+}$  ions calculated with CST[158]. (Figure and caption adapted from Jung, *et al.* [157])

is positioned in front of the magnetic field. *To maximize energy resolution and acceptance angle simultaneously, a strong magnetic field with a large gap between the magnets is required. To overcome these conflicting requirements, a wedged yoke design has been implemented, trading field homogeneity for field strength [157].* The wedge half-angle is  $15^\circ$  with the a gap of 10 mm at the front of the yoke and 62 mm at the far end. In order to use the whole magnetic field and to achieve an acceptance angle of  $30^\circ$ , the yoke has to be placed at a distance of  $\sim 20$  mm to the particle source. For larger distances, the separation of the magnets in the wedged yoke has to be increased, which will also result in a decreased average magnetic field and hence in reduced energy resolution.

The resulting particle traces on the detector can again be calculated with Lorentz equation, where, in contrast to the TP, the iWASP has a zero electric field (see Eq. 3.8).

#### iWASP angular and energy resolution

As with the TP, *the energy resolution for a specific charge to mass ratio depends on the drift length, the magnetic field and the source magnification. An approximate formula for the energy resolution  $\Delta E_{kin}/E_{kin}$  of the iWASP can be obtained by solving the reduced Lorentz equation in the non-relativistic case and calculating the resulting source magnification  $s$  on the detector plane (see Eq. 3.13 and Eq. 3.14) . To maintain a sufficiently high energy resolution for the setup presented here, the width of the slit must not be bigger than a few tens of micrometers.*

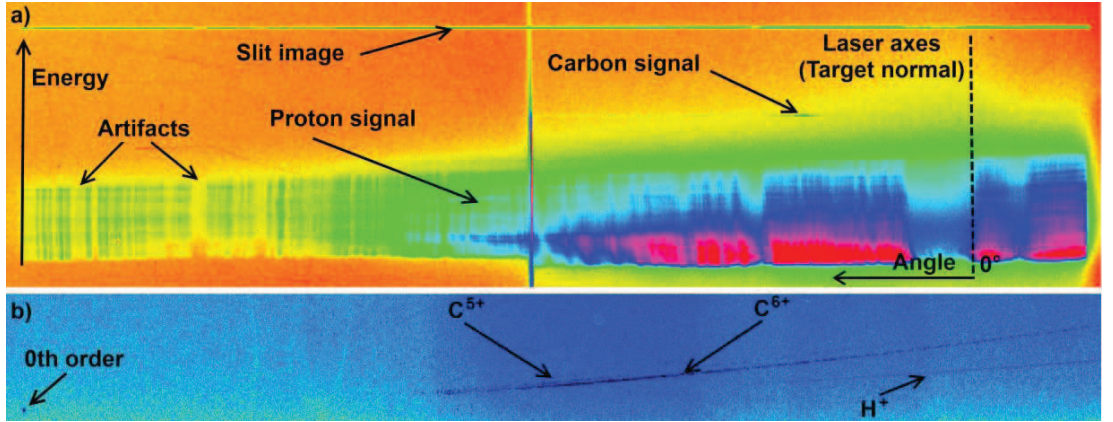


Figure 3.20: a) iWASP data recorded on the IP from a  $1\mu\text{m}$  target (normal incidence) showing the image of the slit on the top, a faint line of carbon ions above the break-through energy (see text) and the proton signal starting at the bottom of the IP at their low energy cutoff of about 11 MeV; color shows particle density in arbitrary units. Note, that vertical features in the data are a result of non-uniformities in the  $20\mu\text{m}$  slit aperture. The thick vertical line in the middle is a result of two pieces of CR39 intersecting in front of the IP; slightly different thicknesses in the CR39 also result in an asymmetry of the low-energy cutoff line visible here. b) Data recorded on a Thomson Parabola from a  $1\mu\text{m}$  solid diamond target showing a proton and a dominant carbon  $\text{C}^{6+}$  signal among a very faint carbon  $\text{C}^{5+}$  line. (Figure and caption adapted from Jung, *et al.* [157])

The angular accuracy of the spectrometer can be derived from a careful trigonometric consideration, assuming an angularly incoherent particle emission. The lower limit of the angular error  $\Delta\alpha$ , *i.e.*, the positive and negative deviation of a given angle  $\alpha$  is

$$\Delta\alpha = \tan^{-1} \left( \tan(\alpha) \pm \frac{x_{s,d}}{2(a+b)} \right), \quad (3.16)$$

where  $x_{s,d}$  is the greater of either the source size or the detector pixel size. It should be noted, that for some detectors, such as the IP, the angular error might be increased by ions passing through two or more pixels of the detector due to their oblique incidence. This effect can be reduced by a curved detector plane. While this gives the angular error for a single ion, the binning of the data (to extract a complete energy spectrum) will dominate the final angular uncertainty (set  $x_{s,d}$  as the binning size), resulting in uncertainties below  $100\mu\text{mrad}$  for the parameters presented here. [157]

In the experiments conducted for this thesis, a slit made of 6 mm thick solid

### 3. METHODS: LASER, TARGETS AND DIAGNOSTICS

---

tungsten with a slit width of approximately  $14\ \mu\text{m}$  has been placed directly in front of the yoke. The slit's distance to the target was  $\sim 20\ \text{mm}$  resulting in an acceptance angle of about  $25^\circ$ . *A drift of 320 mm to the detector measured from the end of the yoke yields an angular uncertainty of  $\ll 100\ \mu\text{rad}$  (along iWASP center) and a resolution of 5% for protons and 8% for carbon  $\text{C}^{6+}$  at energies of 50 MeV and 40 MeV/nucleon, respectively; the source image size  $s = (300 \pm 50)\ \mu\text{m}$  has been extracted from the IP data and the average magnetic field has been measured to be about 440 mT (see Fig. 3.20 and Eq. 3.13). The solid angle captured by the iWASP is  $\sim 0.25\ \text{msr}$  [157].*

#### Charge separation in the iWASP

*Although the iWASP lacks the charge to mass separation of a TP, it is still suitable for many laser ion acceleration experiments, where two (or more) species with significantly different mass are accelerated; e.g. from proton-carbon targets (or similar proton-ion targets) such as diamond, diamond-like carbon (DLC) or  $\text{CH}_x$  foils [157].* Here, one can use a stacked detector to distinguish between the different species by their different stopping powers provide that all species are fully ionized. In the experiments conducted at Trident, a high-intensity laser pulse is incident on a nm-scale diamond target. When the target turns relativistic transparent, the high electric field of the laser acts on all target atoms; hence, it can be expected that the target is fully ionized in the area of the focal spot (where the ion acceleration takes place); this has been verified with TP measurements over many target shots at Trident. In Fig. 3.20 b) a typical TP spectrum obtained at Trident from a DLC target is shown, where the dominant charge state of carbon is 6.

The detector stacks used during the experiments on Trident consist of a CR39 plate and a IP. The carbon signal is recorded on the CR39; the IP that is placed behind the CR39, detects the protons; the whole stack is covered in a layer of Al of  $\sim 26\ \mu\text{m}$  thickness to protect the IP from direct and scattered laser light. With a CR39 thickness of 1 mm, carbon ions with  $\geq 230\ \text{MeV}$  (break-through energy) can pass the CR39 and additionally be detected on the IP; however, these high energy carbon ions will still leave measurable tracks on the CR39. At the same time protons of  $\geq 11\ \text{MeV}$  can pass the CR39 and be detected on the IP. They will also create tracks in the CR39, which can easily be suppressed with a short etching time; with the correct etching time only pits of heavier ions - the carbon

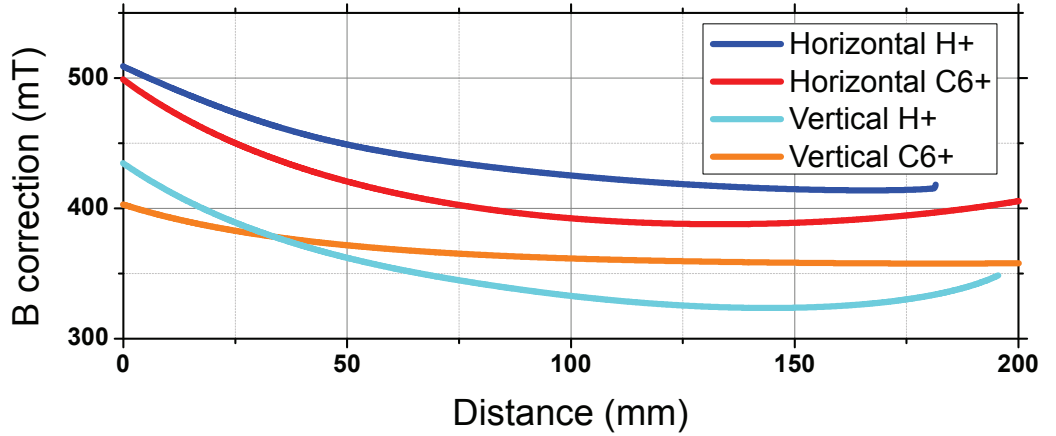


Figure 3.21: Calibration curves for the iWASP for different iWASP setups; the calibration lines have been obtained from the low energy cutoff lines of either the protons or the carbon  $C^{6+}$  ions (see Fig. 3.20).

ions - will become visible, while the size of pits created by protons stays below the detection limit [159] of the scanning microscope. It should be noted that the low energy deposition of high energy protons might not be enough to create tracks at all, relaxing the above issue. Provided protons with the highest energy are deflected less than the most energetic carbon ions, both distributions can be measured simultaneously without overlap. A typical spectrum measured on the IP with the iWASP is shown in Fig. 3.20 a). Here, the image of the slit aperture can be seen on the top, followed by a faint signal of carbon ions with energies above 200 MeV, i.e., beyond their break-through energy for the CR39; below follows the proton signal starting at the bottom of the IP at about 11 MeV. Energy increases from the bottom of the figure towards the slit. In an advanced setup of the iWASP, charge to mass separation capability could be added for selected angles; vertical slits in the detector can be used to transport the ion beam behind the detector through pairs of electrodes to introduce charge to mass separation within the electric fields [157].

### Data analysis

The analysis of the data measured by the iWASP closely follows the analysis of the TP data. The raw data is binned in constant spatial steps along the energy axis and also binned along the angular dimension. Energy spectra are extracted for each of the angular increments, which results in a set of single energy spec-

### 3. METHODS: LASER, TARGETS AND DIAGNOSTICS

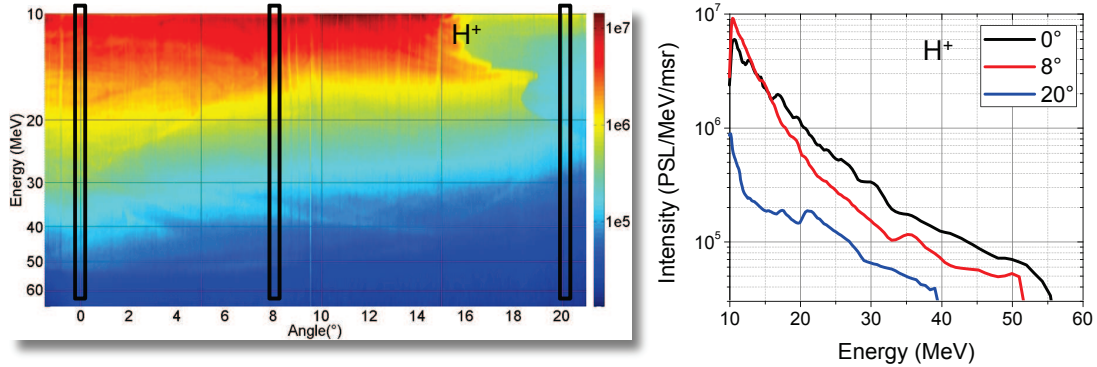


Figure 3.22: a) Angularly resolved proton spectrum measured with the iWASP. The 3 black rectangles represent typical angles of TP measurements. b) averaged spectra obtained from these 3 rectangles as they would have been seen by TP-spectrometers at these angles, showing significant differences in the spectral shape and cutoff energy.

tra similar to the TP traces. A modified version of the TP software afterwards joins the single traces into an angularly resolved energy spectrum. It should be noted that each single spectrum has to be calculated with a slightly different travel time/length in the magnet and a slightly different drift to the detector, depending on the specific angle of the trace and the current setup of the iWASP. In addition, for each angle, the magnetic field itself is slightly different due to the wedged design of the yoke that results in a rather non-uniform magnetic field distribution. However, instead of calculating the parameter change for each angular increment, one can use the low-energy cutoff lines on the detector to extract a single angular dependent correction factor  $k_B(\theta)$  for the B-field. Following Eq. 3.11 the correction is done by

$$y(E_k) = k_B(\theta) \frac{qBl_B(D_B + 0.5l_B)}{\sqrt{2mE_k}} \quad (3.17)$$

Fig. 3.21 shows this correction factor for carbon ions and protons (which will pass the magnetic field at different heights) for two different iWASP setups, one, where the spectrometer is positioned vertical and one, where it is positioned perpendicular to the laser polarization axis. This, however, is still only a rather coarse correction, as  $k_B$  also indirectly depends on  $q/m$  and the particle energy  $E_k$ , which will change the path the particle takes through the in-homogeneous magnetic field of the yoke. In future, a more accurate correction will be done by

mapping the full 3D magnetic field of the yoke.

#### **Prospects of the iWASP**

As a final remark on the advantages of the iWASP, Fig. 3.22 (left frame) shows a typical proton spectrum measured with this spectrometer; the three black rectangles mark positions, where in earlier experiments ion spectra have been detected with TPs. In the right frame the corresponding energy spectra are plotted, as they would have been measured by these TP. While this demonstrates that the iWASP can be treated as a continuous set of TP traces along the measured angle, it also shows the great advantage of this spectrometer. Each spectrum at the three different angles shows a different high-energy cutoff and a different spectral shape. Estimates of the conversion efficiency deduced from these spectra, as it is often done, are a crude approximation at best, especially with a strongly non-uniform ion beam.

Although the iWASP cannot measure a full beam profile, it can still significantly improve conversion efficiency estimates. For most laser-accelerated ion beams, one can expect a non-uniform, yet radial symmetric beam due to the radial laser focus symmetry. This has been shown for the Trident laser - despite its linear polarization - for many shots (with exception of the high-energy tail, see Chap. 4.4).

# Chapter 4

## Ion acceleration during relativistic transparency

Laser-driven ion acceleration has been investigated experimentally for over a decade now, yet generated ion beams are still far from being suitable for many applications. This is partially due to the too low ion energies and the typically exponentially decaying energy spectra and partially due to the too low conversion efficiencies of laser energy into ion energy. That is, proton energies of  $\sim 60$  MeV [6, 15] were measured ten years ago, but have not been increased since then; for ions with  $Z > 1$  the situation is even worse, they have only been accelerated to a few MeV in the TNSA regime (see Chap 2.3.1). However, advanced applications, such as hadron cancer therapy [22] or ion fast ignition [24, 25, 47], have a demand for much higher ion energies. For instance, carbon-ion fast ignition requires a mono-energetic beam of  $C^{6+}$  ions with  $E_k \approx 450$  MeV with a maximum bandwidth of 10%, and for the hadron cancer therapy protons of 250 MeV or  $C^{6+}$  ions of 4-5 GeV are necessary, ideally at a repetition rate of 10 Hz.

### Objectives and goals

The experimental results gathered in the framework of this thesis and presented in this chapter are devoted to the investigation of these problems, i.e., bringing laser-driven ion acceleration one step closer to a broad range of advanced applications. The Break-out afterburner mechanism has the potential to accelerate protons as well as ions with  $Z > 1$  to extreme energies far beyond energies achievable with TNSA. In particular, with BOA, ion acceleration occurs during

---

the relativistic transparency of the target induced by an ultra-high intensity laser. According to VPIC simulations and the analytical model (see Chap. 2.3.3), BOA acceleration shows a number of key signatures and differences to other acceleration mechanisms:

1. maximum ion energies are much higher compared to TNSA (see Sec. 4.2)
2. there is an optimum foil thickness for a given set of laser parameters as a result of relativistic transparency (see Sec. 4.2.1)
3. protons do not impede acceleration of heavier ions ( $Z > 1$ ) as in TNSA due to their low inertia and high charge to mass ratio (see Sec. 4.2.3)
4. an angular symmetry break of the particle beam for the fastest ions (from high resolution 3D VPIC simulation) as compared to TNSA, where the beam is Gaussian like with maximum energies and particle numbers on the laser axis (see Sec. 4.2.4)

Hence, the first major objective of this thesis is to experimentally demonstrate BOA and to measure these key signatures, i.e., show that the measured spectra of the laser-accelerated proton and ion beams are indeed a result of BOA and not (a variation of) TNSA or even RPA. It is worth noting that according to the VPIC simulations and the analytical model, BOA acceleration with Trident parameters requires nm-scaled targets; the optimum thickness is predicted to be between 100 nm to 200 nm, where temporal overlap of the laser pulse peak with the relativistic transparency of the target is predicted to be best. Hence, exploring the BOA regime experimentally has only become possible by the combination of two key technologies, the production of nm-scaled free-standing foil targets (see Chap. 3.2) and ultra-high contrast at relativistic laser intensities. The latter has been achieved by the OPAPE cleaning technique (see Chap. 3.1.5). The significantly improved on-target contrast of the Trident laser to about  $10^{-7}$  at -4 ps ensures that a nm-scaled target is not destroyed in the laser pedestal and the laser can interact with an initially highly overdense target.

The second major objective of this thesis is to improve the understanding of BOA, including aspects that are rather difficult to investigate with PIC simulations due to their high time consumption (for parametric scans) or the difficulty to correctly

## 4. ION ACCELERATION DURING RELATIVISTIC TRANSPARENCY

---

model pre-plasma and laser contrast or just particle diagnostics. Some of these aspects are:

1. the conversion efficiency of laser light into particles, which can in general be investigated with PIC simulations, but is rather complicated to measure precisely in an experiment due to spectrometer limitations (see Sec. 4.2.5)
2. the energy scaling with laser parameters, which has been derived in the model and investigated with VPIC with a coarse thickness scan, but has yet to be verified or falsified by experimental data (see Sec. 4.2.6)
3. the control over the spectral shape of the accelerated ions in order to make the particle beams useful for advanced applications such as the ion beam therapy of tumors or ion fast ignition (see Sec. 4.4)

The following sections will discuss all of these questions in detail. For this, a total of 6 campaigns ( $\hat{a}$  6 weeks) has been fielded at the Trident laser facility (see Chap. 3.1.3) over the course of 3 years. This means, a total of 506 laser-target shots has been fired with the Trident “single-shot” laser, which corresponds to 380 hours of continuous laser operation at an average of 45 min round time per laser shot.

As a result, a comprehensive, novel and unprecedented set of data has been collected investigating thickness and intensity scalings, angular beam dependency, conversion efficiency and the control of the energy spectra for both proton and carbon  $C^{6+}$  ions in the BOA ion acceleration regime.

The experimental research and investigations conducted in the framework of this thesis resulted in new record energies for laser-driven proton and carbon  $C^{6+}$  ions (with  $\sim 120$  MeV and  $\sim 1$  GeV, respectively, see Sec. 4.3) and led to the discovery of a new acceleration scheme, the BOA-soliton mechanism (see Sec. 4.4.1). In addition, the unprecedented data for the angular energy dependency of the carbon ions and protons significantly extended the understanding of the BOA mechanism by enabling accurate measurements of conversion efficiency and the investigation of more complex BOA key signatures, such as the generation of electron and ion lobes.

## 4.1 Experimental Setup

The general experimental setup has been quite similar throughout all 6 campaigns. The 8 inch (20 cm) laser beam that is exiting the compressor, is reflected from the final turning mirror and focused with an off-axis parabolic (OAP) mirror onto diamond (-like) targets. In most experiments an F/3 OAP has been used to focus the 500 – 700 fs and  $\sim 80$  J laser pulse; in some campaigns an F/8 OAP has also been used. The laser irradiates targets between 3 nm and 25  $\mu\text{m}$  with peak intensities of up to  $5 \times 10^{20}$  W/cm<sup>2</sup> - depending on the actual OAP, laser energy, pulse duration and target alignment - with normal incidence. (The laser focus and target alignment has been described in detail in Chap. 3.1.4 and Chap. 3.3.) A  $3\omega$ -backscatter diagnostic [160] is installed behind the compressor, where the backscattered  $3\omega$  light from the target (generated via CWE [122, 123] and/or ROM [51, 121]) is analyzed; its main purpose is, to identify whether the target was still intact during the main laser-plasma interaction or the target has already been destroyed by a decreased contrast or a pre-pulse in the laser beam (see Chap. 3.1.5).

Behind the target are the ion beam diagnostics positioned (and in some cases also in front of the target). There are two different diagnostic configurations, the TP-setup and the iWASP-setup. The first uses a number of TP spectrometers (up to 5 per shot) at different angles to measure (a rather small fraction of) the ion beam with high charge to mass separation; the latter uses only the iWASP to measure angularly resolved ion energy spectra at the expense of blocking almost all other diagnostic being positioned closely behind the target. In Chap. 3.4.2 the TP and the iWASP have been described in detail.

The advantage of the TP-setup is the possibility to add a number of secondary diagnostics, such as electron spectrometers, UV- and X-ray spectrometers and laser beam diagnostics. The electron spectrometer works in the same way as the iWASP, with the exception that electrons are deflected in the opposite direction of the positively charged ions; results from the electron spectrometer measurements are published in Ref. [101]. The laser beam diagnostics include (visible) optical spectrometers and a FROG (frequency-resolved optical gating) [161]. Their purpose is to measure the temporal shape of either the incident, the reflected or transmitted laser pulse [63] (data not shown).

Both setups are depicted in Fig. 4.1, where the left frame shows the TP-setup

## 4. ION ACCELERATION DURING RELATIVISTIC TRANSPARENCY

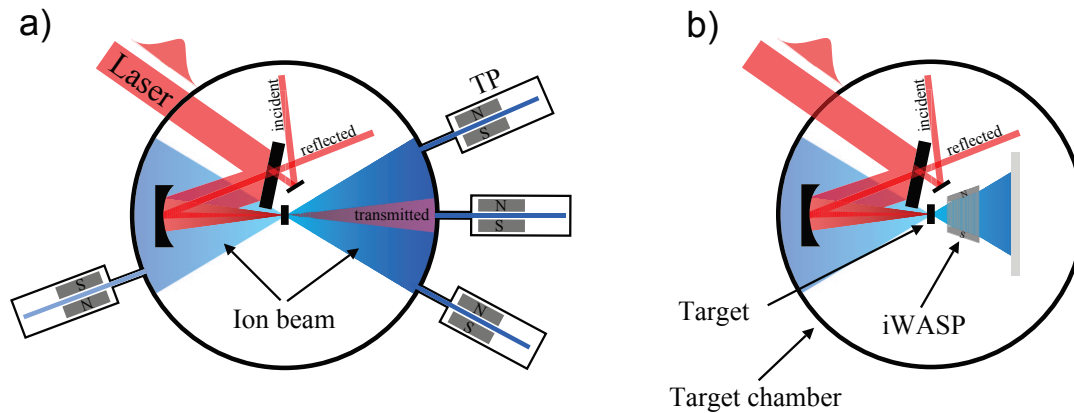


Figure 4.1: Experimental setup with a) the TP-setup, where a number of different TPs analyzes the particle beam at different positions around the target. A variety of secondary diagnostics can be employed, such as electron spectrometers and laser pulse diagnostics; b) the iWASP-setup, where the iWASP measures the ion spectra angularly resolved; due setup constraints, no other diagnostic can be used in this configuration. In both setups is the laser (CP and LP) focused by an F/3 (F/8) off-axis parabolic mirror on a nanometer-scaled diamond like target.

and the right frame the iWASP-setup. Independent of the used setup are protons always recorded on BAS-TR image plates (IP) and carbon ions typically with CR39 nuclear track detectors (see Chap. 3.4). The CR39 is a single hit detector and gives absolute numbers. Since there is no absolute calibration published for the combination of IPs and IP-scanner (FLA-7000) used here, particle numbers for protons are only relative and always given in arbitrary units.

### 4.2 Proton and carbon ion acceleration

In order to investigate, analyze and compare laser-driven ion acceleration it is necessary to find and measure meaningful parameters of the ion beams. The most used and best accessible parameter is the high energy cutoff or the maximum energy of the ion spectra. Full beam profile measurements and other parameters, such as the conversion efficiency are in general much more complicated to obtain. This is partially due to the harsh environment of the laser-matter interactions - EMP, (hard) X-rays, electrons, and a mixture of protons and ions make measurements challenging - and partially due to spectrometer constraints. The temperature of an ion spectrum, for instance, typically suffers from the limited

## 4.2. PROTON AND CARBON ION ACCELERATION

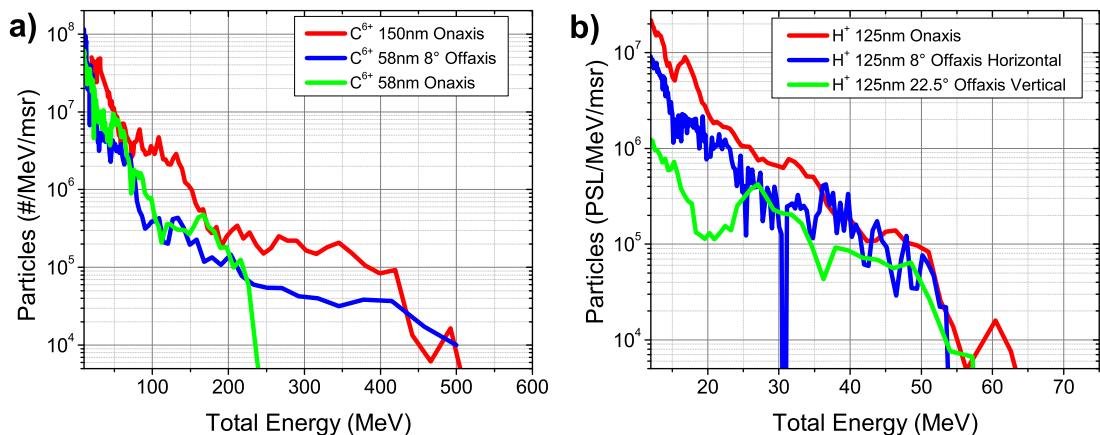


Figure 4.2: Particle spectra measured by TPs at different angles for shots that yielded peak energies a) for carbon  $C^{6+}$  ions and b) for protons.

bandwidth of a spectrometer; the low energy tail of the spectra, where in general most of the particles are, is often truncated due to the low energy cutoff of the spectrometer, which can be several MeV to tens of MeV depending on the setup.

The following discussion will start with the analysis of maximum ion energies measured in the framework of this thesis. A selection of typical ion energy spectra for carbon  $C^{6+}$  and protons is shown in Fig. 4.2; the maximum energy is usually visible as a sharp cutoff at the high energy tail (but can also be smeared out by high levels of background, depending on the used detector). For the  $C^{6+}$  ions the highest energy cutoffs are exceeding 500 MeV, which is more than an order of magnitude above (heavy) ion ( $Z > 1$ ) energies measured with TNSA. For protons, cutoff energies are well in excess of 50 MeV for diamond targets, which is comparable to results from TNSA. Energies exceeding 100 MeV can be achieved with  $CH_2$  targets as will be shown later in Sec. 4.3.

From the first campaign on, large fluctuations in the maximum ion energies have been observed; one objective of the following campaigns was to improve the repeatability and accuracy of the measured cutoff energies. This included upgrading the ion spectrometers (see Chap. 3.4.2), developing a novel ion wide angle spectrometer (iWASP) (see Chap. 3.4.3) and continuously improving positioning accuracy of the targets and the laser focus (see Chap. 3.1.4). In Fig. 4.3 high energy cutoff data from 5 of the 6 campaigns is shown for thicknesses from 3 nm up to 700 nm; the left frame shows the carbon  $C^{6+}$  energies and the right frame the corresponding proton energies.

## 4. ION ACCELERATION DURING RELATIVISTIC TRANSPARENCY

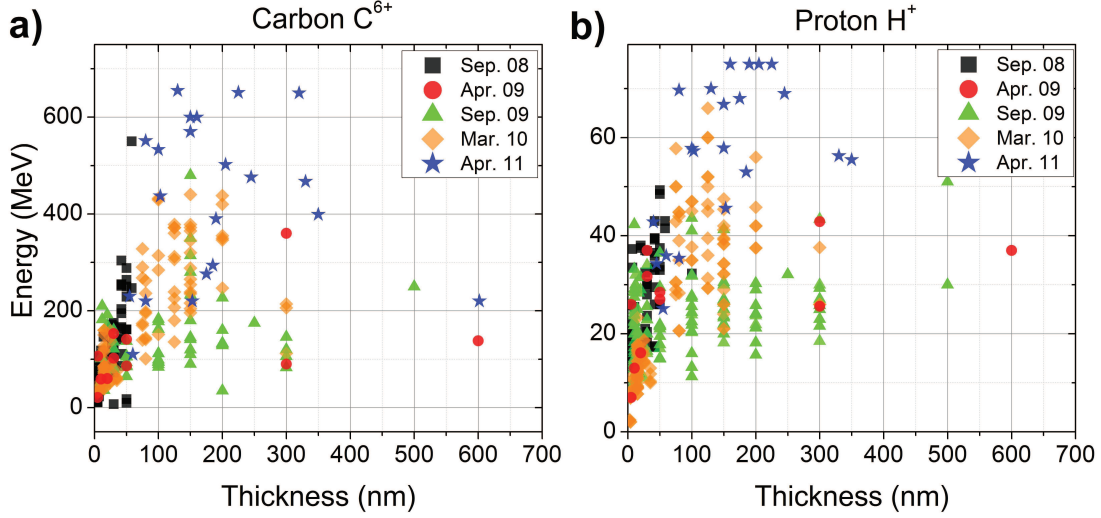


Figure 4.3: Experimental data of 5 of the 6 campaigns showing the efforts in improving repeatability and accuracy of the measured maximum carbon  $C^{6+}$  ion a) and proton b) energies. The campaigns from Apr.08 through Mar.10 were done in the TP-setup, the last one in the iWASP-setup that covers a much larger solid angle of the ion beam. Campaigns from Mar.10 on also used the improved target and focusing system as described in Chap. 3.3.

- For the first campaign (Sep08, black squares) only DLC targets (produced at the LMU) from 3 nm to 58 nm were available [131]. The highest energy for  $C^{6+}$  is 550 MeV, which was measured only once during the roughly 100 shots of this run. It is worth noting that this run had the highest average laser energy of almost 100 J per shot as compared to 80 J in all the following campaigns (explaining the slightly higher energies at lower target thicknesses (see Chap. 2.3.3)).
- The next campaign (Apr09, red circles) was primarily dedicated to investigate electron spectra for ultra-thin targets with  $< 10$  nm [101]. In addition, commercially available diamond targets [141] between 300 nm and  $1 \mu\text{m}$  were tested for ion acceleration.
- In the following run (Sep09, green triangles) commercially available diamond targets [141] between 100 nm and 300 nm were added to the thickness range. This run, however, showed an overall decrease in ion energies for carbon  $C^{6+}$  ions as well as protons. The exact cause for this is unknown,

## 4.2. PROTON AND CARBON ION ACCELERATION

---

but a decreased contrast and/or target misalignment seem to be the most plausible reasons.

- This triggered the development of a new target and focusing system (see Chap. 3.3) to improve repeatability in the on-target intensity and also the installation of on-shot beam diagnostics to identify contrast fluctuations. The improvements resulted in a much more consistent data set (Mar10, orange diamonds). Diamond targets down to 30 nm were incorporated in this run for a finer thickness scan.
- All prior campaigns were done in the TP-setup, i.e., ion energies are obtained from TP-spectrometers, analyzing only a very small fraction of the ion beam on the order of  $10^{-5}$  msr. In this campaign (Apr11, blue stars) the iWASP-setup was used. The iWASP measured the spectra over almost  $30^\circ$  with a solid angle of 0.1 msr. Hence, chances to measure the “correct” maximum energy of the ion beam were much higher. 10 shots out of 25 in the optimum thickness range showed  $C^{6+}$  of more than 500 MeV, 11 other shots energies between 400 MeV and 500 MeV and only 4 considerably less.

In summary, the improved target and focus system and the development and fielding of the iWASP finally resulted in much more consistent and also higher ion energies. It is worth noting that there is still considerable scatter in the data, i. e., energies fluctuate by approximately a factor of two, especially for the carbon  $C^{6+}$  ions. The reason for this is most likely fluctuations in the laser contrast and intensity, which will be addressed in detail in the next section.

### 4.2.1 Thickness scaling

Ion acceleration in the Break-Out afterburner regime (see Chap. 2.3.3) occurs, when the target turns relativistically transparent during the laser irradiation. The relativistic transparency sets in at a time  $t_1 < 2\tau_\lambda$ , when  $n' > 1 > n'\gamma$  (with  $n' = n_e(t)/n_c$ , see Chap. 2.2.3); at the time  $t_2$  the target turns classically underdense so that  $n' < 1$ . In between, ions gain most of their kinetic energy according to the BOA model and VPIC simulations [28, 35, 86, 104]. Optimum acceleration occurs, when the target is relativistically transparent during the interaction of the

#### 4. ION ACCELERATION DURING RELATIVISTIC TRANSPARENCY

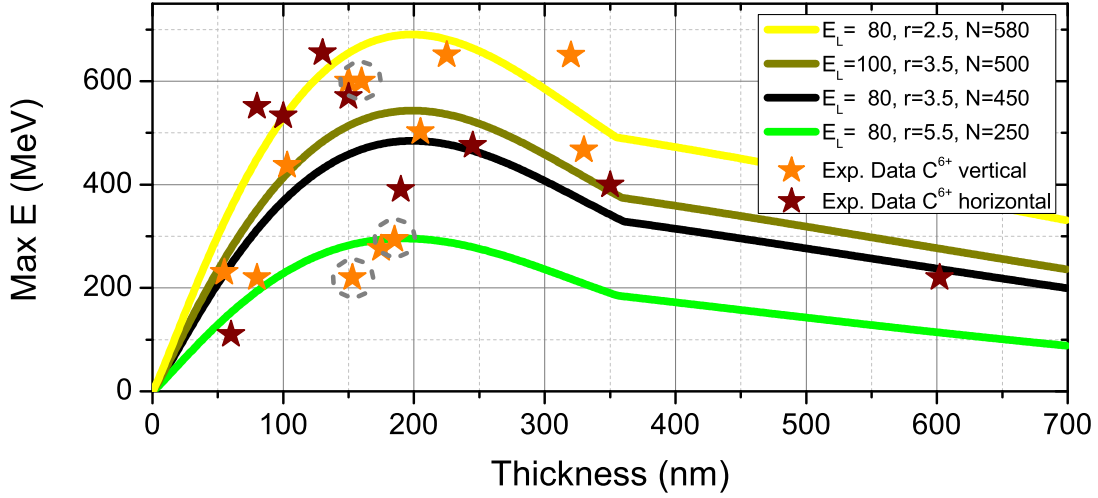


Figure 4.4: Thickness scan for carbon  $C^{6+}$  ions (red stars) measured with the iWASP covering an angle of  $22^\circ$  in the direction parallel (orange, marked as “vertical”) and perpendicular (dark red, marked as “horizontal”) to the laser polarization axis with a solid angle of  $\sim 0.1$  msr. The solid lines are predictions by the analytical model for different combinations of the laser energy and focus to account for variations in the laser and the target alignment. The initial target density has been adjusted to keep the optimum thickness at 200 nm (see text for details). For the three data points marked with a gray dashed circle the on-shot laser contrast is shown in Fig. 4.5 b).

peak pulse with the plasma. If the target is too thin, the relativistic transparency sets in too early and the target turns classically underdense prior to the arrival of the main pulse, preventing efficient acceleration. If the target is too thick, the relativistic transparency might not be reached at all so that the acceleration is more likely dominated by TNSA or FSA mechanisms.

The thickness scan of the last campaign is now compared with the predictions by the BOA analytical model and the VPIC simulations. In this campaign, the iWASP was used to more accurately measure maximum carbon  $C^{6+}$  ion and proton energies, simultaneously, with its orders of magnitude larger solid angle. In Fig. 4.4 the measured maximum energies are plotted for carbon  $C^{6+}$  ions and protons (left and right frame, respectively). For both species a distinct peak in the maximum energy is visible around a thickness of 200 nm; ion energies drop rapidly left of the peak towards the electron blow out regime and decrease more moderately towards thicker targets. The electron blow out regime is reached, when the electrostatic pressure is smaller than the radiation pressure so that

## 4.2. PROTON AND CARBON ION ACCELERATION

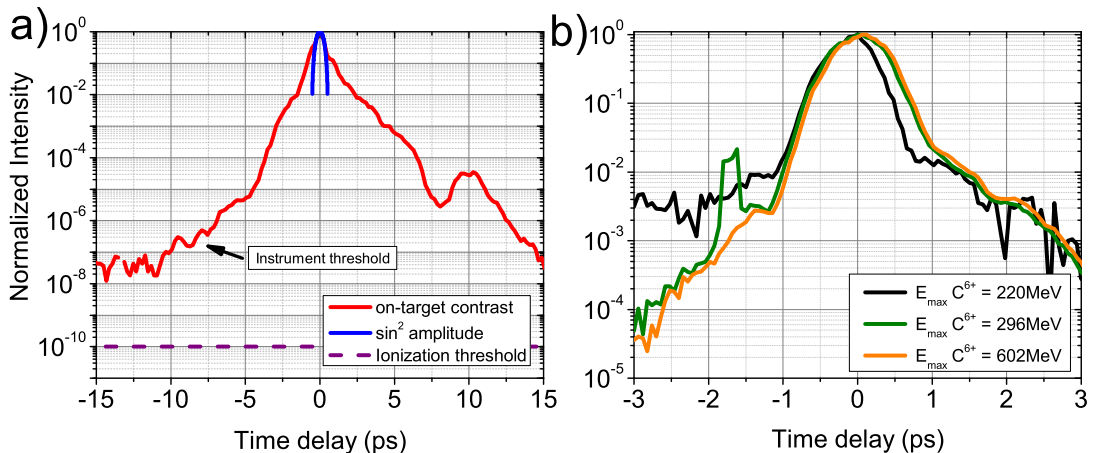


Figure 4.5: Typical single-shot measurement of the on-target laser contrast (red solid line, without firing amplifiers) in comparison with a  $\sin^2$  laser envelope as used by the analytical model and the VPIC simulations. The dashed orange line indicates the ionization threshold. b) actual on-shot contrast (full laser amplification) for the three shots marked with a gray dashed circle in Fig. 4.4. The shot with a high energy cutoff of 602 MeV (orange solid line) shows the best contrast (at a level of  $10^{-4}$ ) before the peak pulse. The shots with much lower cutoff energies show a deteriorated contrast; one with a prepulse on the  $10^{-2}$  level (green solid line) and one with a much higher pedestal intensity (black solid line).

electrons are eventually expelled from the target permanently (at  $d < a_0 \lambda_L / n'_0$ , see Chap. 2.3.2), preventing acceleration by charge separation fields. For thicker targets, the acceleration turns into the TNSA regime once the target does not turn relativistically transparent. This case will be discussed in more detail in the following sections.

In order to address the scatter in the experimental data, a series of predictions by the BOA analytical model is plotted for different combinations of the laser energy and focus; the pulse duration is kept constant at an average of 550 fs. The black solid line represents the average Trident parameters with a laser energy of 80 J focused in a  $3.5 \mu\text{m}$  radius. The light and dark yellow solid lines denote the corresponding predictions for a smaller focus and a higher laser energy, respectively. The first simulates an increased intensity by a smaller focus due to relativistic self-focusing (see Chap. 2.2.4), the latter by a higher laser energy, which naturally fluctuates by  $\pm 10$  J. The green solid line accounts for a reduced intensity due to target and/or laser misalignment, resulting in an increased focal spot size.

Changing the initial target density does not effect the peak energy, but the op-

## 4. ION ACCELERATION DURING RELATIVISTIC TRANSPARENCY

---

imum thickness and could be linked to the actual on-shot laser contrast. In this plot the target density is slightly adjusted for each case to keep the optimum target thickness at 200 nm. The experimental data for the maximum carbon  $C^{6+}$  ion energies falls within the highest and lowest model predictions in Fig. 4.4. Assuming that the measured maximum energies are accurate, the scatter of a factor of 2 in the carbon maximum energies seems to be mostly caused by fluctuations in the laser energy and pulse duration and by the focal radius (self-focusing/alignment). It should further be noted that although the laser contrast does not influence the overall maximum possible peak energy in the model, it still can have an effect on the maximum energies measured for a certain thickness. With a worth contrast (though still good enough to allow BOA, i.e. interaction with an overdense target) the optimum thickness shifts towards thicker targets as will be explained in more detail in the next paragraph. As a result, with different on-shot laser contrast, the same thickness can result in different maximum ion energies. This theory is supported by on-shot laser contrast measurements shown in Fig. 4.5 b) for the shots that are marked with a gray dashed circle in Fig. 4.4. The shot with a high energy cutoff of 602 MeV (orange solid line in Fig. 4.5 b)) shows the best contrast (at a level of  $10^{-4}$ ) before the peak pulse for all three shots. The two shots with much lower cutoff energies (220 MeV and 280 MeV) show a deteriorated contrast; one of them has a prepulse on the  $10^{-2}$  level (green solid line) and one has a significantly higher pedestal intensity (black solid line). (It should however be noted here that these on-shot measurements have a dynamic range of only 4 orders of magnitude, while ionization and hence target expansion happen at much lower intensities.)

To which degree any of the laser parameters contributes to a reduced maximum ion energy is not obvious and remains to be investigated in more detail.

### **The problem with the optimum target thickness**

The optimum target thickness, as observed in the experiment, ranges between approximately 100 nm to 300 nm with the same maximum carbon  $C^{6+}$  ion energies of  $\sim 650$  MeV. As mentioned before, the initial target density does not effect the overall maximum energy in the analytical model, but does significantly effect the optimum thickness at which the maximum energy occurs. A lower initial density leads to earlier relativistic transparency of the target and hence requires a thicker target to compensate and to have the time frame from  $t_1$  to  $t_2$  overlap with the

## 4.2. PROTON AND CARBON ION ACCELERATION

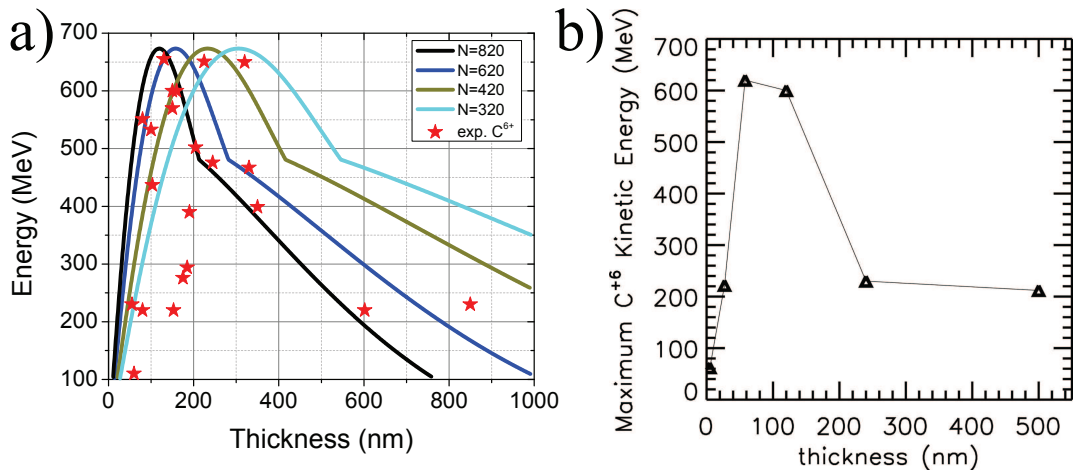


Figure 4.6: a) Maximum carbon  $C^{6+}$  ion energies measured with the iWASP (red stars) and predictions by the analytical model with optimum Trident parameters and varying initial target density to account for variations in the laser contrast and hence the pre-mature expansion of the target. b) Thickness scan as obtained from the VPIC simulations for Trident parameters and an initial density of  $n'_0 = 660$  (left frame adapted from Ref. [106]).

main pulse. A larger initial density will accordingly do vice versa. Although the “cold” target density has, of course, always been the same for all the experiments, the initial target density the main laser pulse interacts with largely depends on the laser contrast in each target shot.

The pedestal of a relativistic laser pulse typically ionizes a target up to several ps before the main pulse, which leads to pre-mature expansion and hence a density decrease. Neither the model nor the VPIC simulations explicitly account for the laser contrast; in fact, both typically use a perfect  $\sin^2$  temporal laser pulse envelope. In Fig. 4.5 a) a typical on-target contrast measurement is shown (laser propagating through the full laser chain without amplification, see Chap. 3.1.5 for details) together with such a  $\sin^2$  temporal intensity envelope; the dashed purple line roughly indicates the ionization threshold. (Fig. 4.5 b) shows three on-shot laser contrast measurements with full amplification in the laser chain.) It is immediately obvious that the simulation and the model only account for the main high intensity part of the whole interaction and that density related effects might not be modeled correctly.

In the analytical model one can change the initial target density to account for this pre-expansion in the laser pedestal; for the VPIC simulations this is much

## 4. ION ACCELERATION DURING RELATIVISTIC TRANSPARENCY

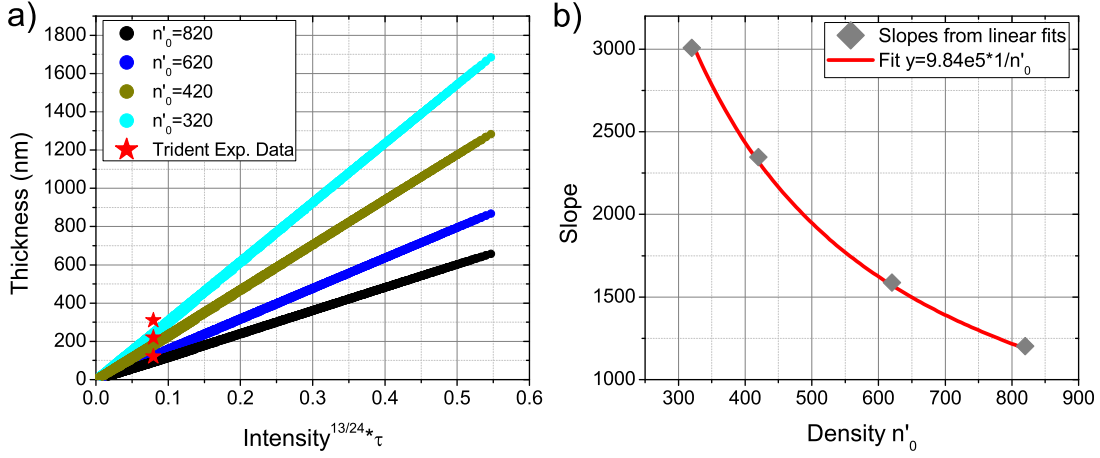


Figure 4.7: a) Results of a parametric scan of the analytical model for the BOA acceleration with different initial densities  $n'_0$ ; maximum  $C^{6+}$  ion energies for different thicknesses are displayed as red stars, as shown in Fig. 4.6; b) Allometric fit of the slopes from a) (see text for details).

more time consuming and has not been done yet. Fig. 4.6 a) shows the maximum energy vs. the target thickness for the optimum Trident parameters yielding the highest intensity (see Fig. 4.4) for different values of the initial target density  $n'_0$ . With densities from  $n'_0 = 820$  (“cold” target) to  $n'_0 = 320$  (strongly expanded target) the model shows an optimum thickness ranging from 100 nm to approximately 350 nm, which is in remarkably good agreement with the experimental data. Fig. 4.6 b) shows the maximum energies obtained from the VPIC simulations for an initial target density of 660 with an optimum thickness between 60 nm and 120 nm.

One can still use the analytical model as a guide for the optimum target thickness (always keeping in mind that the laser contrast reduces the initial target density to a typically unknown value below the density of the cold target). A parametric scan has been used to optimize the analytical model for a maximized acceleration window  $\Delta t$  and to obtain a scaling for the optimum thickness in the BOA regime. Fig. 4.7 a) shows the result of the optimization, where the optimum thickness is plotted vs. the  $I_L^{13/24} \tau_\lambda$  for different initial densities  $n'_0$ . For each density a linear fit has been done with  $y = mx$ ; the slopes have been plotted over the density in Fig. 4.7 b) and fitted with an allometric function to  $m = 9.84 \times 10^5 * 1/n'_0$ . From

## 4.2. PROTON AND CARBON ION ACCELERATION

---

the fits of the optimization follows that the optimum thickness  $d_{\text{opt}}$  scales as

$$d_{\text{opt}}[\text{nm}] \approx 9.84 \times 10^5 \frac{1}{n'_0} I_L^{\frac{13}{24}} \left[ \frac{\text{W}}{\text{cm}^2} \right] \tau_\lambda[\text{fs}] \propto \frac{a_0 \tau_\lambda}{n'_0}. \quad (4.1)$$

With an initial  $n'_0$  of 820 (420), which is (half) the original  $n'_0$  for DLC targets with a density of  $2.7 \text{ g/cm}^3$ , the formula gives a  $d_{\text{opt}}$  of approximately 95 nm (186 nm) for average Trident parameters, which is in good agreement with the experimental results. The red stars in Fig. 4.7 a) represent the maximum energies measured for different target thicknesses at Trident as shown in Fig. 4.6 a).

The “optimum” condition for the BOA acceleration, as a consequence of this analysis of the optimum target thickness, is as follows:

1. Isochoric heating of the target in the laser pedestal with the target turning relativistically transparent right at the beginning of the main pulse
2. Subsequent expansion of the target after  $t_1$  has to be slow enough so that  $t_2$  occurs close to the end of the main pulse, leading to a  $\Delta t \rightarrow 2\tau_\lambda$

This could be achieved with an ultra-high intensity square pulse and a largely reduced pedestal (below the ionization threshold), where the target is heated to the relativistic transparency within the first cycle of the main laser pulse. The subsequent expansion of the target could be “slowed” by a radially rapidly increasing density profile.

### 4.2.2 The problem with the protons

Although the only atomic component of a pure diamond is carbon, there are typically a lot of protons accelerated during the acceleration from diamond targets (unless the target is heated). The protons mostly originate from surface hydro-carbon contaminations, but can also come from the core of the target due to contamination during the CVD or CAD process. In the following the acceleration of protons is investigated in more detail in order to better understand BOA acceleration from multi-species targets. Two important question are how the different species influence each other during the laser-plasma interaction and whether there is a way to optimize BOA acceleration for a specific species. The

#### 4. ION ACCELERATION DURING RELATIVISTIC TRANSPARENCY

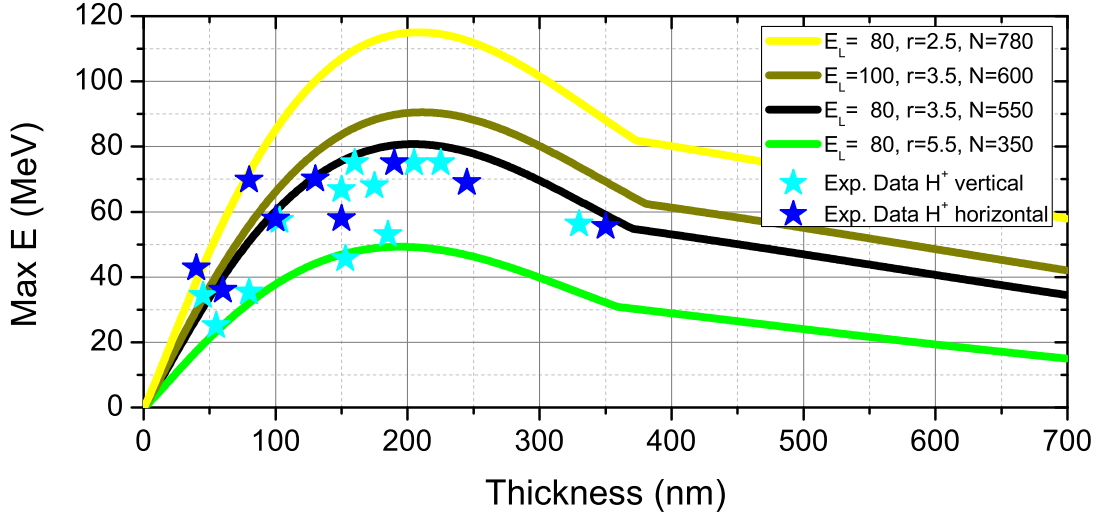


Figure 4.8: Thickness scan for protons (blue stars) measured with the iWASP covering an angle of  $22^\circ$  in the direction parallel (light blue, marked as “vertical”) and perpendicular (blue, marked as “horizontal”) to the laser polarization axis with a solid angle of  $\sim 0.1$  msr. The solid lines are predictions by the analytical model for different combinations of the laser energy and focus to account for variations in the laser and the target alignment. The initial target density has been adjusted to keep the optimum thickness at 200 nm (see text for details).

first one will now be investigated by comparing the proton maximum energies with the predictions of the analytical model and with the carbon maximum energies.

Fig. 4.8 shows the proton maximum energies for the same shots shown in Fig. 4.4. The overall energies of up to 70 MeV are not as high as predicted by the model using the same laser fluctuations. It is furthermore interesting to note that the scatter for the protons is much less than for the carbon ions. The discrepancy between the maximum proton energies predicted by the model and measured in the experiment can be explained by the so-called *self-cleaning* of the target (see Chap 2.3 and Ref. [28]). In the time before the target turns relativistically transparent, it undergoes a phase of strong volumetric heating. All electrons are subsequently heated by the laser ponderomotive force and set up a sheath field on the front and the back side of the target (similar to the TNSA mechanism). The sheath fields are strong enough to accelerate the low inertia protons throughout the whole target, resulting in an evacuation of the protons out of the target before the main BOA acceleration takes place.

## 4.2. PROTON AND CARBON ION ACCELERATION

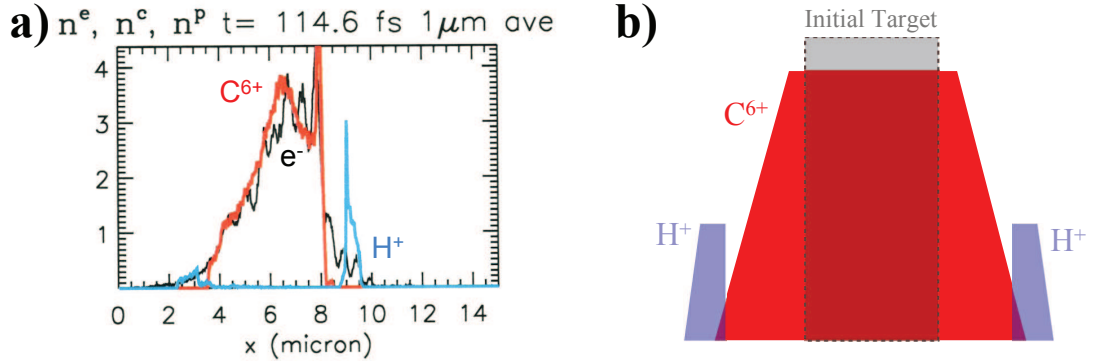


Figure 4.9: a) Snapshot of a 2D VPIC simulation showing the electron (black solid line), carbon  $C^{6+}$  (red solid line) and proton (blue solid line) density during the BOA acceleration. The depletion of protons in the target is caused by self-cleaning of the target due to the high charge to mass ratio and low inertia of protons. The self cleaning is sketched in b) and results in different acceleration dynamics for the protons (see text for details).

Fig. 4.9 a) is a snapshot of a VPIC simulation for Trident parameters and a 30 nm thick diamond target; the snapshot shows the electron, carbon  $C^{6+}$  and proton density at a time of 114.6 fs, which is right after the target turned relativistically transparent in the simulation (with a FWHM pulse duration of 550 fs). At this time frame all target protons are located at the very front and end of the target, while the majority of the electrons is located at the core of the target where the much heavier carbon ions are; this is schematically depicted in Fig. 4.9 b). The self-cleaning effect is further enhanced by the initial low proton bulk concentration in DLC ( $< 10\%$ ) and diamond targets. Hence, the acceleration of protons does most likely not follow the same dynamics as the carbon ions do. In order to more accurately calculate proton acceleration with a PIC simulation, the initial target conditions - given by the laser contrast - need to be known more precisely. Preliminary PIC studies by H. Wu have shown, that the initial proton distribution in the target can significantly effect the final proton energies as well as the spectral shape of the proton beam. For instance, if protons are populated dominantly in the bulk, they eventually gain more energy as they are more likely effected by the main BOA acceleration. In order to increase the energy of the protons in a real experiment, one could hence think about

- significantly increasing the laser contrast to reduce the self-cleaning.
- significantly increasing the proton bulk concentration or use a pure hydro-

## 4. ION ACCELERATION DURING RELATIVISTIC TRANSPARENCY

---

gen target.

In Sect. 4.2.3 the latter case is discussed in more detail; there, a CH<sub>2</sub> target has been used to successfully increase proton energies by a factor of 2.

### 4.2.3 Efficient acceleration of ions with $Z > 1$

Laser-driven ion acceleration in the TNSA regime dominantly accelerates protons; they are accelerated most efficient in the quasi sheath field due to their high charge to mass ratio and their low inertia, and consequently screen the accelerating field to heavier ions. Prior target cleaning with cw-laser heating, resistive heating or ion gun etching has successfully been used to accelerate ions with  $Z > 1$  more efficiently (this procedure is similar to the self-cleaning in the BOA). However, energies for carbon ions still only reach  $\sim 5$  MeV per nucleon [7, 20, 21]. The highest carbon energies shown in Fig. 4.4 and Fig. 4.2 are about 600 MeV (50 MeV per nucleon), i.e., one order of magnitude higher than previously reported from ion acceleration in the TNSA regime. In order to quantify this, the per nucleon energy ratio of the carbon C<sup>6+</sup>ions to the protons is plotted against the thickness in Fig. 4.10. This also corresponds to a direct comparison of the particle velocities  $v_i$ , as  $v_i = \sqrt{2E_k/Zm_p}$  and  $m_i = Zm_p$ , where  $Z$  is the mass number and  $m_i$  the mass of the ion. The figure shows, that the carbon velocities approach and also exceed the proton velocities towards the optimum thickness; for increasing target thickness the ratio falls down to 0.1.

If one considers that acceleration of ions in the TNSA regime is due to a virtual cathode, one can calculate the maximum possible velocity ratio. The velocity of the particle is given by Lorentz equation in the non-relativistic case as

$$m_i \frac{dv}{dt} = q_i E_s \quad (4.2)$$

where  $E_s$  is the sheath field set up by the hot electrons ( $E_s \approx k_B T_h / e \lambda_{Deh}$  [7]), which is assumed to be slowly varying in space and time on the scale of the laser frequency. The velocity ratio for carbon C<sup>6+</sup>ions to protons is hence  $v_c/v_p = m_p q_c / m_c q_p = 0.5$ , provided that both species are accelerated over the same time in this field and neglecting screening of the field by the protons. All data points

## 4.2. PROTON AND CARBON ION ACCELERATION

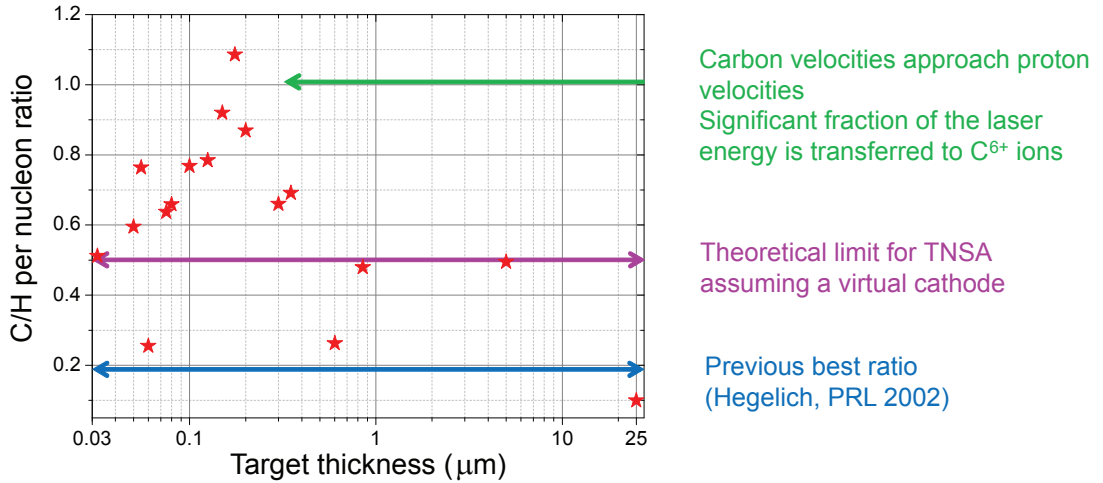


Figure 4.10: Ratios of the per nucleon energy for carbon and proton maximum energies. The ratio goes up to 1.1 at the optimum thickness, where carbon ions have a slightly higher velocity than the protons. The theoretical limit in a TNSA dominated acceleration by a virtual cathode is 0.5 and the highest experimentally measured value for TNSA is 0.2.

between 30 nm and 1  $\mu\text{m}$  are above this theoretical upper limit of 0.5. For thickness from 1  $\mu\text{m}$  to 5  $\mu\text{m}$  the ratio stays at 0.5 and then drops below. The highest so far reported ratio from TNSA acceleration is 0.2 [7]. In other words, in the BOA regime, acceleration of heavier ions is strongly enhanced over the TNSA regime.

This is explained by the fact that in the BOA regime acceleration of ions occurs along the whole ionized target and the accelerating field moves with the maximum of the charge distribution, usually provided by the highest charged species. In TNSA, on the other hand, acceleration only occurs at the target surface. In combination with the previously introduced self-cleaning, field screening by protons is less likely to hinder acceleration of heavier ions. The consequences of this volumetric acceleration are discussed in more detail in Sect. 4.2.5.

The answer to the question why the highest ratio is close to one at the optimum thickness is not obvious, since protons and carbons should mostly experience different acceleration dynamics due to the self-cleaning, so that there should be no correlation between their final velocities. A very simple way to look at this could be that the protons are still accelerated first and consequently always run ahead of heavier ions. In case the carbon distribution with its co-moving electric field is catching up with them, they would be further accelerated and end up with at

## 4. ION ACCELERATION DURING RELATIVISTIC TRANSPARENCY

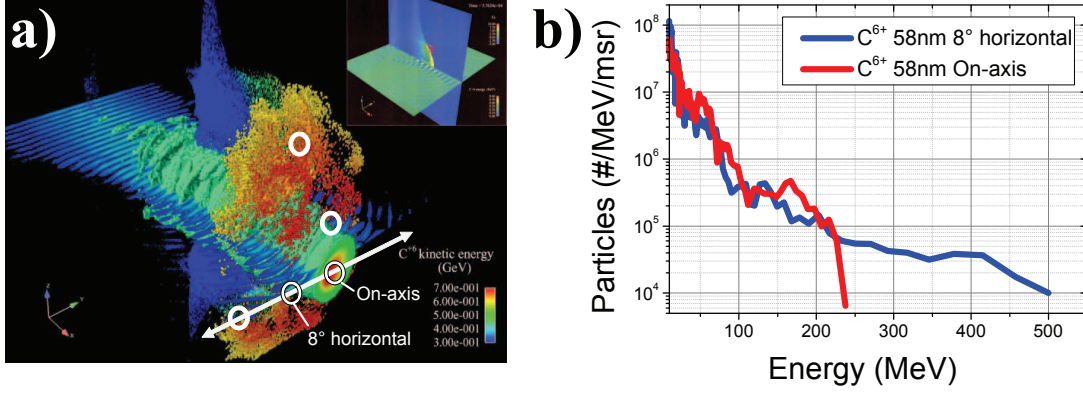


Figure 4.11: a) Snapshot of BOA acceleration in a 3D VPIC simulation, where the white line indicates the laser polarization axis and the white circles positions of TP-spectrometers in the TP-setup. The iWASP analyzed the particle beam along and perpendicular to the polarization axis. b) Typical TP-spectra measured on- and off-axis exhibiting significantly different high energy cutoffs.

least the same velocity as the carbons. However, some shots have already shown carbon to proton velocity ratios exceeding 1 (although only slightly); further research will be necessary to answer this question.

### 4.2.4 Angular energy dependency

This section is devoted to the complex angular structure of the particle beams obtained from the BOA acceleration due to 2D and 3D effects. Considering an application like the hadron cancer therapy, it can be necessary to guide the beam away from the target by, for instance, collimating and/or focusing the particle beam. This requires detailed knowledge about the beam in terms of its divergence and the angular ion energy dependency. As an example, in Ref. [162] a set of quadrupole lenses is used to focus a laser-driven ion beam; the initial divergence of the beam sets the parameters for the quadrupole lenses and also limits the throughput of particles and the needed particle flux.

A snapshot of a carbon  $C^{6+}$  beam from a 3D VPIC simulation for Trident similar parameters (with a shorter  $\tau_\lambda = 312$  fs to reduce computing time) is shown in the left frame of Fig 4.11. The snapshot shows iso-energy surfaces of carbon  $C^{6+}$  ions with energies between 400 MeV and 700 MeV (see color bar of the figure) and the laser electric field in the center; the time of the snapshot is  $t = t_2$  for this simulation, i.e., at the end of the main acceleration phase of BOA. The parti-

## 4.2. PROTON AND CARBON ION ACCELERATION

---

cles are gathered almost symmetrically around the laser in a ring-like structure, but the azimuthal symmetry is broken for these highest energies along the solid white line that indicates the polarization direction of the LP laser pulse of the simulation. The azimuthal symmetry is not broken for the low energy particles with  $< 400$  MeV (compare Fig. 4.14). The laser spot itself shows a depletion of high-energy particles above 400 MeV in the center.

This depletion of high energy particles on the laser axis has been confirmed by the measurements conducted in the framework of this thesis, first with TP measurements and later with the iWASP. Fig 4.11 b) shows carbon  $C^{6+}$  energy spectra measured by TP-spectrometers positioned on-axis and off-axis  $8^\circ$  parallel to the polarization axis (as marked in Fig 4.11 a)); the white circles indicate all positions, where in earlier campaigns TP-spectrometers measured the particle beam (typically at  $0^\circ$  and at  $8^\circ$  and  $21^\circ$  in the horizontal and vertical plane with respect to the laser polarization axis). The spectra typically show significantly lower maximum energies measured on-axis (red solid line) than off-axis (blue solid line), which agrees qualitatively with the 3D simulation.

Analyzing such a complex beam structure with common TPs is however difficult and can also be very inaccurate due to the small acceptance angle of these spectrometers. The following more accurate investigation of the angular beam structure has become possible by the novel ion wide angle spectrometer (iWASP) [157] that has been designed and build in the framework of this thesis. The solid white line that indicates the laser polarization axis marks the plane of the particle beam, that has been analyzed by this wide angle spectrometer. In order to investigate the azimuthal symmetry of the beam, the plane perpendicular to the polarization direction has also been analyzed with the iWASP.

In Fig 4.12 maximum energies have been extracted from the angularly resolved energy spectra for thicknesses from 30 nm up to  $25 \mu\text{m}$ ; the plots show the maximum energy measured on-axis (blue circles) and the overall maximum energy measured in the whole angularly resolved spectra between  $0^\circ$  and  $22.5^\circ$  (red triangles) for carbon ions (left frame) as well as protons (right frame). The measurements revealed that carbon  $C^{6+}$  maximum ion energies are emitted off-axis in the optimum BOA thickness range around 200 nm. In this thickness range, the energies measured on-axis are typically much lower. For targets exceeding  $1 \mu\text{m}$ , where the acceleration starts to be dominated by the TNSA mechanism, maximum energies are emitted on the laser axis at  $0^\circ$ . This general angular

## 4. ION ACCELERATION DURING RELATIVISTIC TRANSPARENCY

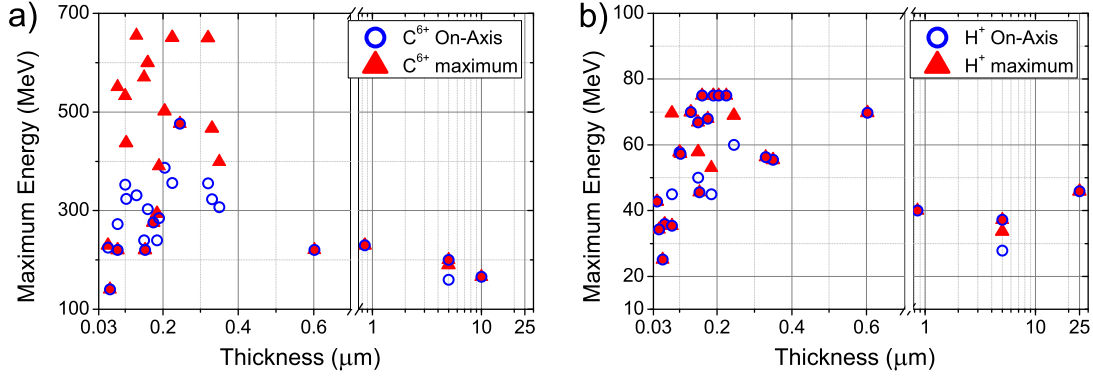


Figure 4.12: Overall maximum energies (red triangles) and cutoff energies seen on-axis at  $0^\circ$  (blue circles) for carbon  $\text{C}^{6+}$  ions a) and protons b). For protons maximum energies are emitted on-axis regardless of the target thickness, whereas maximum carbon ion energies are emitted off-axis in the BOA regime ( $\ll 1 \mu\text{m}$ ) and on-axis in the TNSA regime ( $> 1 \mu\text{m}$ ).

dependency of the maximum energies is in good agreement with the previous TP measurements and the 3D VPIC simulation.

At the same time maximum proton energies are always found target normal at  $0^\circ$  regardless of the target thickness, as depicted in the right frame of Fig 4.12. This is most likely caused by the previously discussed self-cleaning of the target in the BOA acceleration, which causes the protons to experience different acceleration dynamics as they leave the target prior to the arrival of the peak pulse (see Sect. 4.2.1 and Fig.4.9). This angular dependency also shows that measurements of maximum ion energies with conventional TPs can give misleading results by not picking the “optimum” angle and that the maximum ion energy measured might not be the overall maximum ion energy achieved in the interaction.

In order to further understand this dependency, the particle emission over the whole angle of the planes in the polarization direction and perpendicular to it are analyzed in more detail. Fig.4.13 shows the measured integrated particle numbers  $n_i$  for different target thicknesses in the polarization plane of the laser; Fig.4.13 a) shows the results for carbon  $\text{C}^{6+}$  ions and Fig.4.13 b) for protons. It should be noted that results for the measurements perpendicular to the laser polarization axis are very similar (data not shown); the symmetry break seen in the simulations, only occurs at the highest energies and is, if present in the experiment, washed out by the integration in this figure. The plots are shown for angles from  $-22.5^\circ$  to  $+22.5^\circ$ , where the negative angles are the mirrored image of the posi-

## 4.2. PROTON AND CARBON ION ACCELERATION

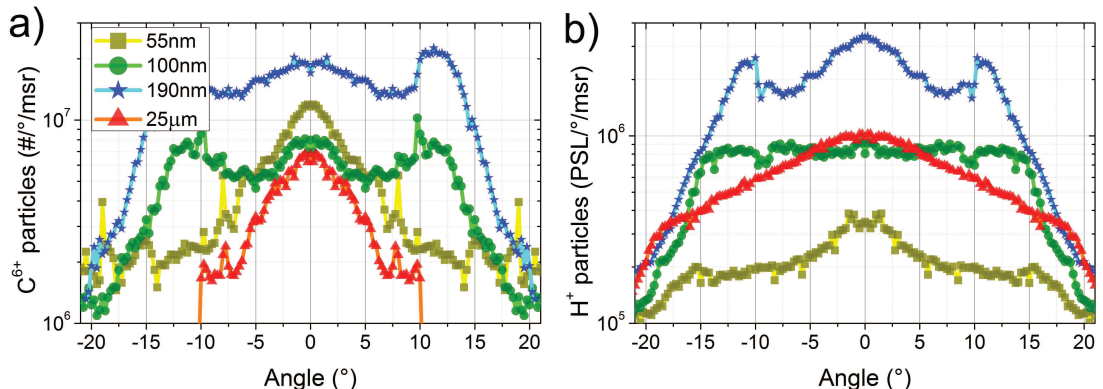


Figure 4.13: Integrated particle numbers against the angle for different target thicknesses for carbon ions a) and protons b) (particle numbers are in PSL for protons). Typical angular distributions are shown for sub-optimal BOA targets at 45 nm (yellow squares) and 100 nm (green circles), a optimum BOA target at 190 nm (blue stars) and a target for pure TNSA interaction at 25  $\mu$ m (red triangles.)

tive angle region, which corresponds to the actual measurements of the iWASP. The thicknesses of 55 nm, 190 nm correspond to interaction before and at the optimum target thickness for BOA, the 600 nm are right at the turnover from the BOA to TNSA regime and the thickness of 25  $\mu$ m corresponds to a purely TNSA dominated interaction. The area under the curves of the different thicknesses indicates the conversion efficiency of laser light into ions; this will be discussed in more detail in the next section.

For the 25  $\mu$ m case (red line with triangles), the typical TNSA distribution can be seen, which is Gaussian-like and peaking at the target normal at 0° [163]. Here, the opening angle is twice as large for protons as for the carbon ions, which supports that ion acceleration ( $Z > 1$ ) is suppressed and very inefficient in the TNSA regime. For the 600 nm case, the opening angles are almost equal for the carbon and the proton beam; in particular, at about  $\pm 10^\circ$  wings start to develop, with most particles still being emitted target normal at 0°. The wings are even more pronounced at the optimum BOA thickness in the 190 nm case, where now the particle flux of the carbons exceeds the flux on-axis; for protons, the particle flux is still maximal at 0°, which is in agreement with the prior discussed angular dependency of the maximum energies. For the 55 nm case, acceleration is again less efficient, as the target turns classically underdense before the laser peak hits

#### 4. ION ACCELERATION DURING RELATIVISTIC TRANSPARENCY

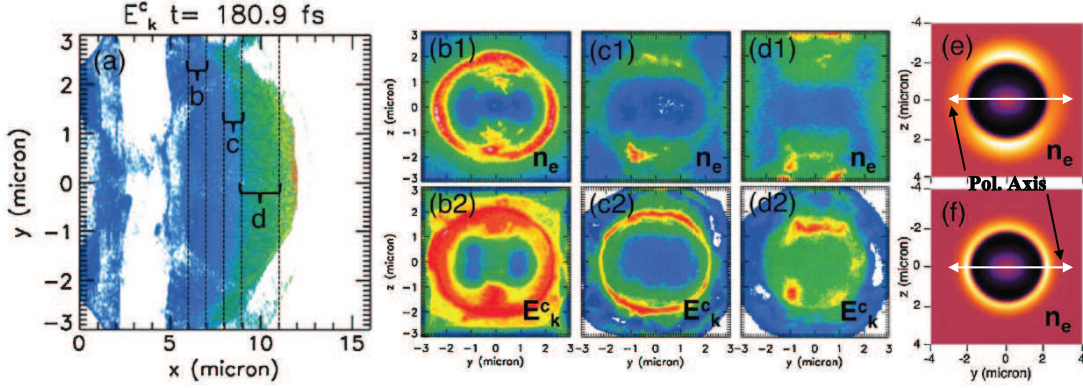


Figure 4.14: a) - d) 3D VPIC simulation results of the BOA at time  $t = 180.9$  fs during the relativistic transparency. Panel a) shows  $E_k^c$  and depicts regions over which the data are averaged in panels b) ( $x = 6 - 7 \mu\text{m}$ ), c) ( $8 - 9 \mu\text{m}$ ), and d) ( $9 - 11 \mu\text{m}$ ); b1) to d1) show averages of  $n_e$  and in b2) to d2) is  $E_k^c$  displayed. e) and f) shows  $n_e$  from 2D hydromodeling without and with electrostatic forces from the ions on the expelled electrons, respectively (shown after 3 fs) (Figure and caption from Ref. [164]).

the target; 2D-PIC simulations (data not shown) and the analytical model give a  $t_2$  ( $n'=1$ ) of 500 fs and 530 fs, respectively, for Trident parameters with a FWHM pulse duration of 550 fs and an initial density  $n'_0$  of 820.

In order to explain the wings visible at  $\pm 10^\circ$  in the optimal BOA target thickness range, the motion of a single electron in a tightly focused relativistic laser needs to be recalled (see Chap. 2.1.1). The electron is expelled from the laser focus due to the ponderomotive force of the LP laser pulse, where the angle with respect to the laser axis is given as

$$\tan^2(\theta) = \left( \frac{\vec{p}_\perp}{\vec{p}_x} \right) = \frac{2}{\gamma_s - 1}, \quad (4.3)$$

with  $\vec{p}_\perp = E_{\text{pond}}/c$  and the longitudinal momentum  $\vec{p}_x = \vec{p}_\perp/(2m_e c)$ ;  $\gamma_s = 1 + a^2/2$  denotes the Lorentz factor for a single electron in units of the normalized laser amplitude. This gives a maximum angle  $\theta$  of  $\sim 7^\circ$  for a single electron at an  $a_0 \approx 16$  for Trident.

In a real laser-plasma interaction, the collective expulsion of electrons from the laser focus eventually results in an enhanced transverse acceleration of the ions, which could cause the generation of wings in the particle beam. This theory is justified by the 3D simulation shown in Fig 4.11. In particular, Fig. 4.14 shows

## 4.2. PROTON AND CARBON ION ACCELERATION

---

electron densities (upper panels *b1* to *d1*) and carbon ion kinetic energies (lower panels *b1* to *d1*) in the plane perpendicular to the laser propagation direction  $x$  at 3 different distances to the original target position. The left most frame shows a cut in the  $x$ - $y$  plane of the 3D simulation shown above; the 3 different positions for the electron densities and ion energies are correspondingly marked as *b*, *c* and *d*. The *b* and *c* panels show a ring structure with a clear azimuthal symmetry of the beam with an opening angle of about  $15^\circ$ ; the electron density plots have an area of strong depletion in the center, which cause the ion energies to peak at the edge of the ring structure. In other words, ion acceleration is enhanced along the electron ejection trajectories in the simulation, which is in good agreement with experimental results.

Moreover, for the panel *d2*, which represents the most energetic carbon ions, the azimuthal symmetry is broken and ions are piled up perpendicular to the laser polarization axis. This is caused by a symmetry brake in the radial ponderomotive force that leads to a pile up of electrons perpendicular to the polarization axis. A complete analytical derivation with the full 3D dynamics of the BOA acceleration is beyond the scope of this section. Yin, *et al.* [164] published a 2D analytical theory for this generation of *ion lobes*, where the perpendicular momentum  $\vec{p}_{e\perp}^s$  of the electrons by the secular (non-oscillatory) part of the ponderomotive force shows a  $m = 2$  variation with  $\cos(2\theta)$ . This variation leads to the symmetry break perpendicular to the laser polarization axis, as observed in the simulation (panels *d1* and *d2*). For the panels *b* and *c*, which show slower ions, the symmetry break is canceled by the electrostatic force of the ion background overcoming the electron ponderomotive motion.

The effect of the electrostatic force by the ion background is illustrated in the panels *e* and *f*, which show the electron densities from a 2D hydromodeling without and with the electrostatic forces, respectively. Panel *e* shows a clear symmetry break for the modeling without electrostatic forces, while *f* shows an almost azimuthally symmetric electron distribution.

The formation of electron and ion lobes and the azimuthal symmetry of the particle beam with the depletion on the laser axis is a key signature of the BOA acceleration. As shown in the experimental data, the ion distributions are significantly different for TNSA dominated acceleration, which show the typical Gaussian like distribution peaked on the laser axis. It should further be noted that experimental evidence for the azimuthal symmetry break for the higher en-

## 4. ION ACCELERATION DURING RELATIVISTIC TRANSPARENCY

---

ergies is complicated and challenging and not possible with the iWASP, since it can only be used to analyze either of both planes at the same time. However, first analysis of the measurements perpendicular and parallel to the laser polarization indicate such a symmetry break (data not shown); more data is needed to improve the statistics for a more conclusive result.

### 4.2.5 Conversion efficiency

The conversion efficiency (CE) of laser light into ions - mediated by the plasma electrons - is an important parameter for the acceleration mechanism. Every application using these laser-driven ion beams, has a specific requirement in terms of how many particles are needed at a specific energy. The hadron cancer therapy, for instance, requires about  $10^9$  particles [165] at the respective energy in a small bandwidth. With a known CE for a specific acceleration mechanism, one can derive the necessary laser parameters for each of the applications (provided the acceleration mechanism delivers the necessary ion energies).

In order to derive a correct and absolute CE, a full spectral beam profile (with all energies and full solid angle) would be necessary. This, however, is typically not possible as

- ion spectrometers typically have a low and high energy detection limit, mostly due to the detector material.
- ion spectrometers typically have a limited acceptance angle, so that a full beam profile cannot be measured in a single shot.
- multi species targets complicate these measurements even further, by demanding charge to mass separation in the ion spectrometer.

Most CE measurements, that have been published [32, 87] for multi species targets, have used TP data as basis for the CE-estimates; these estimates have inherently large uncertainties with regards to the ion beam profile, due to the very low acceptance angle of TP spectrometers.

Here, the CE is estimated using the iWASP with its order of magnitude larger solid angle, utilizing the previously discussed azimuthal symmetry of the particle beam. The afore mentioned symmetry break at high energies is negligible for the

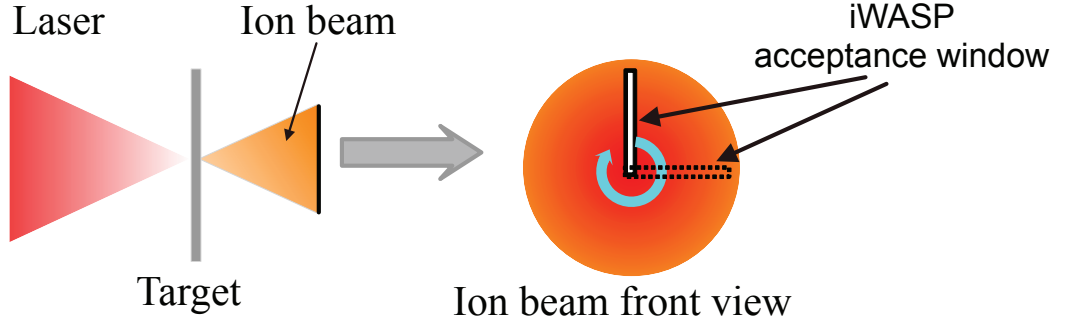


Figure 4.15: Estimating the conversion efficiency from the measurements: the conversion efficiency is calculated for the solid angle captured by the iWASP, where measurements have been done parallel and perpendicular to the polarization axis. The conversion efficiency is then “rotated” by  $360^\circ$  assuming azimuthal symmetry of the beam (see text for details).

CE calculation, due the low number of particles at these energies (see Fig. 4.2 and Fig. 4.11b). The low-energy cutoff of the iWASP is 33 MeV and 11 MeV for carbon  $C^{6+}$  ions and protons, respectively, due to a  $32\ \mu\text{m}$  Al filter in front of a 1 mm CR39 and the IP (see Chap 3.4 for details). Its acceptance angle goes from  $-2.5^\circ$  to  $22.5^\circ$ , where  $0^\circ$  is the laser axis and target normal; measurements were done perpendicular and parallel to the laser polarization axis (see Fig 4.11a).

A caveat of the iWASP is, that it cannot resolve different carbon charge states in an evaluable way, unlike a TP-spectrometer. This will lead to an overestimate of the CE for carbon ions, when the lower charge states are evaluated as  $C^{6+}$  and erroneously attributed with higher particle energies. Measurements in the earlier campaigns at Trident - where TPs have been used to measure the beam with full charge to mass separation - have shown that the target is typically fully ionized for thicknesses in the BOA regime, when the target is relativistically transparent during the interaction. Here,  $C^{6+}$  and  $H^+$  are the only species present, which are well resolved by the iWASP. For thicker targets with  $d > 700\ \text{nm}$  (for Trident parameters), where the target does not turn relativistically transparent anymore and TNSA is predominant, population of lower carbon charge states is increased, leading to the previously mentioned overestimate of the CE for carbon ions.

In order to estimate the CE, the experimental data between the angle from  $0^\circ$  to  $22.5^\circ$  are taken into account (neglecting the angles from  $-2.5^\circ$  to  $0^\circ$ ). The CE is first calculated for the measured solid angle of the iWASP and than “ro-

#### 4. ION ACCELERATION DURING RELATIVISTIC TRANSPARENCY

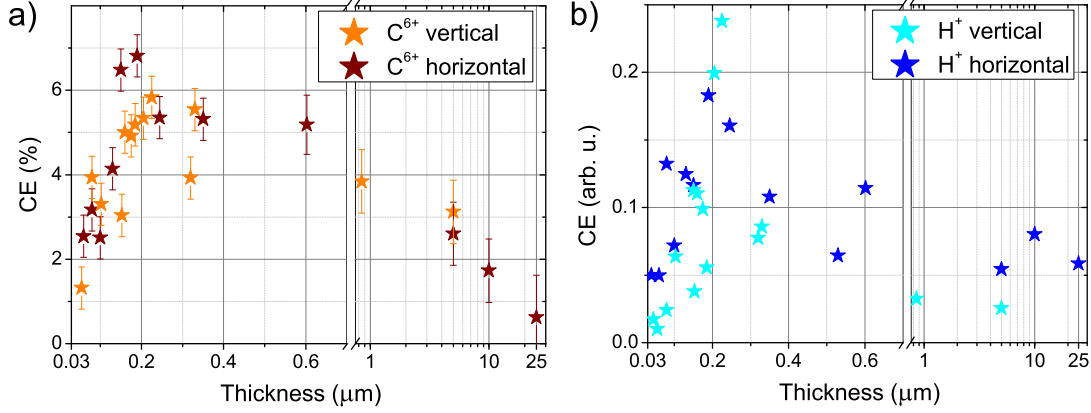


Figure 4.16: Conversion efficiencies for a) carbon  $C^{6+}$  (absolute) and b) protons (in arb. u.) for thickness from 30 nm to 25  $\mu\text{m}$ . The conversion efficiency peaks for both species at the optimum BOA thickness  $d_{\text{opt}} = 200$  nm, with almost 7% for  $C^{6+}$  and a 5-fold increase for protons as compared with thicknesses larger than 1  $\mu\text{m}$ .

tated” by  $360^\circ$ , assuming azimuthal symmetry of the ion beam (see Fig. 4.15). The estimates of the CE are hence given for carbon  $C^{6+}$  ions above 33 MeV and protons above 11 MeV into a cone with a half angle of  $22.5^\circ$ . Since carbon ions are measured on nuclear track detectors, the CEs are given in absolute numbers; for protons that are measured with IPs, the numbers are in arbitrary units, as an absolute IP calibration for this setup is missing. In Fig. 4.16 the CE is plotted for target thicknesses from 30 nm up to 25  $\mu\text{m}$  for carbon  $C^{6+}$  ions in the left frame and for protons in the right frame. The plot has a linear thickness scale from 50 nm to 700 nm, where acceleration happens in the BOA regime and log-scale for thickness  $>700$  nm, where the acceleration turns into the TNSA regime. For both species the CE peaks at a thickness of 200 nm, which is also the optimum target thickness for maximum ion energies; for thinner and thicker targets the CE rapidly decreases. The peak carbon CE reaches up to 7% at the optimum thickness. At a thickness of 25  $\mu\text{m}$  the acceleration is purely TNSA and efficient acceleration of carbon ions has nearly ceased. The proton CE, however, stays almost constant for thicknesses exceeding 1 micron (at a quarter of its peak CE), which agrees well with the fact that TNSA predominantly accelerates protons. In summary, the CE increases by factor of about 11 and 5 for carbon ions and protons, respectively, comparing the 200 nm optimum BOA thickness with the 25  $\mu\text{m}$ , where acceleration is purely TNSA for the Trident parameters.

## 4.2. PROTON AND CARBON ION ACCELERATION

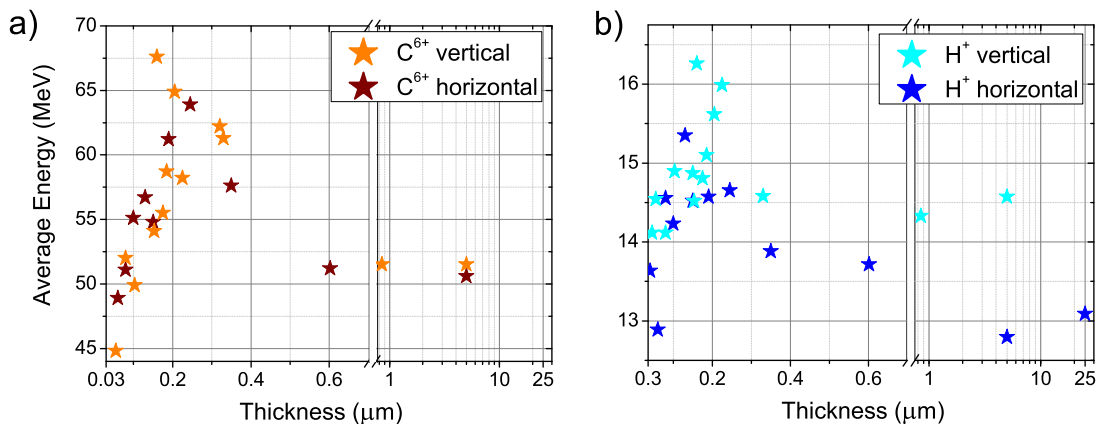


Figure 4.17: Thickness dependency of the average particle energy for carbon  $\text{C}^{6+}$  a) and protons b) for thicknesses ranging from 30 nm up to 25  $\mu\text{m}$ . The low energy detection limit for the carbons is 33 MeV and 11 MeV for the protons. The peak at 200 nm corresponds to the optimum BOA target thickness for Trident parameters. The error for the mean ion energy is expected to be close to the instrument's energy resolution (6% for protons and 10% for carbon ions at 50 MeV/amu).

In order to further investigate the CE and to determine the cause for the increase in efficiency at the optimum BOA target thickness, the number of accelerated particles and the average particle energies are analyzed. In Fig. 4.17 the average energies of the measured iWASP spectra for carbon  $\text{C}^{6+}$  ions a) and protons b) are shown for the same thickness range. Note, that the average energies are calculated for energies above the detection threshold for each of the species (33 MeV and 11 MeV for  $\text{C}^{6+}$  and  $\text{H}^+$ ). The average  $\text{C}^{6+}$  particle energies range from 50 MeV in the TNSA (1-25  $\mu\text{m}$ ) to 67 MeV ( $\ll 1 \mu\text{m}$ ) in the BOA regime, which corresponds to only small increase by a factor of  $\sim 1.3$ . The same factor of 1.3 can be seen for the proton average energies, which go from 13 MeV to 17 MeV at the same thicknesses. Moreover, the average particle energies are for both species more or less independent of the target thickness with  $d > 1 \mu\text{m}$ .

It is worth noting that at the same time the maximum energies increase from 60 MeV to 650 MeV (factor of 11) and from 40 MeV to 75 MeV (factor of 1.9) for  $\text{C}^{6+}$  and protons, respectively. The influence of the maximum energies on the average energy and hence the CE is marginal since the particle numbers at the high energy tail (i.e., at the maximum energy) of the spectra are typically 2 to 4 orders of magnitude lower, but energies are only up to one order of magnitude

#### 4. ION ACCELERATION DURING RELATIVISTIC TRANSPARENCY

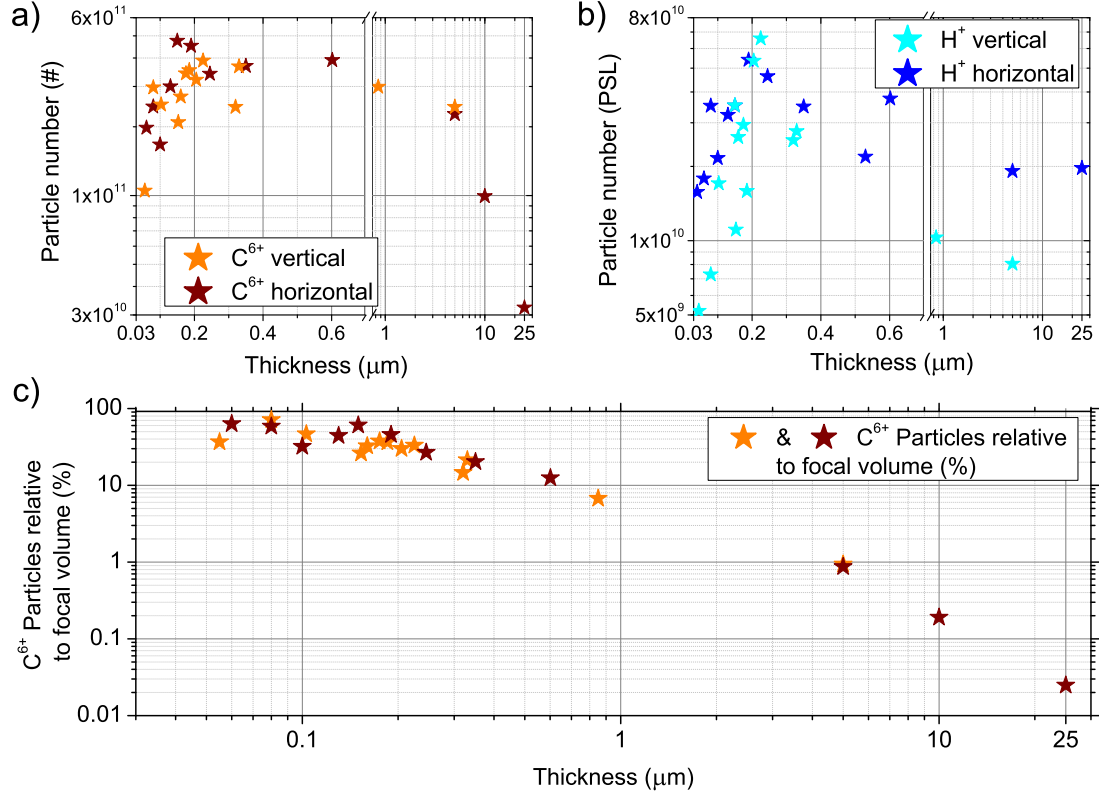


Figure 4.18: Thickness dependency of particle numbers for carbon  $C^{6+}$  a) and protons b) for thicknesses ranging from 30 nm up to 25  $\mu\text{m}$ . The peak at 200 nm corresponds to the optimum BOA target thickness for Trident parameters. For thicknesses  $> 1 \mu\text{m}$  acceleration turns over to TNSA. Note that particle numbers for protons are given in PSL due to missing absolute calibration of the IP.

higher.

Fig. 4.18 shows the measured particle numbers for carbon  $C^{6+}$  ions a) and protons b), where particle numbers for protons are given in photo-stimulated luminescence (PSL) and absolute for carbon. The plots show the same qualitative thickness dependency as the CE in Fig. 4.16 with a peak at 200 nm. At the peak  $5 \times 10^{11}$  carbon particles above 33 MeV have been accelerated; this corresponds to  $\sim 70\%$  of the carbon ions contained within a  $3.5 \mu\text{m}$  focal volume of a 200 nm target irradiated by the laser, but drops rapidly below 1% for targets exceeding  $1 \mu\text{m}$  as depicted in Fig. 4.18 c). As with the CE, carbon particle numbers rapidly decrease for the micron-thick targets, while the proton numbers are almost constant for these thicknesses. Comparing the values for 200 nm (BOA regime) and  $\gg 25 \mu\text{m}$  (purely TNSA regime) the carbon  $C^{6+}$  and proton particle numbers in-

## 4.2. PROTON AND CARBON ION ACCELERATION

	C <sup>6+</sup> 200 nm	H <sup>+</sup> 200 nm	C <sup>6+</sup> 25 μm	H <sup>+</sup> 25 μm	C <sup>6+</sup> Ratio	H <sup>+</sup> Ratio
Particles	5e11	5e10 (PSL)	4e10	1e10 (PSL)	12.5	5
Avg. E	65MeV	17MeV	50MeV	13MeV	1.3	1.3
Max. E	650MeV	75MeV	60MeV	40MeV	10.8	1.9
CE	7%	0.25 (arb. u.)	0.6%	0.05 (arb. u.)	10.6	5

Table 4.1: Comparison of particle numbers, average and maximum energies and conversion efficiency. Values have been picked at 200 nm (BOA) and 25 μm (TNSA) for carbon C<sup>6+</sup> and protons; the ratios in the two columns to the right of the table are calculated by value-BOA/value-TNSA.

creases by factor of about 12 and 5, respectively.

This indicates, that the observed 12-fold and 5-fold increase in CE between the 200 nm and the 25 μm targets is dominated by an increase in accelerated particles in the relativistic transparency. In the BOA regime the whole volume of the irradiated target interacts with the laser due to the relativistic transparency, while for TNSA mainly surface hydro-contaminants are affected by the acceleration (see Fig. 4.18 c)). Hence, proton particle numbers and average ion energies are almost constant beyond 1 μm and independent of the target thickness. The diverging behavior of protons and carbons in the micron-target range (where the proton acceleration is enhanced) is in agreement with the theory; TNSA preferably accelerates protons, while BOA efficiently couples laser energy into all target ions. Moreover, considering that the CE is increased by accelerating more particles, the reduced proton bulk concentration and the self-cleaning in the BOA explain the factor of 2 lower increase in CE for the protons in the BOA regime. In order to approximate absolute CE for protons, one can use the proton-IP calibrations published in Ref. [148] and Ref. [149] (both for a different set of IP and scanner type). The calibrations give an IP sensitivity of 0.01 and 0.08 PSL/proton in the more or less constant tail curve far behind the Bragg-peak, which gives a peak CE for protons at 200 nm of 1.5 to 12% (and 0.5 to 3% for targets in the micron thickness range). This approximation is in agreement with the typical CE of about 1% for protons in TNSA [16, 17] and the here measured relative increase of a factor of 5. In total, this gives a CE exceeding 10% (or 8J of the laser energy) into carbon ions and protons above the low energy detection threshold at the optimum target thickness.

All values presented beforehand are summarized in Tab. 4.1.

## 4. ION ACCELERATION DURING RELATIVISTIC TRANSPARENCY

---

### An analytical model for the conversion efficiency

In order to develop a qualitative model for the CE scaling, VPIC simulation results are analyzed and combined with the BOA analytical model. The CE model is restricted to ion acceleration in the BOA regime, when the target turns relativistically transparent during the interaction. The model is furthermore only valid for the dominant ion species, which is effected by the BOA process; in the case of DLC and Diamond, the protons experience different acceleration dynamics due to the self-cleaning.

As derived in Chap. 2.3.3 acceleration in the BOA regime occurs during the relativistic transparency of the target between the time  $t_1$  (when  $n'/\gamma \approx 1$ ) and the time  $t_2$ , when the target turns classically underdense with  $n' \approx 1$  and  $n'/\gamma \ll 1$ .  $t_1$  is calculated via a 1D expansion of the target (see Eq. 2.43) and  $t_2$  (see Eq. 2.46) is derived from a 3D isospheric expansion in the relativistically transparent phase. For the calculation of the CE in the BOA phase, one can make the phenomenological ansatz that

$$CE = k_{\text{eff}} \frac{1}{\tau} \int_{t_1}^{t_2} \sin^2 \left( \frac{t}{\tau} \pi \right) dt = k_{\text{eff}} E_f, \quad (4.4)$$

where  $k_{\text{eff}}$  is the fraction of the delivered laser energy  $E_f$  between  $t_1$  and  $t_2$  that is mediated to the ions. Energy transfer before  $t_1$  and after  $t_2$  is neglected. The fraction  $k_{\text{eff}}$  of the laser energy that is transferred to the ions, is calculated heuristically based on two characteristic features of the BOA acceleration

1. the optimum acceleration occurs when the  $\Delta t = t_2 - t_1$  is maximal and overlaps with the peak of the pulse
2. the energy transfer rate peaks at  $t_1$  and then drops steadily towards  $t_2$ , as seen in the VPIC simulations (see Fig. 4.19)

The first feature has been illustrated in the previous sections and discussed in detail in Chap. 2.3.3. In order to illustrate the second feature, the energy transfer rate is analyzed from 2D-PIC simulations with parameters close to the Trident laser as depicted in Fig. 4.19. The plot shows the energy gain (black circles) and its derivative, the energy transfer rate (orange triangles), for a 120 nm target. Most of the energy transfer occurs during the relativistic transparency, which is between 550 fs and 990 fs (grayed area; the analytical model gives 450 fs and

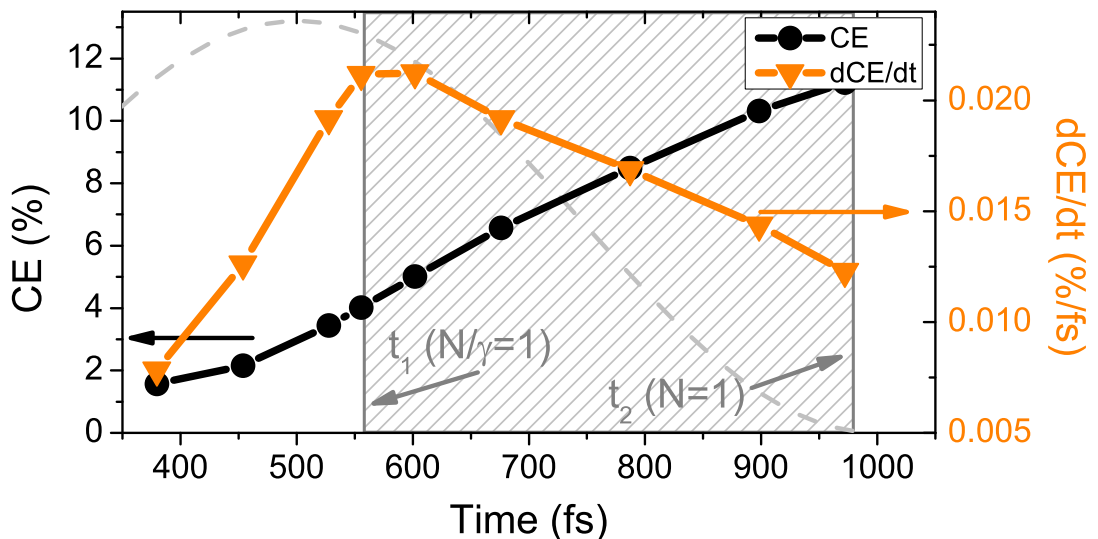


Figure 4.19: Time dependent CE as obtained from 2D-VPIC simulation for a 120 nm target, with the conversion efficiency over  $t$  (black circles) and  $dCE/dt$  over  $t$  (orange triangles). The grayed area (550 fs to 990 fs) indicates the time of relativistic transparency during the simulation. The simulation domain is  $20 \mu\text{m} \times 25 \mu\text{m}$  in the  $(x, z)$  plane, the laser pulse has a time-varying intensity  $I(t) = I_0 \sin^2(t\pi/\tau)$  with  $I_0 = 2.0 \times 10^{20} \text{ W/cm}^2$  and  $\tau/2$  is the FWHM (500 fs,  $\lambda=1054 \text{ nm}$ ) and propagates along  $x$ . The laser pulse is Gaussian-shaped with best focus at the target surface with  $E_y, E_z \sim \exp(-z^2/w^2)$  with  $w = 6.8 \mu\text{m}$ . The targets ( $\text{C}^{6+}$  with 5% protons in number density) are of solid density  $N = 821$  ( $2.8 \text{ g/cm}^3$ ) with a step-function density profile at the beginning of the simulation. The cell size is  $\Delta x = 0.3\lambda_D^0$  (0.3 nm) and  $\Delta z = 1.7\lambda_D^0$ ; 500 electrons per cell are used ( $T_e = 18 \text{ keV}$  and  $T_i = 10 \text{ eV}$  for carbon ions and protons, initially). (Figure and caption adapted from Jung, *et. al.* [166])

990 fs, respectively, for these parameters). The energy transfer rate peaks at  $t_1$  ( $n'/\gamma \approx 1$ ) and then decreases towards  $t_2$  ( $n'/\gamma \ll 1$ ) so that the energy transfer seems to be connected to the 3D isospheric expansion of the plasma, transferring more energy the higher the electron density, i.e, coupling energy to more particles. The coefficient  $k_{\text{eff}}$  is hence given as

$$k_{\text{eff}} = \frac{1}{(t_2 - t_1)} \int_{t_1}^{t_2} k_V k_I dt, \quad (4.5)$$

where  $k_V = [(t_2 - t)/(t_2 - t_1)]^{1/3}$  connects the energy transfer rate with the 3D plasma expansion of the target between  $t_1$  and  $t_2$  with  $k_V(t_1) = 1$  and  $k_V(t_2) = 0$ . The factor  $k_I = \epsilon \sin^2(t\pi/\tau)$  accounts for the influence of the laser pulse intensity

#### 4. ION ACCELERATION DURING RELATIVISTIC TRANSPARENCY

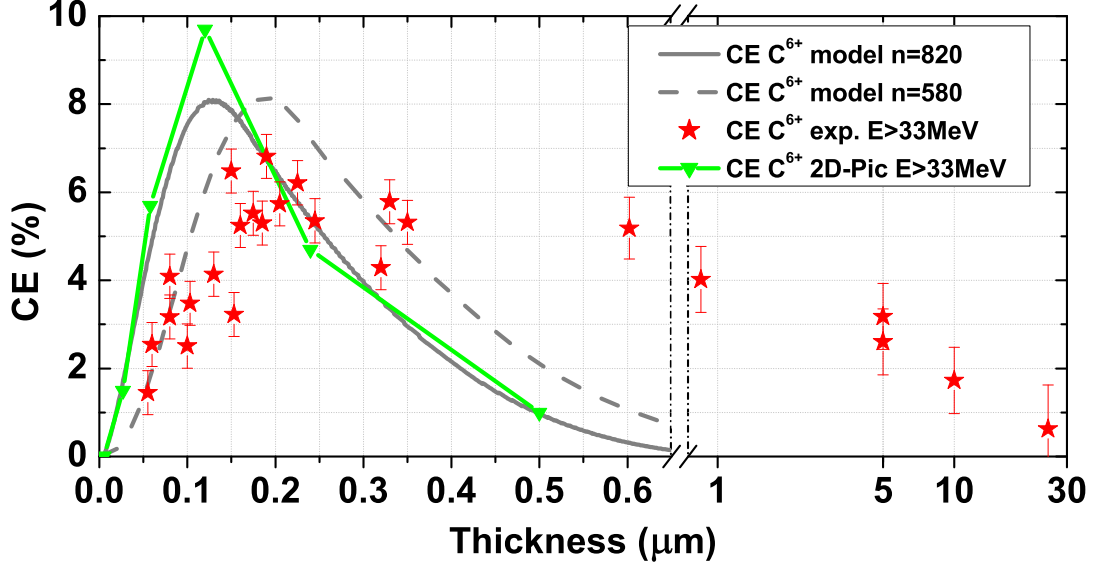


Figure 4.20: Thickness scaling of the CE as obtained from the experiment with ion energies greater than 33 MeV (red stars) in comparison with 2D-PIC simulation (green triangles with  $E > 33$  MeV) and the model using an initial normalized critical density of 820 (gray solid line) and 580 (gray dashed line) to account for expansion of the target under the laser pedestal. Note, that the model loses its applicability in the TNSA dominated regime ( $d > \sim 700$  nm for Trident parameters). (Figure and caption adapted from Jung, *et. al.* [166])

on the CE, i.e., optimum energy transfer occurs when  $\Delta t$  overlaps with the peak of the laser pulse;  $\epsilon = 0.5$  is the estimated absorption coefficient of laser energy into target electrons [107] that mediate the energy to the ions.

The CE has additionally been extracted from 2D-VPIC simulations for targets of 5 nm, 27 nm, 58 nm, 120 nm, 240 nm and 500 nm thickness (see caption of Fig. 4.19 for simulation parameters). Fig. 4.16 shows the CE (gray solid line) calculated by the model for the average Trident parameters with an initial density of  $n'_0 = 820$ . The model shows a CE scaling peaking at 8.1% at a thickness of  $\sim 120$  nm, which is in good agreement with the PIC results (green solid line with triangles for carbon  $C^{6+}$  with energies of  $> 33$  MeV). With a reduced initial target density of  $n'_0 = 580$  - to account for the pre-expansion before  $t_1$ , as discussed in the previous sections (see Fig. 4.6) - the peak shifts up to 200 nm, in good agreement with the experimental data. Accordingly, the optimum target thickness is slightly lower in the VPIC results, as the simulations do not accurately account for the pre-expansion of the target due to the slower than  $\sin^2$  rise of the real laser pulse. In

## 4.2. PROTON AND CARBON ION ACCELERATION

---

addition, the size of the simulation box was chosen to yield optimum resolution in the BOA regime, but was too small to accurately model acceleration in the TNSA-regime for thicker targets.

It should be noted that this simple heuristic model also closely reproduces the experimental data presented by Steinke, *et al.* [88], where a different set of laser and target parameters was used. The model furthermore implies that the CE can be optimized by reducing the rate of plasma expansion during its phase of relativistic transparency. This is in close relation to the results of Sect. 4.2.1; a reduced rate of density decrease will result in a later  $t_2$  and increase  $\Delta t$  - the overall duration of the acceleration - which eventually results in higher ion energies and CE.

### 4.2.6 Energy scaling

In the previous sections, thickness scalings and optimization methods for a given set of laser parameters, the Trident laser, have been discussed in detail. To complete this discussion and to give a full overview of the capabilities of the BOA acceleration mechanism, the energy scaling is now investigated, i.e., the dependency on the pulse duration and the laser energy. A predictive scaling is necessary in order to design optimized laser systems for applications and future research that have specific requirements in terms of ion energies (and efficiency). For TNSA, scalings have been proposed purely depending on the laser intensity (see Chap. 2.3.1), where  $E_{\max} \propto T_h \propto a_0 \propto \sqrt{I_L}$  [81, 82, 85]. However, these scalings are rather doubtful and do not agree very well with experimental data from different laser systems (Ti:Sapphire and Nd:Glass). For the RPA mechanism the scaling can be derived as  $E_{\max} \propto (\tau_L I_L)^2$  from the non-relativistic analytical theory (see Chap. 2.3.2), however no experiments in the valid regime (1D,  $I_L > 10^{22} \text{W/cm}^2$ ) are possible with current lasers.

In the BOA analytical model, the maximum energy depends on the response of the (non-relativistic) ions to the electrostatic field, i.e., to the characteristic electron energy  $\bar{E}_0$  and the duration  $\Delta t$  of the relativistic transparency of the target as

$$E_{\max} = (2\alpha + 1) q_i \bar{E}_0 \left( (1 + \omega_p(t_2 - t_1))^{\frac{1}{2\alpha+1}} - 1 \right), \quad (4.6)$$

which has been explained in detail in Chap. 2.3.3 and Ref. [108]. In Fig. 4.21 the maximum energy is plotted against the laser Energy  $E_L$  for typical pulse

## 4. ION ACCELERATION DURING RELATIVISTIC TRANSPARENCY

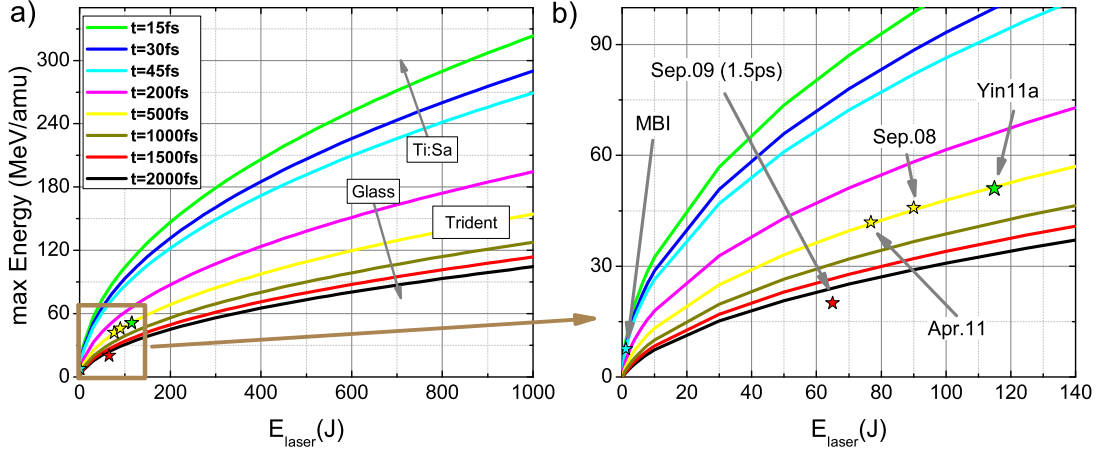


Figure 4.21: a) Pulse duration dependency of the BOA mechanism. Green, blue and light blue solid lines represent typical Ti:Sa pulse durations with 15 fs to 45 fs; the remaining lines correspond to Glass laser systems with pulse durations  $> 100$  fs. The yellow stars are experimental results from Trident, the green star marked with “Yin11” is the result of a 2D VPIC simulation with Trident parameters [106]. The red star is obtained at Trident with a pulse duration of 1.5 ps. The blue star represents experimental results obtained at the MBI in Berlin [87]. b) zoomed in view of the brown rectangle in a) showing laser energies accessible with Trident

durations of Ti:Sapphire lasers ( $\tau_\lambda = 15$  fs to 45 fs) and (mixed-)Glass laser systems ( $\tau_\lambda = 200$  fs to 2 ps). The yellow line with  $\tau_\lambda = 500$  fs corresponds to the Trident laser. Overlaid are data points from experiments at Trident with different laser energies (yellow stars) and longer pulse duration (red star, corresponding to the red solid line) and from the Max Born Institute (MBI) using a Ti:Sapphire laser at 45 fs (blue star, corresponding to the blue solid line). The data point marked as Yin11 in Fig. 4.21 b) (green star) is from a 2D VPIC simulation with Trident parameters as published in Ref. [106].

In order to derive the energy scaling for the BOA mechanism, a parametric study of the BOA analytical model is used, since  $\Delta t$  and  $\bar{E}_0$  in Eq. 4.6 have a rather complex dependency on the laser energy, spot size and pulse duration. Fig. 4.22 a) shows the result of this study. It has been found that  $E_{max}$  scales in good approximation as

$$E_{max} \propto I_L^{\frac{1}{2}} \tau_\lambda^{\frac{1}{3}} \propto a_0 \tau_\lambda^{\frac{1}{3}} \propto \sqrt{\frac{E_L [\text{J}]}{r_L [\text{cm}^2] \tau_L^{\frac{1}{3}} [\text{fs}]}} , \quad (4.7)$$

## 4.2. PROTON AND CARBON ION ACCELERATION

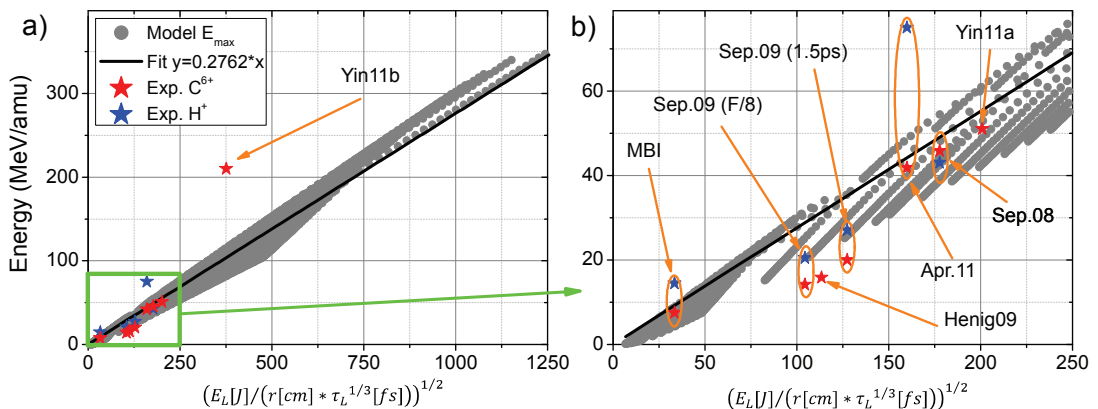


Figure 4.22: a) Parametric scan of the analytical BOA model (gray circles) plotted as maximum ion energy vs.  $\sqrt{E_L / (r_L \tau_L^{1/3})}$ . The black solid line is a linear fit of the parametric study with a slope of 0.2762. The red and blue stars are experimental results for carbon  $C^{6+}$  and proton maximum energies. The data point marked as “MBI” was obtained from measurements at the MBI in Berlin [87], “Henig09” at Trident with double plasma mirrors [30], the remaining points represent data from the six campaigns fielded at Trident (with optimal parameters or an F/8 OAP or a longer pulse duration of 1.5 ps). The points “Yin11a” and “Yin11b” represent simulation results with Trident laser parameters using a F/3 and a F/1 OAP, respectively. The latter represents a planned follow-up experiment at Trident to test the predictive capabilities of the model and the simulations. b) zoomed in view of the brown rectangle in a) showing parameters accessible with Trident

where  $r_L$  is the laser focus radius. The gray circles are maximum ion energies calculated for laser energies ranging from 0.2 mJ up to 1 kJ and pulse durations from 5 fs up to 2 ps with a constant focal radius of  $3.5 \mu\text{m}$ ; the data points are plotted vs.  $I_L^{1/2} \tau_L^{1/3}$ . The black solid line indicates a linear fit of the data, which gives for the maximum energies  $E_{\text{max}} \approx 0.2762 \sqrt{E_L / (r_L \tau_L^{1/3})}$ . Note, that the simulation points deviating from the fit have an  $a_0 \approx 1$  and are thus not fully in the BOA regime.

The scaling shows a much larger dependency on the laser energy than on the pulse duration, i.e., it is preferable to increase the laser energy rather than reducing the pulse duration. In this matter, the preferable laser system would be a mixed-Glass laser like the “Texas Petawatt” [167]; the mixed glass allows pulse durations of 150 fs (magenta line in Fig. 4.21), where the possibility of making large amplifiers enables hundreds of Joules in the beam as compared to

## 4. ION ACCELERATION DURING RELATIVISTIC TRANSPARENCY

---

Ti:Sapphire lasers. However, to optimize spectral shape as well and obtain truly monoenergetic ion beams, simulations indicate that shorter pulses in combination with a short rise time are required, advocating laser systems with both high energy and high bandwidth/short pulses.

For validation of the derived scaling, experimental data is added to the parametric study shown in Fig. 4.22 a); a zoomed-in view of the area of interest is shown in Fig. 4.22 b) with a description for each data point. The red stars mark carbon data and the blue stars proton data, where the rather poor agreement of the proton data with the model can be explained by the BOA-associated self-cleaning of the target (see Chap. 4.2.3). The data point marked as “MBI” has been measured at the Max Born Institute in Berlin, the remaining data points correspond to the Trident laser with varying laser parameters by using an F/8 OAP, double plasma mirrors or a longer pulse duration. Data points from the two different laser systems agree well with the analytical model in this parameter space.

The data point marked as “Yin11b” is a prediction of a VPIC simulation also presented in Ref. [106]. The data point represents a planned follow-up experiment on Trident to test the scaling and the predictive capabilities of the VPIC simulation with an F/1.5 and F1 OAP; the simulation is for Trident parameters using a F/1 OAP with  $r_L \approx 1.5$  instead of a F/3 OAP with  $r_L = 3.5$  for the point marked as “Yin11a”. The VPIC simulation predicts a factor of two higher maximum ion energies than the model. More experimental data, including results from experiments of other laser systems working in the BOA regime, will be necessary to verify or falsify the predictions of the analytical model and the VPIC simulation.

### 4.3 Optimizing BOA for maximum carbon and proton energies

In the previous section a comprehensive set of experimental data has been used in combination with VPIC simulations and the BOA analytical model, to investigate and optimize acceleration in the BOA regime. It has been found in Sect. 4.2.3 that self-cleaning of the target due to imperfect contrast is a likely cause for protons not being efficiently accelerated; they leave the target before the BOA acceleration

### 4.3. OPTIMIZING BOA FOR MAXIMUM CARBON AND PROTON ENERGIES

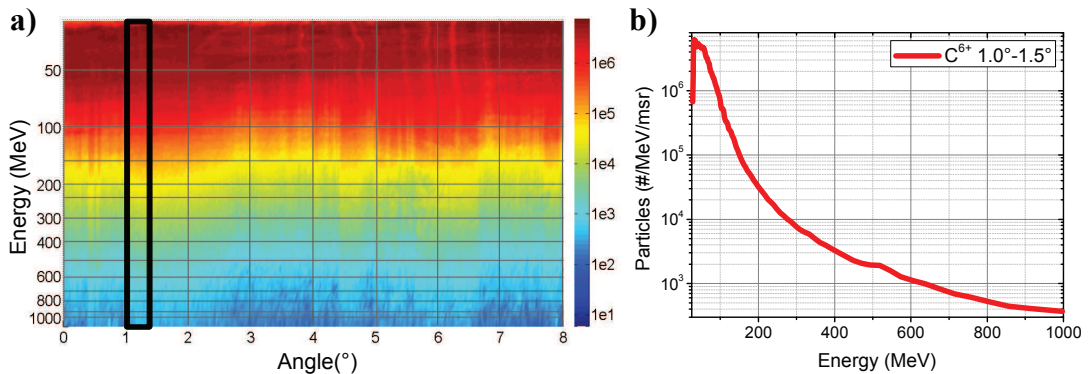


Figure 4.23: a) Angularly resolved carbon  $C^{6+}$  ions measured at Trident from a heated target measured with the iWASP. b) averaged spectrum between  $1^\circ$  and  $1.5^\circ$  with a cutoff energy exceeding 1 GeV.

starts, so that acceleration of carbon ions is enhanced. This understanding can be applied to optimize both carbon acceleration as well as proton acceleration.

For the case of boosting carbon acceleration, target heating has been employed to remove proton contamination from the target. This ensures that the laser interacts with an almost pure carbon target and that protons from surface hydrocarbon contaminations cannot interfere with the accelerated carbon beam. In the experiment, a green Coherent Verdi cw-laser [168] has been used to heat the target; the laser has a wavelength of 532 nm and has been focused to a  $\sim 100 \mu\text{m}$  spot overlapping the Trident laser focus. The carbon ion energies from the heated target exceeded 1 GeV, where the maximum ion energies without heating peak at 650 MeV (see Fig. 4.4). The carbon ions have been recorded with the iWASP; the angularly resolved spectrum as obtained from the CR39 is shown in Fig. 4.23 a); an averaged spectrum between  $1^\circ$  and  $1.5^\circ$  is shown in Fig. 4.23 b). Note, that a similar technique has been employed by Hegelich, *et al.* in the TNSA regime to successfully boost acceleration of ions with  $Z > 1$  [7].

In order to boost acceleration of protons, the bulk concentration of protons in the target needs to be increased to ensure that protons actually experience BOA acceleration as opposed to self-cleaned protons from the surface contamination layer. The highest proton content can be achieved with a pure (frozen) hydrogen target; however, such a target requires cryogenic setups and precise thickness control and currently does not exist in any lab in a deployable form. Instead, TPX foil targets produced by C. Hamilton have been used. TPX is the trade name for

#### 4. ION ACCELERATION DURING RELATIVISTIC TRANSPARENCY

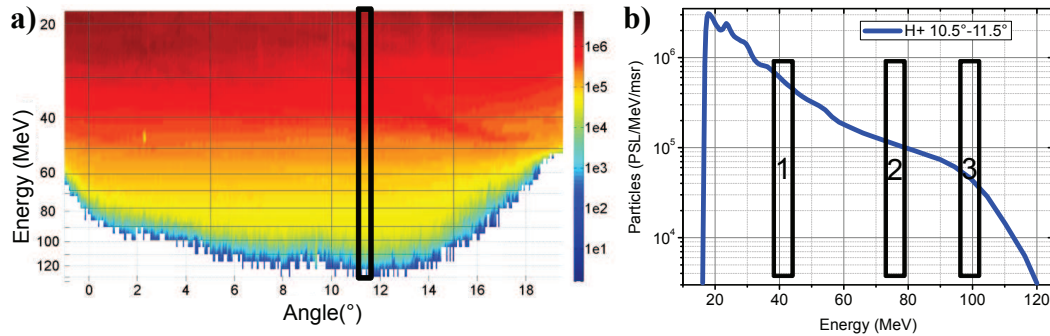


Figure 4.24: a) Angularly resolved proton spectrum measured at Trident from a CH<sup>2</sup> target measured with the iWASP (see text for details). b) averaged spectrum between 10.5° and 11.5° with a cutoff energy exceeding 100 MeV.

poly(4-methyl-1-pentene) and is also known as PMP [169]. This polymer mostly consists of CH<sub>2</sub> compounds and has hence a significantly increased natural proton bulk concentration; for diamond and DLC targets the bulk concentration is very low ( $\ll$  10% number density) and protons mostly originate from surface hydrocarbon contaminations. The TPX foil targets have a density of 0.8 g/cm<sup>3</sup> and thicknesses between 200 nm and 500 nm and  $\sim$  66% proton number density or 1/7 mass density.

Fig. 4.24 a) shows the angularly resolved energy spectrum for a 300 nm TPX foil target as measured on the IP in the iWASP. The right frame shows the averaged spectrum between 10.5° and 11.5° with a maximum energy of 120 MeV. This is almost a factor of two higher than maximum energies from DLC and diamond targets that peak at 75 MeV (see Fig. 4.8). The proton data that has been recored on IPs, has additionally been verified with a stack of CR39; (IPs are sensitive to a variety of ionizing radiation, including electrons and X-rays, so that the source of a measured signal on the IP always should be identified unambiguously.) The three black rectangles (1, 2 and 3) mark the energy ranges that the stack of three CR39s covered; the stack has 2.5 mm of copper on the front, followed by three layers each consisting of a 0.5 mm CR39 and a 3.3 mm tantalum plate. The front surface of the last CR39 layer (marked with a 3) thus measured protons with energies of about 100 MeV in a narrow window of  $\sim$  0.1 MeV; the narrow bandwidth of the last layer is a result of the strongly non-linear stopping power. A preliminary microscopic scan of this CR39 showed proton numbers on the order of 10<sup>6</sup> in this energy window.

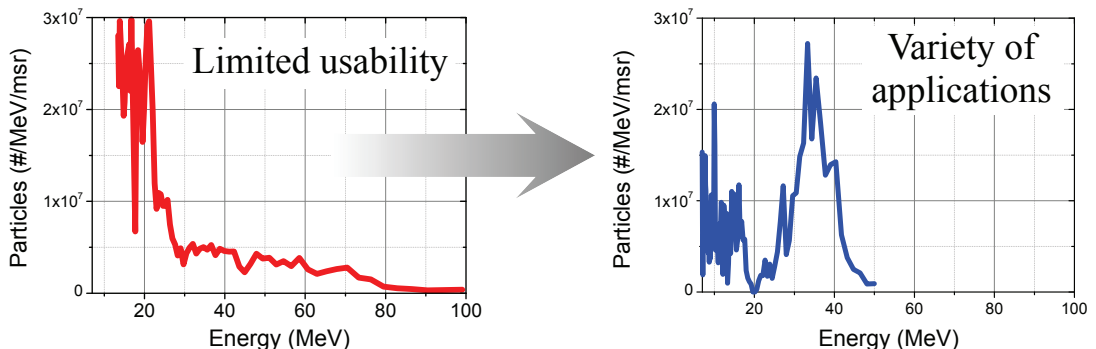


Figure 4.25: a) exponentially decaying (see Sect. 4.2 to Sect. 4.3 for details) and b) mono-energetic ion spectra obtained at Trident (see Sect. 4.4.1 for details), where the latter is preferred for most applications using proton/ion beams.

It should be noted that the results for these maximum carbon and proton energies are preliminary and more experimental data is needed in order to verify them. Additional VPIC simulations will be necessary to support the theory that the increase in the maximum particle energy is a result of the modified self-cleaning in the BOA regime.

## 4.4 Mono-energetic ion beams from BOA

All experiments presented in the previous sections were done with linearly polarized (LP) Trident laser pulses, and all of the measured ion spectra are exponentially decaying. The same in general applies for ions accelerated in the TNSA regime. Almost all applications, however, utilizing proton and ion beams, including oncology [165, 170], proton imaging [23] and inertial confinement fusion [47], demand mono-energetic particle beams with a low energy spread (illustrated in Fig. 4.25). While conventional rf-accelerators can generate mono-energetic ion beams with a very sharp energy bandwidth, laser-driven ion acceleration has so far failed in generating mono-energetic spectra with suitable high efficiencies. In the past, quasi-monoenergetic spectra have been observed by using longitudinally [26] or transversally limited double layer targets [27], but with a very low ion flux due to the largely reduced source size. In a different approach, the exponentially decaying spectrum is sent through an *ion chicane*, which blocks the unwanted energies and artificially generates a mono-energetic spectrum. Such a chicane has been designed and build in the framework of this thesis, and is cur-

## 4. ION ACCELERATION DURING RELATIVISTIC TRANSPARENCY

---

rently tested at the Max-Planck institute for Quantum Optics in Munich. The chicane, however, has a very low efficiency in selecting energies due to the used quadrupole lenses, which have a very limited acceptance angle, so that this approach is not useful for energies at the high energy tail of exponentially decaying spectra.

Simulations predict that ion acceleration in the radiation pressure acceleration (RPA) [10–13] regime promises to generate mono-energetic ion beams with extreme energies and high efficiency (see Chap. 2.3.2). In particular, in the laser piston regime the light pressure of a linearly polarized (LP) fs-laser pulse ( $I_L > 10^{23}$  W/cm<sup>2</sup>) accelerates an overcritical target ( $n'/\gamma > 1$ ) [14]; however, these laser intensities are not available at the moment and the requirement of a 1D interaction, i.e., a large laser focus, make an experimental implementation in the near future doubtful. At lower intensities RPA can be achieved with circularly polarized (CP) laser light (with pulse durations of a few 10 fs), where simulations predict that *for a single species target, the laser can drive the plasma as a single block to a mono-energetic ion spectrum; in a multi-species target, lighter ions with higher charge to mass ratio “snowplow” ahead of the heavier species [28, 103]. Experimental evidence of RPA has proven to be difficult; first experimental data indicating signatures of RPA has been reported by Henig et al. [32], however mono-energetic ion spectra have not been generated (excerpt from D. Jung et al.).*

In the following, experimental results obtained at Trident are presented using CP laser light (which is generated with a KDP quarter wave plate [114]). Due to the long pulse duration of  $\tau_\lambda > 500$  fs (FWHM), the interaction is quite different from the one described in the RPA mechanism. Although the ultra-high contrast of Trident (enabled by the OPAPE technique [115]) reduces the premature ionization, expansion of the target in the pedestal of the laser pulse ( $\sim 10^{-5}$  @ 5 ps, i.e.  $> 10^{15}$  W/cm<sup>2</sup>) still occurs. The target deforms under the long irradiation of the tightly focused laser leading to partially oblique laser incidence and increased  $\vec{j} \times \vec{B}$  heating of the plasma electrons. Given that the target is thin enough, it will still turn relativistically transparent in spite of the reduced heating associated with CP. In particular, the onset of the relativistic transparency has been observed in measurements at Trident for nm-thin targets of less than 100 nm regardless of the laser polarization [62, 63]. The measurements indicate that the transparency sets in during the early rise phase of the laser pulse (data

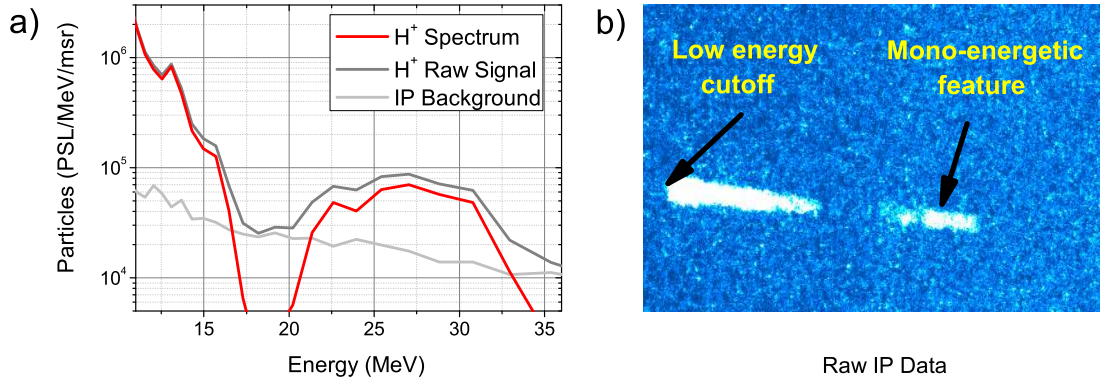


Figure 4.26: a) Mono-energetic spectrum measured at Trident with CP from a 42 nm DLC foil. The red solid line shows the raw signal (dark gray solid line) subtracted from the background (light gray solid line). The raw data measured with a TP is shown in b) with increasing energy from left to right.

not shown).

### Mono-energetic protons with CP

The discussion of the data obtained with CP laser light will start with the protons. (It should be noted, that all data and hence spectra for acceleration with CP have been acquired by TP-spectrometers.) Isolated mono-energetic proton spectra have been measured with CP laser pulses for target thicknesses of 5 nm to 42 nm. Fig 4.26 a) shows a typical mono-energetic spectrum obtained from a 42 nm DLC foil target. Fig 4.26 b) shows the corresponding raw data measured with a TP; the energy increases from left to right.

VPIC simulations for these thicknesses with CP and LP laser light for Trident parameters have shown mono-energetic features regardless of the laser polarization. In the experiment however, the same thicknesses resulted in exponentially decaying spectra with LP (some of the spectra have shown strong modulations with random monoenergetic features). The discrepancy of the VPIC code to the measured proton spectra from diamond or DLC targets can be attributed to the self-cleaning that typically occurs in the BOA and the inability to correctly model the laser contrast, as discussed in detail in the previous sections: protons experience different acceleration dynamics than the carbon ions for LP and most likely also in the CP case.

Although the target still turns relativistically transparent during the interaction with the CP laser, it is likely that the interaction includes a brief RPA-like phase

## 4. ION ACCELERATION DURING RELATIVISTIC TRANSPARENCY

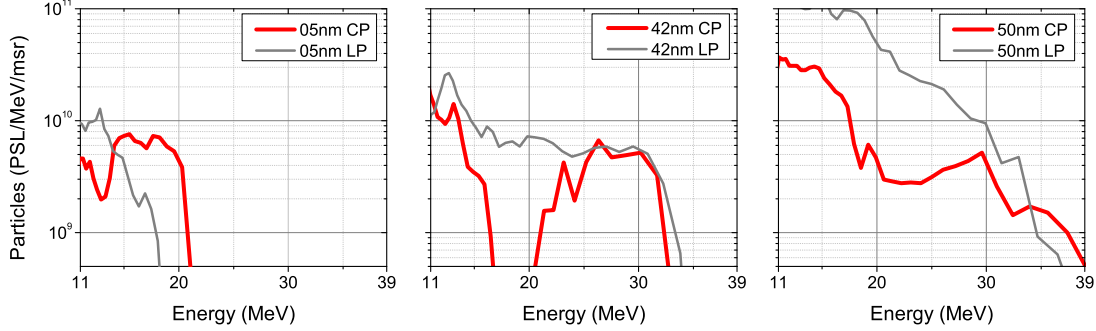


Figure 4.27: Mono-energetic spectra measured at Trident with CP (red solid line) and LP (gray solid line) from a) 5 nm, b) 42 nm and c) 50 nm DLC foil targets.

before the onset of the relativistic transparency. According to the description in Chap. 2.3.2, for RPA the normalized areal density  $\sigma = n'd/\lambda_L$  of the target has to be on the order of the normalized laser amplitude  $a_0$ . If this balance condition between the light pressure and the restoring electrostatic force of the ion background induced by the charge displacement is satisfied, a compressed layer of electrons may be formed and steadily be pushed by the radiation pressure. Protons within the electron layer might be synchronously accelerated and bunched, yielding a mono-energetic and quasi-neutral beam. In particular, the areal densities of the targets with thicknesses of 5 nm to 42 nm correspond to a  $\sigma$  ranging from 4 to 34 ( $n' = 820$ ,  $\lambda_L = 1054$  nm), which is on the order of the normalized laser amplitude  $a_0 \approx 12$  for Trident with CP (due to the factor of  $\sqrt{2}$  reduced laser electric field). Note, that expansion of the plasma will reduce the areal density accordingly.

Fig 4.27 shows proton spectra measured for 5 nm [ $\sigma = 4(2)$  with  $n'_0 = 820(410)$ ], 42 nm [ $\sigma = 34(17)$ ] and 50 nm [ $\sigma = 41(21)$ ]. The red solid lines show the spectra obtained with CP and the gray solid lines with LP. The 5 nm target, which is in the electron blow-out regime, i.e., electrons are eventually completely detached from the target, shows low proton energies with a monoenergetic spectrum. The 42 nm target, that has an areal density closest to the normalized laser amplitude, exhibits a strong mono-energetic feature peaking at 27 MeV with a bandwidth of  $\pm 15\%$ . The 50 nm target still has a modulated spectrum, but is mostly exponentially decaying as its counterpart with LP.

Whether the appearance of the mono-energetic proton beams with CP can be attributed to an RPA-like phase before the relativistic transparency of the target

or not is not conclusive at this point. Follow-up experiments are necessary in order to identify the interaction dynamics in more detail, so that PIC simulations can be run with the correct initial conditions of the target. It should further be noted that the particle numbers within the mono-energetic features are not exceeding the particle numbers obtained for LP in the same energy bandwidth; i.e., although the spectra are mono-energetic, no efficiency gain occurs compared to the LP case.

##### 4.4.1 BOA soliton acceleration<sup>1</sup>

While an unambiguous identification of the prevailing acceleration mechanism is not possible for the protons given the available data and simulations, a novel acceleration mechanism has been identified for the carbon ions in the BOA regime with CP laser light. In particular, high-resolution 2D VPIC simulations have been performed analyzing the carbon ion acceleration with laser and target parameters matching the experiment conditions closely. The results show that the acceleration is dominated by the generation of a carbon ion soliton before and its propagation within the target during its relativistic transparency, where the soliton like acceleration yields quasi-monoenergetic carbon spectra with a narrow energy spread.

In the experiments conducted at Trident, isolated monoenergetic  $C^{6+}$  spectra were observed for very thin targets of 5 nm to 10 nm thickness and CP laser light. Thicker targets ( $> 10$  nm) resulted in exponentially decaying spectra regardless of the laser polarization, which is in contrast to the protons, where monoenergetic spectra could be obtained for thickness up to  $\sim 40$  nm. LP light always resulted in exponentially decaying energy spectra.

Fig. 4.28 a) shows the  $C^{6+}$  spectra obtained from 5 nm thin DLC foil targets with CP (red triangles) and LP (green squares). In the LP case, the energy spectrum is exponentially decaying. In the CP case, a monoenergetic spectrum peaking at  $35 \pm 5$  MeV ( $2.9 \pm 0.4$  MeV/nucleon) with a narrow energy spread of  $\pm 15\%$  has been measured. In both cases the high energy cutoff is at about 50 MeV, where the particle numbers in the CP case are up to a factor of 2 higher in the monoenergetic feature as compared to the LP spectrum. (This has not been the case

---

<sup>1</sup>This section is in part a summary of Jung, *et al.* [34], which has been written by the author of this thesis.

## 4. ION ACCELERATION DURING RELATIVISTIC TRANSPARENCY

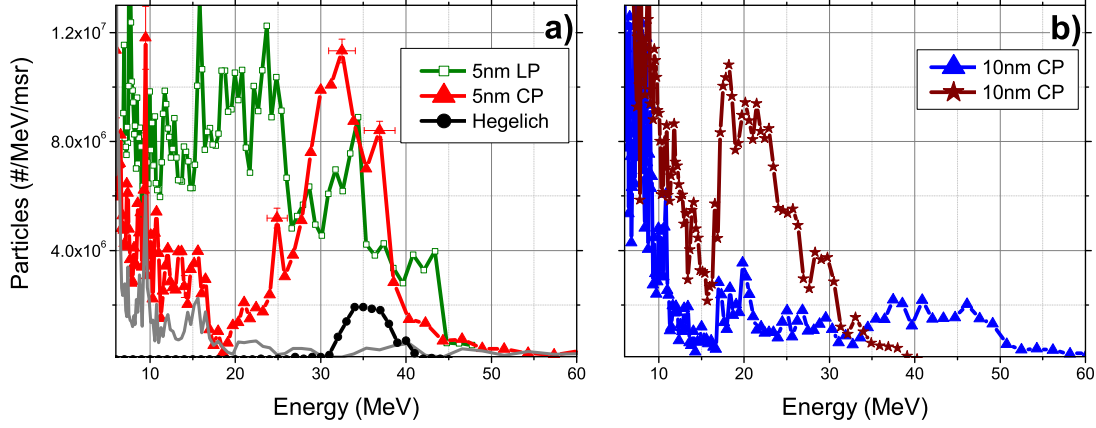


Figure 4.28: a) Carbon  $C^{6+}$  spectra measured with CP (spectrum with red triangles, signal noise with gray solid line) and LP (green squares) from a 5 nm DLC foil target and the carbon spectrum obtained from a  $10 \mu\text{m}$  Ti target as published in Hegelich et al. [26]; b) Carbon  $C^{6+}$  spectra measured with CP from two different shots on 10 nm DLC showing deterioration of the monoenergetic structure at increased target thickness as BOA-soliton conditions are not met anymore. (Figure and caption from Jung, *et al.* [34])

for the proton monoenergetic features.) Moreover, the conversion efficiency and the particle numbers within the mono-energetic feature are more than an order of magnitude higher than those obtained in the TNSA regime by using longitudinally limited double layer targets in Hegelich et al. [26] (black solid line with circles in Fig. 4.28). Fig. 4.28 b) shows  $C^{6+}$  spectra from shots on 10 nm foil targets and CP laser light, which still exhibit monoenergetic-like features; however, the bandwidth is increased so that the monoenergetic peak is broadened and less distinct (which will be explained in more detail in the next paragraph).

### BOA-soliton acceleration in the VPIC simulations

High-resolution 2D VPIC simulations have been performed analyzing the carbon ion acceleration with laser and target parameters matching the experiment conditions closely. *The 2D simulation domain is  $20 \times 25 \mu\text{m}$  in the  $(x, z)$  plane, where the laser pulse propagates along  $x$  and has time-varying intensity  $I(t) = I_0 \sin^2(t\pi/\tau)$  with  $I_0 = 2.0 \times 10^{20} \text{ W/cm}^2$  and  $\tau/2$  is the FWHM (500 fs,  $\lambda = 1054 \text{ nm}$ ). A Gaussian-shaped pulse in  $z$  is used with best focus at the target surface, where  $E_y, E_z \sim \exp(-z^2/w^2)$  with  $w = 6.8 \mu\text{m}$ . The targets ( $C^{6+}$  with 5% protons in number density) are of solid density  $n'_0 = 821$  ( $2.8 \text{ g/cm}^3$ ) with thickness of 5 nm*

#### 4.4. MONO-ENERGETIC ION BEAMS FROM BOA

and a step-function profile at the beginning of the simulation. The cell size is  $\Delta x = 0.3\lambda_D^0$  (0.3 nm) and  $\Delta z = 1.7\lambda_D^0$  ( $\lambda_D^0 = \omega_p^{-1}\sqrt{T_e/m_e}$  is the initial electron Debye length); 500 electrons per cell are used ( $T_e = 18$  keV and  $T_i = 10$  eV for carbon ions and protons) (excerpt from D. Jung *et al.* [34]). Fig. 4.29 a) shows the carbon energy spectra for CP (solid curves) and LP (dashed curves) laser pulses obtained from the simulation along a  $1\ \mu\text{m}$  average over  $z$  centered at  $z = 0$ . In the LP case the simulation results in a broad (exponential) spectrum. In the CP case the spectrum has a quasi-monoenergetic peak at 50 MeV, which is a slightly higher energy than observed in the experiment (see Fig 4.28). The energy spread of  $\pm 10\%$  is in good agreement with the bandwidth of  $\pm 15\%$  measured in the experiment for the same target thickness and laser parameters. In particular, in the experiment, the spectrum is measured  $x = 120$  cm behind the target; the carbon  $\text{C}^{6+}$  beam can hence expand from self-Coulomb forces. This is not modeled in the VPIC simulation, which is stopped shortly after  $t_2$  and gives energies at  $x = 2 \times 10^{-3}$  cm.

A detailed analysis of the 2D-VPIC simulation for the CP case reveals ion-acceleration based on the generation of a carbon ion soliton before and its stable propagation and energy gain during the relativistic transparency of the target. The time before the relativistic transparency of the target is a highly transient RPA phase. In the simulation, the ponderomotive force of the CP laser pushes a fraction of the electrons forward which in turn creates a charge separation field that pushes the carbon ions from the surface of the target forward. This leads to a compression of the target, i.e., to a density spike in the carbon distribution at the front of the target, as shown in Fig. 4.29 b) at 204 fs. This compression is similar to the processes described by the RPA mechanism [12, 171]), where all electrons are pushed forward by the ponderomotive force of the laser accelerating all ions as a single plasma bunch. During the compression of the target front, the nm-thin target is also deformed leading to oblique laser incidence and heating of the electrons at the front surface of the target via relativistic  $\vec{J} \times \vec{B}$ -heating. In the time before the target turns relativistically transparent ( $t = 204$  fs with  $n'/\gamma \sim 1$ ), the ion energies reach  $\sim 6$  MeV. This is only a small fraction of their final energy and most of the acceleration happens during the relativistic transparency as it does in the BOA acceleration with LP laser light.

It should be noted, that the thickness of the 5 nm target is comparable to the initial (classical) skin depth  $\delta_e = c/\omega_p \approx 5.6$  nm (with  $\omega_p$  the plasma frequency

#### 4. ION ACCELERATION DURING RELATIVISTIC TRANSPARENCY

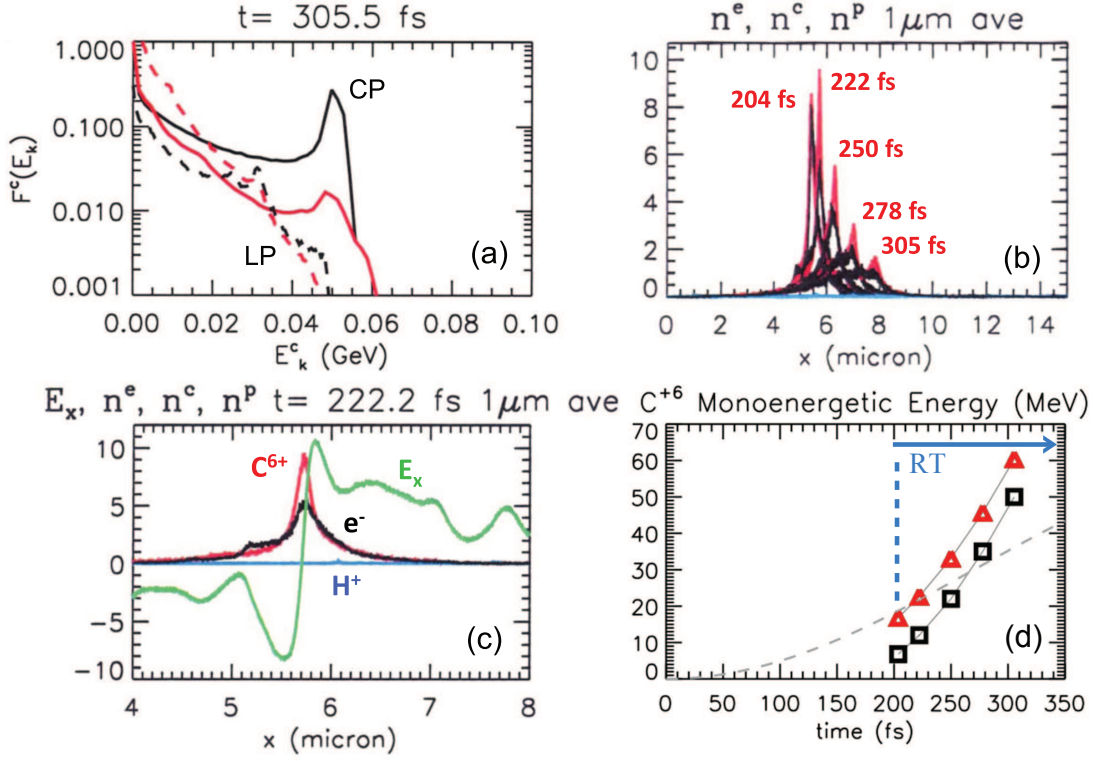


Figure 4.29: Results from a 2D simulation: (a) carbon  $C^{6+}$  spectra at 305 fs (end of the acceleration phase) for CP (solid) and LP (dashed) laser obtained along a 1-micrometer average over  $z$  centered at  $z = 0$  (black) and from the whole simulation domain (red); (b) time evolution of carbon ion (red curves) and electron density (black), both normalized to  $n_{cr}$ , during the transparency phase (the blue trace is the proton density); (c) bipolar electric field structure in  $E_x$  (green) co-moving with the solitary carbon density spike (red); (d) monoenergetic ion energy (black squares) obtained from ion spectrum vs. time during the acceleration phase as compared with the soliton “energy”  $\frac{1}{2}m_i v_p^2$  (red triangles) estimated from the soliton speed  $v_p$  (the laser intensity profile is indicated in arbitrary units as gray dashed line). (Figure and caption from Jung, *et al.* [34])

as in Eq. 2.21). However, taking the relativistic skin depth  $\delta_e = \sqrt{\gamma}\delta_{e0}$  and the 1D-like expansion prior to  $t_1$  into account, one gets

$$\frac{L}{\delta_e} = \frac{L_0 F}{\delta_{e0} \sqrt{F} \gamma} = \frac{L_0}{\delta_{e0}} \sqrt{\frac{F}{\gamma}}, \quad (4.8)$$

where simulations have shown that the expansion of the initial target thickness  $L_0$  by the factor  $F$  offsets the increase in  $\gamma$  [35]. Hence, the target is optically thick to the laser in the RPA-like phase before  $t_1$ .

#### 4.4. MONO-ENERGETIC ION BEAMS FROM BOA

---

When the target has turned relativistically transparent, an epoch of dramatic ion acceleration occurs, where the ions gain approximately 90% of their final energy, as shown by the black squares in Fig. 4.29 d), which indicate the ion energy at the different time steps. Associated with stark increase in ion energy during the phase of transparency is a sharp and persistent ion density spike that propagates and accelerates through the target in  $x$  as shown in Fig. 4.29 b). This carbon density spike, as displayed in Fig. 4.29 b) and c) (red solid line), co-moves with the electric field in  $E_x$  (green curve). The electrons are insufficiently mobile in  $x$  due to the intense laser field that is penetrating the relativistically transparent target, and cannot short out the electric field. Their charge (black curve) and current densities vary smoothly across the ion density spike, i.e., the soliton-like structure. The dominant epoch of ion energy gain goes from the onset of the relativistic transparency at  $t_1 = 204$  fs, but unlike in the LP case, where the acceleration lasts until  $t_2$ , it only continues until  $t = 305$  fs, when the ion soliton reaches the back of the expanding target.

It should be noted that simultaneous, non-optimized RPA-like dynamics may also be present, but not as the dominant acceleration mechanism, as it is most likely for the protons prior to  $t_1$ . This is justified by the fact, that 90% of the ion energy gain in simulations occurs after  $t_1$ , not before, which contradicts RPA dynamics, where the efficiency would decrease significantly with the onset of the relativistic transparency of the target. In addition, as pointed out before, protons are not affected by this acceleration mechanism, due to the self-cleaning of the target in the intense laser field.

Although protons show monoenergetic spectra, too, the measured proton energies are about an order of magnitude higher (20 MeV to 40 MeV, see Fig. 4.27) than the carbon energies per nucleon. This is also in stark contrast to ion acceleration in a RPA-dominated regime, where all ions should gain approximately the same velocities, including the theory for RPA of double species targets proposed by Qiao et al. [103], where the carbon ions suffer from rapid Coulomb explosion induced by the protons that are “snowplowed” ahead (i.e., the fastest carbon ions still have the same velocity as the slowest protons in the monoenergetic feature). In order to analytically describe the nonlinear structures observed in the simulation, a generalization of the Akhiezer-Polovin (AK) problem [172, 173] can be used, which describes the nonlinear propagation of an intense electromagnetic wave in cold plasma. Here, the AK theory has been extended by B. Albright in

#### 4. ION ACCELERATION DURING RELATIVISTIC TRANSPARENCY

---

Jung, *et al.* [34] and Yin, *et al.* [35] to include ion as well as electron dynamics. Considering a soliton that propagates (self-similarly) at a speed  $v_s$  in  $x$ , one can use a two-fluid relativistic description of the ions and electrons (i.e., the ion Eulerian momentum equations, neglecting pressure) and Maxwell's equations to obtain the longitudinal momentum equation in terms of the local charge density as

$$\frac{d}{d\tau} \left[ \left( 1 - \frac{v_{ix}}{v_s} \right) \frac{dp_{ix}}{d\tau} \right] = -4\pi Z_i e^2 v_s (Z_i n_i - n_e), \quad (4.9)$$

where  $\tau = t - x/v_p$  is the similarity variable and  $Z_i$  the ion core charge;  $n_i$  and  $n_e$  indicate the ion and electron densities and  $v_{ix}$  and  $p_{ix}$  the velocity and momentum of the ions along  $x$ . Here, the local charge density  $Z_i n_i$  follows

$$Z_i n_i - n_e = n_e \left( \frac{v_s - v_{ex}}{v_s - v_{ix}} \right), \quad (4.10)$$

where  $v_{ex}$  is the electron speed in  $x$ . The denominator in the last equation shows that a stable, localized ion density spike requires the ion speed  $v_{ix}$  to be slightly less than the soliton speed  $v_s$ . This is displayed in Fig. 4.29 d), where the monoenergetic ion energy (black squares) obtained from the ion spectrum in the simulation is slightly less than the soliton “energy”  $1/2 m_i v_s^2$  (red triangles).

It should further be noted, that the propagation of the ion soliton during the relativistic transparency of the target, as depicted in Fig. 4.29 b), requires an intense laser field across the soliton. Without an intense laser field, the electrons short out the bipolar field  $E_x$  preventing the propagation of the soliton; in the simulations the density spike forms before  $t_1$  but does not propagate. In this regard, the BOA-soliton mechanism is fundamentally different from the laser-driven ion-acoustic solitons by Zhidkov, *et al.* [174].

In order to increase the energies of the ion soliton, it is necessary to understand where the free energy accelerating particles in the soliton originates. *The soliton ion density spike gives rise to a longitudinal electric field, which changes the electron parallel momentum  $p_z$  across the soliton. The relatively slowly varying change in  $p_z$  leads to a corresponding change in laser index of refraction in the vicinity of the soliton. This variation reflects some of the laser light from the soliton, leading to an enhancement of the electrostatic field further accelerating the ions and sharpening the ion density spike. The rate of energy coupling within the soliton can be increased by having a larger initial ion density spike (i.e., larger*

#### 4.4. MONO-ENERGETIC ION BEAMS FROM BOA

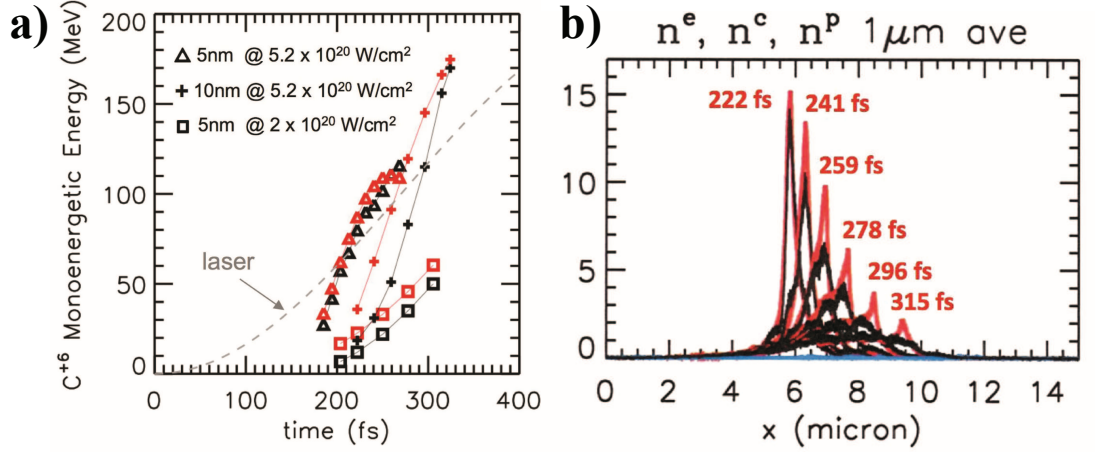


Figure 4.30: a) Results from 2D simulations for the BOA-soliton acceleration at higher laser intensities: using a 5 nm and 10 nm-thick carbon target at  $n'_0 = 821$  and a  $\sin^2$  square CP laser with peak intensity  $5.2 \times 10^{20} \text{ W/cm}^2$  (triangles and crosses), in comparison with a 5 nm thick carbon target at peak intensity  $2 \times 10^{20} \text{ W/cm}^2$  representing Trident parameters (squares). The soliton “energies” ( $1/2m_i v_s^2$ ) are red and the ion energies black. b) Temporal evolution of the ion density spike for the 10 nm case with  $5.2 \times 10^{20} \text{ W/cm}^2$  with the carbon density (red) and electron density (black). (Figure from Ref. [35])

variation in electron  $\gamma$  across the soliton and thus larger change in index of refraction) or by having a larger laser amplitude, so that the rate of laser light momentum transfer into the soliton is larger (excerpt from D. Jung *et al.* [34]). The effect of the laser intensity has been investigated in more detail in [35] (see Fig. 4.30). The study has shown that the Trident laser intensity of  $I_0 = 2 \times 10^{20} \text{ W/cm}^2$  (squares) is barely intense enough to generate the necessary density spike in the ion distribution. This results in a less sharp monoenergetic ion beam, which can be seen in the experimental data for the 10 nm target cases in Fig. 4.28 (b), which show largely deteriorated monoenergetic ion features. On the other side, the study revealed monoenergetic carbon ions peaking at 170 MeV for a 10 nm target and an intensity of  $I_0 = 5.2 \times 10^{20} \text{ W/cm}^2$  indicating a very favorable energy scaling. This is displayed in Fig. 4.30 (crosses), where the ion density spike is much more pronounced as shown in Fig. 4.30 b).

The BOA-soliton acceleration with CP laser light is a promising regime for the efficient generation of mono-energetic ion beams. This mechanism, that is experimentally accessible with current lasers, shows that laser-driven ion beams are on

#### 4. ION ACCELERATION DURING RELATIVISTIC TRANSPARENCY

---

the verge of being competitive with conventional rf-accelerators, i.e., ion energies are sufficiently high for ion injectors and medical applications such as hadron therapy of skin or eye tumors. In future experiments increased laser intensity and optimized temporal and spatial pulse profile could be used to even further increase the ion energies.

#### 4.4. MONO-ENERGETIC ION BEAMS FROM BOA

---

# Chapter 5

## Summary and perspectives

Laser-ion acceleration has been of particular interest over the last decade and drawn a lot of attention in fundamental as well as applied sciences [6–8]. In the past, remarkable progress has been made in researching an competitive, cheap and compact alternative to conventional rf-accelerators with laser-driven particle acceleration [78, 175, 176]. Proton and heavy ion ( $Z > 1$ ) beams have been produced with particle energies of up to 67 MeV [6, 18] and  $< 10$  MeV/amu [7, 20, 21, 92]. The majority of the research and experiments have been done in the Target Normal Sheath Acceleration (TNSA) [15–17] regime using comparatively thick targets in the (tenth of)  $\mu\text{m}$  range.

In the framework of this thesis nm-scaled diamond targets have been employed to demonstrate and research ion acceleration in the BOA regime. In the experiments conducted and presented in this thesis, proton energies have been doubled to approximately 120 MeV and carbon energies have been increased by one order of magnitude to more than 1 GeV (85 MeV/amu). The conversion efficiency of laser light into the carbon ions has been found to exceed 5%, which is in stark contrast to TNSA, where acceleration of heavier ions is suppressed as the low inertia protons with their high charge to mass ratio are accelerated first and subsequently shield the accelerating field.

Most of the prospective applications for laser-driven ion beams, such as oncology [22], proton imaging [23] and ion fast ignition [24, 25] require quasi-monoenergetic beams with a low energy spread. In the TNSA regime, quasi-monoenergetic spectra have been generated by using in-situ engineered targets, but with a very low ion flux [26, 27]. The difficult control over the spectral shape of the accelerated particles and the low energies and conversion efficien-

cies, especially for heavier ions, make the TNSA mechanism unattractive to most applications. In the framework of this thesis, a new acceleration mechanism has been found that generates monoenergetic ion spectra with an almost two orders of magnitude higher flux and hence conversion efficiency. This BOA-soliton mechanism is a promising candidate for generating monoenergetic particle beams that can be used in advanced applications and making laser-driven ion sources a cheap, compact and competitive alternative to conventional rf-accelerators.

### 5.1 Summary and conclusions

The Break-Out afterburner acceleration that has been identified in simulations by B. Albright and L. Yin [28, 29, 104] shows promising features in terms of ion energies, conversion efficiency and scaling. In contrast to the TNSA, ions are here accelerated during the relativistic transparency of the target ( $n' > 1 \gg n'/\gamma$ ). In the simulations, the laser starts to ionize the surface of the initially opaque target and successively heats more and more electrons to relativistic energies. Provided, the target is thin enough and has not blown apart under the irradiation of the laser pedestal, the laser will eventually promote all electrons within the focal volume to hot electrons and turn the target relativistically transparent. At this time, which is referred to as  $t_1$ , strong acceleration of the plasma ions over the whole volume occurs, where the accelerating electric field co-moves with the ions and the laser continuously replenishes the energy, the electrons transferred to the ions. The acceleration ceases, when the plasma turns classically underdense ( $n' \leq 1$ ). Due to the volumetric acceleration of the particles, this scheme has the potential for much higher conversion efficiencies and the fact that not only protons but virtually any ion species is accelerated, offers a great advantage for many of the envisioned applications.

However, in order to enter the BOA regime with the laser systems available to today (100 TW to a PW) targets from 5-500 nm are necessary; with thicker targets the relativistic transparency will not be reached and acceleration will be dominated by the TNSA mechanism. The use of ultra-thin nm-scaled targets also demands ultra-high laser contrast, so that premature expansion does not destroy the target prior to arrival of the peak pulse. LANL's Trident laser, which has a power slightly above 100 TW (80 J in 550 ps FWHM) and a focused peak

## 5. SUMMARY AND PERSPECTIVES

---

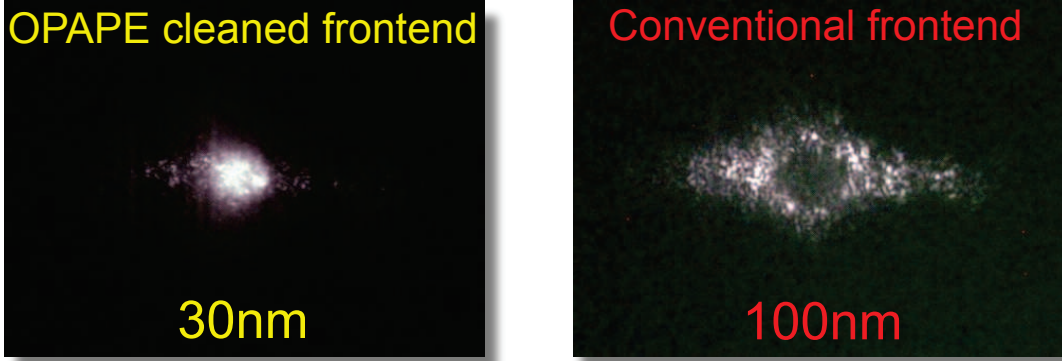


Figure 5.1:  $3\omega$  backscatter from a 30 nm target with the OPAPE cleaned frontend (left frame) and from a 100 nm target with the old low contrast frontend. With the OPAPE cleaning the contrast is good enough, so that the main pulse still interacts with a overcritical target generating third harmonic radiation over the whole focal spot, which is measured in the backscatter diagnostic

intensity of  $\sim 5 \times 10^{20} \text{ W/cm}^2$  ( $a_0 \approx 17$ ), has recently been upgraded with the OPAPE cleaning technique and has a feasible laser contrast of approximately  $10^7$  at  $-5 \text{ ps}$  [115]. In the framework of this thesis, a lab for the production and characterization of nm-scaled (3 nm up to 60 nm) and free-standing diamond-like carbon foils has been setup at the Meier-Leibnitz Laboratory at the LMU Munich. First experiments conducted at Trident in 2008 have shown that the laser contrast is high enough to ensure interaction of the main pulse with an overcritical target for thicknesses as thin as 3 nm (see Fig. 5.1).

In 5 consecutive experiments fielded at Trident in the framework of this thesis, a comprehensive set of data for the BOA dominated laser-driven particle acceleration has been collected, studied and also been compared with the TNSA regime. In the experiments targets with thicknesses from 3 nm up to  $25 \mu\text{m}$  have been used, where targets thicker than 30 nm have later been supplemented by commercially available CVD diamond foils [141]. A high resolution and high dispersion Thomson parabola (TP) spectrometer [150] and a high resolution ion wide angle spectrometer (iWASP) [157] have been designed and build in the framework of this thesis to measure the particle beam parameters with high accuracy in terms of their maximum energy, charge distribution and their angular structure. The optimum target thickness for acceleration in the BOA regime at Trident parameters has been experimentally measured to be between 100 nm and 250 nm depending on the the actual pulse contrast and on-target intensity. In the

## 5.1. SUMMARY AND CONCLUSIONS

---

high resolution V-PIC simulations [105] that use a perfect  $\sin^2$  temporal envelope, i.e., neglecting any contrast effects, the optimum thickness has been found to be between 60 nm and 100 nm. The results agree well with parametric studies of the analytical model for BOA based on the  $t_1/t_2$  dynamics, where

$$d_{\text{opt}}[\text{nm}] \approx 9.84 \times 10^5 \frac{1}{n'_0} I_L^{\frac{13}{24}} \left[ \frac{\text{W}}{\text{cm}^2} \right] \tau_\lambda[\text{fs}] \propto \frac{a_0 \tau_\lambda}{n'_0}. \quad (5.1)$$

For targets thinner than the optimum thickness, the plasma turns relativistically transparent well before the peak of the laser pulse and consequently turns classically underdense early in the interaction, stopping the acceleration. For targets around the optimum thickness, the acceleration window between  $t_1$  and  $t_2$  optimally overlaps with the peak intensity of the laser pulse.

Here, maximum carbon  $\text{C}^{6+}$  energies of 650 MeV and 1 GeV have been measured for unheated and heated targets, respectively, where in the latter case the removal of the hydro-carbon contaminants boosts the acceleration of the carbon ions. These energies are 1-2 orders of magnitude above ion energies measured for TNSA dominated acceleration from micron thick targets. For the optimum target thickness, protons have been measured with maximum energies of 75 MeV, slightly above the top energies achieved with TNSA. It has been found in simulations that the acceleration of protons in the BOA regime suffers from their low inertia and their high to charge mass ratio: the protons are subject to self cleaning before the main acceleration occurs. Protons are here evacuated from the target during the interaction of the pedestal and rising edge of the laser with the plasma so that they typically do not experience the same BOA dynamics as the much heavier carbon ions do. The effect is furthermore enhanced by the fact that the natural proton bulk concentration of DLC and diamond is very low ( $> 10\%$ ) and most protons are contained in the surface contamination layer. For this reason,  $\text{CH}_2$  targets have been employed that have a much higher proton bulk concentration. With these targets proton energies exceeding 100 MeV have been measured, which is an increase of a factor of two over TNSA results and marks a big step towards use of these beams in advanced applications.

The use of the iWASP enabled unprecedented and novel measurements of angularly resolved energy spectra for carbon  $\text{C}^{6+}$  ions and protons, simultaneously. The much higher solid angle captured by this spectrometer ( $\sim 0.1$  msr) in com-

## 5. SUMMARY AND PERSPECTIVES

---

parison with conventional TPs ( $10^{-4}$  msr to  $10^{-5}$ msr) also allowed to investigate the thickness dependency of particle numbers, average energy and the conversion efficiency (CE) with significantly improved accuracy. Measurements of the particle beam perpendicular and parallel to the laser polarization indicate an azimuthal symmetry of the beam and simplify calculations of the absolute number of accelerated particles and hence the CE. In particular, the beam consists of an outer more intense ring and a slightly less intense center on the laser axis. This beam structure is most distinct for the optimum target thickness and turns into a Gaussian distribution for thicker targets, where the TNSA mechanism is dominant, with peak energies and particle numbers on the laser axis. The ring structure of the beam is a result of the ponderomotive force that volumetrically pushes the electrons of the relativistically transparent plasma out of the focus. In simulations, the symmetry is broken for the highest ion energies, where the low number of particles is insufficient to generate a strong enough electrostatic background to break down the actual azimuthal asymmetry of the ponderomotive force [164].

The measured thickness dependency of the number of accelerated particles and the CE follows the thickness dependency of the maximum energy. At the optimum thickness of 200 nm within the Break-Out Afterburner, the average particle energy is 65 MeV with roughly  $5 \times 10^{11}$  carbon  $C^{6+}$  particles in a cone with  $22.5^\circ$  opening angle. The CE of the  $C^{6+}$  ions reaches up to 7% and steadily decrease far below 1% for targets of several micrometer thickness. The number of accelerated particles increases by up to a factor of 10 at the optimum, while the average particle energy only increases a factor of 1.3. In contrast to TNSA, where particles are accelerated from a thin (several nm) surface of the target, BOA accelerates particles from the whole focal volume, where the plasma has turned relativistically transparent, causing the tremendous increase in the CE. The increase in maximum particle energies of 1-2 orders of magnitude for the carbon ions only marginally contributes to the overall CE, since their numbers are several orders of magnitude lower. The measurements for the protons are only relative, due to the missing absolute calibration for image plates (IP). The dependencies for the protons are very similar to the carbon ions, with the exception that the increase in accelerated particles and hence the CE is less ( $\times 5$ ) due to the intrinsic low bulk concentration and the still comparably efficient acceleration at thicker targets in the TNSA regime.

## 5.1. SUMMARY AND CONCLUSIONS

---

All these experiments have been done with linearly polarized laser light and resulted mostly in exponentially decaying energy spectra. For the production of monoenergetic ions the effect of circular polarization (CP) on the acceleration has been studied in more detail in the framework of this thesis. Ion acceleration with CP by the radiation pressure acceleration (RPA) [10–13] has recently drawn a lot of attention, as it promises to generate narrow monoenergetic ion beams. Here, the light pressure of the laser drives an overcritical ( $n'/\gamma^e > 1$ ) nm-scaled target, where the CP laser reduces the electron heating due to the missing oscillating secular term in the ponderomotive force. Thus, the target expansion is greatly reduced; the electrons that are pushed into and compressed within the target by the laser light, ideally accelerate it as a single block of plasma to a monoenergetic ion spectrum, where all ions gain the same final velocity. In the case of a multi-species target, it is however more likely that lighter ions with higher charge to mass ratio “snowplow” ahead of the heavier species [28, 103]. The experimental realization of RPA has proven to be difficult due to the requirement of a 1D interaction geometry (i.e., no strong target expansion or denting that would give rise to increased electron heating). First experimental data indicating signatures of RPA has been reported by Henig et al. [32], however monoenergetic ion spectra have not been generated.

For long pulse durations ( $\tau_\lambda > 100$  fs) it is unlikely to realize RPA with CP laser light. The imperfect laser contrast and the long pulse duration will result in strong electron heating during the interaction and cease a RPA dominated acceleration. Especially at Trident, although it offers an unprecedented laser contrast due to the OPAPÉ cleaning technique, the long pulse duration of 500 fs (FWHM) and its shoulders of  $\sim 10^{-6}$  @ 5 ps (i.e.  $> 10^{15}$  W/cm<sup>2</sup>) lead to pre-expansion and denting of the target (resulting in oblique laser incidence) and a qualitative difference in the interaction compared with a pure RPA dominated interaction. Even with the use of CP laser light, the onset of relativistic transparency has been observed experimentally for the Trident Laser and nm-thick targets ( $< 100$  nm) regardless [63], where the relativistic transparency sets in early in the rising edge of the pulse. Still, experiments conducted at Trident in the framework of this thesis with CP light have shown monoenergetic carbon C<sup>6+</sup> and proton spectra with energy spreads as low as  $\pm 15\%$ . The central energy of the monoenergetic feature ranges between 20 MeV and 35 MeV for both carbon ions and protons, i.e. their velocities differ by a factor of  $\sim 3.5$  as opposed to the prediction for

## 5. SUMMARY AND PERSPECTIVES

---

RPA. For the carbon ions the CE of laser light into particles of the monoenergetic feature is 1-2 order magnitude higher than obtained previously in the TNSA regime [26], but is with approximately 0.1% still very low. From high resolution 2D-VPIC simulations (done by L. Yin and B. Albright) it has been found that the acceleration of the carbon ions is based on the production of a carbon ion soliton before and its stable propagation during the relativistic transparency of the target [35]. Here, the ponderomotive force of the CP laser compresses the target in a transient RPA phase, similar to that described in previous studies of the RPA mechanism [12, 171] and a pronounced carbon ion density spike forms. In this stage, the target is subject to distortion and strong electron heating at the front surface of the target, where  $\gamma_e$  increases due to the transverse variation of the laser intensity. While the ion energy gain is modest prior to transparency, dramatic ion acceleration occurs during the relativistic transparency of the target. The simulations show a persistent, sharp ion density structure that propagates and accelerates forward into the target accompanied by a bipolar electric field structure that co-moves with this spike. The electrons are insufficiently mobile to short out the bipolar field by virtue of their orbits in the intense laser field. The nonlinear structures observed indeed appear to be ion solitons. In fact, the properties of this nonlinear structure can be obtained from a generalization of the Akhiezer-Polovin (AK) problem [172, 173] including ion as well as electron dynamics [35].

### 5.2 Outlook and perspectives

The results presented in this thesis are an important basis for future research of laser-driven ion-acceleration and will potentially enable laser-based implementation of advanced applications such as IFI or cancer therapy. In order to use these laser-accelerated ion beams for any of the envisioned applications there are still many problems that have to be investigated and solved. For most of the applications the CE and particle energies are still too low and almost all prospective applications, including cancer therapy [22], proton imaging [23], proton active interrogation [50] or ion fast ignition [24, 25] require quasi-monoenergetic beams with a low energy spread. For the carbon ion fast ignition a monoenergetic beam of carbon ions is needed with an energy spread  $\Delta E/E$  of less than 10% at a

## 5.2. OUTLOOK AND PERSPECTIVES

---

central energy of  $\sim 450$  MeV [24] (for typical pellet dimensions), where for an ion beam power density of  $\sim 10$  kJ/10 ps a conversion efficiency of 10% relates to a 1 kJ drive laser for the ion acceleration. For the cancer treatment monoenergetic protons of up to  $\sim 250$  MeV or mono-energetic carbon  $C^{6+}$  ions of up to  $\sim 300$  MeV are necessary, depending on the depth of the tumor. For the active interrogation with protons, which offer a much better attenuation length, energies of 1 GeV are advantageous (they would penetrate 0.5 m of lead shielding).

To solve these problems, the scaling of the ion energies with respect to the laser parameters should be investigated first. A scaling model with predictive capabilities will enable the design of the right laser (in terms of laser energy and pulse duration) for an optimized acceleration scheme. From parametric studies of the analytical model for the BOA acceleration a scaling law has been derived, where the maximum energy scales as

$$E_{\max} \propto I_L^{\frac{1}{2}} \tau_\lambda^{\frac{1}{3}} \propto a_0 \tau_\lambda^{\frac{1}{3}} \propto \sqrt{\frac{E_L}{r_L \tau_L^{\frac{1}{3}}}}. \quad (5.2)$$

The scaling shows a linear dependency in  $a_0$ , but a dependency in the pulse duration to the power of 1/3. Thus, higher laser energies are favorable over shorter laser pulses, which agrees well with experimental results from Trident and the Max Born Institute in Berlin, where a similar on-target intensity (with 0.7 J in 45 fs) resulted in much lower ion energies. In order to further verify or falsify the model and to ensure its predictive capabilities, more experimental data points are needed. This can either be done using different laser systems or by changing essential parameters for the experiments with Trident. While the first could suffer from strongly varying and probably unknown contrasts between the different laser systems, the latter only offers very few possibilities to change the on-target intensity. In experimental campaigns planned for the future, different off-axis parabolic (OAP) mirrors will be used at Trident to change the laser focal spot and hence the on-target intensity. With an F/1.5, F/3 and F/8 OAP peak intensities of  $> 10^{19}$  W/cm<sup>2</sup>,  $5 \times 10^{20}$  W/cm<sup>2</sup> and  $2 \times 10^{21}$  W/cm<sup>2</sup> can be achieved, respectively. The current model predicts proton and carbon ion energies of 200 MeV and 1.3 GeV, respectively, for intensities of  $2 \times 10^{21}$  W/cm<sup>2</sup>, which could be achieved at Trident with a F/1.5 OAP.

The LMU Munich is currently building the new Center for advanced laser ap-

## 5. SUMMARY AND PERSPECTIVES

---

plications (CALA). The main laser source of this system will be a Ti:Sapphire system that delivers pulses of 60 J and 20 fs duration. For these parameters the BOA analytical model predicts  $C^{6+}$  ion energies of about 1 GeV and proton energies exceeding 150 MeV. Although these energies are lower than the ones that can be reached at Trident with a F/1.5 OAP, the CALA system has the great advantage that it can run at a repetition rate of 1 Hz as opposed to the 1hour shot cycle of Trident.

For improvement of the production of monoenergetic ion beams in the BOA-soliton regime, additional simulations [35] have shown that Tridents current laser field of  $I_0 = 2 \times 10^{20} \text{ W/cm}^2$  is not sufficiently intense to generate the necessary density spike in the ion distribution and hence cannot generate a sharp monoenergetic ion beam. For an average intensity of  $I_0 = 5.2 \times 10^{20} \text{ W/cm}^2$ , which can easily be achieved with an F/1.5 OAP, these simulations predict monoenergetic carbon ions peaking at 170 MeV, which would be very suitable for a wide range of applications.

For the conception and design of future laser systems with even higher power and on-target intensities, the laser contrast will become an even greater challenge. With each order of magnitude in intensity, the contrast also has to increase by one order; otherwise premature target expansion might render ion-acceleration ineffective or even impossible. PIC simulations typically use a perfect  $\sin$ ,  $\sin^2$ , Gaussian or even a trapezoidal temporal pulse envelope and neglect contrast effects on the laser-plasma interaction, such as pre-mature expansion and target deformation, which potentially results in wrong proton energies seen in these simulations. The current incapability of the PIC simulations to correctly model pre-plasma conditions by imperfect laser contrast needs to be investigated in order to achieve better predictability of these simulations on a much wider parameter range than the analytical model offers.

Matching the experimental conditions as closely as possible with simulations is very challenging due to the high densities found in these plasmas. Optical probing of the plasma to evaluate its density necessitates high-energy x-rays of 10th of keV in a narrow bandwidth. The x-ray generation from  $K_\alpha$  emission in high-intensity laser-matter interactions via electron impact ionization has been studied in the past [177] and energies from 8 keV up to 98 keV can be achieved for materials from Cu to U, suitable for probing of a wide range of plasmas. However, this technique suffers from low conversion efficiencies on the order of  $10^{-4}$ . Recently,

## 5.2. OUTLOOK AND PERSPECTIVES

---

a modification of this technique has been proposed by Sefkov, *et al.* [178]).

Here a beam of high energy electrons and ions is generated in the BOA regime with a nm-thick foil. This beam is then used to generate  $K_\alpha$  emission in a second micron-thick target positioned closely behind the first one. The volumetric heating of the first target results in high populations of  $K_\alpha$ -relevant hot electrons and ions for the second target; a more than tenfold increase in the conversion efficiency has been seen in simulations, yielding X-ray powers of  $70 \text{ mJ ps}^{-1}$  with Trident relevant laser parameters.

Such a BOA-driven wide-range x-ray source would mark a breakthrough in experimental high energy density physics (HEDP), as these measurements potentially allow a better validation/falsification of simulations and theories. It could also offer a sufficiently bright and narrow bandwidth source for phase-contrast imaging of large objects at 50-70 keV.

For the experimental results presented in this thesis, PIC simulations show discrepancies especially in terms of the proton acceleration. The protons are much more susceptible to contrast changes due to their low inertia and high charge to mass ratio. The proton self-cleaning effect occurring in the pedestal requires precise knowledge about the initial plasma conditions to allow reliable studies with PIC simulations.

With this question answered, research should be carried out to maximize the acceleration time in the BOA regime for a given laser pulse duration. This means,  $t_1$  should be reached shortly before the peak of the pulse and  $t_2$  should be reached as late as possible, preferably after the full pulse has passed the target. With precise PIC simulations probably in combination with hydro codes, accounting for pre-plasma conditions due to the real temporal laser pulse envelope, the target design could easily be optimized for such a scheme boosting proton and ion energies and conversion efficiencies into regions that could make laser-driven ion sources a competitive alternative to conventional rf-accelerators.

# References

- [1] A. Einstein. Die grundlage der allgemeinen relativitätstheorie. *Annalen der Physik*, 354(7):769–822, 1916. [1](#), [43](#)
- [2] T. H. Maiman. Stimulated optical radiation in ruby. *Nature*, 187(4736):493–494, Aug 1960. [1](#), [43](#)
- [3] F. J. McClung and R. W. Hellwarth. Giant optical pulsations from ruby. *J. Appl. Phys.*, 33(3):828–829, 1962. [1](#)
- [4] L. E. Hargrove, R. L. Fork, and M. A. Pollack. Locking of he-ne laser modes induced by synchronous intracavity modulation. *Appl. Phys. Lett.*, 5(1):4–5, 1964. [1](#)
- [5] M. DiDomenico. Small-signal analysis of internal (coupling-type) modulation of lasers. *J. Appl. Phys.*, 35(10):2870–2876, 1964. [1](#)
- [6] R. A. Snavely, M. H. Key, S. P. Hatchett, T. E. Cowan, M. Roth, T. W. Phillips, M. A. Stoyer, E. A. Henry, T. C. Sangster, M. S. Singh, S. C. Wilks, A. MacKinnon, A. Offenberger, D. M. Pennington, K. Yasuike, A. B. Langdon, B. F. Lasinski, J. Johnson, M. D. Perry, and E. M. Campbell. Intense high-energy proton beams from petawatt-laser irradiation of solids. *Phys. Rev. Lett.*, 85(14):2945–2948, Oct 2000. [1](#), [2](#), [26](#), [27](#), [79](#), [131](#)
- [7] M. Hegelich, S. Karsch, G. Pretzler, D. Habs, K. Witte, W. Guenther, M. Allen, A. Blazevic, J. Fuchs, J. C. Gauthier, M. Geissel, P. Audebert, T. Cowan, and M. Roth. Mev ion jets from short-pulse-laser interaction with thin foils. *Phys. Rev. Lett.*, 89(8):085002, Aug 2002. [2](#), [28](#), [30](#), [95](#), [96](#), [116](#), [131](#)

- 
- [8] Gerard A. Mourou, Toshiki Tajima, and Sergei V. Bulanov. Optics in the relativistic regime. *Rev. Mod. Phys.*, 78(2):309–371, Apr 2006. [131](#)
- [9] G. Petrov and J. Davis. Laser acceleration of light ions from high-intensity laser-target interactions. *Applied Physics B: Lasers and Optics*, 96:773–779, 2009.
- [10] O. Klimo, J. Psikal, J. Limpouch, and V. T. Tikhonchuk. Monoenergetic ion beams from ultrathin foils irradiated by ultrahigh-contrast circularly polarized laser pulses. *Phys. Rev. ST Accel. Beams*, 11(3):031301, Mar 2008. [3](#), [30](#), [31](#), [33](#), [119](#), [136](#)
- [11] A P L Robinson, P Gibbon, M Zepf, S Kar, R G Evans, and C Bellei. Relativistically correct hole-boring and ion acceleration by circularly polarized laser pulses. *Plasma Physics and Controlled Fusion*, 51(2):024004, 2009.
- [12] X. Q. Yan, C. Lin, Z. M. Sheng, Z. Y. Guo, B. C. Liu, Y. R. Lu, J. X. Fang, and J. E. Chen. Generating high-current monoenergetic proton beams by a circularly polarized laser pulse in the phase-stable acceleration regime. *Phys. Rev. Lett.*, 100(13):135003, Apr 2008. [33](#), [124](#), [137](#)
- [13] Andrea Macchi, Silvia Veghini, and Francesco Pegoraro. “light sail” acceleration reexamined. *Phys. Rev. Lett.*, 103(8):085003, Aug 2009. [30](#), [31](#), [119](#), [136](#)
- [14] T. Esirkepov, M. Borghesi, S. V. Bulanov, G. Mourou, and T. Tajima. Highly efficient relativistic-ion generation in the laser-piston regime. *Phys. Rev. Lett.*, 92(17):175003, Apr 2004. [1](#), [3](#), [26](#), [30](#), [31](#), [32](#), [119](#)
- [15] Stephen P. Hatchett, Curtis G. Brown, Thomas E. Cowan, Eugene A. Henry, Joy S. Johnson, Michael H. Key, Jeffrey A. Koch, A. Bruce Langdon, Barbara F. Lasinski, Richard W. Lee, Andrew J. Mackinnon, Deanna M. Pennington, Michael D. Perry, Thomas W. Phillips, Markus Roth, T. Craig Sangster, Mike S. Singh, Richard A. Snavely, Mark A. Stoyer, Scott C. Wilks, and Kazuhito Yasuike. Electron, photon, and ion beams from the relativistic interaction of petawatt laser pulses with solid targets. *Physics of Plasmas*, 7(5):2076–2082, 2000. [1](#), [2](#), [27](#), [29](#), [79](#), [131](#)

## REFERENCES

---

- [16] J. Fuchs, P. Antici, E. d’Humieres, E. Lefebvre, M. Borghesi, E. Brambrink, C. A. Cecchetti, M. Kaluza, V. Malka, M. Manclossi, S. Meyroneinc, P. Mora, J. Schreiber, T. Toncian, H. Pepin, and P. Audebert. Laser-driven proton scaling laws and new paths towards energy increase. *Nat Phys*, 2(1):48–54, Jan 2006. [2](#), [29](#), [108](#)
- [17] A. P. L Robinson, A. R. Bell, and R. J. Kingham. Effect of target composition on proton energy spectra in ultraintense laser-solid interactions. *Phys. Rev. Lett.*, 96(3):035005, Jan 2006. [2](#), [29](#), [108](#), [131](#)
- [18] S. A. Gaillard, T. Kluge, K. A. Flippo, M. Bussmann, B. Gall, T. Lockard, M. Geissel, D. T. Offermann, M. Schollmeier, Y. Sentoku, and T. E. Cowan. Increased laser-accelerated proton energies via direct laser-light-pressure acceleration of electrons in microcone targets. *Phys. Plasmas*, 18(5):056710, 2011. [2](#), [29](#), [131](#)
- [19] T.E. Cowan, J. Fuchs, H. Ruhl, Y. Sentoku, A. Kemp, P. Audebert, M. Roth, R. Stephens, I. Barton, A. Blazevic, E. Brambrink, J. Cobble, J.C. Fernandez, J.-C. Gauthier, M. Geissel, M. Hegelich, J. Kaae, S. Karsch, G.P. Le Sage, S. Letzring, M. Manclossi, S. Meyroneinc, A. Newkirk, H. Ppin, and N. Renard-LeGalloudec. Ultra-low emittance, high current proton beams produced with a laser-virtual cathode sheath accelerator. *Nuclear Instruments and Methods in Physics Research Section A: Accelerators, Spectrometers, Detectors and Associated Equipment*, 544(1-2):277–284, 2005. Proceedings of the 15th International Symposium on Heavy Ion Inertial Fusion - HIF 2004, 15th International Symposium on Heavy Ion Inertial Fusion. [2](#)
- [20] E. L. Clark, K. Krushelnick, M. Zepf, F. N. Beg, M. Tatarakis, A. Machacek, M. I. K. Santala, I. Watts, P. A. Norreys, and A. E. Dangor. Energetic heavy-ion and proton generation from ultraintense laser-plasma interactions with solids. *Physical Review Letters*, 85:1654–1657, 2000. [2](#), [30](#), [95](#), [131](#)
- [21] P. McKenna, K. W. D. Ledingham, T. McCanny, R. P. Singhal, I. Spencer, M. I. K. Santala, F. N. Beg, K. Krushelnick, M. Tatarakis, M. S. Wei, E. L. Clark, R. J. Clarke, K. L. Lancaster, P. A. Norreys, K. Spohr, R. Chapman, and M. Zepf. Demonstration of fusion-evaporation and direct-interaction

- nuclear reactions using high-intensity laser-plasma-accelerated ion beams. *Phys. Rev. Lett.*, 91:075006, Aug 2003. [2](#), [30](#), [95](#), [131](#)
- [22] F. Pegoraro, S. Atzeni, M. Borghesi, S. Bulanov, T. Esirkepov, J. Honrubia, Y. Kato, V. Khoroshkov, K. Nishihara, T. Tajima, M. Temporal, and O. Willi. Production of ion beams in high-power laser & plasma interactions and their applications. *Laser and Particle Beams*, 22(01):19–24, 2004. [2](#), [27](#), [79](#), [131](#), [137](#)
- [23] M Borghesi, A Schiavi, D H Campbell, M G Haines, O Willi, A J MacKinnon, L A Gizzi, M Galimberti, R J Clarke, and H Ruhl. Proton imaging: a diagnostic for inertial confinement fusion/fast ignitor studies. *Plasma Physics and Controlled Fusion*, 43(12A):A267, 2001. [2](#), [118](#), [131](#), [137](#)
- [24] J. C. Fernández, B. J. Albright, K. A. Flippo, B. M. Hegelich, T. J. Kwan, M. J. Schmitt, and L. Yin. Progress on ion based fast ignition. *Journal of Physics: Conference Series*, 112(2):022051, 2008. [2](#), [6](#), [79](#), [131](#), [137](#), [138](#)
- [25] J J Honrubia, J C Fernández, M Temporal, B M Hegelich, and J Meyerter Vehn. Fast ignition by laser-driven carbon beams. *Journal of Physics: Conference Series*, 244(2):022038, 2010. [2](#), [79](#), [131](#), [137](#)
- [26] B. M. Hegelich, B. J. Albright, J. Cobble, K. Flippo, S. Letzring, M. Paffett, H. Ruhl, J. Schreiber, R. K. Schulze, and J. C. Fernandez. Laser acceleration of quasi-monoenergetic mev ion beams. *Nature*, 441-444(7075):4, 2006. [2](#), [30](#), [118](#), [123](#), [131](#), [137](#)
- [27] H. Schwoerer, S. Pfotenhauer, O. Jackel, K.-U. Amthor, B. Liesfeld, W. Ziegler, R. Sauerbrey, K. W. D. Ledingham, and T. Esirkepov. Laser-plasma acceleration of quasi-monoenergetic protons from microstructured targets. *Nature*, 439(7075):445–448, Jan 2006. [2](#), [30](#), [118](#), [131](#)
- [28] L. Yin, B. J. Albright, B. M. Hegelich, K. J. Bowers, K. A. Flippo, T. J. T. Kwan, and J. C. Fernandez. Monoenergetic and gev ion acceleration from the laser breakout afterburner using ultrathin targets. *Physics of Plasmas*, 14(5):056706, 2007. [3](#), [26](#), [34](#), [86](#), [93](#), [119](#), [132](#), [136](#)
- [29] B. J. Albright, L. Yin, Kevin J. Bowers, B. M. Hegelich, K. A. Flippo, T. J. T. Kwan, and J. C. Fernandez. Relativistic buneman instability in

## REFERENCES

---

- the laser breakout afterburner. *Physics of Plasmas*, 14(9):094502, 2007. [25](#), [34](#), [36](#), [132](#)
- [30] A. Henig, D. Kiefer, K. Markey, D. C. Gautier, K. A. Flippo, S. Letzring, R. P. Johnson, T. Shimada, L. Yin, B. J. Albright, K. J. Bowers, J. C. Fernández, S. G. Rykovanov, H.-C. Wu, M. Zepf, D. Jung, V. Kh. Liechtenstein, J. Schreiber, D. Habs, and B. M. Hegelich. Enhanced laser-driven ion acceleration in the relativistic transparency regime. *Phys. Rev. Lett.*, 103(4):045002, Jul 2009. [3](#), [114](#)
- [31] B.M. Hegelich, D. Jung, B.J. Albright, J.C. Fernandez, D.C. Gautier, C. Huang, T.J. Kwan, S. Letzring, S. Palaniyappan, R.C. Shah, H.-C. Wu, L. Yin, A. Henig, R. Hrlein, D. Kiefer, J. Schreiber, X.Q. Yan, T. Tajima, D. Habs, B. Dromey, and J.J. Honrubia. Experimental demonstration of particle energy, conversion efficiency and spectral shape required for ion-based fast ignition. *Nuclear Fusion*, 51(8):083011, 2011. [3](#), [26](#), [67](#), [68](#)
- [32] A. Henig, S. Steinke, M. Schnürer, T. Sokollik, R. Hörlein, D. Kiefer, D. Jung, J. Schreiber, B. M. Hegelich, X. Q. Yan, J. Meyer-ter Vehn, T. Tajima, P. V. Nickles, W. Sandner, and D. Habs. Radiation-pressure acceleration of ion beams driven by circularly polarized laser pulses. *Phys. Rev. Lett.*, 103(24):245003, Dec 2009. [3](#), [34](#), [103](#), [119](#), [136](#)
- [33] Charlotte A. J. Palmer, N. P. Dover, I. Pogorelsky, M. Babzien, G. I. Dudnikova, M. Ispiriyanyan, M. N. Polyanskiy, J. Schreiber, P. Shkolnikov, V. Yaki-menko, and Z. Najmudin. Monoenergetic proton beams accelerated by a radiation pressure driven shock. *Phys. Rev. Lett.*, 106(1):014801, Jan 2011. [3](#)
- [34] D. Jung, L. Yin, B. J. Albright, D. C. Gautier, R. Hörlein, D. Kiefer, A. Henig, R. Johnson, S. Letzring, S. Palaniyappan, R. Shah, T. Shimada, X. Q. Yan, K. J. Bowers, T. Tajima, J. C. Fernández, D. Habs, and B. M. Hegelich. Monoenergetic ion beam generation by driving ion solitary waves with circularly polarized laser light. *Phys. Rev. Lett.*, 107:115002, Sep 2011. [3](#), [122](#), [123](#), [124](#), [125](#), [127](#), [128](#)
- [35] L. Yin, B. J. Albright, D. Jung, K. J. Bowers, R. C. Shah, S. Palaniyappan, J. C. Fernandez, and B. M. Hegelich. Mono-energetic ion beam acceleration

- in solitary waves during relativistic transparency using high-contrast circularly polarized short-pulse laser and nanoscale targets. *Physics of Plasma*, 18(5):053103, May 2011. 3, 86, 125, 127, 128, 137, 139
- [36] HIT. Heidelberg ion-beam therapie center. [online] <http://www.klinikum.uni-heidelberg.de/Startseite-HIT.113005.0.html>. 4
- [37] D. Ondreka and Weinrich U., editors. *The Heidelberg Ion Therapy (HIT) accelerator coming into operation*, volume EPAC08, 2008. 4
- [38] ITER. International thermonuclear experimental reactor. [online] <https://www.iter.org/org>. 5
- [39] T. J. Dolan. *Fusion Research; Volume 1: Principles*. Pergamon, 1982. 5
- [40] C. M. Braams and E. P. Stott. *Nuclear Fusion: Half a Century of Magnetic Confinement Fusion Research*. Inst of Physics Pub Inc, 2002. 5
- [41] R. R. Kidder. Energy gain of laser-compressed pellets: a simple model calculation. *Nuclear Fusion*, 16:405, 1976. 5
- [42] J. Meyer-ter Vehn. On energy gain of fusion targets: The model of kidder and bodner improved. *Nuclear Fusion*, 22:561–566, 1982. 5
- [43] Stephen E. Bodner, Denis G. Colombant, John H. Gardner, Robert H. Lehmborg, Stephen P. Obenschain, Lee Phillips, Andrew J. Schmitt, John D. Sethian, Robert L. McCrory, Wolf Seka, Charles P. Verdon, James P. Knauer, Bedros B. Afeyan, and Howard T. Powell. Direct-drive laser fusion: Status and prospects. *Phys. Plasmas*, 5(5):1901–1918, 1998. 5
- [44] G.H. Miley and H. Hora. Laser interaction and related plasma phenomena. *Nuclear Fusion*, 38(7):1113, 1998. 5
- [45] NIF. National ignition facility. [online] <https://lasers.llnl.gov>. 6
- [46] Max Tabak, James Hammer, Michael E. Glinsky, William L. Kruer, Scott C. Wilks, John Woodworth, E. Michael Campbell, Michael D. Perry, and Rodney J. Mason. Ignition and high gain with ultrapowerful lasers. *Phys. Plasmas*, 1(5):1626–1634, 1994. 6

## REFERENCES

---

- [47] M. Roth, T. E. Cowan, M. H. Key, S. P. Hatchett, C. Brown, W. Fountain, J. Johnson, D. M. Pennington, R. A. Snavely, S. C. Wilks, K. Yasuike, H. Ruhl, F. Pegoraro, S. V. Bulanov, E. M. Campbell, M. D. Perry, and H. Powell. Fast ignition by intense laser-accelerated proton beams. *Phys. Rev. Lett.*, 86(3):436–439, Jan 2001. [6](#), [79](#), [118](#)
- [48] William Bertozzi and Robert J. Ledoux. Nuclear resonance fluorescence imaging in non-intrusive cargo inspection. *Nuclear Instruments and Methods in Physics Research Section B: Beam Interactions with Materials and Atoms*, 241(1-4):820 – 825, 2005. The Application of Accelerators in Research and Industry: Proceedings of the Eighteenth International Conference on the Application of Accelerators in Research and Industry (CAARI 2004). [7](#)
- [49] J. Church. Detection of fissionable material in cargo containers using active neutron interrogation. *APS Division of Nuclear Physics Meeting Abstracts*, :G5+, Oct 2006. [7](#)
- [50] C. L. Morris, K. Chung, S. Greene, G. Hogan, M. Makela, F. Mariam, E. C. Milner, M. Murray, A. Saunders, R. Spaulding, Z. Wang, L. Waters, and F. Wysocki. Active interrogation using energetic protons. In *Institute of Nuclear Materials Management 51th Annual Meeting*, 2010. [7](#), [137](#)
- [51] B. Dromey, M. Zepf, A. Gopal, K. Lancaster, M. S. Wei, K. Krushelnick, M. Tatarakis, N. Vakakis, S. Moustazis, R. Kodama, M. Tampo, C. Stoeckl, R. Clarke, H. Habara, D. Neely, S. Karsch, and P. Norreys. High harmonic generation in the relativistic limit. *Nat. Phys.*, 2:456–459, 2006. [9](#), [53](#), [82](#)
- [52] F. Amiranoff, S. Baton, D. Bernard, B. Cros, D. Descamps, F. Dorchies, F. Jacquet, V. Malka, J. R. Marquès, G. Matthieussent, P. Miné, A. Modena, P. Mora, J. Morillo, and Z. Najmudin. Observation of laser wakefield acceleration of electrons. *Phys. Rev. Lett.*, 81:995–998, Aug 1998. [9](#)
- [53] D. Batani, C. J. Joachain, S. Martellucci, and A. N. Chester. *Atoms, Solids, and Plasmas in Super-Intense Laser Fields*. Kluwer Academic / Plenum Publishers, 2001. [10](#), [11](#), [12](#), [13](#)
- [54] Paul Gibbon. *Short Pulse Laser Interactions with Matter: An Introduction*. Imperial College Press, 2005. [13](#), [14](#), [15](#), [16](#), [17](#), [21](#), [23](#), [24](#), [44](#)

- 
- [55] L. V. Keldysh. Ionization in the field of a strong electromagnetic wave. *JETP*, 20(5):1307, 1965. [16](#)
- [56] M. N. Saha. On a physical theory of stellar spectra. *Royal Society of London Proceedings Series A*, 99:135–153, 1921. [17](#)
- [57] Y. T. Lee. A model for ionization balance and l-shell spectroscopy of nonlte plasmas. *Journal of Quantitative Spectroscopy and Radiative Transfer*, 38(2):131–145, 1987. [17](#)
- [58] S. Eliezer. *The Interaction of High-Power Lasers with Plasmas*. Institute of Physics Publishing, 2002. [17](#), [25](#)
- [59] W. L. Kruer. *The Physics of Laser Plasma Interaction*. Allan M. Wylde, 1988. [17](#), [22](#), [23](#), [24](#)
- [60] S. C. Wilks, W. L. Kruer, M. Tabak, and A. B. Langdon. Absorption of ultra-intense laser pulses. *Phys. Rev. Lett.*, 69:1383–1386, Aug 1992. [19](#)
- [61] P. Mulser and D. Bauer. *High-Power Laser-Matter Interaction*. Springer-Verlag Berlin, 2010. [19](#), [22](#)
- [62] S. Palaniyappan, R. Shah, H.C. Wu, C. Gautier, D. Jung, L. Yin, S Letzring, B. Dromey, B. J. Albright, R. P. Johnson, T. Shimada, J. C. Fernández, and B. M. Hegelich. High resolution dynamics of ultra-fast optical switching in relativistically transparent overdense plasma. *Nat. Phys.*, submitted:, 2011. [20](#), [119](#)
- [63] R. Shah, S. Palaniyappan, H.C. Wu, C. Gautier, D. Jung, R Horlein, D. Offermann, J. Ren, L. Yin, B. J. Albright, R. P. Johnson, T. Shimada, J. C. Fernández, and B. M. Hegelich. Laser pulse shortening via femtosecond dynamics of relativistic transparency. *Nat. Phys.*, submitted:, 2011. [20](#), [82](#), [119](#), [136](#)
- [64] C. Gahn, G. D. Tsakiris, A. Pukhov, J. Meyer-ter Vehn, G. Pretzler, P. Thirolf, D. Habs, and K. J. Witte. Multi-mev electron beam generation by direct laser acceleration in high-density plasma channels. *Phys. Rev. Lett.*, 83:4772–4775, Dec 1999. [21](#)

## REFERENCES

---

- [65] J. Meyer-ter Vehn and S. Atzeni. *The Physics of Inertial Fusion*. Oxford Science Publications, 2004. [22](#), [24](#), [25](#)
- [66] R. O. Dendy. *Plasma Physics: An Introductory Course*. Cambridge University Press, 1995. [22](#)
- [67] A. J. McAlister and E. A. Stern. Plasma resonance absorption in thin metal films. *Phys. Rev.*, 132:1599–1602, Nov 1963. [22](#)
- [68] W. L. Kruer and K. Estabrook. Jb heating by very intense laser light. *Physics of Fluids*, 28(1):430–432, 1985. [22](#)
- [69] F. Brunel. Not-so-resonant, resonant absorption. *Phys. Rev. Lett.*, 59:52–55, Jul 1987. [22](#), [23](#)
- [70] J. Y. Hsu, K. Matsuda, M. S. Chu, and T. H. Jensen. Stochastic heating of a large-amplitude standing wave. *Phys. Rev. Lett.*, 43:203–206, Jul 1979. [23](#)
- [71] L. D. Landau and S. I. Pekar. On the vibration of the electronic plasma. *J. Phys. USSR*, 25:, 1946. [23](#)
- [72] P. J. Catto and R. M. More. Sheath inverse bremsstrahlung in laser produced plasmas. *Phys. Fluids*, 20(4):704–705, 1977. [23](#)
- [73] F. F. Chen. *Plasma Physics and Controlled Fusion*. Plenum Press, 1984. [25](#), [26](#)
- [74] J. Schreiber. private communication. , 2011. [25](#)
- [75] R. J. Goldston and P. H. Rutherford. *Plasma Physics*. Intstitute of Physics Publishing, 1995. [25](#)
- [76] O. Buneman. Dissipation of currents in ionized media. *Phys. Rev.*, 115:503–517, Aug 1959. [25](#)
- [77] D. Kovalev, A. Smirnov, and Ya. Dimant. Study of kinetic effects arising in simulations of farley-buneman instability. *Plasma Physics Reports*, 35:420–425, 2009. [25](#)

- 
- [78] T. E. Cowan, J. Fuchs, H. Ruhl, A. Kemp, P. Audebert, M. Roth, R. Stephens, I. Barton, A. Blazevic, E. Brambrink, J. Cobble, J. Fernández, J.-C. Gauthier, M. Geissel, M. Hegelich, J. Kaae, S. Karsch, G. P. Le Sage, S. Letzring, M. Manclossi, S. Meyroneinc, A. Newkirk, H. Pépin, and N. Renard-LeGalloudec. Ultralow emittance, multi-mev proton beams from a laser virtual-cathode plasma accelerator. *Phys. Rev. Lett.*, 92(20):204801, May 2004. [27](#), [131](#)
- [79] T. Ditmire, T. Donnelly, A. M. Rubenchik, R. W. Falcone, and M. D. Perry. Interaction of intense laser pulses with atomic clusters. *Phys. Rev. A*, 53:3379–3402, May 1996. [27](#)
- [80] T. Esirkepov, Y. Sentoku, K. Mima, K. Nishihara, F. Califano, F. Pegoraro, N. Naumova, S. Bulanov, Y. Ueshima, T. Liseikina, V. Vshivkov, and Y. Kato. Ion acceleration by superintense laser pulses in plasmas. *JETP Letters*, 70:82–89, 1999. [27](#)
- [81] S. C. Wilks, A. B. Langdon, T. E. Cowan, M. Roth, M. Singh, S. Hatchett, M. H. Key, D. Pennington, A. MacKinnon, and R. A. Snavely. Energetic proton generation in ultra-intense laser-solid interactions. *Phys. Plasmas*, 8(2):542–549, 2001. [27](#), [29](#), [112](#)
- [82] P. Mora. Plasma expansion into a vacuum. *Phys. Rev. Lett.*, 90:185002, May 2003. [28](#), [29](#), [112](#)
- [83] M. Passoni and M. Lontano. One-dimensional model of the electrostatic ion acceleration in the ultraintense laser-solid interaction. *Laser and Particle Beams*, 22(02):163–169, 2004.
- [84] M. Passoni, V. T. Tikhonchuk, M. Lontano, and V. Yu. Bychenkov. Charge separation effects in solid targets and ion acceleration with a two-temperature electron distribution. *Phys. Rev. E*, 69:026411, Feb 2004.
- [85] J. Schreiber, F. Bell, F. Grüner, U. Schramm, M. Geissler, M. Schnürer, S. Ter-Avetisyan, B. M. Hegelich, J. Cobble, E. Brambrink, J. Fuchs, P. Audebert, and D. Habs. Analytical model for ion acceleration by high-intensity laser pulses. *Phys. Rev. Lett.*, 97:045005, Jul 2006. [29](#), [112](#)

## REFERENCES

---

- [86] B. J. Albright, L. Yin, B. M. Hegelich, Kevin J. Bowers, T. J. T. Kwan, and J. C. Fernández. Theory of laser acceleration of light-ion beams from interaction of ultrahigh-intensity lasers with layered targets. *Phys. Rev. Lett.*, 97:115002, Sep 2006. [28](#), [34](#), [86](#)
- [87] S. Steinke, A. Henig, M. Schnrer, T. Sokollik, P.V. Nickles, D. Jung, D. Kiefer, R. Hrlein, J. Schreiber, T. Tajima, X.Q. Yan, M. Hegelich, J. Meyer-ter Vehn, W. Sandner, and D. Habs. Efficient ion acceleration by collective laser-driven electron dynamics with ultra-thin foil targets. *Laser and Particle Beams*, 28(01):215–221, 2010. [29](#), [103](#), [113](#), [114](#)
- [88] Sven Steinke, Andreas Henig, Matthias Schnuerer, Thomas Sokollik, Rainer Hoerlein, Daniel Kiefer, Daniel Jung, Joerg Schreiber, B. M. Hegelich, X. Q. Yan, J. Meyer ter Vehn, T. Tajima, P. V. Nickles, Wolfgang Sandner, and Dietrich Habs. Laser - ion acceleration in the laser transparency regime. In *Quantum Electronics and Laser Science Conference*, page JFB1. Optical Society of America, 2010. [29](#), [40](#), [112](#)
- [89] T. Esirkepov, M. Yamagiwa, and T. Tajima. Laser ion-acceleration scaling laws seen in multiparametric particle-in-cell simulations. *Phys. Rev. Lett.*, 96:105001, Mar 2006. [29](#)
- [90] J. Fuchs, Y. Sentoku, S. Karsch, J. Cobble, P. Audebert, A. Kemp, A. Nikroo, P. Antici, E. Brambrink, A. Blazevic, E. M. Campbell, J. C. Fernández, J.-C. Gauthier, M. Geissler, M. Hegelich, H. Pépin, H. Popescu, N. Renard-LeGalloudec, M. Roth, J. Schreiber, R. Stephens, and T. E. Cowan. Comparison of laser ion acceleration from the front and rear surfaces of thin foils. *Phys. Rev. Lett.*, 94:045004, Feb 2005. [29](#)
- [91] A. Henig, D. Kiefer, M. Geissler, S. G. Rykovanov, R. Ramis, R. Hörlein, J. Osterhoff, Zs. Major, L. Veisz, S. Karsch, F. Krausz, D. Habs, and J. Schreiber. Laser-driven shock acceleration of ion beams from spherical mass-limited targets. *Phys. Rev. Lett.*, 102:095002, Mar 2009. [29](#)
- [92] P. McKenna, K. W. D. Ledingham, J. M. Yang, L. Robson, T. McCanny, S. Shimizu, R. J. Clarke, D. Neely, K. Spohr, R. Chapman, R. P. Singhal, K. Krushelnick, M. S. Wei, and P. A. Norreys. Characterization of proton

- and heavier ion acceleration in ultrahigh-intensity laser interactions with heated target foils. *Phys. Rev. E*, 70:036405, Sep 2004. [30](#), [131](#)
- [93] Andrea Macchi, Federica Cattani, Tatiana V. Liseykina, and Fulvio Cornolti. Laser acceleration of ion bunches at the front surface of over-dense plasmas. *Phys. Rev. Lett.*, 94:165003, Apr 2005. [30](#), [31](#)
- [94] Andrea Macchi, Silvia Veghini, Tatyana V Liseykina, and Francesco Pegoraro. Radiation pressure acceleration of ultrathin foils. *New Journal of Physics*, 12(4):045013, 2010. [30](#), [31](#)
- [95] N. Naumova, T. Schlegel, V. T. Tikhonchuk, C. Labaune, I. V. Sokolov, and G. Mourou. Hole boring in a dt pellet and fast-ion ignition with ultraintense laser pulses. *Phys. Rev. Lett.*, 102:025002, 2009. [31](#)
- [96] N. Naumova, T. Schlegel, V. T. Tikhonchuk, C. Labaune, I. V. Sokolov, and G. Mourou. Ponderomotive ion acceleration in dense plasmas at super-high laser intensities. *The European Physical Journal D - Atomic, Molecular, Optical and Plasma Physics*, 55:393–398, 2009.
- [97] T. Schlegel, N. Naumova, V. T. Tikhonchuk, C. Labaune, I. V. Sokolov, and G. Mourou. Relativistic laser piston model: Ponderomotive ion acceleration in dense plasmas using ultraintense laser pulses. *Phys. Plasmas*, 16(8):083103, 2009.
- [98] Igor V. Sokolov, Natalia M. Naumova, John A. Nees, Victor P. Yanovsky, and Gérard A. Mourou. Radiation back-reaction in relativistically strong and qed-strong pulsed laser fields. *AIP Conference Proceedings*, 1228(1):305–322, 2010. [31](#)
- [99] Victor V. Kulagin, Vladimir A. Cherepenin, Min Sup Hur, and Hyyong Suk. Theoretical investigation of controlled generation of a dense attosecond relativistic electron bunch from the interaction of an ultrashort laser pulse with a nanofilm. *Phys. Rev. Lett.*, 99:124801, Sep 2007. [32](#)
- [100] D. Habs, M. Hegelich, J. Schreiber, M. Gross, A. Henig, D. Kiefer, and D. Jung. Dense laser-driven electron sheets as relativistic mirrors for coherent production of brilliant x-ray and gamma-ray beams. *Applied Physics B: Lasers and Optics*, 93(2-3, SI):349–354, Nov 2008.

## REFERENCES

---

- [101] D. Kiefer, A. Henig, D. Jung, D. C. Gautier, K. A. Flippo, S. A. Gaillard, S. Letzring, R. P. Johnson, R. C. Shah, T. Shimada, J. C. Fernandez, V. Kh. Liechtenstein, J. Schreiber, B. M. Hegelich, and D. Habs. First observation of quasi-monoenergetic electron bunches driven out of ultrathin diamond-like carbon (dlc) foils. *EUROPEAN PHYSICAL JOURNAL D*, 55(2):427–432, Nov 2009. [32](#), [82](#), [85](#)
- [102] Tong-Pu Yu, Alexander Pukhov, Gennady Shvets, and Min Chen. Stable laser-driven proton beam acceleration from a two-ion-species ultrathin foil. *Phys. Rev. Lett.*, 105(6):065002, Aug 2010. [34](#)
- [103] B. Qiao, M. Zepf, M. Borghesi, B. Dromey, M. Geissler, A. Karmakar, and P. Gibbon. Radiation-pressure acceleration of ion beams from nanofoil targets: The leaky light-sail regime. *Phys. Rev. Lett.*, 105(15):155002, Oct 2010. [34](#), [119](#), [126](#), [136](#)
- [104] L. Yin, B. J. Albright, B. M. Hegelich, and J. C. Fernández. GeV laser ion acceleration from ultrathin targets: The laser break-out afterburner. *Laser and Particle Beams*, 24(02):291–298, 2006. [34](#), [36](#), [86](#), [132](#)
- [105] K. J. Bowers, B. J. Albright, L. Yin, B. Bergen, and T. J. T. Kwan. Ultrahigh performance three-dimensional electromagnetic relativistic kinetic plasma simulation. *Physics of Plasmas*, 15(5):055703, 2008. [34](#), [134](#)
- [106] L. Yin, B. J. Albright, D. Jung, R. C. Shah, S. Palaniyappan, K. J. Bowers, A. Henig, J. C. Fernández, and B. M. Hegelich. Break-out afterburner ion acceleration in the longer laser pulse length regime. *Physics of Plasmas*, 18(6):063103, Jun 2011. [35](#), [36](#), [40](#), [90](#), [113](#), [115](#)
- [107] B J Albright, L Yin, B M Hegelich, K J Bowers, C Huang, A Henig, J C Fernández, K A Flippo, S A Gaillard, T J T Kwan, X Q Yan, T Tajima, and D Habs. Ultraintense laser interaction with nanoscale targets: a simple model for layer expansion and ion acceleration. *Journal of Physics: Conference Series*, 244(4):042022, 2010. [37](#), [111](#)
- [108] X. Yan, T. Tajima, M. Hegelich, L. Yin, and D. Habs. Theory of laser ion acceleration from a foil target of nanometer thickness. *Applied Physics B: Lasers and Optics*, 98:711–721, 2010. [38](#), [39](#), [112](#)

- 
- [109] F. Mako and T. Tajima. Collective ion acceleration by a reflexing electron beam: Model and scaling. *Physics of Fluids*, 27(7):1815–1820, 1984. [39](#)
- [110] John Nuckolls, Lowell Wood, Albert Thiessen, and George immerman. Laser compression of matter to super-high densities: Thermonuclear (ctr) applications. *Nature*, 239(5368):139–142, September 1972. [43](#)
- [111] M.T Tobin and et al. Target area for nova upgrade: containing ignition and beyond. *Fusion Engineering*, :650–655, 1991. Retrieved on May 7, 2008. [43](#)
- [112] J. A. Glaze. Shiva: A 30 terawatt glass laser for fusion research. *NASA STI/Recon Technical Report N*, 791:13361, Feb 1978. [43](#)
- [113] W. Koechner. *Solid-State Laser Engineering*. Springer Series in Optical Sciences, 1996. [44](#)
- [114] E. Hecht. *Optics*. Addison-Wesley Publishing Company, 1987. [45](#), [49](#), [119](#)
- [115] Rahul C. Shah, Randall P. Johnson, Tsutomu Shimada, Kirk A. Flippo, Juan C. Fernandez, and B. M. Hegelich. High-temporal contrast using low-gain optical parametric amplification. *Opt. Lett.*, 34(15):2273–2275, 2009. [46](#), [50](#), [51](#), [119](#), [133](#)
- [116] R. P. Johnson, N. K. Moncur, J.A Cobble, R. G. Watt, and Gibson R. B. Trident as an ultrahigh irradiance laser. Los Alamos National Laboratory, 1995. LA-UR-9541. [47](#)
- [117] J. Workman, J. Cobble, K. Flippo, D. C. Gautier, and S. Letzring. High-energy, high-resolution x-ray imaging on the trident short-pulse laser facility. *Review of Scientific Instruments*, 79(10):10E905, 2008. [47](#)
- [118] A. E. Siegman. *Lasers*. University Science Books, 1986. [48](#), [49](#), [50](#)
- [119] M. Born and E. Wolf. *Principles of Optics*. Pergamon Press, 1975.
- [120] A. F. Jenkins and E. W. Harvey. *Fundamentals of Optics*. McGraw-Hill Book Company, Inc., 1937. [49](#)
- [121] B. Dromey, S. Kar, C. Bellei, D. C. Carroll, R. J. Clarke, J. S. Green, S. Kneip, K. Markey, S. R. Nagel, P. T. Simpson, L. Willingale,

## REFERENCES

---

- P. McKenna, D. Neely, Z. Najmudin, K. Krushelnick, P. A. Norreys, and M. Zepf. Bright multi-keV harmonic generation from relativistically oscillating plasma surfaces. *Phys. Rev. Lett.*, 99:085001, Aug 2007. [53](#), [82](#)
- [122] F. Quéré, C. Thaury, P. Monot, S. Dobosz, Ph. Martin, J.-P. Geindre, and P. Audebert. Coherent wake emission of high-order harmonics from overdense plasmas. *Phys. Rev. Lett.*, 96:125004, Mar 2006. [53](#), [82](#)
- [123] M. K. Gupta, R. P. Sharma, and S. T. Mahmoud. Generation of plasma wave and third harmonic generation at ultra relativistic laser power. *Laser and Particle Beams*, 25(02):211–218, 2007. [53](#), [82](#)
- [124] I. G. Brown. Cathodic arc deposition of films. *Annual Review of Material Science*, 28:243–269, 1998. [54](#), [55](#)
- [125] Wolfgang Kautek, Simone Pentzien, Andrea Conradi, Jrg Krger, and Klaus-Werner Brzezinka. Pulsed-laser deposition and boron-blending of diamond-like carbon (dlc) thin films. *Applied Surface Science*, 106:158 – 165, 1996. Proceedings of the Second International Conference on Photo-Excited Processes and Applications. [54](#)
- [126] G. Reisse, S. Weissmantel, and D. Rost. Preparation of super-hard coatings by pulsed laser deposition. *Applied Physics A: Materials Science & Processing*, 79:1275–1278, 2004.
- [127] P.M. Ossi, C.E. Bottani, and A. Miotello. Pulsed-laser deposition of carbon: from dlc to cluster-assembled films. *Thin Solid Films*, 482(1-2):2 – 8, 2005. EMRS 2004, Symposium J. [54](#)
- [128] Iqbal S. Athwal and Elmer A. Ogryzlo. Dlc films by plasma assisted chemical vapor deposition near room temperature. *Diamond and Related Materials*, 2(12):1483 – 1489, 1993. [54](#)
- [129] Kazuhisa Miyoshi, Masao Murakawa, Shuichi Watanabe, Sadao Takeuchi, Shojiro Miyake, and Richard Wu. Cvd diamond, dlc, and c-bn coatings for solid film lubrication. *Tribology Letters*, 5:123–129, 1998.
- [130] A. A. Evtukh, V. G. Litovchenko, N. I. Klyui, R. I. Marchenko, and S. Yu. Kudzinovski. Properties of plasma enhanced chemical vapor deposition

- diamond-like carbon films as field electron emitters prepared in different regimes. *Journal of Vacuum Science Technology B: Microelectronics and Nanometer Structures*, 17(2):679–683, Mar 1999. [54](#)
- [131] Wenjun Ma, V.Kh. Liechtenstein, J. Szerypo, D. Jung, P. Hilz, B.M. Hegelich, H.J. Maier, J. Schreiber, and D. Habs. Preparation of self-supporting diamond-like carbon nanofoils with thickness less than 5nm for laser-driven ion acceleration. *Nuclear Instruments and Methods in Physics Research Section A: Accelerators, Spectrometers, Detectors and Associated Equipment*, 655(1):53–56, 2011. Proceedings of the 25th World Conference of the International Nuclear Target Development Society. [54](#), [85](#)
- [132] J Kutzner and H C Miller. Integrated ion flux emitted from the cathode spot region of a diffuse vacuum arc. *Journal of Physics D: Applied Physics*, 25(4):686–693, 1992. [55](#)
- [133] A Anders, S Anders, and I G Brown. Transport of vacuum arc plasmas through magnetic macroparticle filters. *Plasma Sources Science and Technology*, 4(1):1, 1995. [55](#)
- [134] Yan-Way Li, Yew-Bin Shue, Chia-Fu Chen, Teng-Chien Yu, and Jack Jyh-Kau Chang. Substrate bias effect on amorphous nitrogenated carbon films deposited by filtered arc deposition. *Diamond and Related Materials*, 11(3-6):1227–1233, 2002. [55](#)
- [135] J. Tirira and P. Trocellier. Elastic recoil detection analysis. *Journal of Radioanalytical and Nuclear Chemistry*, 130:311–319, 1989. [57](#)
- [136] G. Gagnon, J. F. Currie, J. L. Brebner, S. C. Gujrathi, and L. Ouellet. The use of elastic recoil detection for stoichiometry determination of reactively evaporated tin layers. *Journal of Applied Physics*, 74(6):4233–4235, Sep 1993. [57](#)
- [137] S.-C. Seo and D. C. Ingram. Fine structures of valence-band, x-ray-excited auger electron, and plasmon energy loss spectra of diamondlike carbon films obtained using x-ray photoelectron spectroscopy. *J. Vac. Sci. Technol. A*, 15(5):2579–2584, 1997. [57](#)

## REFERENCES

---

- [138] C. Popov, W. Kulisch, S. Bliznakov, B. Mednikarov, G. Spasov, J. Pirov, M. Jelinek, T. Kocourek, and J. Zemek. Characterization of the bonding structure of nanocrystalline diamond and amorphous carbon films prepared by plasma assisted techniques. *Applied Physics A: Materials Science & Processing*, 89:209–212, 2007. [57](#)
- [139] A. LiBassi, A. C. Ferrari, V. Stolojan, B. K. Tanner, J. Robertson, and L. M. Brown. Density, sp<sup>3</sup> content and internal layering of dlc films by x-ray reflectivity and electron energy loss spectroscopy. *Diamond and Related Materials*, 9(3-6):771–776, 2000. [57](#), [58](#)
- [140] T. A. Friedmann, J. P. Sullivan, J. A. Knapp, D. R. Tallant, D. M. Follstaedt, D. L. Medlin, and P. B. Mirkarimi. Thick stress-free amorphous-tetrahedral carbon films with hardness near that of diamond. *Appl. Phys. Lett.*, 71(26):3820–3822, 1997. [57](#)
- [141] Joe Tabeling. Applied diamond inc. [online] [www.usapplieddiamond.com](http://www.usapplieddiamond.com). [58](#), [85](#), [133](#)
- [142] J. F. Ziegler, J. P. Biersack, and U. Littmark. The stopping and range of ions in solids. *Pergamon Press*, 1:, 1985. [60](#)
- [143] E. U. Condon and H. Odishaw. *Handbook of Physics*. McGraw-Hill Book Company, Inc., 1958. [60](#)
- [144] R. L. Fleischer, P. B. Price, and R. M. Walker. Ion explosion spike mechanism for formation of charged-particle tracks in solids. *Journal of Applied Physics*, 36(11):3645–3652, 1965. [61](#)
- [145] H. Tawara, T. Doke, T. Hayashi, J. Kikuchi, A. Kyan, S. Nagaoka, T. Nakano, S. Takahashi, K. Terasawa, and E. Yoshihira. Let distributions from cr-39 plates on space shuttle missions sts-84 and sts-91 and a comparison of the results of the cr-39 plates with those of rrm-d-ii and rrm-d-iii telescopes. *Radiation Measurements*, 35(2):119 – 126, 2002. [61](#)
- [146] Junji Miyahara, Kenji Takahashi, Yoshiyuki Amemiya, Nobuo Kamiya, and Yoshinori Satow. A new type of x-ray area detector utilizing laser stimulated

- luminescence. *Nuclear Instruments and Methods in Physics Research Section A: Accelerators, Spectrometers, Detectors and Associated Equipment*, 246(1-3):572–578, 1986. [63](#)
- [147] I J Paterson, R J Clarke, N C Woolsey, and G Gregori. Image plate response for conditions relevant to laserplasma interaction experiments. *Measurement Science and Technology*, 19(9):095301, 2008. [64](#)
- [148] A. Mancic, J. Fuchs, P. Antici, S. A. Gaillard, and P. Audebert. Absolute calibration of photostimulable image plate detectors used as (0.5-20 mev) high-energy proton detectors. *Rev. Sci. Instrum.*, 79(7):073301, 2008. [64](#), [108](#)
- [149] C. G. Freeman, G. Fiksel, C. Stoeckl, N. Sinenian, M. J. Canfield, G. B. Graeper, A. T. Lombardo, C. R. Stillman, S. J. Padalino, C. Mileham, T. C. Sangster, and J. A. Frenje. Calibration of a thomson parabola ion spectrometer and fujifilm imaging plate detectors for protons, deuterons, and alpha particles. *Review of Scientific Instruments*, 82(7):073301, 2011. [64](#), [108](#)
- [150] D. Jung, R. Horlein, D. Kiefer, S. Letzring, D. C. Gautier, U. Schramm, C. Hubsch, R. Ohm, B. J. Albright, J. C. Fernandez, D. Habs, and B. M. Hegelich. Development of a high resolution and high dispersion thomson parabola. *Review of Scientific Instruments*, 82(1):013306, 2011. [64](#), [65](#), [66](#), [67](#), [68](#), [69](#), [70](#), [71](#), [72](#), [133](#)
- [151] J. J. Thomson. The resonance spectra of iodine vapour and their destruction by gases of the helium group. *Philosophical Magazine Series 6*, 22(13):469–481, Oct 1911. [64](#)
- [152] K. Harres, M. Schollmeier, E. Brambrink, P. Audebert, A. Blazevic, K. Flippo, D. C. Gautier, M. Geissel, B. M. Hegelich, F. Nurnberg, J. Schreiber, H. Wahl, and M. Roth. Development and calibration of a thomson parabola with microchannel plate for the detection of laser-accelerated mev ions. *Review of Scientific Instruments*, 79(9):093306, 2008. [65](#), [69](#)
- [153] M. Abramowitz and I. A. Stegun. *Handbook of Mathematical Functions*. United States Department of Commerce, 1964. [66](#)

## REFERENCES

---

- [154] D.C. Carroll, P. Brummitt, D. Neely, F. Lindau, O. Lundh, C.-G. Wahlström, and P. McKenna. A modified thomson parabola spectrometer for high resolution multi-mev ion measurements—application to laser-driven ion acceleration. *Nuclear Instruments and Methods in Physics Research Section A: Accelerators, Spectrometers, Detectors and Associated Equipment*, 620(1):23–27, 2010. [67](#), [68](#), [70](#)
- [155] F. Paschen. Ueber die zum funkenbergang in luft, wasserstoff und kohlen-sure bei verschiedenen drucken erforderliche potentialdifferenz. *Ann. Phys.*, 273:69–96, 1889. [69](#)
- [156] A P L Robinson, P Foster, D Adams, D C Carroll, B Dromey, S Hawkes, S Kar, Y T Li, K Markey, P McKenna, C Spindloe, M Streeter, C-G Wahlstrm, M H Xu, M Zepf, and D Neely. Spectral modification of laser-accelerated proton beams by self-generated magnetic fields. *New Journal of Physics*, 11(8):083018, 2009. [69](#)
- [157] D. Jung, R. Hrlein, D. C. Gautier, S. Letzring, D. Kiefer, K. Allinger, B. J. Albright, R. Shah, S. Palaniyappan, L. Yin, J. C. Fernandez, D. Habs, and B. M. Hegelich. A novel high resolution ion wide angle spectrometer. *Review of Scientific Instruments*, 82(4):043301, 2011. [71](#), [73](#), [74](#), [75](#), [76](#), [98](#), [133](#)
- [158] CST AG. Cst particle studio 2010. [online] [www.cst.com](http://www.cst.com). [73](#)
- [159] Y.V. Rao, A. Davis, T. Spencer, and R.C. Filz. Diameter evolution of proton tracks in cr-39 detector. *Nuclear Instruments and Methods*, 180(1):153–156, 1981. [76](#)
- [160] B. Dromey, C. Bellei, D.C. Carroll, R.J. Clarke, J.S. Green, S. Kar, S. Kneip, K. Markey, S.R. Nagel, L. Willingale, P. McKenna, D. Neely, Z. Najmudin, K. Krushelnick, P.A. Norreys, and M. Zepf. Third harmonic order imaging as a focal spot diagnostic for high intensity laser-solid interactions. *Laser and Particle Beams*, 27(02):243–248, 2009. [82](#)
- [161] Rick Trebino, Kenneth W. DeLong, David N. Fittinghoff, John N. Sweetser, Marco A. Krumbgel, Bruce A. Richman, and Daniel J. Kane. Measuring ultrashort laser pulses in the time-frequency domain using frequency-resolved optical gating. *Rev. Sci. Instrum.*, 68(9):3277–3295, 1997. [82](#)

- 
- [162] M. Schollmeier, S. Becker, M. Geißel, K. A. Flippo, A. Blažević, S. A. Gaillard, D. C. Gautier, F. Grüner, K. Harres, M. Kimmel, F. Nürnberg, P. Rambo, U. Schramm, J. Schreiber, J. Schüttrumpf, J. Schwarz, N. A. Tahir, B. Atherton, D. Habs, B. M. Hegelich, and M. Roth. Controlled transport and focusing of laser-accelerated protons with miniature magnetic devices. *Phys. Rev. Lett.*, 101:055004, Aug 2008. [97](#)
- [163] F. Nürnberg, M. Schollmeier, E. Brambrink, A. Blažević, D. C. Carroll, K. Flippo, D. C. Gautier, M. Geissel, K. Harres, B. M. Hegelich, O. Lundh, K. Markey, P. McKenna, D. Neely, J. Schreiber, and M. Roth. Radiochromic film imaging spectroscopy of laser-accelerated proton beams. *Review of Scientific Instruments*, 80(3):033301, 2009. [100](#)
- [164] L. Yin, B. J. Albright, K. J. Bowers, D. Jung, J. C. Fernández, and B. M. Hegelich. Three-dimensional dynamics of breakout afterburner ion acceleration using high-contrast short-pulse laser and nanoscale targets. *Phys. Rev. Lett.*, 107(4):045003, Jul 2011. [101](#), [102](#), [135](#)
- [165] T. Tajima, D. Habs, and X. Yan. Laser acceleration of ions for radiation therapy. *Rev. Accel. Sci. Tech.*, 2:201–228, 2009. [103](#), [118](#)
- [166] D. Jung, L. Yin, B.J. Albright, D.C. Gautier, S. Letzring, B. Dromey, M. Yeung, R. Hörlein, R. Shah, S. Palaniyappan, K. Allinger, D. Kiefer, K.J. Bowers, J. Schreiber, T. Tajima, J.C. Fernández, D. Habs, and B.M. Hegelich. Conversion efficiency measurements of laser-accelerated carbon ions from nm-scale targets. *Phys. Rev. Lett.*, submitted:, 2011. [110](#), [111](#)
- [167] S.Y. Kalmykov, S.A. Reed, S.A. Yi, A. Beck, A.F. Lifschitz, X. Davoine, E. Lefebvre, V. Khudik, G. Shvets, P. Dong, X. Wang, D. Du, S. Bedacht, Y. Zhao, W. Henderson, A. Bernstein, G. Dyer, M. Martinez, E. Gaul, T. Ditmire, and M.C. Downer. Laser wakefield electron acceleration on texas petawatt facility: Towards multi-gev electron energy in a single self-guided stage. *High Energy Density Physics*, 6(2):200 – 206, 2010. ICHED 2009 - 2nd International Conference on High Energy Density Physics. [114](#)
- [168] Coherent. Coherent inc. [online] [www.coherent.com](http://www.coherent.com). [116](#)
- [169] Mitsui. Mitsui chemicals america, inc. [online] <http://www.mitsuichemicals.com>. [117](#)

## REFERENCES

---

- [170] S.V Bulanov, T.Zh Esirkepov, V.S Khoroshkov, A.V Kuznetsov, and F Pegoraro. Oncological hadrontherapy with laser ion accelerators. *Physics Letters A*, 299(2-3):240 – 247, 2002. [118](#)
- [171] A. P. L. Robinson, M. Zepf, R. G. Kar, S. Evans, and C. Bellei. Radiation pressure acceleration of thin foils with circularly polarized laser pulses. *New Journal of Physics*, 10:013021, 2008. [124](#), [137](#)
- [172] A. I. Akhiezer and R. V. Polovin. Theory of wave motion of an electron plasma. *Sov. Phys. JETP*, 3(696):696–705, 1956. [126](#), [137](#)
- [173] Robert J. Noble. Plasma-wave generation in the beat-wave accelerator. *Phys. Rev. A*, 32(1):460–471, Jul 1985. [126](#), [137](#)
- [174] A. Zhidkov, M. Uesaka, A. Sasaki, and H. Daido. Ion acceleration in a solitary wave by an intense picosecond laser pulse. *Phys. Rev. Lett.*, 89(21):215002, Nov 2002. [127](#)
- [175] B. M. Hegelich, B. Albright, P. Audebert, A. Blazevic, E. Brambrink, J. Cobble, T. Cowan, J. Fuchs, J. C. Gauthier, C. Gautier, M. Geissel, D. Habs, R. Johnson, S. Karsch, A. Kemp, S. Letzring, M. Roth, U. Schramm, J. Schreiber, K. J. Witte, and J. C. Fernandez. Spectral properties of laser-accelerated mid-z mev/u ion beams. *Physics of Plasmas*, 12(5):056314, 2005. [131](#)
- [176] J. Schreiber, M. Kaluza, F. Grner, U. Schramm, B.M. Hegelich, J. Cobble, M. Geissler, E. Brambrink, J. Fuchs, P. Audebert, D. Habs, and K. Witte. Source-size measurements and charge distributions of ions accelerated from thin foils irradiated by high-intensity laser pulses. *Applied Physics B: Lasers and Optics*, 79:1041–1045, 2004. [131](#)
- [177] D. Jung, L. A. Gizzi, L. Labate, D. Neely, M. M. Notley, P. P. Rajeev, M. Roth, and G. Gregori. Experimental characterization of picosecond laser interaction with solid targets. *Physical Review E*, 77(5, Part 2):056403, May 2008. [139](#)
- [178] A. B. Sefkow, G. R. Bennett, M. Geissel, M. Schollmeier, B. C. Franke, and B. W. Atherton. Efficiency enhancement for  $k_{\alpha}$  x-ray yields from laser-

## REFERENCES

---

driven relativistic electrons in solids. *Phys. Rev. Lett.*, 106:235002, Jun 2011. [140](#)

# Peer reviewed publications

## 2011

1. **D. Jung**, L. Yin, B. J. Albright, D. C. Gautier, R. Hörlein, D. Kiefer, A. Henig, R. Johnson, S. Letzring, S. Palaniyappan, R. Shah, T. Shimada, X. Q. Yan, K. J. Bowers, T. Tajima, J. C. Fernández, D. Habs, and B. M. Hegelich. *Monoenergetic ion beam generation by driving ion solitary waves with circularly polarized laser light*. Phys. Rev. Lett., **107** 115002, (2011).
2. **D. Jung**, R. Hrlein, D. C. Gautier, S. Letzring, D. Kiefer, K. Allinger, B. J. Albright, R. Shah, S. Palaniyappan, L. Yin, J. C. Fernndez, D. Habs, and B. M. Hegelich. *A novel high resolution ion wide angle spectrometer*. Review of Scientific Instruments, **82** 043301(2011).
3. **D. Jung**, R. Horlein, D. Kiefer, S. Letzring, D. C. Gautier, U. Schramm, C. Hubsch, R. Ohm, B. J. Albright, J. C. Fernandez, D. Habs, and B. M. Hegelich. *Development of a high resolution and high dispersion thomson parabola*. Review of Scientific Instruments, **82** 013306 (2011).
4. B. M. Hegelich, **D. Jung**, B. J. Albright, J. C. Fernandez, D. C. Gautier, C. Huang, T. J. Kwan, S. Letzring, S. Palaniyappan, R. C. Shah, H.-C. Wu, L. Yin, A. Henig, R. Hörlein, D. Kiefer, J. Schreiber, X. Q. Yan, T. Tajima, D. Habs, B. Dromey, and J. J. Honrubia. *Experimental demonstration of particle energy, conversion efficiency and spectral shape required for ion-based fast ignition*. Nuclear Fusion, **51** 083011 (2011).

- 
5. L. Yin, B. J. Albright, K. J. Bowers, **D. Jung**, J. C. Fernández, and B. M. Hegelich. *Three-dimensional dynamics of breakout afterburner ion acceleration using high-contrast short-pulse laser and nanoscale targets*. Phys. Rev. Lett., **107** 045003 (2011).
  6. L. Yin, B. J. Albright, **D. Jung**, R. C. Shah, S. Palaniyappan, K. J. Bowers, A. Henig, J. C. Fernández, and B. M. Hegelich. *Break-out afterburner ion acceleration in the longer laser pulse length regime*. Physics of Plasmas, **18** 063103 (2011).
  7. L. Yin, B. J. Albright, **D. Jung**, K. J. Bowers, R. C. Shah, S. Palaniyappan, J. C. Fernández, and B. M. Hegelich. *Mono-energetic ion beam acceleration in solitary waves during relativistic transparency using high-contrast circularly polarized short-pulse laser and nanoscale targets*. Physics of Plasma, **18** 053103 (2011).
  8. W. Ma, V. Kh. Liechtenstein, J. Szerypo, **D. Jung**, P. Hinz, B. M. Hegelich, H. J. Maier, J. Schreiber, D. Habs. *Preparation of self-supporting diamond-like carbon nanofolios with thickness less than 5nm for laser-driven ion acceleration*. Nucl. Instr. and Methods in Physics Research Section A, **655** 53-56 (2011)
  9. S. Steinke, M. Schnuerer, T. Sokollik, A. A. Andreev, P. V. Nickles, A. Henig, R. Hoerlein, D. Kiefer, **D. Jung**, J. Schreiber, T. Tajima, M. Hegelich, D. Habs and W. Sandner. *Optimization of Laser-Generated Ion Beams*. Contributions to Plasma Physics **51** 444-450 (2011).

## 2010

10. S. Palaniyappan, R. C. Shah, R. Johnson, T. Shimada, D. C. Gautier, S. Letzring, **D. Jung**, R. Hoerlein, D. T. Offermann, J. C. Fernández and B. M. Hegelich. *Pulse shape measurements using single shot-frequency resolved optical gating for high energy (80 J) short pulse (600 fs) laser*. Review of Scientific Instruments, **81** 10E103 (2010).

## 5. PEER REVIEWED PUBLICATIONS

---

11. S. Steinke, A. Henig, M. Schnrer, T. Sokollik, P.V. Nickles, **D. Jung**, D. Kiefer, R. Hrlein, J. Schreiber, T. Tajima, X.Q. Yan, M. Hegelich, J. Meyer-ter Vehn, W. Sandner, and D. Habs. *Efficient ion acceleration by collective laser-driven electron dynamics with ultra-thin foil targets*. Laser and Particle Beams, **28** 215-221 (2010).

### 2009

12. A. Henig, S. Steinke, M. Schnürer, T. Sokollik, R. Hörlein, D. Kiefer, **D. Jung**, J. Schreiber, B. M. Hegelich, X. Q. Yan, J. Meyer-ter Vehn, T. Tajima, P. V. Nickles, W. Sandner, and D. Habs. *Radiation-pressure acceleration of ion beams driven by circularly polarized laser pulses*. Phys. Rev. Lett., **103** 245003 (2009).
13. A. Henig, D. Kiefer, K. Markey, D. C. Gautier, K. A. Flippo, S. Letzring, R. P. Johnson, T. Shimada, L. Yin, B. J. Albright, K. J. Bowers, J. C. Fernández, S. G. Rykovanov, H.-C. Wu, M. Zepf, **D. Jung**, V. Kh. Liechtenstein, J. Schreiber, D. Habs, and B. M. Hegelich. *Enhanced laser-driven ion acceleration in the relativistic transparency regime*. Phys. Rev. Lett., **103** 045002 (2009).
14. D. Kiefer, A. Henig, **D. Jung**, D. C. Gautier, K. A. Flippo, S. A. Gaillard, S. Letzring, R. P. Johnson, R. C. Shah, T. Shimada, J. C. Fernandez, V. Kh. Liechtenstein, J. Schreiber, B. M. Hegelich, and D. Habs. *First observation of quasi-monoenergetic electron bunches driven out of ultra-thin diamond-like carbon (dlc) foils*. European Physical Journal D, **55** 427-432 (2009).
15. P. G. Thirolf, D. Habs, A. Henig, **D. Jung**, D. Kiefer, C. Lang, J. Schreiber, C. Maia, G. Schaller, R. Schuetzhold and T. Tajima. *Signatures of the Unruh effect via high-power, short-pulse lasers*. European Physical Journal D, **55** 379-389 (2009).

---

## 2008

16. D. Habs, M. Hegelich, J. Schreiber, M. Gross, A. Henig, D. Kiefer, and **D. Jung**. *Dense laser-driven electron sheets as relativistic mirrors for coherent production of brilliant x-ray and gamma-ray beams*. Applied Physics B - Lasers and Optics, **93** 349-354 (2008).
17. **D. Jung**, L. A. Gizzi, L. Labate.; D. Neely, M. M. Notley, P. P. Rajeev, M. Roth and G. Gregori. *Experimental characterization of picosecond laser interaction with solid targets*. Physical Review E, **77** 056403 (2008)

## 2007

18. E. G. Saiz, F. Y. Khattak, G. Gregori, S. Bandyopadhyay, R. J. Clarke, B. Fell, R. R. Freeman, J. Jeffries, **D. Jung**, M. M. Notley, R. L. Weber, L. van Woerkom and D. Riley. *Wide angle crystal spectrometer for angularly and spectrally resolved x-ray scattering experiments*. Review of Scientific Instruments **78** 095101 (2007)

## Submitted Paper

19. **D. Jung**, L. Yin, B. J. Albright, D. C. Gautier, S. Letzring, B. Dromey, M. Yeung, R. Hörlein, R. Shah, S. Palaniyappan, K. Allinger, D. Kiefer, K. J. Bowers, J. Schreiber, T. Tajima, J. C. Fernández, D. Habs, B. M. Hegelich. *Conversion efficiency measurements of laser-accelerated carbon ions from nm-scale targets*. Phys. Rev. Lett. **submitted** (2011)
20. S. Palaniyappan, R. Shah, H.-C. Wu, C. D. Gautier, **D. Jung**, L. Yin, S. Letzring, B. Dromey, B. J. Albright, R. P. Johnson, T. Shimada, J. C. Fernández and B. M. Hegelich. *High Resolution Dynamics of Ultra-fast Optical Switching in Relativistically Transparent Overdense Plasma*. Nat. Phys. **submitted** (2011)

## 5. PEER REVIEWED PUBLICATIONS

---

21. R. Shah, S. Palaniyappan, H. C. Wu, D. C. Gautier, **D. Jung**, R. Hörlein, D. Offermann, J. Ren, L. Yin, B. J. Albright, R. P. Johnson, T. Shimada, J. C. Fernández and B. M. Hegelich. *Laser Pulse Shortening via Femtosecond Dynamics of Relativistic Transparency*. Nat. Phys. **submitted** (2011)

---

## Acknowledgements

Finally, I would like to thank all my collaborators, colleagues and friends. Their help and continuous support has been an important contribution to this thesis.

Special thanks go to Prof. Dietrich Habs for being an enthusiastic and also very visionary supervisor.

I would like to thank Prof. Manuel Hegelich for giving me the chance to work at the Los Alamos National Laboratory, which has been an excellent scientific environment for my PhD work. He was not only a great mentor, but is also a good friend.

I am also grateful to Prof. Jörg Schreiber for agreeing to be the second referee of my PhD thesis.

Daniel Kiefer, Andreas Henig and Rainer Hörlein have not only been excellent collaborators spending countless hours in the labs, but are also good friends that share many good and some bad, but mostly funny moments with me.

I would also like to thank Cort Gautier, who has been a good friend spending a great amount of time with me in the lab. His experience in the lab has been of great help and I will remember many of the fruitful, although mostly not physics related discussions.

I am very grateful for the excellent support and many helpful discussions with Sam Letzring. He is one of the most skilled persons I have ever met and it has been an honor to work with him.

I also thank Rahul Shah and Sasikumar Palaniyappan for their great work on analyzing the Trident laser. Their work has been an essential part in understanding the details of the Break-Out Afterburner. Many thanks also go to Lin Yin, Hui Chun Wu and especially to Brian Albright for sharing their wisdom and extraordinary expertise in the field of theoretical physics with me. Their work on PIC simulations

and analytical theory has been a very important contribution to this thesis.

I am furthermore thankful for the support in the target preparation by Jerzy Szerypo, Hans-Jörg Maier and Dagmar Frischke. Special thanks go to the technical staff and the mechanical workshop at LMU, including Rolf Öhm and Johannes Wulz, for their crucial help in preparing many different experimental setups. Thanks also go to the TRIDENT crew, including Randy Johnson, Tom Shimada, Fred Archuletta, Ray Gonzales and Sha-Marie Reid for providing the worlds best laser system.

I acknowledge the International Max-Planck Research School on Advanced Photon Science for financial and intellectual sponsorship throughout my PhD studies.

Finally I want to express my deepest gratitude to my parents Monika and Werner that supported me throughout my whole life. This thesis is the result of their continuous support and help.

Last but not least, my very special tanks go to my wife Jennifer. Thank you for your loving support during my study, even when doing research abroad, and also for our two beautiful children Luka and Lara.